l'université nantes angers le mans

PÔLE DE RECHERCHE ET D'ENSEIGNEMENT SUPÉRIEUR

UNIVERSITÉ DE NANTES

Thèse de Doctorat

Xiaoting XIAO

Mémoire présenté en vue de l'obtention
du grade de Docteur de l'Université de Nantes
Sous le label de l'Université Nantes Angers Le Mans

Discipline : Electronique, microélectronique, nanoélectronique et micro-ondes
Laboratoire : l'Institut français des sciences et technologies des transports, de l'aménagement et des réseaux

Soutenue le 8 Décembre 2015

École doctorale : Sciences et technologies de l'information, et mathématiques
Thèse N° : 00000000

Détermination de gradients de teneur en eau dans les bétons par méthodes électromagnétiques

JURY

Rapporteurs :	**M. Lambot Sébastien**, Professeur des universités, Université catholique de Louvain (BE) **M. Balayssac Jean-Paul**, Professeur des universités, INSA de Toulouse
Examinateurs:	**M. Taillade Frédéric**, Ingénieur de recherche titulaire de l'HDR, EDF-R&D **M. Khelidj Abdelhafid**, Professeur des universités, IUT de Saint Nazaire **M. Pottier Eric**, Professeur des universités, Universié de Rennes 1
Invité:	**M. Bourlier Christophe**, Directeur de recherche, École polytechnique de l'université de Nantes
Directeur de thèse :	**M. Dérobert Xavier**, Ingénieur divisionnaire des travaux publics de l'Etat, HDR, Université de Nantes
Co-directeur de thèse :	**M^{me} Villain Géraldine**, Ingénieur divisionnaire des travaux publics de l'Etat, HDR, Ifsttar, Nantes
Co-encadrant de thèse :	**M. Ihamouten Amine**, Ingénieur des travaux publics, Cerema, Angers

Acknowledgments

The successful completion of this thesis would not have been possible without the support and help of many people.

The Ph.D. was done under the supervision of Dr. Xavier Dérobert, Dr. Géraldine Villain and Dr. Amine Ihamouten. The author would like to thank them, for their listening, advices and patience; this adventure was wonderful at your sides.

I would also like to thank Dr. Christophe Bourlier and Prof. Abdelhafid Khelidj for their contribution to this work.

I am grateful to Odile Coffec, Anaëlle Joubert, Jean-Luc Geffard, Jacques Kerveillant, Olivier Durand and Jean-luc Sorin for their invaluable assistance during the measurement campaigns.

I am grateful to the reviewers of my defence committee: Prof. Jean-Paul Balayssac and Prof. Sébastien Lambot for investing their expertise and time to review this dissertation. I am also grateful to Dr. Frédéric Taillade and Prof. Eric Pottier for their highly appreciated participation in the defence committee.

I would like to thank the "Institut français des sciences et technologies des transports, de l'aménagement et des réseaux (Ifsttar)" and the "Pays de la Loire" regional council for funding my research work.

Many thanks go to my friends in France for their constant support.

I owe the utmost gratitude to my parents for their endless love...

Nantes, October 2015

Titre: Détermination de gradients de teneur en eau dans les bétons par méthodes électromagnétiques

Résumé:
Les problèmes de vieillissement des structures de génie civil nécessitent l'évaluation des indicateurs de durabilité (comme la porosité) et des paramètres d'état (comme la teneur en eau et la teneur en chlorure). Parmi les techniques de contrôle non destructif électromagnétique (EM), le radar géophysique (GPR) est utilisé pour estimer la permittivité du béton.
L'étude générale est composée de trois objectifs. Tout d'abord, établir une interaction physique et mathématique entre les ondes et les matériaux. Pour mieux comprendre la propagation des ondes EM à l'intérieur du matériau, nous avons étudié plusieurs modèles de dispersion caractérisant les propriétés diélectriques de béton: le modèle de Debye et le modèle de Jonscher proposant de bonnes performances. Deuxièmement, développer une nouvelle méthode d'auscultation pour détecter les gradients de permittivité dans un matériau dispersif en considérant le matériau comme un guide d'ondes. La vitesse de phase des ondes électromagnétiques guidées est utilisée pour extraire les informations diélectrique et géométrique de celui-ci. Une nouvelle méthode d'inversion est mise en oeuvre pour répondre au problème. Le guide d'onde à une couche est ensuite décliné en guide d'ondes à plusieurs couches à l'aide d'un modèle de mélange diélectrique: le modèle parallèle. Ainsi, le nouveau modèle de guide d'onde multi-couches est validé à la fois sur des données synthétiques et expérimentales. Enfin, un suivi expérimental d'imbibition d'eau dans du béton est réalisé avec cette nouvelle méthode d'auscultation, les résultats étant comparés à ceux de gammadensimétrie, considérée comme référence.

Mots-clés: Radar géophysique, constante diélectrique, ondes guidées dispersives, inversion, béton, teneur en eau

Title: Determination of water content's gradients in concretes using electromagnetic methods

Abstract:
Considering the aging problems of civil engineering structures induces the evaluation of durability indicators (such as porosity) and durability monitoring parameters (such as water content and chloride content). From the electromagnetic (EM) non-destructive testing, Ground penetrating radar (GPR) is used by surveying permittivity inside concrete.
The general study is composed of three objectives. Firstly, establish a physical and mathematical interaction between the waves and the materials. To better understand the propagation of EM waves inside the material, we have studied on several dispersion models characterizing the dielectric properties of concrete, and used Debye's model and Jonscher's model getting good working performance. Secondly, develop a new method for GPR to detect the gradients of relative permittivity in a dispersive material. With knowledge of the speed of radar waves travelling through the medium, we are able to know the relative permittivity of the material. As the material can form a waveguide for EM waves. The phase velocity of the guided EM waves is used to extract the dielectric and geometric information of it. Then, a new inversion method is implemented to estimate the dielectric permittivity and geometry of the waveguides. The one-layer waveguide is developed into multi-layer waveguide by a dielectric mixing model: parallel model. Thus, the new multi-layer waveguide model is validated both on synthetic and experimental data. Finally, monitor water transferring inside the concrete slabs with the new developed method, the results being compared with those from gammadensimetry, considered as reference.

Keywords: Ground penetrating radar, dielectric constant, waveguide dispersion, inversion, concrete, water content

Contents

List of Figures

List of Tables

Acronyms and Abbreviations

AC : Alternating Current

ACI : American Concrete Institute

AFGC : Association Français de Génie Civil

ASTM : American Society for Testing and Materials

AW : Air Wave

CMP : Common Midpoint

DC : Direct Current

DT : Destructive Testing

DW : Direct Wave

ECS : Embedded Capacitor Sensor

EM : Electromagnetic

EMAT : Laser and Electromagnetic Acoustic Transducers

ERT : Electrical Resistivity Tomography

FDTD : Finite-Difference Time-Domain

FFT : Fast Fourier Transform

GGBS : Ground Granulated Blast Furnace Slag

GPR : Ground Penetrating Radar

HP : High-Pass

LP : Low-Pass

NDT : Nondestructive Testing

PEC : Perfect Electric Conductor

PFA : Pulverized Fly Ash

PML : Perfectly Matched Layers

REV : Representative Elementary Volume

RH : Relative Humidity

RW : Reflected Wave

SF : Silica Fumes

TE : Transverse Electric

TM : Transverse Magnetic

UT : Ultrasonic Testing

VNA : Vector Network Analyzer

WARR : Wide Angle Reflexion Refraction

WG : Waveguide

W/C : Water to Cement Ratio

Chapter 1

Introduction

Contents

1.1 Context

With the development of human civilization, the constructions of housing, factories, commercial buildings, bridges, tunnels and other infrastructures require enormous quantities of building materials. Concrete, especially reinforced concrete, is certainly the most popular material today. By volume, the largest manufactures product in the world today is concrete [Mehta, P. Kumar, 2006]. In China, reinforced concrete is the main material used in the industrial constructions. As the establishment of concrete's technical standards, the construction quality becomes one of the main topics to be concerned and improved in the future [Jiang, 2015]. For durability reasons, efficient techniques are required to ensure that durability criteria are satisfied during construction [Kosmatka and Wilson, 2011]. Furthermore, existing structures need some means to monitor their performance and to predict their durability over the service life [Song and Saraswathy, 2007; Torres-Luque et al., 2014].

Concerning concrete, many factors can cause degradation or deterioration of it. The physical processes include freezing-thawing cycles, fire, water erosion, etc. The freezing-thawing cycles cause cracks in concrete, which decrease the concrete strength and increase its permeability [Wang et al., 1997]. Fire causes complex physicochemical transformations in concrete by heating, which may lead to structural failure [Khoury, 2000]. Water erosion, especially abrasive erosion, results in surface damage of concrete structures [Liu et al., 2006]. The chemical ones refer to carbonation, chloride ingress, steel corrosion and so on. The carbonation of concrete increases concrete strength. However, it decreases the pH value. Once the carbonation reaches the reinforcement, the low pH environment will lead to the depassivation of steel reinforcement, and as a result, accelerate the corrosion [Villain et al., 2007]. Chloride and water penetrating into the concrete are the main cause of the steel corrosion, regarded as the main cause of degradation [AFGC, 2007; Villain

et al., 2012]. As a conclusion, almost all the processes are combined with water. The evaluation of water content in concrete thus becomes a considerable subject to study.
Many studies have been done on the tests of concrete to address durability problems [AFGC, 2007]. Traditional destructive testing (DT) methods are usually expensive and time consuming, and the most importantly, cause damage to the tested structures. Non-destructive testing (NDT) methods have therefore been developed to be more efficient means for concrete assessment. Commonly used NDT techniques include ultrasonic test [Zhang et al., 2012; Garnier et al., 2013], half-cell potential test [Babaei, 1986], resistivity test [du Plooy, 2013] and electromagnetic methods, such as capacitive technique and Ground Penetrating Radar (GPR) [Dérobert et al., 2008]. Among the NDT techniques, electromagnetic (EM) methods have been introduced to the non-destructive evaluation of concrete since EM waves are sensitive to the geometrical properties as well as the dielectric properties of the materials [Rhim and Büyüköztürk, 1998; Büyüköztürk, 1998]. In summary, EM techniques are sensitive to the presence of water and chloride and can be used to monitor the condition of concrete over time.

1.2 Problem Statement

Though EM techniques have already been widely used in the NDT of concrete, the study on the applications for assessing durability indicators, such as carbonation depth, chloride content, water content, is still at the early stage.
To determine the carbonation depth, the existing technique includes colorimetric test by spraying the phenolphthalein [AFGC, 2007], thermogravimetry and gammadensimetry according to the work of Villain et al. [Villain and Thiery, 2006]. However, the methods are either destructive or in need of drilling cores for the measurement.
In most studies for evaluating the water content or chloride content, concrete is conditioned in homogeneous state [Klysz and Balayssac, 2007; Hugenschmidt and Loser, 2007; Balayssac et al., 2012]. However, for in situ assessment, the concrete condition is much more complex.
The existing concrete structures may be degraded by several reasons, such as the carbon dioxides, the water and sea water. Moreover, the distribution of carbonation, water or chloride usually varies through the depth of the structure. The influence on EM response varies at different depths since these factors usually distribute gradients inside concrete [Kalogeropoulos et al., 2013]. Some work of the gradients determination for concrete with EM methods has been reported as the variation of water content or chloride content [Louis et al., 2012; du Plooy et al., 2015a; Kalogeropoulos et al., 2013]. Some studies have been contributed to the modeling of planar layered media with Green's function [Lambot et al., 2004, 2007; Ardekani and Lambot, 2014]. However, there still needs more work to be done in this field. The research therefore focuses on the investigation of gradients of dielectric properties in concrete, which can be linked with the gradients of water content and chloride content.

1.3 Objectives

The final objective of this work is to determine the water content gradients in concrete by electromagnetic (EM) methods. To achieve it, the objectives at different steps can be

summarized as follows:

I Adopting a dispersion model to characterize the dielectric properties of dispersive media such as concrete, as a function of frequency in the radar frequency range. This model is capable of reproducing propagation effects of EM waves in dispersive media.

II Modeling EM waves' propagation in concrete with the adopted dispersion model to study the extraction of dispersion curves from GPR measurements, showing the phase velocities versus frequency.

III Developing a multi-layer model of the surveyed medium to characterize the gradients of dielectric properties of dispersive layers.

IV Using homogenization theory to build links between the durability indicators of concrete, such as carbonation depth, chloride content, water content, and the dielectric permittivity of the material.

V Determining the gradients of dielectric permittivity of concrete with EM waves' propagation in order to determine the gradients of chloride and (or) water content of concrete.

1.4 Structure of the thesis

The main part of this dissertation consists of five chapters. The following of this section is an overview of the five chapters:

- Chapter 2 introduces the composition of concrete and its aging problem. Some parameters are closely related to the durability of concrete, such as the durability indicator: porosity; and the durability monitoring parameters: water content, chloride content, carbonation depth. Then, to evaluate these parameters, we have some evaluation methods presented here in two categories: destructive methods and non-destructive (ND) methods. Each method is discussed with its principle and applications to the indicator and parameters of durability. The ground penetrating radar (GPR), applied as the main EM ND method in our study, is proved to be very sensitive to the variation of water content. Two semi-destructive methods, requiring cylindrical samples of concrete, are associated with the application of GPR. The EM coaxial/cylindrical cell (also called EM cell), offering frequency dependent complex permittivity, is used as a calibration of water content and chloride content for GPR. The results of gammadensimetry are used as the reference results of water content gradient in concrete slabs in the tests of water imbibition.

- Chapter 3 presents the study on propagation of EM waves in concrete in two steps. First, it presents some basic theories of EM wave's propagation and some dielectric models to characterize concrete. The models include two dispersion models: Debye's model and Jonscher's model, and one homogenization model: Lichtennecker-Rother equation. A survey on the availability of the two dispersion models is conducted with the non-linear curve fitting of EM cell data of concrete. Debye's model works well in certain frequency bandwidth and is simpler to be applied with the GPR modeling software Gprmax. Jonscher's model is available in wider bandwidth and can be used to

do the extrapolation for EM cell data. Second, the GPR system used in our study is discussed with its configurations and transmitting signals. The received signals in the air match well with the synthetic signals generated by Debye's model.

- Chapter 4 studies the multi-layer waveguide (WG) model in forward problem and inverse problem. The accuracy of phase velocity dispersion curve depends on the acquisition and pre-processing of GPR data. In forward study, the multi-layer WG model is validated for two-layer, three-layer and arctan(x) models. The dispersion curves from synthetic WG model match well with the GPR numerical model. Then, the WG inversion is validated for two-layer model with numerical data and multi-offset GPR measurement (in common midpoint (CMP) configuration) on two layers of homogeneous materials. The arctan(x) model, modeling the gradient curve in concrete during imbibition, is validated with the numerical data of two gradient configurations.

- Chapter 5 presents the plans of all the experiments in this thesis. Two projects are integrated in the experiments: EvaDéOS and APOS. In project EvaDéOS (a French national project), there are two programs of experiments. The first one is to test the concrete slabs with four different carbonation depths: 0 mm, 10 mm, 20 mm and 40 mm. The second one is the test of water imbibition by capillary effects. The project APOS (a Ifsttar-Cerema collaborated project) also includes two programs of experiments. One is the water imbibition with non-reinforced concrete slabs. The other one is the sea water imbibition with reinforced concrete slabs. The chloride content of the water is 35 g/L. The experiments of each project are presented in the objectives, concrete formulation, the specimens, preconditioning process, tests planning, etc. A preview of the experimental results decides the results to be analysed in next chapter. Then the results of EM cell for the concrete of the two projects are given as a calibration of the NDT results.

- Chapter 6 analyses the experimental results of GPR measurements from the experiments presented in chapter 5. There are generally three kinds of experiments presented in this chapter: carbonation, water imbibition and sea water imbibition. The GPR signals are first analysed by extracting the normalized peak-to-peak amplitudes. Then the dielectric constants of carbonated slabs are calculated from the 4-offset GPR data. The penetrating of water and sea water are monitored by the waveguide inversion with two-layer model and arctan(x) model. The inversion results are then compared with the measurements of gammadensimetry.

Finally, the dissertation ends with a summary of our main contributions and some prospectives for the future research.

Chapter 2

Causes of Degradation of Reinforced Concrete

Contents

2.1 Introduction

The objective of this chapter is to have a general view of the degradation problem of concrete, and then to find suitable (Non-destructive testing) NDT methods for evaluating the problem.

In natural environment, many factors can cause the degradation and deterioration of concrete, such as the water, carbonation, chloride, etc. They are usually presented as gradients inside concrete. The durability of concrete strongly depends on these factors. An efficient and harmless method determining the gradients in concrete is therefore required for the monitoring of durability.

This chapter starts by a general description of concrete during ageing, introducing the composition, the ageing of concrete, and its durability. We are not going to talk about early age concrete, because we care more about the built concrete and its performance during service life. Some durability indicators and monitoring parameters will be introduced in the section of durability. Then we will discuss and compare the commonly used test methods on concrete: destructive and non-destructive ones. Some conclusions will be summarized in the end.

2.2 Description of Concrete

Concrete, known as a complex composite construction material, has several kinds of components inside. In this section, we are going to have an overview of concrete's components, its main properties and how it reacts with the outside environment. All the reactions presented in this section are related to the degradation and durability of concrete.

2.2.1 Components

The primary components of concrete includes aggregates like fine sand and coarse gravel; cement, with water to harden in forms of the shape and dimensions of the desired structure [Baron and Sauterey, 1982; Neville, 1995; Nilson et al., 2010]. Sometimes, mineral additions and chemical admixtures are also added in concrete mix designs to obtain certain characteristics. Also, as concrete has high compressive strength, but weak tensile strength, reinforcements put into the concrete can increase the tensile performance. Such material is called reinforced concrete. It is the most widely used concrete in civil engineering constructions. Here is a brief introduction of main components used in the concrete mix design [Neville, 1995; Mehta, P. Kumar, 2006].

2.2.1.a Cement

Cement is a material serving as a binder for aggregates. Cements, that not only harden by reacting with water but also form a water resistant product, are called hydraulic cements (ex. Portland cement). So, they can harden even underwater or when constantly exposed to wet weather. Portland cement (Type CEM I in European standard [EN197-1, 2000]) and its various modifications (CEM II mainly) are the principal cements for making concrete in construction engineering today.

2.2.1.b Aggregates

Aggregates are generally coarse gravels or crushed rocks such as limestone, or siliceous aggregates like granite, along with fine aggregates (diameter ≤ 4 mm) such as sand. Unlike cement, aggregates are supposed not to have any chemical reaction with the water, so they are treated as inert filler in concrete. They occupy about 60% to 80% of the total volume. Aggregate characteristics that are significant for making concrete include porosity, grading or size distribution, moisture absorption, shape and surface texture, crushing strength, elastic modulus, and the type of deleterious substances present [Mehta, P. Kumar, 2006].

2.2.1.c Reinforcement

Because concrete has weak tensile strength, steel bars or wires are embedded inside to increase it. However, the corrosion of steel is a common durability problem in reinforced concrete structures. Typically, concrete is alkaline and the pH value equals to about 13. This high pH leads to the formation of a protective layer on steel, phenomenon called passivation of reinforcement. When carbon dioxide or chloride ions penetrate into concrete, the pH of concrete goes down. When the value drops below about 10 or 11, the rebars are not passivated any more and the corrosion can start [MacGregor et al., 1997]. The passive layer protecting the steel is disrupted, causing the steel to rust. For corrosion

to occur, there must be a source of oxygen and moisture. Therefore, several problems should be paid attention to prevent corrosion [AFGC, 2007; Nilson et al., 2010]. First, the concrete covering thickness over reinforcing bars must be sufficient. Second, cracks of the concrete will facilitate the penetration of corrosion agents. Indeed, once the steel is exposed to the air, it can rust very rapidly. Third, water to cement (W/C) ratio is low enough to slow down the carbonation and the penetration of chloride. To lower the W/C ratio, we can reduce water content or increase cement content. Some mineral additions and admixtures can be used for such properties.

2.2.1.d Mineral additions

In recent years, there is a trend to include mineral additions in the concrete mix, either for economic reasons or for improvements to the environmental performance of cement. Mineral additions are defined as fly ash, silica fumes (SF), ground granulated blast furnace slag (GGBS), limestone additions or siliceous additions [AFGC, 2007]. It is already reported that silica fume, ground granulated blast furnace slag and pulverized fly ash (PFA) can improve the mechanical performance and durability of concrete, first by filling the pores and aggregates inter spaces [De Larrard and Sedran, 2002] and second by increasing strength due to supplementary hydraulic or pozzolanic reactions. From the work of Sonebi [Sonebi, 2006], GGBS reduces the porosity and the pores also become finer which results in a reduction of the water absorption. The incorporation of SF significantly reduces the chloride permeability.

2.2.1.e Admixtures

The chemical products which can give extra properties to concrete are called admixtures. They are used to improve the performance of the concrete. Commonly, the types of admixtures are as follows: super-plasticizer, water reducing admixture, hardening accelerator, set retarder, air entraining agent, anti-freezing admixture, etc. We add water reducing admixtures (plasticizing chemicals in the U.S.) into the composition of concrete. It is possible either to increase the plasticity of the concrete without increasing the water content, or to reduce the water content while maintaining a given consistency [Mehta, P. Kumar, 2006].

2.2.1.f Water

Though water is not a solid material used to make concrete, it plays an important role in the formation of concrete. It is needed for the setting and hardening of cement and the hydration of concrete. Due to the chemical interactions between cement and water, cement is hardened and aggregates are bound into solid mass. Additional water above the amount consumed in the chemical reaction produces pores in the cement paste, which increases the porosity and decreases the strength of the cement paste. For normal concrete, the water/cement ratio is roughly between 0.4 and 0.6, while for high strength concretes, the value can be as low as 0.21 [Nilson et al., 2010]. Therefore, the lower porosity or water/cement ratio, the better durability of concrete. In addition, fresh concretes need to be kept in a moist environment at certain temperature during the first few days or weeks to maintain their strength [Mehta, P. Kumar, 2006; Nilson et al., 2010]. This process is called curing, where water is also needed.

2.2.2 Ageing of concrete

The ageing of concrete will occur a few or decades of years after the concrete constructions finished, causing the degradation and deterioration of concrete [U.S.B.R., 2005]. The damages of concrete are unavoidable since it can be damaged by many processes, including the physical processes, such as freezing-thawing cycles, fire, water erosion and the chemical processes, such as carbonation, chloride penetration, steel corrosion, etc.
Freezing-thawing deterioration is the physical destruction caused by ice formation within the cement pores [U.S.B.R., 2005]. Water erosion is the act that concrete is worn away by the water, which usually happens at the surface of hydraulic structure like dams, spillways and tunnels [PCA, 2002]. Two forms of process are involved in the carbonation of concrete: the diffusion of CO_2 in gaseous phase and the dissolution of CO_2 in the pore water as carbonic acid H_2CO_3, its dissociation as HCO_3^- and CO_3^{2-} ions [Thiery et al., 2007b]. The penetration of CO_2 is 10000 times faster by gas diffusion than in ionic form by dissolution in liquid. But the diffusion of CO_2 needs water to decompose in ions [Villain, 2012]. The optimal saturation degree for carbonation is between 40% and 60% [Wierig, 1984]. The chloride ions penetrate by diffusion in water and convection transported in water penetration by capillary absorption [Baroghel-Bouny et al., 2011, 2012]. So we can see that during ageing of concrete, most important physical and chemical processes of deterioration are associated with water.
Considering the ageing problems, we need to obtain a good durability of concrete.

2.2.3 Durability of concrete

According to ACI (American Concrete Institute) [ACI, 2008], durability of Portland cement concrete is defined as its ability to resist weathering action, chemical attack, abrasion, or any other process of deterioration.
To define concrete characteristics related to its durability, evaluating of durability indicators (such as porosity) and durability monitoring parameters (such as water content and chloride content) is often processed in the research [AFGC, 2007; Villain et al., 2009, 2010; Villain, 2012]. In this section, we are going to introduce some important processes of deterioration and the relative parameters used for monitoring and assessment.

2.2.3.a Porosity

Porosity is widely known as a method of calculating the total volume of capillary voids. It can be defined by the ratio of void space volume (V_V) and bulk volume (V_T) of material:

$$\phi = \frac{V_V}{V_T} \tag{2.1}$$

Porosity is a fraction between 0 and 1, typically ranging from less than 0.01 for solid granite to more than 0.5 for peat and clay. For concrete, porosity varies from 3% to 16% [AFGC, 2007] that as the value increases, the potential durability of concrete decreases. The structure of porosity strongly influences the performance of concrete.
Porosity is widely regarded as one of the factors influencing the dielectric properties of the material. Though its effect is smaller than that of the water, it can not be ignored. Lai et al. [Lai et al., 2006] showed that the higher the porosity of the materials is, the

higher will be the contribution of pore water to the dielectric constant (to be discussed in Chapter 3) when the water content increases.

2.2.3.b Water content and saturation degree

In the early age of concrete, water content is considered as one of the important parameters influencing the drying shrinkage and creep. Also, as we mentioned before, water is an agent of deterioration. Not only in concrete, but also in many porous solids, water causes both physical and chemical processes of degradation.
Measuring the water content is particularly delicate. The definition of parameters characterizing material moisture are presented as follows [Baroghel-Bouny, 1994; Villain, 2012]:
Saturation degree S

$$S = \frac{water\ volume}{air\ volume} = \frac{(M_t - M_{sec})}{(M_{sat} - M_{sec})} \tag{2.2}$$

Water content by mass w

$$w = \frac{water\ mass}{solid\ mass} = \frac{(M_t - M_{sec})}{M_{sec}} \tag{2.3}$$

Water content by volume W

$$W = \frac{water\ volume}{total\ volume} = \frac{(M_t - M_{sec})}{(M_{sat} - M_{hydro})} = \phi S \tag{2.4}$$

With M_{sec} is the solid mass, M_{sat} is the saturated mass, M_t is the mass at any time t and M_{hydro} is the mass weighted by hydro-static weighing. In the following of this thesis, if it is not precise, the water content is the volumetric water content W.
Another commonly used definition for the moisture condition study is the relative humidity, which can be given by [Buck, 1981]

$$RH = \frac{p_w}{p_{w,max}} \times 100\% \tag{2.5}$$

where where p_w is the partial pressure of water vapour (H_2O) in the air, $p_{w,max}$ is the saturating vapour pressure of water at a given temperature.
To obtain the water content W or saturation rate S from RH, it is necessary to know the characteristics of adsorption/desorption isotherm curves of the material reflecting the balance between relative humidity and saturation rate [Baroghel-Bouny, 1994; Andrade et al., 1999; Villain, 2012].

2.2.3.c Carbonation

Carbonation is the result of reactions between carbon dioxide CO_2 (from environment) and calcium hydroxide (in hydrated Portland cement paste) which can be shown by the following reaction formulas [Villain, 2012]:

$$Ca(OH)_2 \rightarrow Ca^{2+} + 2OH^- \tag{2.6}$$

$$CO_2 + H_2O \rightarrow CO_3^{2-} + 2H^+ \tag{2.7}$$

$$Ca(OH)_2 + CO_2 \rightarrow CaCO_3 + H_2O \tag{2.8}$$

The CO_2 or the ions HCO_3^- and CO_3^{2-} participating the reactions in concrete mostly come from the the air surrounding and natural water with high carbon dioxide concentration. Moreover, some natural occurring water like seawater and ground water may be acid [Mehta, P. Kumar, 2006]. Under certain conditions, such as sheltered bays and estuaries, the high concentration of carbon acid makes the water more aggressive to the concrete structures.
Generally, there are two kinds of effects of carbonation on concrete. One one side, carbonation increases the compressive and tensile strengths of concrete. This is beneficial to the use of concrete. On the other side, carbonation reduces the pH level of concrete. Like the chloride ingress, carbonation is also a chemical corrosion process which mainly causes depassivation of rebars [Villain et al., 2007; Thiery et al., 2007b, 2008]. Due to this problem, the study on carbonation with the surrounding environment is necessary for the durability of reinforced concrete.

2.2.3.d Water penetration and chloride ingress

Permeability is the ease of aggressive water penetrating into the concrete structure, which is related to the porosity that varies in accordance with the composition of the concrete. Permeability is defined as the property that governs the rate of flow of a fluid into a porous solid. For steady-state flow, the coefficient of permeability (K) is determined from Darcy's expression [Villain, 2012]:

$$Q = \frac{\mathrm{d}q}{\mathrm{d}t} = -K\frac{A}{mu_g} \cdot \frac{\mathrm{d}P}{\mathrm{d}z} \tag{2.9}$$

where $\frac{\mathrm{d}q}{\mathrm{d}t}$ = rate of fluid flow (m^3/s), μ_g = dynamic viscosity of the fluid (Pa·s), A = surface area (m^2), $\frac{\mathrm{d}P}{\mathrm{d}z}$ = pressure gradient (Pa). Generally, permeability depends on the total porosity. Furthermore, permeability depends on the way in which porosity is distributed. The chloride ions ingress is one of the main reasons of depassivation of the reinforcements, and then leads to their corrosion. The extent of the corrosion process is related to the chloride content and permeability. The penetration of seawater or de-icing chemicals is a frequent source of chloride ions. Chloride ions ingress into concrete needs the presence of liquid. It depends on the material's properties and the wetting-drying cycles (duration, climatic conditions).
For a saturated concrete, the chloride ions penetrate the concrete by diffusion because of a concentration gradient. For an unsaturated concrete, there exists a gradient of liquid phase. The water can penetrate by capillary absorption. Chloride ions move along with the penetration of water. On the other hand, in the process of wetting-drying cycles, the chlorides can migrate with the liquid phase by convection. Then the chlorides diffuse into saturated areas. The diffusion process can be described by Fick's laws.
- Effective chloride ion diffusion coefficient-Fick's first law [AFGC, 2007]:
If the ions move in a direction perpendicular to the surface of entry in a uniform medium, the mass flux J (in kg· m^{-2}· s^{-1}), representing the quantity of ions moving through a concrete surface unit in one second, is given by:

$$J = -D_{eff} \cdot \frac{\mathrm{d}C_f}{\mathrm{d}x} \tag{2.10}$$

where D_{eff} ($m^2 \cdot s^{-1}$) is the effective chloride diffusion coefficient in the material, C_f ($kg \cdot m^{-3}$) is the free chloride concentration of the interstitial solution, at depth x and at time t.
- Apparent chloride ion diffusion coefficient-Fick's second law [AFGC, 2007]:
When the effective chloride diffusion coefficient does not depend on the ion concentration, it is written as follows:

$$\frac{\partial C_f}{\partial t} = D_{app} \cdot \frac{\partial^2 C_f}{\partial x^2} \tag{2.11}$$

where D_{app} ($m^2 \cdot s^{-1}$) is the apparent chloride diffusion coefficient in the material.
This equation is generally used to describe chloride ingress by diffusion into saturated concrete in non-steady-state conditions.

2.2.4 Conclusion

In this section, we firstly introduced the components of concrete. The performance of the concrete strongly depends on the composition of these materials. Also, different compositions affects some indicators related to the durability of concrete. The higher water/cement ratio usually obtains higher porosity. The added GGBS helps reduce the porosity as well as the chloride permeability.
Then, we discussed about the ageing and the durability of concrete. It is unavoidable for concrete to get degraded as time goes by. The study on the durability therefore becomes rather important to the existing concrete structures. From the study, we find 4 factors mainly related to the durability: porosity, water content, carbonation and chloride ingress. The porosity of concrete is identified as the durability indicator, which affects the strength of the concrete and also influence the penetration of water and chloride. The other factors are usually evaluated as monitoring parameter, such as water content, carbonation depth and chloride ingress depth. The evaluation methods of these indicator and parameters will be discussed in the following sections.

2.3 Destructive Methods

The test methods developed to analyse or evaluate the concrete, can be classified as destructive and non-destructive ones. To select one technique from the destructive or non-destructive methods for a particular situation, the evaluation of access, damage, cost, time and reliability will be important.
Destructive testing methods are those test methods that cause damage to the concrete, normally requiring sample extraction. In this section, we will introduce some widely used destructive tests applied to concrete.

2.3.1 Core drilling

Coring is widely used in destructive and semi-destructive tests. Samples are taken in the form of cores drilled from concrete and can be used for some physical tests or chemical analysis [Bungey et al., 2006]. Making good samples brings good precision of the test. Though these methods cause damage to concrete and may be slow and expensive, they are widely used for various investigations on concrete, such as thickness of pavement

[Morcous and Erdogmus, 2010], corrosion of embedded steel [Andrade and Alonso, 2004], compressive strength [Malhotra and Carino, 2004], durability and deterioration of concrete [Hugenschmidt and Loser, 2007; Villain et al., 2010]. They can usually obtain direct and reliable results with recommended number and locations of the test and provide a calibration to non-destructive methods.
In fact, taking cores is the most reliable way to do the in-situ strength assessment even though it causes most damage and is slow and expensive. It is also used for interior inspection of concrete for its density, water absorption and as samples for chemical analysis, etc.
Some criteria have to be met for taking cores. The location of core should avoid unrepresentative concrete, such as the carbonated surface or the part around reinforcement. The recommended size of cores is that the diameter is at least three times the nominal maximum aggregate size. That means for a core with a diameter of 75 mm, the maximum aggregate size should be less than 25 mm. We have to be very careful while choosing the location and size and also for cutting, since many factors can influence the testing results. The factors consist of concrete characteristics, such as moisture condition; and testing variables, such as length/diameter ratio, diameter of core, direction of drilling, reinforcement, etc. Moreover, core tests have some limitations like cost, inconvenience and damage. It is therefore highly recommended to be used with other methods which are less destructive or non-destructive (ND) in a second step, after realizing ND tests. The destructive testing methods become representative of the corresponding zone.

2.3.2 Physical tests

Compression and tensile strength tests are two major strength tests conducted on concrete. The strength of concrete shows us the general quality of concrete because it is directly related to the structure of cement paste.

2.3.2.a Compression test

The compressive strength of concrete can be decreased by the effects of corrosion, caused by carbonation and chloride ingress. Compression test is used to determine the compressive strength of concrete. Cubes and cylinders are used as specimens in the test.
The procedure of this test is to put the specimen in a compression testing machine to add a compressive axial load on it. The load is provided at a rate within a prescribed range until failure occurs. The details of the method are described in the standard of ASTM [ASTM:C39/C39M-12a, 2012].

2.3.2.b Tensile test

The pull-off test is a commonly used method to obtain tensile strength of concrete surfaces [ASTM:C1583/C1583M-13, 2010]. The test is performed on the surface of prepared concrete. A shallow core is often drilled around the test surface to eliminate surface skin effects. Steel disk is bonded to the top surface of the test specimen with an epoxy or polyester resin. The tensile force required to pull this disc out from the surface is measured. Then, the tensile stress at failure is calculated.

2.3.3 Chloride diffusion tests

As mentioned in §2.3.4, the diffusion process can be described by Fick's laws. The diffusion test is based on Fick's laws to analyse the chloride diffusion coefficient in the profiles.
Fick's first law gives the effective chloride diffusion coefficient D_{eff}, which can be applied to the diffusion test in steady-state conditions. Fick's second law gives the apparent chloride diffusion coefficient D_{app}, which can be applied to the diffusion test in non-steady-state conditions. The first law tests only the ionic transport while the second law also takes into account chlorides binding with cement phases. It should be noticed that the tests of D_{eff} in steady-state conditions are very slow. This problem can be overcome by an electrical field that accelerates the movement of chloride ions [Castellote et al., 2001].
One coefficient can deduce the other one by the formula (2.12), by knowing the porosity of the material and the chloride-matrix interactions:

$$D_{app} = \frac{D_{eff}}{\left(\Phi + \rho_d \cdot \frac{\partial m_b}{\partial C_f}\right)} \tag{2.12}$$

where Φ is the porosity of the material accessible to chlorides (in $m^3 \cdot m^{-3}$), m_b is the mass of bound chlorides per unit mass of dry solid (in $kg \cdot kg^{-1}$), and ρ_d is the bulk density of the material in the dry state (in $kg \cdot m^{-3}$).

2.3.4 Chemical tests

Chloride ingress and carbonation are two important phenomena causing the deterioration of concrete. Carbonation decreases the pH value of concrete, which starts the depassivation of embedded reinforcement. Chloride penetrating into the concrete promotes the corrosion of steel reinforcement.
Here we will introduce two colourimetric methods to evaluate the chloride ingress depth and the carbonation depth.

2.3.4.a Chloride ingress depth

The depth of chloride ingress refers to the position of the chloride ingress "front", where the free chloride ions reaches the critical concentration ($[Cl^-_{free}] \approx [Cl^-_{free}]_{crit.}$). The samples of concrete are made in the laboratory or taken from concrete structures in two ways: powder sampling and core drilling [AFPC-AFREM, 1997]. Two methods of colorimetry can be applied to estimated estimate the chloride ingress depth.
The first method is the *Maultzsch* method . In this method, the sample is axially split into two parts. The 0.1 N $AgNO_3$, and then K_2CrO_4 are sprayed on the featured surface area [Baroghel-Bouny et al., 2002].
The second method is the *Collepardi* method. The fluoreseine is sprayed on the featured surface of the sample, and then the silver nitrate solution 0.1 N. The concrete turns pink in the absence of free chloride. With free chloride, AgCl is produced and the colour quickly becomes dark exposed to the sunlight [Collepardi, 1995].

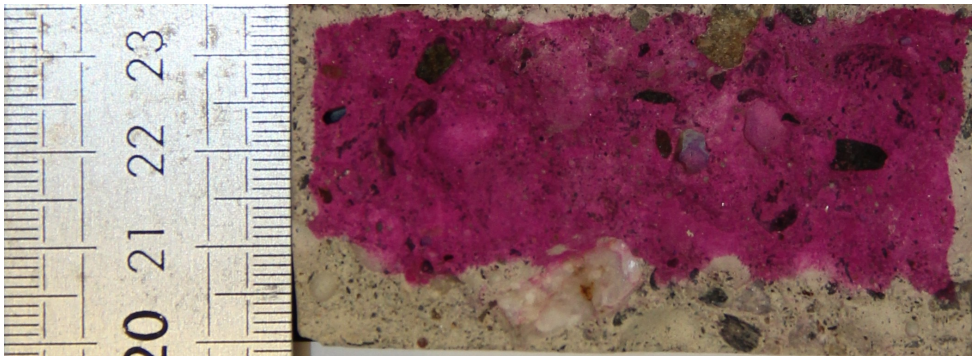

Figure 2.1: Evaluation of carbonation depth using a coloured indicator on concrete B1-2

2.3.4.b Carbonation depth

The carbonation depth refers to the position of carbonation "front", where pH $\approx$ 9. The testing samples and procedure is similar to the test of chloride ingress depth. It can be indicated by a coloured indicator. The most suitable indicator is phenolphthalein [AFGC, 2007]. With phenolphthalein spraying on a concrete sample, the non-carbonated part turns to pink while the carbonated part keeps the same colour.
Figure 2.1 shows a colorimetric test on the split core sample of concrete B1-2 from the EvaDéOS project (more information in Chapter 5). It is clear to see that the average carbonation depth is near 10 mm.

2.3.5 Conclusion

The discussion of destructive methods starts by the core drilling. This method is sometimes considered as semi-destructive test because though taking cores causes damage to the concrete structures, the core samples are used for non-destructive tests. We briefly introduced the physical tests, mainly used to evaluate the compressive and the tensile strength of the concrete. Then the chemical tests for the chloride ions and carbonation are presented. The colorimetric tests for chloride ingress depth and carbonation depth are very efficient methods. To be noticed, however, the method relating to carbonation has better accuracy than the method relating to chlorides [AFGC, 2007].

2.4 Non-destructive Methods

Non-destructive testing (NDT) techniques are a variety of techniques used in industry and scientific research analysing properties of materials, components and structures without causing damage. Nowadays, several NDT techniques have been developed with their applications in civil engineering field. They can be categorized as mechanical waves, electromagnetic methods, infrared thermography, electric methods, radiography, etc [Breysse and Abraham, 2005]. Since each method has its advantages and limitations, these techniques are commonly used on specific problems providing us discrete and indirect information. In such case, civil engineering researchers usually associate a group of NDT techniques to have a relatively complete understanding of the characteristics of the studied materials. The following techniques are already widely used in the geophysical and civil engineering industry and they might be interesting to our study of concrete.

2.4.1 Ultrasonic testing

Ultrasonic wave is a kind of mechanical waves that is widely used in the NDT field. It is often performed on steel and other metals, and also on wood, concrete and some other composites, using high frequency sound energy.

2.4.1.a Principles and features

A typical ultrasonic testing (UT) inspection system consists of several functional units, such as the pulser/receiver, transducer, and display devices. Driven by the pulser, the transducer generates high frequency ultrasonic energy propagating through the materials in the form of waves. When there is a discontinuity (such as a crack) in the wave path, part of the energy will be reflected back from the flaw surface.
There are many advantages using the ultrasonic testing techniques. The high penetrating power of ultrasonic waves allows the detection of flaws deep in the part. It has greater accuracy in detecting the depth of internal flaws and the thickness of objects than other non destructive methods because of its high sensitivity to the mechanical behavior of the physical structures. It also has the capability of estimating the size, orientation, shape and nature of defects [Zhang et al., 2012; Garnier et al., 2013].
Meanwhile, some problems need to be concerned while using the ultrasonic method. Careful attention and extensive technical knowledge are required for the operations and the development of inspection procedures. Parts that are rough, irregular in shape, very small or heterogeneous are difficult to inspect. Furthermore, couplants are needed to provide effective transfer of ultrasonic wave energy between transducers and objects unless a non-contact technique is used. Non-contact techniques include Laser and Electromagnetic Acoustic Transducers (EMAT).

2.4.1.b Ultrasonic pulse velocity method

The ultrasonic pulse velocity method has been used successfully for evaluating the quality of concrete for decades, which is based on the correlation between the concrete strength and the pulse velocity [Jones and Făcăoaru, 1969].
In this method, the time of an ultrasonic wave pulse travelling through concrete is measured on the surface from one point to another. Knowing the positions of the two points, the distance between them is thus known. So the velocity of the wave pulse can be calculated. The frequency f and wavelength λ have the relationship with the propagation velocity V:

$$V = f\lambda \tag{2.13}$$

When ultrasonic pulses propagate through a large solid elastic medium, three types of propagating mechanical waves (or stress waves) will be created: (1) compressional waves, (2) shear waves, (3) and surface waves. For most test configurations, the direct compressional wave is used as it is the first wave arriving at the receiver.
For concrete, the associated wavelength is approximately 10 mm at 500 kHz. When the wavelength of the wave is the same size or smaller than the size of scatterer, the propagating wave will be scattered and rapidly attenuated. Under this condition, the waves can not be traversed effectively because the wavelength is in the size range of aggregates (mostly in the order of $D_{max} \approx 20$ mm). In fact, 500 kHz is suggested to be the upper limit and the usual frequencies in use are from 25 to 100 kHz [Malhotra and Carino, 2004].

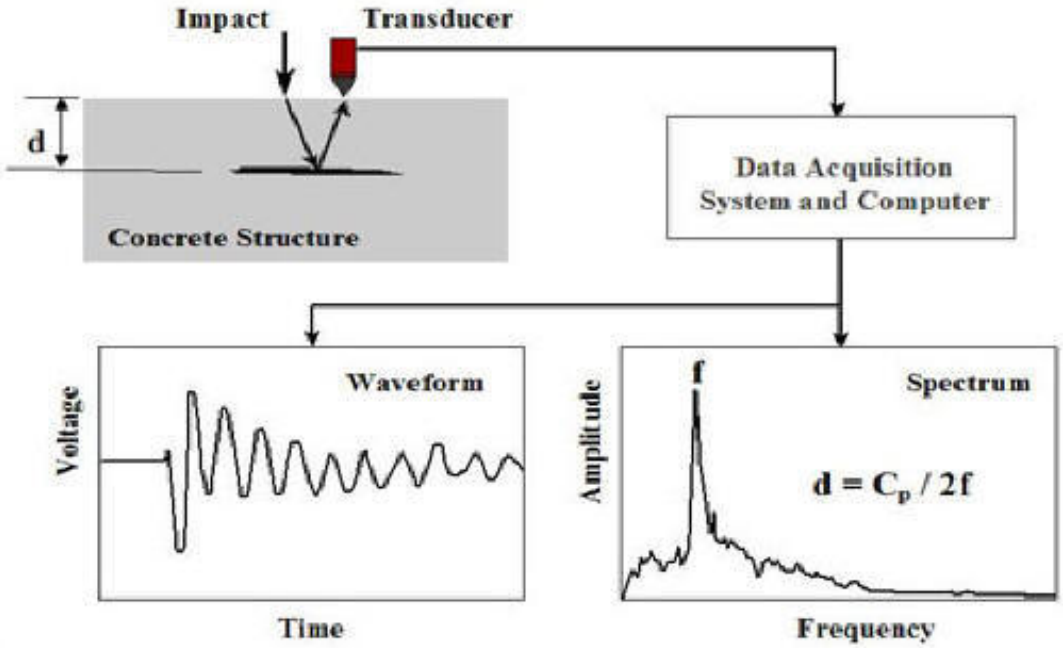

Figure 2.2: Schematic diagram of impact-echo system [Sansalone and Streett, 2005]

2.4.1.c Impact-echo system

The impact-echo system is the recent development in ultrasonic methods which was originally developed for the applications on concrete and masonry structures [Sansalone and Streett, 1997; McCann and Forde, 2001]. It is based on the use of impact-generated stress (sound) waves that propagate through the structure and are reflected by internal flaws and external surfaces.

The wavelengths of these stress waves are typically between 50 mm and 2000 mm. They are much longer than the dimensions of aggregates, air-bubbles and micro-cracks. Therefore, concrete is almost considered as homogeneous to the propagation of the waves. The diagram illustrating how impact-echo works is presented in figure 2.2. It uses a small instrumented impulse hammer to hit the surface of a structure at a given location and records the reflected energy as a waveform. The waveform is then passed to a signal analyser in the computer and transformed into a spectrum. The shift of frequency components to higher range can be interpreted by a void in the tested concrete. The thickness of the slab d can be calculated by the Eq. (2.14):

$$d = \frac{C_p}{2f} \tag{2.14}$$

where C_p (m/s) denotes the compression wave velocity and f is the detected characteristic frequency.

If the frequency of the first symmetrical Lamb mode f_{S1} is detected, then the dynamic Young's modulus E_{dyn} (GPa) can be deduced with an assumption on the Poisson's ratio v_{dyn}. In case of relatively undisturbed signals, the second antisymmetric mode (f_{A2}) of the guided Lamb waves can also be detected. Figure 2.3 is an example of impact-echo results tested on the concrete beam in a tidal zone from the wharf of the Nantes - Saint Nazaire Port. Knowing frequencies f_{S1} and f_{A2}, the Poisson's ratio v_{dyn} and dynamic

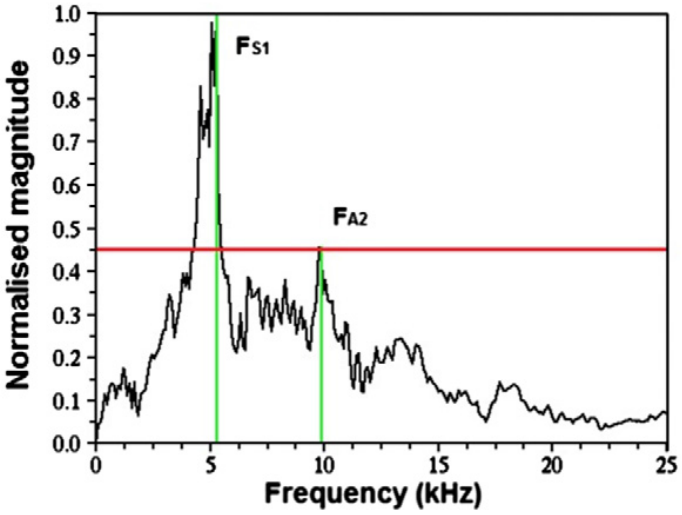

Figure 2.3: Sample impact-echo results for the concrete beam in a tidal zone [Villain et al., 2012]

Young's modulus E_{dyn} are both calculated.

With this system, it is possible to measure the thickness of concrete plates, to determine the location, depth and extent of flaws such as cracks, voids, delaminations, honeycombing and debonding in plain and reinforced concrete structures, and also to give information on the material itself [Villain et al., 2009, 2012].

2.4.1.d Application on determination of concrete's durability indicators

From the results of Villain [Villain et al., 2012], we find that dynamic Young's modulus E_{dyn} is linearly related to the porosity of the concrete. Furthermore, E_{dyn} and the volumetric water content W are found to have a linear relationship between 40% and 100% of the expected saturation degree [Villain et al., 2009, 2011b]. Therefore, the impact-echo system can be used as a NDT method for the durability indicators.

2.4.2 Electric methods

The changes in electrical properties, such as electrical resistance, dielectric constant, and polarization resistance of concrete have been investigated as a basis for the development of various non destructive testing methods [Taylor and Arulanandan, 1974; Malhotra and Carino, 2004; du Plooy, 2013]. Usually, the electric resistivity is measured to evaluate the service life of concrete and the corrosion activity of steel reinforcement. Also, half-cell potential method can be used to assess the corrosion conditions in a reinforced concrete structure.

2.4.2.a Half-cell potential measurement

The half-cell potential is an open-circuit potential since it is measured under the condition that there is no current in the measuring circuit. The use of this method is fully described in American Society for Testing and Materials (ASTM) C876 [ASTM, 2009]. Compared to resistivity measurements, this method is more popular for assessing corrosion of the steel reinforcement [Babaei, 1986; Gu and Beaudoin, 1998]. It is also called corrosion

potential and the readings indicate the probability of corrosion activity of reinforcement located beneath the reference cell.
For measuring, a small hole has to be drilled through the concrete because there needs to get one be contacted with the reinforcement. The concrete should be wet enough to complete the measuring circuit. Then the equipotential lines intersect the surface and the potential at any point of the concrete can be measured. The extents of corrosion activities of the structure are identified by the levels of measured negative potentials. However, totally wet concrete surface can cause more negative potential results significantly [Bungey et al., 2006]. Also, the potential range is very shallow to separate corroding and uncorroding areas. In fact, half-cell potential method is now more commonly used in locating areas in which corrosion may occur and requiring further investigation.

2.4.2.b Resistivity measurements

Concrete electrical resistivity (ρ) can be obtained by applying a current into the concrete and measuring the response voltage. This is a volumetric measurement of the electrical resistance, presenting a comprehensive character regarding to the concrete micro-structure. The electrical resistance, by Ohm's Law, is expressed as the ratio of voltage and direct current applied:

$$R = \frac{E}{I} \tag{2.15}$$

where I is the current in amperes and E is the electrical potential in volts.
The resistance of a material is directly proportional to the length and inversely proportional to the cross-sectional area. Thus:

$$R = \rho \frac{L}{A} \tag{2.16}$$

where R is resistance in ohm, ρ is resistivity in ohm-cm, L is length in cm, and A is the cross-sectional area in cm^2. Resistivity is essentially constant for a given material under constant conditions and is numerically equal to the resistance at a length of 1 cm of the material.
While doing the measurements, the electrodes are placed in a constant separation Wenner array (see figure 2.4) to map the variation of electrical resistivity over the surface of the measured object. The tested surface has to be moist enough to complete the circuit. The major difficulty of this method is to make effective contacts between the electrodes and the concrete structure. The wet sponges are usually put over the electrodes to provide good contact.
As resistivity is known to be sensitive to water, chloride content, temperature and many other factors, we must pay attention to some facts that may change our test results [Bungey et al., 2006]:

i). the water/cement ratio

ii). the presence of steel reinforcement

iii). the carbonation or water on the surface

iv). the location is on a small section or close to the edge

v). the temperature

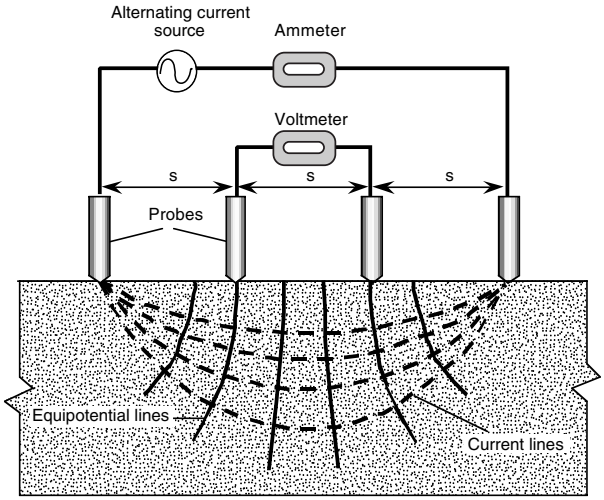

Figure 2.4: Four-probe resistivity test [Malhotra and Carino, 2004]

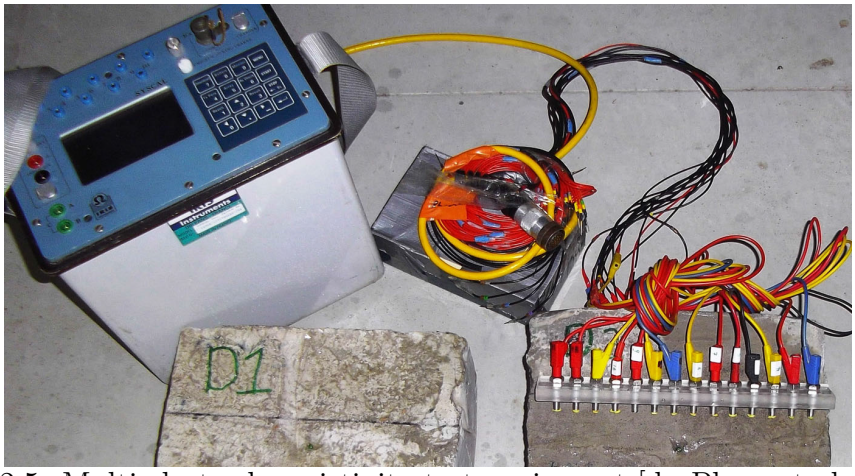

Figure 2.5: Multi-electrode resistivity test equipment [du Plooy et al., 2015a]

As a development over Wenner array, a multi-electrode resistivity probe was developed by Ifsttar, France in 2012 [du Plooy et al., 2015a; Villain et al., 2015b]. Figure 2.5 is a photo of the newly developed multi-electrode resistivity probe, equipped with a Syscal Pro multi-channel resistivity meter. The probe has 14 electrodes which are spaced with an interval of 20 mm. The Wenner configuration can therefore be selected among 26 possibilities and the resistivity of concrete to be obtained as a function of depth. This equipment simplifies the way we do multiple surface measurements, from which to get the electrical resistivity tomography (ERT) [Daily et al., 1993, 2004].

2.4.2.c Application on determination of concrete's durability indicators

When it comes to the durability problem, we are more interested in the applications of these methods on the water content and chloride content. From some former study, we find that the resistivity is sensitive to the chloride content and the water content. The results of the SENSO project show a linear relationship between the logarithm of resistivity and the volumetric water content [Balayssac et al., 2012]. The resistivity decreases as the water content increases. Furthermore, the increment of chloride concentration significantly decreases the resistivity. With the application of the multi-electrode resistivity

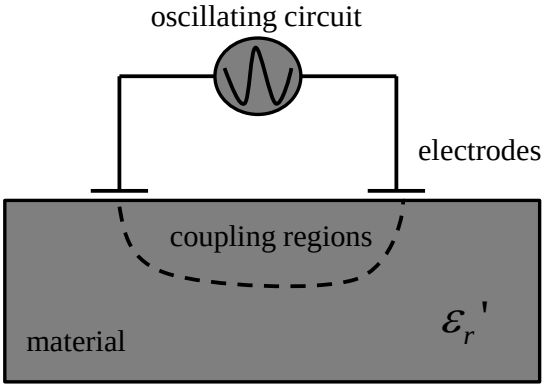

Figure 2.6: Diagram of capacitive device

probe, we are able to determine the resistivity gradient inside concrete, in order to monitor the penetration of water and chloride solution into concrete as a function of time [du Plooy et al., 2015a; Villain et al., 2015b; Fares et al., 2015].

2.4.3 Electromagnetic methods

Electromagnetic non-destructive testing technology has the advantage to be non-destructive, simple, fast and easy for large area tests. As it is mainly sensitive to water and chloride content, it has been widely used in the detection and evaluation of concrete quality in engineering projects such as civil construction, water conservancy, electric power, etc. In this section, we intend to introduce two practical electromagnetic methods, for they are the main methods used in our study.

2.4.3.a Capacitive technique

Currently, one of the most widely used NDT techniques in concrete industry seems to be based on capacitive probes, which can be used for monitoring durability indicators like water content and chloride content.
Typically, for moisture measurement, capacitive sensors are installed in direct contact with the measured object. Since the dielectric constant of dry concrete is rather small compared to that of water, capacitive sensing maintains usually a stable result. Nevertheless, direct contact with samples causes mechanical wearing to the sensors. So occasional re-calibration and ultimately replacement will be required for the sensors. Another way of applying capacitive technique is Embedded Capacitor Sensor (ECS), which has been developed for evaluating the corrosion activity of reinforcement in concrete.

The principle of capacitive measurement is based on the calculation of the resonant frequency of an alternating electric oscillating circuit (around 30 - 35 MHz) between the electrodes (figure 2.6), which are in contact with the upper face of the medium to auscultate. The data is inferred from capacitive method by measuring capacitance or the dielectric constant of concrete [Hudec et al., 1986; Dérobert et al., 2008]. The change of the measured data involves a variation in the resonant frequency f_{osc} of the system

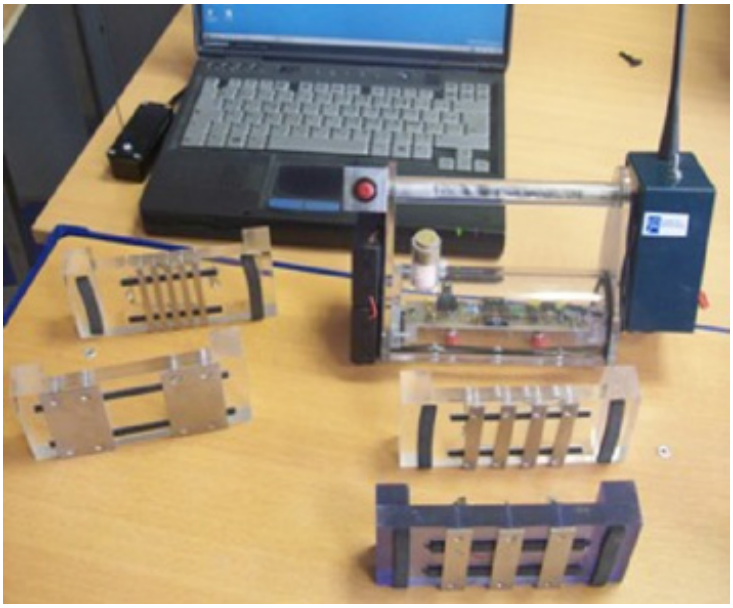

Figure 2.7: Photo of capacitive probes testing equipment in Ifsttar

according to the relation:

$$f_{osc} = \frac{1}{2\pi\sqrt{LC}} = \frac{1}{2\pi\sqrt{LK_{geo}\varepsilon'_r}} \tag{2.17}$$

where L is the system inductance, K_{geo} is a geometric constant and ε'_r is the real relative permittivity of the medium.
Figure 2.7 is a photo of the capacitive testing equipment (around 33 MHz) developed by Ifsttar, France [Dérobert et al., 2008; Villain et al., 2012]. The different sizes of the electrodes correspond to different investigation depth, with depth equal to 2 - 3 mm for small-sized electrodes, 1 - 2 cm for medium-sized electrodes, and 6 - 8 cm for larger sizes. A calibration allows to obtain the dielectric constant of concrete ε'_r, which is closely related to the water content and the mixing components.

2.4.3.b Ground Penetrating Radar (GPR)

Ground penetrating radar (GPR), regarded as one of the most popular electromagnetic non destructive methods, is to propagate high frequency EM waves (30 MHz - 3 GHz) underground, and receive the reflected wave back to the ground through the receiving antenna. According to the received EM wave's waveform, amplitude and time variation, we are able to profile the location, structure and buried depth of the underground medium. GPR is mainly used in processing of rebar location in structure, thickness of the pavement measurement and also for some other potential uses. For example, in our study, it will be used to determine water content by surveying permittivity inside concrete.

Basic principles The GPR system usually concludes two antennas: transmitter and receiver in one box. The transmitting antenna transmits a series of high frequency electromagnetic pulses to the object to be detected or the underground. Signals received by receiving antenna will be stored by the digital control unit and appear on the GPR monitor in forms of cross-sectional view through a time section (see figure 2.8).

(a) GPR device

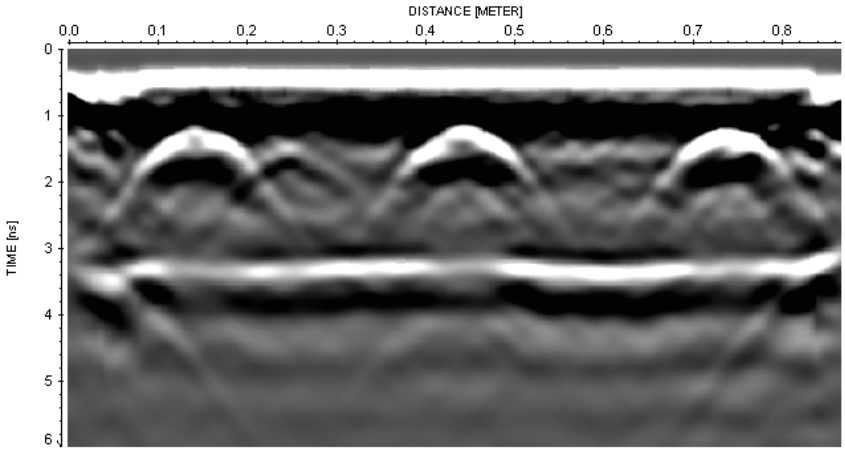

(b) B-scan

Figure 2.8: An example of (a) GPR device [from web. GSSI] and (b) monitoring time - diagram from GPR

While EM waves propagating in the medium, reflection and refraction may happen on the interface where the physical or dielectric properties of the material change. In such case, the propagation paths, amplitudes and shapes of the waves will also change. Based on the received diagram, by analysing the wave's propagation speed, amplitude, waveform and other information, it is possible to determine the composition and structure distribution inside the medium.
Considering the waves scattered from the testing object, there are three kinds of pulses to be recorded by the receiving antenna. The first pulses will be the waves that travel directly through the air. The second pulses to be recorded will be the pulses travelling directly through the material. The third pulses will be the pulses that travel into the material and reflected back to the surface. The travelling velocity v inside the material is often determined by the relative permittivity of the material, as seen in the following equation:

$$v = \frac{c}{\sqrt{\varepsilon_r'}} \tag{2.18}$$

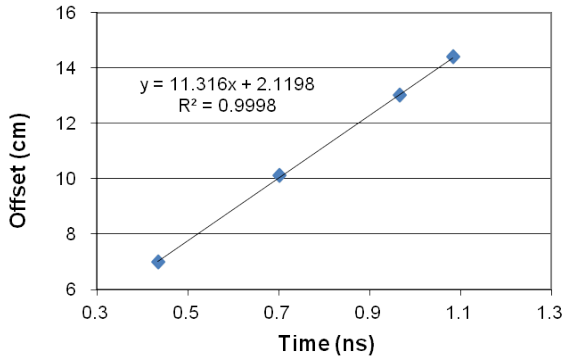

Figure 2.9: Example of 4-offset measurement. The slope of the tendency curve refers to the group velocity of the EM wave in tested material.

where c is the velocity of light in vacuum, ε'_r is the real part of the relative permittivity (dielectric constant) of the medium in question. It is an approximation for EM waves at high frequencies where the conductivity can be neglected.

Determination of dielectric constant with 4-offset measurement This is a simple approach using the surface wave transmitted directly from the transmitter to the receiver through the material [Dérobert et al., 2008; LMDC, 2009]. The group velocity v_g of the surface wave is determined from 4 measurements with 4 offsets. Then the dielectric constant ε'_r can be calculated from v_g by $\varepsilon'_r = \left(\frac{c}{v_g}\right)^2$, where $c = 3 \times 10^8$ m/s is the speed of light.
A commercial bi-static antenna, with the central frequency of 1.5 GHz, is used in this test. At each testing point, we apply 5 times of GPR scans with each offset. The result of each point is therefore obtained by average. The travel time is picked from the first peak of the received signal. By plotting the distance and travel time of each offset, the slope of the tendency curve refers to the group velocity of the EM wave in tested material. Figure 2.9 is an example of 4-offset measurement and the linear tendency curve. According to the curve, the group velocity $v_g = 11.316$ cm/ns. The value of dielectric constant can therefore be obtained.

WARR and CMP measurement The most common means of determining the velocity of GPR waves are wide-angle reflection and refraction (WARR) and common midpoint (CMP) measurements [Huisman et al., 2003; van der Kruk et al., 2006]. The configurations of GPR are shown in figure 2.10. The difference of the two configurations is that the transmitter in WARR measurement keeps at the same location while in CMP measurement, the transmitter and the receiver move synchronously from the middle to the two ends. For heterogeneous materials, like concrete, such CMP stacking can improve the signal to noise ratio around the detected point [Butler, 2005]. Therefore, we choose CMP technique to obtain the direct wave and reflected wave propagating in concrete.
With a knowledge of the speed of radar waves travelling through concrete, we are able to know the relative permittivity of concrete. Since this change is closely dominated by the variation of saturation degree [Klysz and Balayssac, 2007; Villain et al., 2010], GPR has been applied as a good means of detecting water content in concrete.

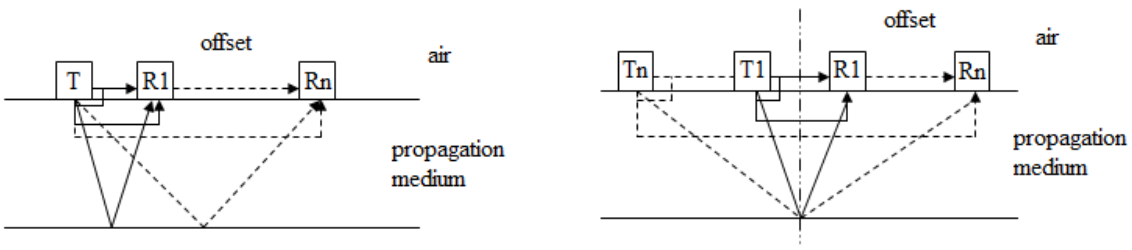

(a) WARR (b) CMP

Figure 2.10: multi-offset requirement configurations

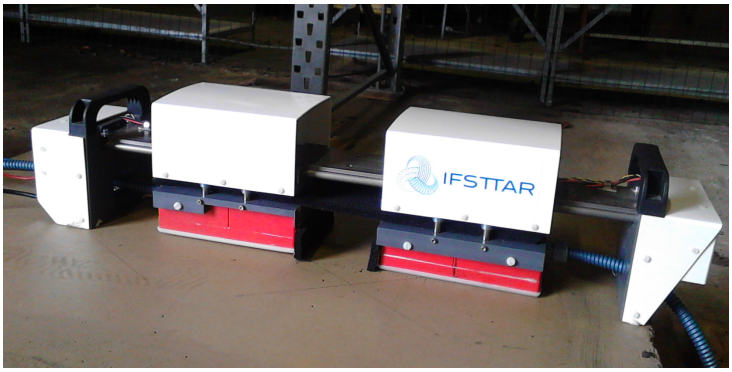

Figure 2.11: Robot carrying GPR antennas for CMP measurement

Robot for CMP and nano radar In our old way of CMP acquirements, a lot of time and labour work was consumed by: drawing scale on the testing sample, moving antennas manually step by step and controlling the radar system to scan at each step. Moreover, the accuracy of measurements cannot be ensured by this human work. Fortunately, a robot prototype moving GPR antennas with CMP mode has been developed in the lab of GERS, Ifsttar. The mechanical part of this prototype can be seen in figure 2.11. This prototype facilitates us to conduct CMP measurements with smaller displacements and more moving steps in an automatic way.

There are mainly two parts in this prototype: a mechanical device carrying antennas to move and a software (named Nano_radar, installed on Windows 7) controlling the device and the GPR system at the same time.

The GPR antennas are two 1.5 GHz or 2.6 GHz antennas from GSSI (Geophysical Survey Systems, Inc.), activated by a SIR-3000 radar system. For each moving step, the robot carries up the antennas from the material surface to move laterally from the center to the two ends with determined distance, and then couples the antennas back to the surface. After each step, the radar system is launched to record one scan. From Nano_radar, the minimum movement of one antenna is defined as 1 mm. The transmitter and receiver move simultaneously during the measurement. The minimum displacement is therefore 2 mm. The maximum distance between the transmitter and receiver is 234 mm, due to the limit of the robot's length. The displacement, starting point and end point can be determined in Nano_radar before starting the measurements.

2.4.3.c Application on determination of concrete's durability indicators

Electromagnetic methods are very suitable to the detection of water content since EM waves are very sensitive to it [Balayssac et al., 2012]. The dielectric constant obtained from the capacitive technique is usually used to detect the water content of the material [Dérobert et al., 2008; Villain et al., 2012].
Though GPR was firstly developed for investigations of underground structures, it is more and more applied to the evaluation of concrete's durability indicators or monitoring parameters for the following reasons. The observables of GPR signals can be the amplitude, conductivity, dielectric constant, etc. The amplitude is used for the assessment of water content and chloride content as it is sensitive to both monitoring parameters [Laurens et al., 2002; Sbartaï et al., 2006a; Villain et al., 2015b]. The conductivity is linearly linked with the water content [Klysz et al., 2008]. It is also very sensitive to the variation of chloride content [Kalogeropoulos et al., 2013]. The dielectric constant, closely related to the velocity, is widely used to determine the water content [Dérobert et al., 2009; Kalogeropoulos et al., 2011].

2.4.4 Methods in cell

Here we will present two non-destructive methods used in our study requiring cylindrical samples of the materials. For in-situ measurements, these methods need core drilling that causes damage to the structures. Therefore, they can also be regarded as semi-destructive methods.

2.4.4.a EM coaxial/cylindrical cell

Electromagnetic coaxial cell is a device using transition line system to assess complex permittivity for material characterization in laboratory. It is developed from coaxial line measurements and performed for concrete by M. Adous [Adous et al., 2006] on a broadband (50 MHz - 1.6 GHz). In the work of [Robert, 1998], it is showed that for heterogeneous materials such as concrete, material sample dimensions should be at least three times greater than the maximum dimensions of the major aggregate. Therefore, in order to measure a 20 mm aggregate hydraulic concrete, the representative elementary volume (REV) should be 60 mm× 60 mm× 60 mm.
In the use of a classical coaxial line, the material under testing has to be drilled as an annulus core to precisely fit the sizes of outer and inner conductors, which is a complex and time consuming work. In this case, this technique is also a semi-destructive test method. By comparison, the cylindrical samples fitted for EM coaxial/cylindrical cell are much easier to get by using commercial coring devices. Furthermore, it extends the high frequency limit. While testing, the sample is placed in a cylindrical wave-guide holder which is connected to the coaxial line. The profile of the configuration can be seen in the figure 2.12.
As concrete is a porous heterogeneous material containing different sizes of aggregates, it is essential to study the representative element volume (REV). To determine the effective properties of the concrete slabs, it is recommended to use an REV 3 times more than D_{max}. The maximum diameter of the aggregates in our studied concrete is $D_{max} = 22$ mm. Indeed, the cores measured by EM cell have the dimension Ø75 × 70 mm. More information about RVE can be found in [Adous et al., 2006; Ihamouten, 2011].

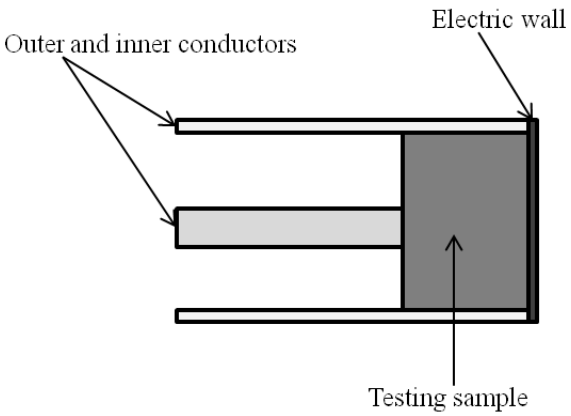

Figure 2.12: The coaxial/cylindrical transition line [Adous et al., 2006]

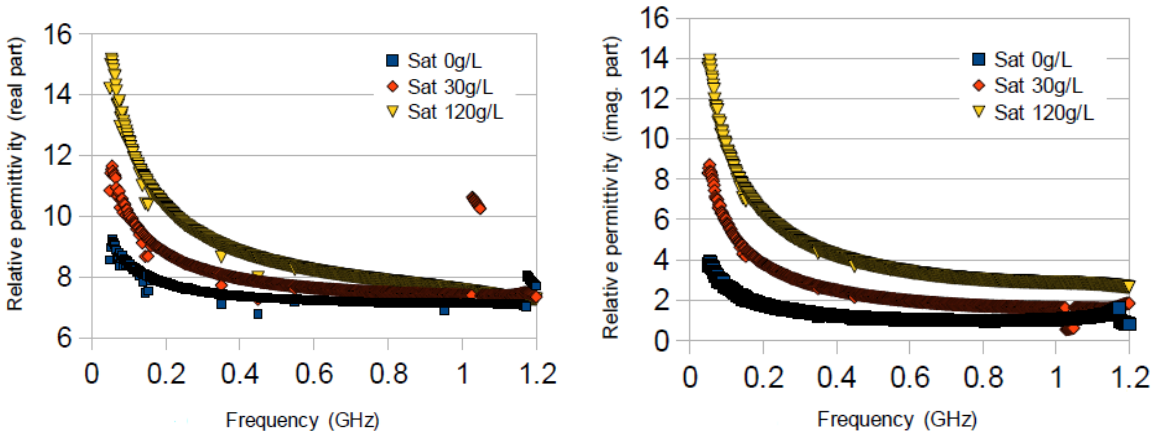

(a) Real part (b) Imaginary part

Figure 2.13: Example of complex relative permittivity measured by EM cell on saturated concrete with varying chloride content [Dérobert et al., 2009]

Then the transition line is connected to the vector network analyzer (VNA). A mode-matching technique is used to obtain the relation between the material's permittivity and the reflection coefficient at the coaxial to cylindrical transition. Model results were validated from the simulation results of the software HFSS. The permittivities are retrieved using an iterative optimization procedure. The VNA and coaxial line calibration is performed using an original calibration kit by placing three different terminations (short, open and load) at the reference transition plane.

Figure 2.13 is an example of the complex relative permittivity measured by EM cell on saturated concrete. By using this device, we are able to measure the permittivity of concrete with large dimensions of aggregates on a broad frequency band.

2.4.4.b Gammadensimetry

The use of γ-rays as a non-destructive means to test concrete has developed well in recent years. It is valuable to determine the position and condition of reinforcement, defects in concrete and its density. Gammadensimetry [Villain and Thiery, 2006] is a γ-radiometry technique commonly used to test the density of civil engineering materials by coring or inserting a probe into the concrete or pavement to be checked. It was then designed and

improved to determine the variations in density over time, particularly these due to drying or water absorption.

Principle and technique The measurement method is based on the absorption of gamma photons emitted by a radioactive source of Cesium C_S^{137}, with energy 0.662 MeV, after passing through a material with the thickness x (cm). This absorption follows Lambert's law:

$$N = N_0 \exp(-z\mu'\rho x) \tag{2.19}$$

where N_0 is the number of incident photons and N is the number (in counts per second) of collected photons, μ' (cm^2/g) is the mass absorption coefficient of the tested material, ρ (g/cm^3) is the density and z is the correction coefficient defined by the geometry of the device.
The density can therefore be given by the equation:

$$\rho = -\frac{1}{z\mu' x} ln\left(\frac{N_0}{N}\right). \tag{2.20}$$

Knowing z, μ' and the thickness of the material x makes it possible to calculate the density ρ.
If $\rho(t_0)$ is the density at the initial time t_0 and $\rho(t)$ at the instant t, both measured at the same point, the variation of density is related to the variation of mass water content (w) of the material sample by the relation :

$$w(t_0) - w(t) = \frac{\rho(t_0) - \rho(t)}{\rho_{sec}} \tag{2.21}$$

where ρ_{sec} is the dry density at the dry state after drying at 105°C, $w(t_0)$ is the mass water content at time t_0 and $w(t)$ is the mass water content at time t.

Experimental device The measurements are performed using a gamma horizontal frame. It is composed of the transmitter (radioactive source of C_S^{137}) and the receiver (scintillator), placed on either side of the specimen to be studied. The scintilla detector converts the gamma photons into electrical impulses which are counted during a given time, providing a count rate in counts per second (cps) (see in figure 2.14).
Auscultation is done step by step or continuously through the sample displacement (straight and circular). In our study, since the specimens are cylindrical, auscultation is conducted circularly as specimen's thickness is equal to the diameter of the collimation (the specimen is auscultated in rotation). The time required for counting N_0 and N are selected according to the desired accuracy of the density measurements. They depend on the activity of the radioactive source and the thickness of the material.

Advantages and limitations Gammadensimetry is a very convenient method to determine the water state, porosity and carbonation profiles of concrete without destroying the specimens. With a high γ-ray absorption coefficient of water, it is actually possible to detect small variation of water content in concrete. In recent years, it is used to measure water content gradients of specimens. Also, it is proved to be very powerful to quantify the carbonation progression in concrete.

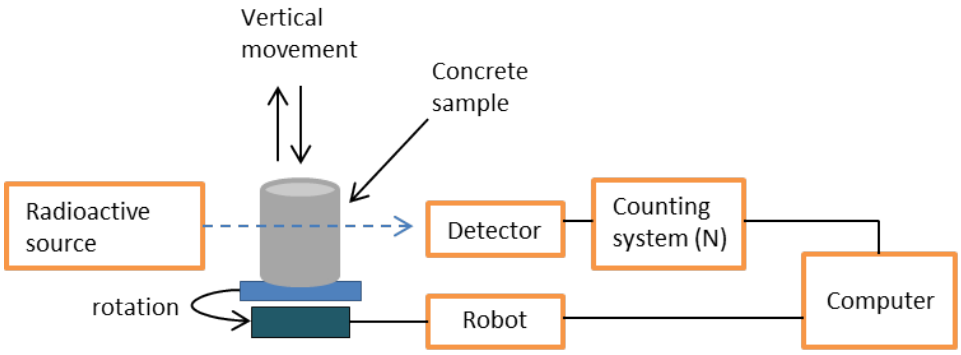

Figure 2.14: Diagram of γ-ray measurement device

A major problem with γ-radiometry is the expense of the detecting equipment. Even though they are becoming more commercial gauges and easier to use, the operation of the equipment normally requires professional skills. Moreover, this method is not totally non-destructive as it uses cores of the tested material at most times.

2.4.4.c Application on determination of concrete's durability indicators

The EM cell can give very reliable results of frequency dependent complex permittivity. However, it is only available for homogeneous measurement. Therefore, concrete samples are conditioned in homogeneous state and the measurements of EM cell are used calibrations of the water content and the chloride content [Dérobert et al., 2009; Villain et al., 2011a; Ihamouten, 2011].
The gammadensimetry is a means to measure the concrete's density by γ-rays. Though it is not sensitive to the presence of chloride, it can be used to determine the variation of the water content according to the depth and the time [Villain and Thiery, 2006; Villain et al., 2015b]. It can therefore be a reference methods for other NDT methods in the experiments of water imbibition.

2.4.5 Conclusion

This section presented some commonly used NDT methods applied to concrete. The applications of these methods to the evaluation of concrete's durability indicators and monitoring parameters were discussed. The result of ultrasonic method was found to be correlated to the water content. However, it is more often used for mechanical properties, such as cracks and voids in concrete. The electric methods and electromagnetic methods are found to be very suitable for the evaluation of the water content and chloride content. Two methods in cell provide references of the other NDT measurements.
GPR is chosen as a major means in this work as it is a very efficient EM method and its signals can penetrate through the concrete structure. Also, we are trying to compare the results of GPR with the resistivity and capacitive probes. The results of the other two techniques can be found in [Fares, 2015].

2.5 Conclusion

In this chapter, we have a general view on concrete's composition, its ageing problem and different test methods used on it.
As we mentioned before, concrete is a complex composite construction material with several kinds of components inside. It is also the most widely used construction material in civil engineering. Under this circumstance, its durability becomes a very important subject to us. When we talk about its durability, several indicators are closely related to it and have to be mentioned: porosity, water content, carbonation, chloride content, etc. Having a good knowledge of these indicators is essential to monitor the degradation and deterioration of concrete structures.
So we have found in literature the most widely used test methods on concrete, categorized as destructive and non-destructive methods. Destructive methods are usually slow and cause damage to the concrete, but can usually provide reliable testing results. Non-destructive methods consist of a large variety of techniques with different applications and limitations. Among all of them, the electromagnetic methods present the major advantage to be sensitive to water content. They are popular as they are simple, fast and repeatable, especially for GPR.
Finally, GPR becomes the main instrument for measurements in our study of water content gradients while it presents a high potential of innovative adaptation to this problem. The results will be compared with those of the semi-destructive methods: EM coaxial cell and gammadensimetry.

Chapter 3

Propagation of Electromagnetic Waves in Concrete

Contents

3.1 Introduction

The objective of this chapter is to understand how the EM (electromagnetic) waves propagate in a dispersive medium like concrete at the frequency range of GPR. A bibliographic research of relative basic theories of electromagnetism will be presented at the beginning of this chapter. Then we will compare two representative models, Jonscher's model [Jonscher, 1983] and Debye's model [Debye, 1929], for characterizing the dielectric properties of concrete. Lichtennecker-Rother equation [Lichtenecker and Rother, 1931], as a dielectric mixing model, will also be introduced. Finally, we will talk about general working principles of GPR and its emitting signals. The availability of Debye's model for modelling electromagnetic waves propagating in concrete will also be discussed.

3.2 Basic Theories of Electromagnetism

Water content, the indicator we are mainly interested in, is considerably important to know while assessing the durability performance of concrete [Bungey, 2004]. Though the measurement of internal water content is rather difficult, more and more research has been done for it in recent years [Klysz and Balayssac, 2007; Villain et al., 2009, 2012, 2015b; du Plooy et al., 2015b].
Electromagnetic waves are found to be sensitive to the variation of water content in concrete [Robert, 1998; Sbartaï et al., 2006a; Balayssac et al., 2012]. The propagation mechanism of EM waves is primarily governed by the dielectric properties of the propagation medium. Thus one of the main objectives of our work is to establish the physical and mathematical interaction between the waves and the materials.
This chapter presents a brief introduction of electromagnetic wave theory when propagation is in a dielectric dispersive medium. Then the principal electromagnetic parameters are recalled along with a research of the frequency dependent dielectric response.

3.2.1 Maxwell's equations

The electromagnetic wave theory plays a significant role in the development of radio, radar, remote sensing, and many other applications. Maxwell's four equations rigorously describe the electric and magnetic fields produced by the changing electric charges and currents.
Maxwell's equations in differential form are determined as [Kraus and R.Carver, 1973]:

$$\nabla \times \mathbf{E}(\mathbf{r}, t) = -\frac{\partial \mathbf{B}(\mathbf{r}, t)}{\partial t} \tag{3.1}$$

$$\nabla \times \mathbf{H}(\mathbf{r},t) - \frac{\partial}{\partial t}\mathbf{D}(\mathbf{r},t) = \mathbf{J_c}(\mathbf{r},t) \tag{3.2}$$

$$\nabla \cdot \mathbf{B}(\mathbf{r},t) = 0 \tag{3.3}$$

$$\nabla \cdot \mathbf{D}(\mathbf{r},t) = \rho(\mathbf{r},t) \tag{3.4}$$

where $\mathbf{E}$,$\mathbf{B}$,$\mathbf{H}$,$\mathbf{D}$,$\mathbf{J_c}$ and ρ are real functions of position and time. They are all in three-dimensional vector notation: $\mathbf{E}(\mathbf{r},t)$ is the electric field strength [V/m], $\mathbf{B}(\mathbf{r},t)$ is the magnetic flux density [W/m^2], $\mathbf{H}(\mathbf{r},t)$ is the magnetic field strength [A/m], $\mathbf{D}(\mathbf{r},t)$ is the electric displacement [C/m^2], $\mathbf{J_c}(\mathbf{r},t)$ is the electric current density [A/m^2], $\rho(\mathbf{r},t)$ is the electric charge density [C/m^3], ∇ is the vector differential operator $(\partial/\partial x, \partial/\partial y, \partial/\partial z)$. Equation (3.1) is Faraday's induction law. Equation (3.2) is the generalized Ampere's circuit law. Equation (3.3) and (3.4) are Gauss' laws for magnetic and electric fields. If we take the divergence of (3.2) and substitute (3.4) into it, we can find that:

$$\nabla \cdot \mathbf{J_c}(\mathbf{r},t) + \frac{\partial}{\partial t}\rho(\mathbf{r},t) = 0 \tag{3.5}$$

This is the conservation law of electric charge and current density. We can also find that (3.3) and (3.4) are not independent equations. They can be derived from (3.1), (3.2) and (3.5).
Since all the fields are functions of space and time, the electric field can be expressed as:

$$\mathbf{E} = \mathbf{E}(x,y,z,t) = \mathbf{E}(\mathbf{r},t) \tag{3.6}$$

By using inverse Fourier transforms, it is assumed that all fields have time dependence $e^{i\omega t}$(for which $\omega = 2\pi f$), and then the fields can be written as:

$$\mathbf{E}(\mathbf{r},t) = \Re\{\mathbf{E}(\mathbf{r})e^{i\omega t}\} \quad \text{and} \quad \mathbf{H}(\mathbf{r},t) = \Re\{\mathbf{H}(\mathbf{r})e^{i\omega t}\} \tag{3.7}$$

The phase amplitudes $\mathbf{E}(\mathbf{r})$ and $\mathbf{H}(\mathbf{r})$ are complex values. In harmonic time field, time derivatives $\partial/\partial t$ become multiplications by $i\omega$:

$$\frac{\partial \mathbf{E}(\mathbf{r},t)}{\partial t} = \Re\{\mathbf{E}(\mathbf{r})i\omega e^{i\omega t}\} \tag{3.8}$$

Therefore, Maxwell's equations (3.1) - (3.4) are rewritten as:

$$\nabla \times \mathbf{E}(\mathbf{r},\omega) = -i\omega\mathbf{B}(\mathbf{r},\omega) \tag{3.9}$$

$$\nabla \times \mathbf{H}(\mathbf{r},\omega) - i\omega\mathbf{D}(\mathbf{r},\omega) = \mathbf{J_c}(\mathbf{r},\omega) \tag{3.10}$$

$$\nabla \cdot \mathbf{B}(\mathbf{r},\omega) = 0 \tag{3.11}$$

$$\nabla \cdot \mathbf{D}(\mathbf{r},\omega) = \rho(\mathbf{r},\omega) \tag{3.12}$$

3.2.2 Conductivity and permittivity

In homogeneous isotropic dielectric and magnetic materials, we have the following relations:

$$\mathbf{D}(\mathbf{r},t) = \varepsilon_0\varepsilon_r\mathbf{E}(\mathbf{r},t) \tag{3.13}$$

$$\mathbf{B}(\mathbf{r},t) = \mu_0\mu_r\mathbf{H}(\mathbf{r},t) \tag{3.14}$$

$$\mathbf{J_c}(\mathbf{r},t) = \sigma\mathbf{E}(\mathbf{r},t) \tag{3.15}$$

where $\varepsilon_0 \approx 8.854 \times 10^{-12}$ F/m is the free space permittivity, $\mu_0 \approx 4\pi \times 10^{-7}$ H/m is the free space permeability; ε_r is the material-dependent relative permittivity, μ_r is the material-dependent relative permeability; σ is the material-dependent conductivity in the units of S/m. If we separate the free space part and the material-dependent part of a dielectric material, the material part can be characterized by a polarization vector $\mathbf{P}$ such that:

$$\mathbf{D} = \varepsilon_0\mathbf{E} + \mathbf{P} \tag{3.16}$$

The polarization $\mathbf{P}$ symbolizes the electric dipole moment per unit volume of the dielectric material [Kong, 1986].
The electric susceptibility χ is a dimensionless proportionality constant that indicates the degree of polarization of a dielectric material in response to an applied electric field. The electric susceptibility influences the electric permittivity of the material and thus influences many other phenomena in that medium. We have also got the equations as follows:

$$\mathbf{P} = \varepsilon_0\chi\mathbf{E} \tag{3.17}$$

$$\chi = \varepsilon_r - 1 \tag{3.18}$$

So in the case of a vacuum, $\chi = 0$. The equation (3.16) can be written as:

$$\mathbf{D} = \varepsilon_0(1+\chi)\mathbf{E} = \varepsilon_0\varepsilon_r\mathbf{E} \tag{3.19}$$

Conduction is defined as the movement of the free charges present on the energy layer of an atom greater than another. The process of electrical conduction in the material is defined by the electrical conductivity σ [S/m]. It is a complex quantity that measures a material's ability to conduct an electric current:

$$\sigma = \sigma' + i\sigma'' \tag{3.20}$$

where $i = \sqrt{-1}$. The real part σ' represents the migration of free charges through ohmic conduction and the imaginary part σ'' the polarization ability of the free charges due to inter-facial polarization.
In electromagnetism, permittivity is to measure how an electric field affects, and is affected by, a dielectric medium. By using the law of conservation of charge, we obtain an expression for the displacement current density vector $\mathbf{J_d}(\mathbf{r},t)$ [A/m^2] depending on the electric field:

$$\mathbf{J_d}(\mathbf{r},t) = \varepsilon\frac{\partial\mathbf{E}(\mathbf{r},t)}{\partial t} \tag{3.21}$$

Just like the electrical conductivity, the phenomena of displacement and polarization are caused by the presence of an electric field resulting in energy loss [David K. Cheng, 1989]. The complex dielectric permittivity characterizes the response of normal dielectric materials to external fields:

$$\varepsilon = \varepsilon' - i\varepsilon'' \tag{3.22}$$

where ε' is the real part of the permittivity, which is related to the stored energy within the medium; ε'' is the imaginary part of the permittivity, which is related to the dissipation

(or loss) of energy within the medium.
Now we can define the total current density as the sum of conduction current density and displacement current density:

$$\mathbf{J}(\mathbf{r},t) = \mathbf{J_c}(\mathbf{r},t) + \mathbf{J_d}(\mathbf{r},t) = \sigma\mathbf{E}(\mathbf{r},t) + i\omega\varepsilon\mathbf{E}(\mathbf{r},t) \tag{3.23}$$

$$\mathbf{J}(\mathbf{r},t) = i\omega\left(\frac{\sigma}{i\omega} + \varepsilon\right)\mathbf{E}(\mathbf{r},t) = i\omega\varepsilon_e\mathbf{E}(\mathbf{r},t) \tag{3.24}$$

So that,

$$\varepsilon_e = \varepsilon - i\frac{\sigma}{\omega} \tag{3.25}$$

where $\varepsilon_e = \varepsilon_e' - i\varepsilon_e''$ is the effective complex dielectric permittivity. From (3.20) and (3.22), the real and imaginary parts of ε_e are given by:

$$\varepsilon_e' = \varepsilon' + \frac{\sigma''}{\omega} \tag{3.26}$$

$$\varepsilon_e'' = \varepsilon'' + \frac{\sigma'}{\omega} \tag{3.27}$$

One of the most appropriate ways for calculating the loss in the medium is the loss tangent:

$$\tan\delta = \frac{\varepsilon_e''}{\varepsilon_e'} \cong \frac{\sigma}{\omega\varepsilon} \tag{3.28}$$

The quantity δ in equation (3.28) may be called the loss angle.

3.2.3 Wave equations

A plane wave propagating in a dielectric medium satisfies the Maxwell's equations (3.1) - (3.4) and (3.15). Taking the curl of (3.1) and substituting (3.2), also using the vector identity $\nabla\times(\nabla\times\mathbf{E}) = \nabla(\nabla\cdot\mathbf{E}) - \nabla^2\mathbf{E}$ and (3.15), we can easily derive the wave equation:

$$\nabla^2\mathbf{E}(\mathbf{r},t) = \sigma\mu\frac{\partial}{\partial t}\mathbf{E}(\mathbf{r},t) + \mu\varepsilon\frac{\partial^2}{\partial t^2}\mathbf{E}(\mathbf{r},t) \tag{3.29}$$

In an entire similar way, we can also obtain the equation of $\mathbf{H}$:

$$\nabla^2\mathbf{H}(\mathbf{r},t) = \sigma\mu\frac{\partial}{\partial t}\mathbf{H}(\mathbf{r},t) + \mu\varepsilon\frac{\partial^2}{\partial t^2}\mathbf{H}(\mathbf{r},t) \tag{3.30}$$

The Laplacian operator ∇^2 (also denoted as Δ) in a rectangular coordinate system is $\nabla^2 = \frac{\partial^2}{\partial x^2} + \frac{\partial^2}{\partial y^2} + \frac{\partial^2}{\partial z^2}$. Equations (3.29) and (3.30) are homogeneous vector wave equations. In time-harmonic field, they can be written as:

$$\nabla^2\mathbf{E}(\mathbf{r},\omega) + k^2\mathbf{E}(\mathbf{r},\omega) = 0 \tag{3.31}$$

$$\nabla^2\mathbf{H}(\mathbf{r},\omega) + k^2\mathbf{H}(\mathbf{r},\omega) = 0 \tag{3.32}$$

which are homogeneous Helmholtz's equations for a dielectric medium. Then we obtain the dispersion relation $k^2 = \mu\varepsilon_e\omega^2$ [Kong, 1986], where k is the complex wave number:

$$k = \beta - i\alpha = \omega\sqrt{\mu\varepsilon_e} \tag{3.33}$$

The real and imaginary parts α, β [rad/m] are the attenuation factor and propagation constant, respectively.
In this thesis, the propagation media have been regarded as non-magnetic. We only focus on the variation of electric field. In the case of the plane wave propagating in the +z direction, the solutions of the wave equations (3.31) is:

$$\mathbf{E}(z,\omega) = \mathbf{E}(0,\omega)e^{-ikz} = \mathbf{E}(0,\omega)e^{-\alpha z}e^{-i\beta z} \tag{3.34}$$

From the above equation, the wave amplitude attenuates exponentially with the factor $e^{-\alpha z}$ and oscillates with the phase factor $e^{-i\beta z}$. From the equation $k = \beta - i\alpha = \omega\sqrt{\mu\varepsilon_e} = \omega\sqrt{\mu(\varepsilon'_e - i\varepsilon''_e)}$, the attenuation factor α and propagation constant β can be expressed in terms of ε'_e and ε''_e in the following:

$$\alpha = \omega\sqrt{\frac{\mu\varepsilon'_e}{2}\left[\sqrt{1+\left(\frac{\varepsilon''_e}{\varepsilon'_e}\right)^2} - 1\right]} \tag{3.35}$$

$$\beta = \omega\sqrt{\frac{\mu\varepsilon'_e}{2}\left[\sqrt{1+\left(\frac{\varepsilon''_e}{\varepsilon'_e}\right)^2} + 1\right]} \tag{3.36}$$

By using the inverse relations, we obtain the important equations which we use to extract information on effective complex permittivity as follows:

$$\varepsilon'_e(\omega) = \frac{\beta^2 - \alpha^2}{\mu\omega^2} \tag{3.37}$$

$$\varepsilon''_e(\omega) = \frac{2\alpha\beta}{\mu\omega^2} \tag{3.38}$$

3.3 Characterization of Concrete's Dielectric Properties

To understand better the propagation of EM waves in concrete, we need a simple mathematical formula to characterize the concrete's permittivity. We have found several models that are commonly used for dispersive materials like concrete and will be introduced in the following.

3.3.1 Dispersion and dispersion models

A ground penetrating radar (GPR) wavelet can be regarded as a wave packet of different frequency waves. When a wavelet is propagating in a dielectric material like concrete, attenuation occurs and is strongly dependent on frequency. Higher frequency waves are

attenuated much more quickly than lower ones. Therefore, the signals received at early times contains more high frequencies than those arrived at later times after propagating in dielectric materials [Sheriff, 2002; Irving and Knight, 2003]. The wavelet has attenuation and shape distortion due to this phenomenon [Arcone, 1981]. The phase velocity of the wave becomes dependent on frequency. This is identified as transmission dispersion [Annan, 1996]. The media causing this dispersion phenomenon can be termed dispersive media. As a porous dielectric medium, concrete has frequency dependent permittivity, which disperse the phase velocity of EM waves [Ihamouten et al., 2012]. Another widely known dispersion is the waveguide dispersion. In this phenomenon, the phase velocity in a structure depends on the frequency due to the structure's geometry [Arcone, 1984].

3.3.1.a Advancing in dispersion research

In the last few decades, the dispersion in GPR applications has received a considerable attention, which has first been expressed by Arcone [Arcone, 1981]. The different mechanisms which exhibit dispersion in GPR data were studied by Annan [Annan, 1996]. Considering this problem, Turner presented an algorithm to correct it based on the attenuation of some earth materials [Turner, 1994]. In [Irving and Knight, 2003], the dispersion of the GPR wavelet was removed by using the inverse-Q filter.
Numerous studies on concrete have also addressed the importance of taking into account the dispersion in GPR requirements. Experimental results of the real part and the imaginary part of complex dielectric permittivity with respect to frequency are presented in [Dérobert et al., 2009], with dry and saturated concrete samples at different levels of chloride contents. In the work of Lai [Lai et al., 2011], the dispersion of GPR wave in early-aged and hardened concrete was studied using the two frequency dependent parameters: phase velocity $v(\omega)$ and the real part of relative dielectric permittivity (dielectric constant) $\varepsilon'_r(\omega)$.
In fact, for a dielectric material, dispersion is the dependence of permittivity on the frequency of an applied electric field. With the help of EM non-destructive tests, we are able to explore the frequency dependent permittivity of the material and combine it with the characteristics of the material.

3.3.1.b Debye's model

Debye relaxation [Debye, 1929] is an ideal dielectric relaxation response, which means that the electric dipole and external alternating electric field do not interact. It is usually expressed as a frequency-dependent and complex permittivity function:

$$\varepsilon = \varepsilon_\infty + \frac{\varepsilon_s - \varepsilon_\infty}{1 + i\omega\tau} \tag{3.39}$$

where ε_∞ is the dielectric permittivity at theoretically infinite frequency, ε_s the DC (Direct Current, or static) permittivity of the medium, ω the angular frequency and τ the relaxation time of the medium. Considering the existence of a real static conductivity σ_{dc}, the real and imaginary parts of the effective complex permittivity become [Giannopoulos, 1997]:

$$\varepsilon'_e = \varepsilon_\infty + \frac{\varepsilon_s - \varepsilon_\infty}{1 + \omega^2\tau^2} \tag{3.40}$$

$$\varepsilon_e'' = \omega\tau \frac{\varepsilon_s - \varepsilon_\infty}{1+\omega^2\tau^2} + \frac{\sigma_{dc}}{\omega} \tag{3.41}$$

Based on Debye's model, three expressions were developed to cover the non-Debye dielectric behaviour, represented by a general equation:

$$\varepsilon = \varepsilon_\infty + \frac{\varepsilon_s - \varepsilon_\infty}{[1+(i\omega\tau)^{1-\alpha_{CC}}]^{1-\beta_{CD}}} \tag{3.42}$$

where the exponent parameters $0 \leq \alpha_{CC}, \beta_{CD} \leq 1$. It reduces to Debye's model when $\alpha_{CC} = \beta_{CD} = 1$. Different cases are determined by the following criteria:

- $\alpha_{CC} \neq 0, \beta_{CD} = 0$ Cole - Cole formula [Cole and Cole, 1941, 1942]
- $\alpha_{CC} = 0, \beta_{CD} \neq 0$ Cole - Davidson formula [Davidson and Cole, 1951]
- $\alpha_{CC} \neq 0, \beta_{CD} \neq 0$ Havriliak - Negami formula [Havriliak and Negami, 1967]

The two - parameter formula is more capable of expressing the dielectric information of the observed results. Even though, the expressions have the limitation to explain the frequency dependence of the permittivity because α_{CC}, β_{CD} have no physical significance of dielectric interactions. Concerning this point, Jonscher's model is applied to describe the universal dielectric response.

3.3.1.c Jonscher's model

Jonscher's model, also known as the universal dielectric response, is based on universality in the form of dielectric response [Jonscher, 1983]. When the electromagnetic waves are propagating in the medium, there is a known relationship about electric susceptibility. The frequency-dependent dielectric susceptibility is the Fourier transform of the response function $f(t)$, then:

$$\chi(\omega) = \chi'(\omega) - i\chi''(\omega) = \int_0^\infty f(t)\exp(-i\omega t)\,dt \tag{3.43}$$

This is the base of describing the dielectric properties of materials. By Kramers-Kronig relations [Jonscher, 1983], $\chi''(\omega)$ and $\chi'(\omega)$ follow the same frequency dependence. The ratio between the real part and imaginary part is independent of frequency:

$$\chi''(\omega)/\chi'(\omega) = \cot(n\pi/2) \tag{3.44}$$

where n is the dispersion index and $0 < n < 1$. If we select reference frequency f_r arbitrarily, χ_r is the value of χ' under the reference frequency, so that:

$$\chi'(\omega) = \chi_r \left(\frac{\omega}{\omega_r}\right)^{n-1} \tag{3.45}$$

Therefore, the effective complex permittivity $\varepsilon_e(\omega)$ can be indicated by susceptibility $\chi(\omega)$, instantaneous dielectric response ε_∞ and DC conductivity σ_{dc}:

$$\begin{aligned} \varepsilon_e(\omega) &= \varepsilon_0\chi(\omega) + \varepsilon_\infty - i\frac{\sigma_{dc}}{\omega} \\ &= \varepsilon_0\chi_r \left(\frac{\omega}{\omega_r}\right)^{n-1} [1 - i\cot(n\pi/2)] + \varepsilon_\infty - i\frac{\sigma_{dc}}{\omega} \end{aligned} \tag{3.46}$$

In recent years, this model has been validated in different variants for studying dielectric losses of radar waves. Among these variants, the four-parameter (4p) variant (see in equation (3.46), four real constant parameters $[\chi_r, n, \varepsilon_\infty, \sigma_{dc}]$) is already confirmed by Ihamouten [Ihamouten et al., 2011] of its validity on a wide range of frequency by comparing with other three variants: two-parameter ($[\chi_r, n]$) variant, extended two-parameter ($[\chi_r, n]+\alpha_0$) variant and three-parameter ($[\chi_r, n, \varepsilon_\infty]$) variant.

3.3.2 Lichtennecker-Rother equation

Despite the effects of dispersion, another phenomenon to be considered is the dielectric gradient inside concrete. A dielectric mixing model found by the authors to efficiently implement the multi-layer waveguide is the Parallel model [Wu et al., 2003]:

$$\varepsilon'_e = \frac{\Sigma_{i=1}^{n} h_i \varepsilon'_i}{\Sigma_{i=1}^{n} h_i} \tag{3.47}$$

where ε'_i and h_i are respectively the dielectric constant and thickness of the i^{th} (i = 1, 2, ..., n) layer, and ε'_e is the equivalent dielectric constant of the n layers. From now on, to simplify the notations, the permittivity $\varepsilon = \varepsilon' - i\varepsilon''$ always represents the relative permittivity. The more general case of equation (3.47) is the well-known Lichtenecker-Rother equation, combining the dielectric properties of each components in a composite with its global dielectric properties [Lichtenecker and Rother, 1931; Martinez and Byrnes, 2001]:

$$\varepsilon'_e = [\Sigma_i V_i (\varepsilon'_i)^a]^{1/a} \tag{3.48}$$

where a is a geometric factor between [-1, 1], V_i and ε'_i are the bulk volume fraction and the permittivity of the i^{th} component, respectively. The parallel model applies to the case that the interfaces among these media are nearly parallel and infinite. And EM field components polarize perpendicularly to the incident wave plane.

3.3.3 Fittings of the dispersion models

There are mainly two objectives in this section: on one hand, to use numerical optimization methods, combining with experimental measurement data, to compare the characterizing performance of Debye's model and Jonscher's model for concrete with different dispersion characteristics of relative permittivity; on the other hand, to obtain the parameter values from the fitting results which are going to be used in the following numerical simulations.

3.3.3.a Concrete samples

The experimental data used here for the fittings are obtained from the project ORSI - APOS (Opération de Recherche Stratégique et Incitative - Auscultation Pour des Ouvrages Sûrs). It is a project collaborated by the institutes Ifsttar, Cerema and the historical monuments laboratory LRMH in France, to obtain gradients in concrete of water and salts and to understand the initiation and spread of corrosion in reinforced concrete subject to external pollution by chloride ions, through embedded sensors and non-destructive testing. The concrete mix designs and characteristics will be introduced in chapter 5.
Two concrete mix designs (named C1 and C3) are made with different cements, causing

different characteristics in concretes. The EM test results of dielectric properties differ due to the impacts of these characteristics. Each concrete has 3 cylindrical samples with dimension Ø75 × 70 mm tested at both ends at radar frequencies between [50MHz – 700MHz] by EM coaxial cell. The present characterization measurements were limited by the upper frequency limit of the measuring equipment EM cell, though the frequency band in the following part dedicated for CMP processing is higher. Each sample is tested in two different moisture conditions corresponding to the relative humidity RH=75% and RH=100%. To decrease the effect of concrete's heterogeneity, the complex dielectric permittivity is obtained as an average of the two measurements for each sample.

3.3.3.b Methodology of fitting

A fitting of the relative complex permittivity of the samples is conducted by nonlinear least-squares fitting operation to minimize the following cost function (Eq. (3.49)) :

$$\min \sum |\varepsilon - \varepsilon^m|^2 \tag{3.49}$$

where m denotes the measured data. The theoretical values of ε are determined by Eq. (3.46) for Jonscher's model and Eq. (3.40 -3.41) for Debye's model. To make sure we find the global minimum, at the beginning of the fitting of Jonscher's model, we have changed the starting values of the two parameters n and ε_∞ for in a wide range. So for each starting value, we have a minimum cost function. The minimum of all the minimum cost functions has been identified as the global minimum. For Debye's model, we have processed the similar calculations by varying the two parameters ε_∞ and ε_s.
The fitting performance is evaluated by the average relative error η, determined by the following equation:

$$\eta = \frac{1}{3N} \sum_{k=1}^{3} \sum_{n=1}^{N} \left| \frac{\varepsilon_{n,k} - \varepsilon_{n,k}^m}{\varepsilon_{n,k}^m} \right| \times 100\% \tag{3.50}$$

in which n stands for the index of frequency points and k for the index of concrete samples, $\varepsilon_{n,k}$ and $\varepsilon_{n,k}^m$ can represent the complex permittivity, calculated and measured respectively.

3.3.3.c Results and discussions

We have conducted the same fitting process for all the 6 samples. The results appear to be similar. Therefore, we have illustrated the comparisons of the fitting curves and experimental data of one representative concrete sample in figures 3.1 and 3.2 with RH equals to 75% or 100%, which means the concrete is unsaturated or saturated. If we compare figures 3.1 and 3.2, we note that when RH=100%, both the real and imaginary parts of the permittivity are higher than that of RH=75%. This difference is enhanced at low frequencies. Moreover, the permittivity changes more significantly for the saturated one. We can say that the saturated concrete is more dispersive and lossy. We also find that Debye's model, as an empirical model for describing frequency dependent permittivity, is not fully adapted to the whole frequency band. For the real part, Debye's model fails to fit the data at low frequencies, especially under 100MHz. For the imaginary part, we observe an increasing discrepancy between the data and Debye's model as the frequency increases. Meanwhile, the 4p variant of Jonscher's model shows good fitting performance with no limitation over the targeted frequency range.

The same fitting procedure has been conducted for all of the 6 samples of concrete. For

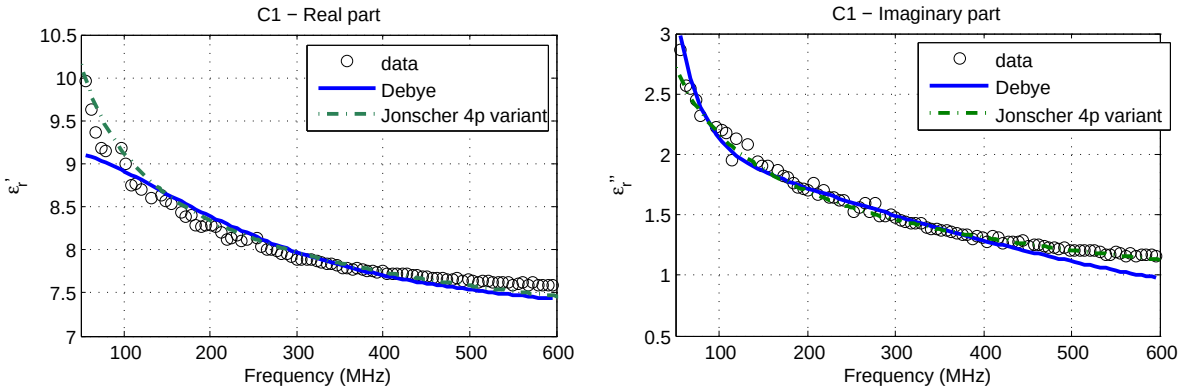

(a) Real part (b) Imaginary part

Figure 3.1: Fitting of the real (a) and imaginary (b) parts of relative permittivity for concrete C1 at RH=75%

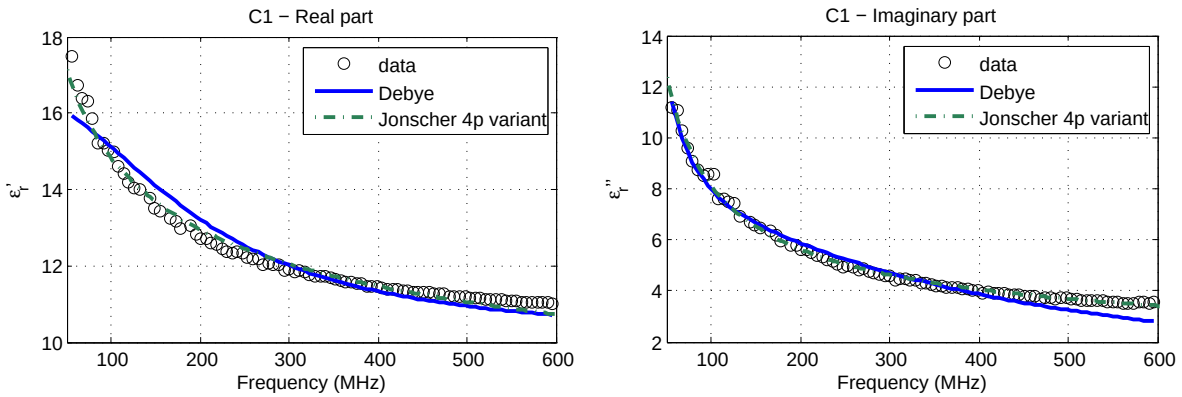

(a) Real part (b) Imaginary part

Figure 3.2: Fitting of the real (a) and imaginary (b) parts of relative permittivity for concrete C1 at RH=100%

each mix design, the results are carried out by calculating the average of the 3 samples, exhibited in table 3.1 and 3.2. For Debye's model, we find that the fitting performance becomes worse in the case of $RH = 100\%$. The value of conductivity σ_{dc} apparently increases as the concrete is saturated, which means the attenuation has increased. Though the relaxation time τ did not show important change in C3, the increment of the dielectric strength $\Delta\varepsilon = \varepsilon_s - \varepsilon_\infty$ has enlarged concrete's dispersion, which can be seen in figures 3.1 and 3.2.

For Jonscher's model shown in table 3.2, we also observe a variation of parameters according to the change of water content. Having the same tendency as the dielectric permittivity, the susceptibility value χ_r increases as water content increases. As concrete becomes saturated, the material is more dispersive, indicated by the reducing of the frequency exponent n. Furthermore, if we compare the results of the two concrete C1 and C3, we can find that, in saturated condition, C1 is more lossy (variation of σ_{dc}) while C3 has an obvious increment of dispersion (variation of n).

Comparing the two models, the values of relative error η in table 3.2 are much smaller than those in table 3.1, showing better fitting performance of Jonscher's model than Debye's model. The two parameters ε_∞ and σ_{dc} have the same definitions as we find in both models. However, the effect of AC (Alternating Current) conductivity neglected in Debye's model should normally be added to the DC conductivity, following the equation of the frequency dependent conductivity [Jonscher, 1983; Yakuphanoglu et al., 2003]:

$$\sigma_{tot}(\omega) = A\omega^n + \sigma_{dc} \tag{3.51}$$

where A is a pre-exponential factor and n is the frequency exponent. That explains why we find higher values of σ_{dc} in table 3.1 than in the results of Jonscher's model (table 3.2). Also, ε_∞ has got higher value in Debye's model due to its divergence of representing the permittivity at infinitely high frequencies.

Table 3.1: Debye's parameters and fitting results (mean value of 2 measurements on 3 samples per concrete)

Concrete	ε_∞	ε_s	τ (ns)	σ_{dc} (S/m)	η (%)
C1 (RH**=75%**)	7.18±0.12	9.22±0.03	0.69±0.08	0.0074±0.0008	1.60±0.08
C3 (RH**=75%**)	8.37±0.81	10.64±1.55	0.86±0.13	0.0091±0.0025	2.29±0.17
C1 (RH**=100%**)	9.84±0.30	15.35±1.02	0.83±0.06	0.024±0.0067	3.11±0.27
C3 (RH**=100%**)	10.85±0.40	15.61±0.70	0.84±0.10	0.019±0.0006	2.32±0.37

Table 3.2: Jonscher's parameters and fitting results (mean value of 2 measurements on 3 samples per concrete)

Concrete	χ_r	n	ε_∞	σ_{dc} (S/m)	η (%)
C1 (RH**=75%**)	2.11±0.25	0.67±0.06	5.60±0.23	0.0014±0.0013	0.79±0.38
C3 (RH**=75%**)	2.60±0.17	0.75±0.03	6.21±0.80	0.0060±0.0034	1.42±0.32
C1 (RH**=100%**)	5.02±0.81	0.65±0.04	5.91±0.60	0.0101±0.0067	1.20±0.13
C3 (RH**=100%**)	3.40±0.13	0.59±0.01	8.41±0.11	0.0048±0.0013	1.13±0.01

3.3.4 Conclusion

In this section, we have introduced two of the commonly used dispersion models: Debye's model and Jonscher's model. And one homogenization model Lichtennecker - Rother equation. The workability of Debye's model and Jonscher's model has been discussed by comparing their fitting performance on concrete's dielectric permittivity.
In this thesis, Debye's model is used for the modelling as it is already employed in many studies of concrete and is available in a wide GPR frequency range. Also because it is integrated in the GPR simulation software GprMax [Giannopoulos, 2005], which facilitates our numerical analysis with finite-difference time-domain (FDTD) technique. Meanwhile, Jonscher's model is preferred to do the extrapolation of experimental data if we want to compare the results to other techniques, such as the results of capacitive probes at 33MHz [Dérobert et al., 2008].

3.4 Ground Penetrating Radar (GPR)

We have introduced some general principles and applications about GPR in last chapter. Here we are going to talk about its system configurations and emitting signals applied in our study.

3.4.1 Definitions of System configurations

The GPR system that we employ in our experiments is the SIR® 3000 system from GSSI (Geophysical Survey Systems, Inc.), being equipped with antennas of two central frequencies: 1.5 GHz and 2.6 GHz. Figure 3.3 shows the internal structures of the two kinds of antennas boxes, when we can see the transmitter and the receiver are built as bowtie antennas. To apply the system to our experiments, several criteria have to be considered in the system settings.

3.4.1.a Central frequency

To choose the central frequency of antennas f (MHz), there should be a trade-off between the spatial resolution, detection depth and portability of the system. The suitable is usually defined by the following equation:

$$f = \frac{150}{x\sqrt{\varepsilon_r}} \tag{3.52}$$

where x is the desired spatial resolution, ε_r is the relative permittivity of the tested material. That is to say, a better resolution requires a higher central frequency.

3.4.1.b Time window

Time window w (ns) determines the maximum time sampling range of the radar signal received by the antenna, sometimes equivalent to the detection depth. It can be approximated by:

$$w = 1.3 \times \frac{2D}{v} \tag{3.53}$$

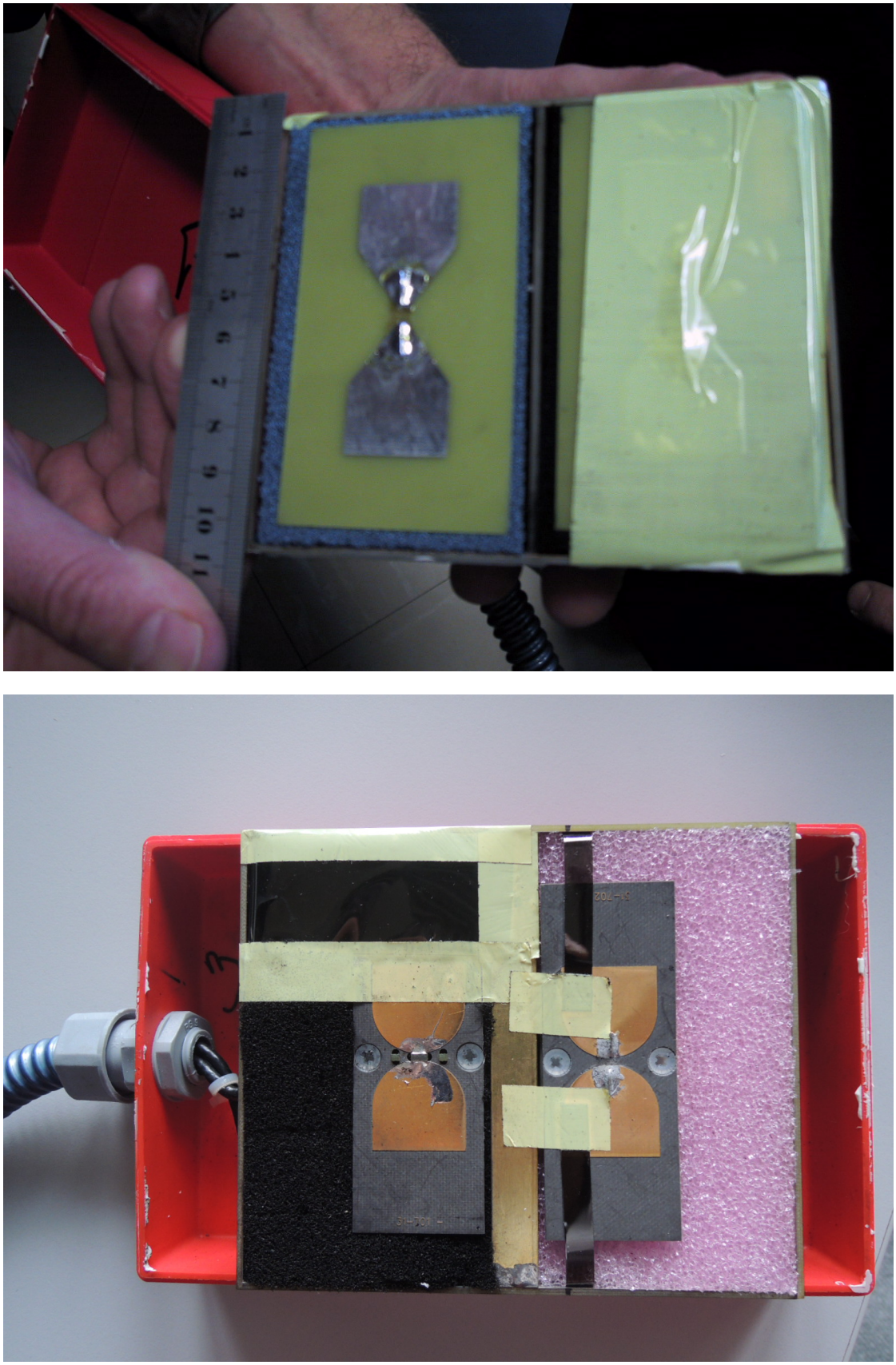

Figure 3.3: Antennas in application with the central frequency (a) 1.5 GHz (b) 2.6 GHz

where D (m) is the maximum detection depth and v (m/ns) is the minimum propagation velocity of the EM wave. The increase of 30% is the estimated margin left for the uncertainty of the wave propagation velocity and depth in the medium. The typical time window applied to 2.6 GHz antennas is around 10 ns while for 1.5 GHz ones, 10 to 15 ns. Even though, the required time window for detecting a wave-guide can be much longer in order to receive the multi-reflections.

3.4.1.c Sampling interval

Sampling interval refers to the time interval between two points on the recorded waveform. It is normally controlled by Nyquist sampling theorem [Oppenheim et al., 1989]. For lossless digitization, the sampling rate should be at least twice the maximum frequency responses. Like for the frequency components of a 2.6 GHz, if $f_{max} = 5$ GHz, the sampling frequency should not be lower than 10 GHz. For a scan with a time window of 10 ns, the sampling number should not be smaller than 100.
In fact, in the SIR® 3000 system, this condition is highly satisfied with a couple of choices. The number of samples per scan can be 256, 512,..., until the maximum 8192. Weighing the resolution and system's storage capacity, we choose 2048 samples per scan for the measurements.

3.4.1.d Filters of signal

Proper setting of filters allow to remove interference or smooth noise and keep the most useful information of the received data. The filters consist of a low-pass (LP) filter, any frequency under which will be allowed to pass by and recorded by the system, and a high-pass (HP) filter, working on the opposite way. Normally, filters are set according to the relationship with the central frequency f_c. So that $f_{LP} = 2f_c$ for low-pass and $f_{HP} = f_c/5$ for high-pass.

3.4.2 Emitting signals

After setting the system configurations for antennas, the emitting signals are collected in the air when the transmitter and the receiver are put at minimum offset.
Then we calculate the signals' spectra using Fast Fourier Transform (FFT). The emitting signals in time domain and their spectra in frequency domain are exhibited in the following figures: figures 3.4 and 3.5.

The temporal signals in figures 3.4 and 3.5 show that the wavelet of GPR is very similar to a Ricker wave. From the spectra of the two signals, we can find the measured central frequency is in fact lower than we expected. For 1.5 GHz antennas, it appears between 1 GHz and 1.5 GHz; while for 2.6 GHz antennas, it is around 2 GHz. Furthermore, when the antennas are coupled to the ground or the dispersive materials such as concrete, the central frequency can be even lower since these media have the low-pass effects. Knowing the real central frequency helps us choose the right frequency band when dealing with GPR data.

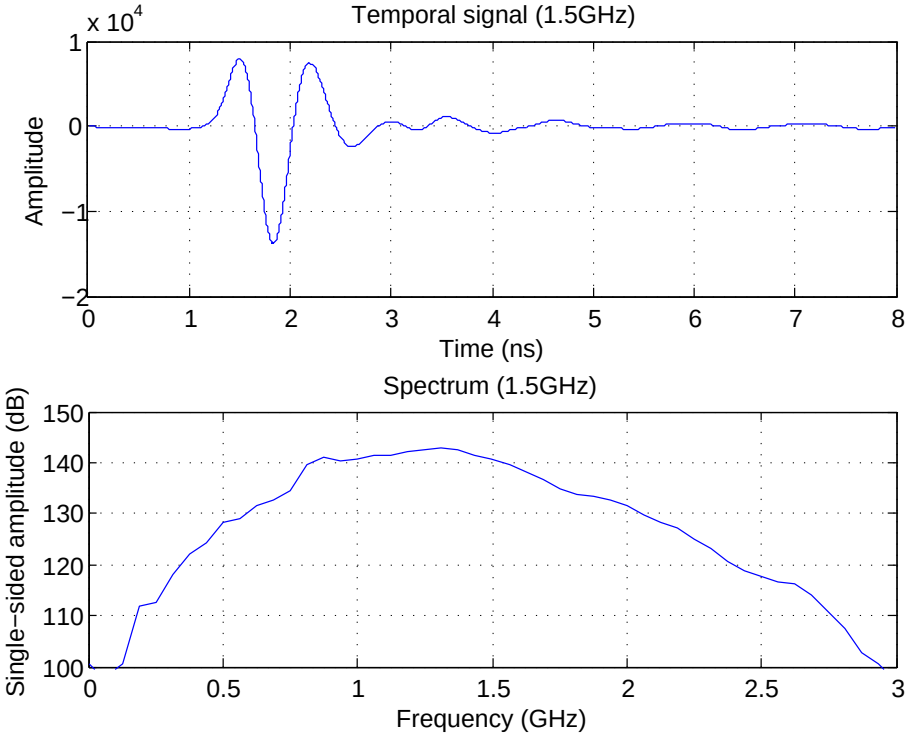

Figure 3.4: Emitting signal of 1.5 GHz antennas and its spectrum in frequency domain

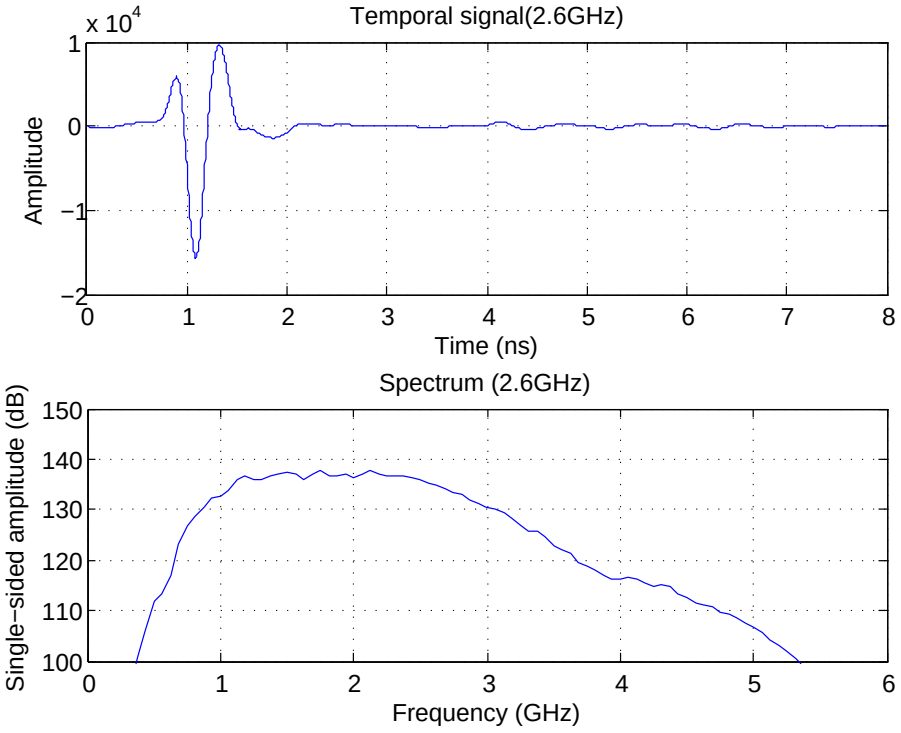

Figure 3.5: Emitting signal of 2.6 GHz antennas and its spectrum in frequency domain

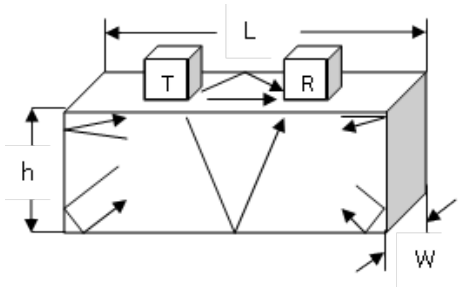

Figure 3.6: Diagram of EM wave propagating in a concrete slab

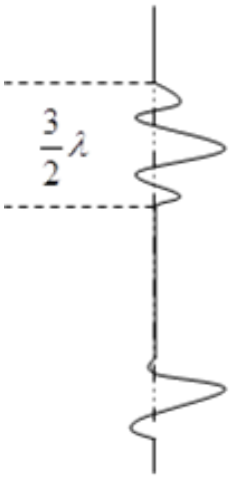

Figure 3.7: Example of EM pulse

3.4.3 Edge effects and dimensions of samples

The dimension of the concrete and the reinforcement inside can strongly affect the propagation of EM waves of GPR. In civil engineering structures, the reinforcements are necessary and can not be removed while measuring. But in the lab, we want to know the ideal dimension of the concrete samples to avoid any edge effects.
This is the progress to get the compromise of the slab's sizes before we conduct the experiments studying the effect of concrete moisture on electromagnetic (EM) waves propagating through concrete laboratory slabs. The wave propagation can be seen in figure 3.6. Generally speaking, two conditions should be satisfied with the concrete slabs.
First, after making the concrete slabs, we need to put them into the oven to homogenize the distribution of water content. In order to put the slabs into this oven, the sizes of the slabs cannot exceed those of the oven. The sizes measured inside the oven for concrete slabs are:

- Length $L = 50$ cm
- Width $W = 40$ cm
- Height $h = 13$ cm

Second, the interferences should be avoided from one signal to another. Two commercial radar systems will be used in our experiments, with antennas at the frequencies 2.6 GHz and 1.5 GHz, respectively. If we observe figure 3.7, the waves transmitted through the concrete are like a series of EM pulses with the length of approximately $3/2\lambda$.

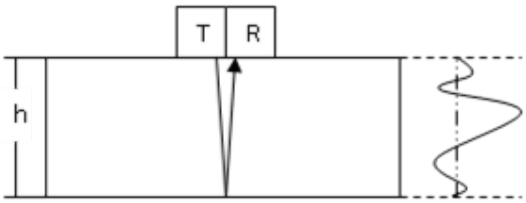

Figure 3.8: EM wave propagating in slab assuming transmitter and receiver in the same position

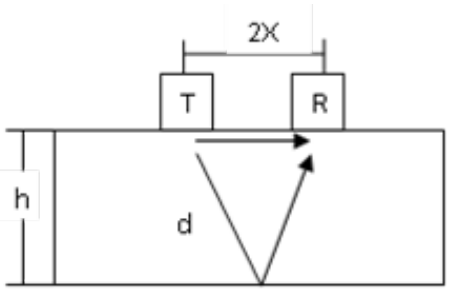

Figure 3.9: EM wave propagating in slab when transmitter and receiver in different positions

3.4.3.a Antenna 1

For the first system, $f = 2.6$ GHz.
Frequency of the emitted signals is actually around $f_c = 2$ GHz, as we can see in figure 3.5. The lowest permittivity for this problem is supposed to be $\varepsilon' = 5$ when concrete is dry. Thus we can get the velocity and wavelength of the EM waves:

$$v = \frac{c}{\sqrt{\varepsilon'}} = 1.34 \times 10^8 \quad \text{m/s} \tag{3.54}$$

$$\lambda = \frac{v}{f} = 6.7 \quad \text{cm} \tag{3.55}$$

(1) As we can see in figure 3.8, the height of the slab should be enough for at least one complete signal, so $h > \frac{3}{2}\lambda = 10$ cm.

(2) For the receiver, the wave on the surface should be separated from the wave reflected from the bottom of the concrete. In our CMP measurements, the maximum distance between the transmitter and receiver $2X$ is defined as 20 cm (figure 3.9). Some criteria have to be satisfied:

$$\begin{aligned} 2d - 2X &> \frac{3}{2}\lambda \\ d &= \sqrt{X^2 + h^2} \\ 2X_{\max} &= 20 \end{aligned} \tag{3.56}$$

Therefore, the height of the slab is $h > 11.2$ cm.

(3) As we can see in figure 3.10, waves a and b are the reflected waves from the edges of the slab. To avoid their interferences, the following conditions should be satisfied.
For wave a: $2x + 2X > 2d + \frac{3}{2}\lambda$, $d = \sqrt{X^2 + h^2}$. According to the oven's size, we suppose

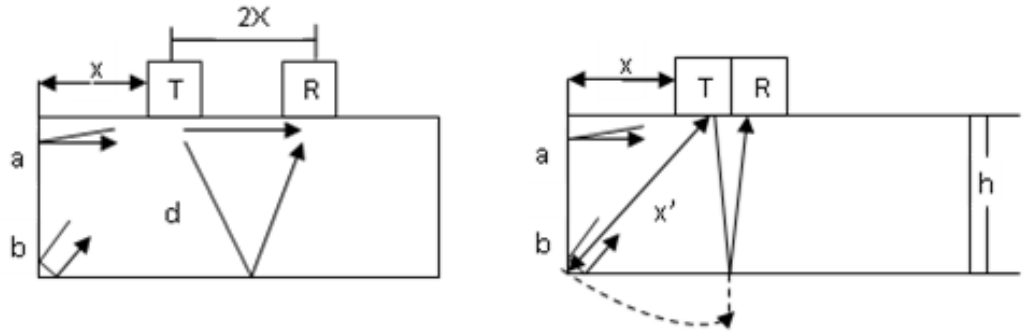

Figure 3.10: EM wave propagating in slab with edge effects

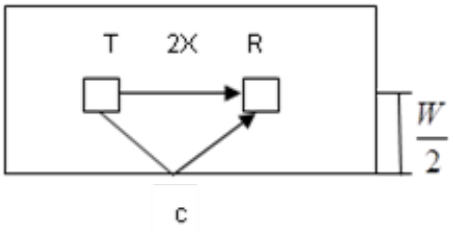

Figure 3.11: EM wave propagating on the upper face of the slab

$h = 13$ cm, then $x > 11.4$ cm.
For wave b: As it is always true that wave b reaches the receiver later than wave a, wave b will not affect the waves we need. The particular situation that needs to be considered is that when transmitter and receiver are co-located (figure 3.10 (right)), when $2(x' - h) > \frac{3}{2}\lambda$. With $x = \sqrt{x'^2 - h^2}$, we can get $x > 12.5$ cm.
For the slab's length L, from above situations, we obtain the length of the slab: $L > x + 2X > 32.5$ cm.

(4) Figure 3.11 shows the waves transmitted on the upper surface. The wave c should be separated, so that: $2\sqrt{X^2 + \left(\frac{W}{2}\right)^2} > 2d + \frac{3}{2}\lambda$. Therefore the width of the slab is $W > 37.8$ cm.

(5) In summary, if the following criteria are met for the size of the slab, interferences can be avoided while the waves are propagating in the slabs:

$$\begin{aligned} 11.2 < h < 13 \quad & \text{cm} \\ 32.5 < L < 50 \quad & \text{cm} \\ 37.8 < W < 40 \quad & \text{cm} \end{aligned} \tag{3.57}$$

3.4.3.b Antenna 2

For the second system, $f = 1.5$ GHz.
The central frequency in concrete is approximately $f_c = 1$ GHz. Still, suppose $\varepsilon' = 5$ when concrete is dry. The velocity and wavelength of the EM waves are as follows: $v = \frac{c}{\sqrt{\varepsilon'}} = 1.34 \times 10^8$ m/s, $\lambda = \frac{v}{f} = 13.4$ cm
Then, we do the same calculations as the first system:

(1) Despite the limitation of the oven, the height of the slab is $h > \frac{3}{2}\lambda = 20$ cm.

(2) The maximum distance between the transmitter and receiver $2X$ is defined as 20 cm (figure 3.9). Some criteria have to be satisfied:

$$\begin{aligned} 2d - 2X &> \frac{3}{2}\lambda \\ d &= \sqrt{X^2 + h^2} \\ 2X_{\max} &= 20 \end{aligned} \tag{3.58}$$

Therefore, the height of the slab is $h > 17.4$ cm.

(3) According to the criteria in (1), we suppose $h = 20$ cm.
For wave a: $2x + 2X > 2d + \frac{3}{2}\lambda$, $d = \sqrt{X^2 + h^2}$. Then we have $x >$22.4 cm.
For wave b: When transmitter and receiver are co-located (figure 3.10 (right)), $2(x' - h) > \frac{3}{2}\lambda$. With $x = \sqrt{x'^2 - h^2}$, we can get $x > 22.5$ cm.
For the slab's length L, from above situations, we obtain the length of the slab: $L > x + 2X >$42.5 cm. The minimum of L will increase if h increases.

(4) As figure 3.11 shows, the wave c should be separated, so that: $2\sqrt{X^2 + \left(\frac{W}{2}\right)^2} > 2d + \frac{3}{2}\lambda$. Since $d = \sqrt{X^2 + h^2}$, the width of the slab is $W > 61.7$ cm. The minimum of W will increase if h increases.

(5) In summary, if the following criteria are met for the size of the slab, interferences can be avoided while the waves are propagating in the slabs:

$$\begin{aligned} h &> 20 \quad \text{cm} \\ L &> 42.5 \quad \text{cm} \\ W &> 61.7 \quad \text{cm} \end{aligned} \tag{3.59}$$

From the calculation results we can find that lower frequency requires larger specimen to avoid the interferences. However, larger specimen means higher cost of fabrication in labor work, materials and time. Furthermore, these criteria have exceeded the dimension of the oven. When the dimension of slabs cannot satisfy these criteria, we should be careful with the edge effects.

3.4.4 Comparison of synthetic and experimental time-domain waveforms

To understand better the propagation of EM waves in concrete and to study the workability of Debye's model, we employ the GPR simulation software GprMax 2D [Giannopoulos, 2005] to model the multi-offset data collected by GPR over concrete. A comparison between the synthetic and experimental were conducted to confirm the validity of the propagation modelling and the Debye's model.

3.4.4.a Parameter setting to model the concrete

In the command of GprMax, the key words 'free_space' and 'pec' which describe air and perfect conductors, respectively, are reserved and can be used directly. For any other media, they have to be defined by the following 6 parameters based on Debye's model:
1.the DC(static) relative permittivity of the medium ε_s
2.the relative permittivity at theoretically infinite frequency ε_∞
3.the relaxation time of the medium τ(seconds)
4.the DC(static) conductivity of the medium σ_{dc}(Siemens/metre)
5.the relative permeability of the medium μ
6.the magnetic conductivity of the medium σ^*
In our study, we focus on the variation of the electric field. Therefore, we set μ=1 and σ^*=0 to make concrete a non-magnetic medium. For each simulation configuration, the parameters of the concrete are defined in two cases, non-saturated and saturated concrete, in order to compare the EM wave propagating in the medium with different levels of dispersion.
We have picked one concrete (B4) as an example for the comparison, from the work of Ihamouten [Ihamouten et al., 2011] to conduct the comparison because it has been tested both by EM cell and GPR under two humidity conditions: RH=30% and RH=100%. The values of Debye's parameters obtained from a former study [Xiao et al., 2014] are exhibited in table 3.3:

Table 3.3: Debye's parameters used for simulation

B4	ε_∞	ε_s	τ**[ns]**	σ_{dc}**[S/m]**	η**[%]**
RH**=30%**	5.20±0.047	5.52±0.051	2.65±0.64	0.0012±0.00016	1.25±0.048
RH**=100%**	9.58±0.79	13.89±0.99	0.86±0.11	0.025±0.0078	2.50±0.085

3.4.4.b Results and discussions

Figure 3.12 shows the emitting signal of 1.5 GHz antennas from GPR and its modelled signal using GprMax 2D. When the source in simulation is set as Ricker wave at 0.9 GHz, the main parts of the two wavelets match well with each other. The difference in the end of the pulses can be explained by the limitation of the 2D software which cannot directly model the antennas.
Then we compared the received signals simulated and measured on concrete B4 with different propagation distances under the humidity conditions RH=30% and RH=100% (see in figures 3.13 and 3.14). The concrete slab was put on the ground to diminish the reflection from its bottom. Meanwhile, in GprMax, the concrete sample is set to be large enough to avoid the edge effects and any reflections. So only the surface wave propagated directly from the transmitter and receiver through the concrete is concerned. We observe for both concretes, as the propagation distance increases, an unexpected wave comes out at the beginning of the surface wave of simulations. It can be notified as the direct wave propagated in the air. Fortunately, the air wave in this measurement has been well shielded by GPR's boxes. Otherwise, we will have to filter it in order to remove its effect of interference. From figure 3.13 we can see, in dry concrete when medium is less dispersive, the simulated waves and measured waves follow almost the same

transformation rules. However, for saturated concrete in figure 3.14, there are obvious positioning shifts between the model and the measurement. It increases as the propagation distance of EM wave increases. We already know from last section that the fittings of Debye's model for saturated concretes obtain higher residues compared to non-saturated ones, which confirms this result.

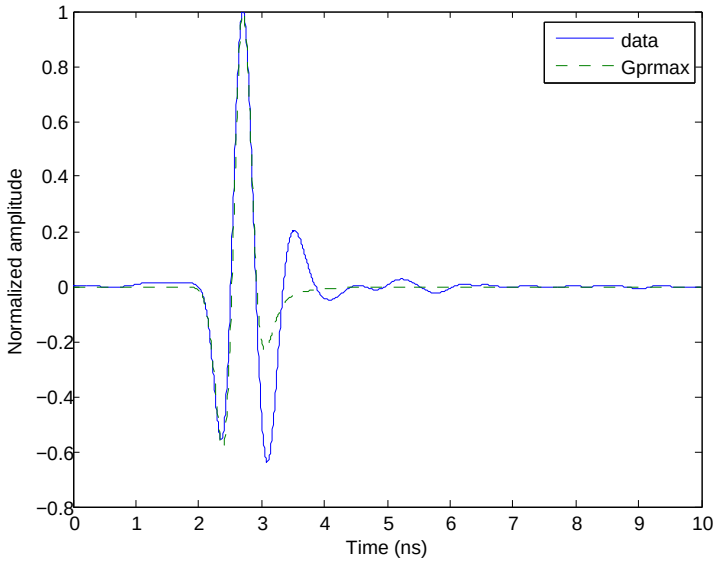

Figure 3.12: Emitting signals of 1.5 GHz antennas from GPR and Simulation

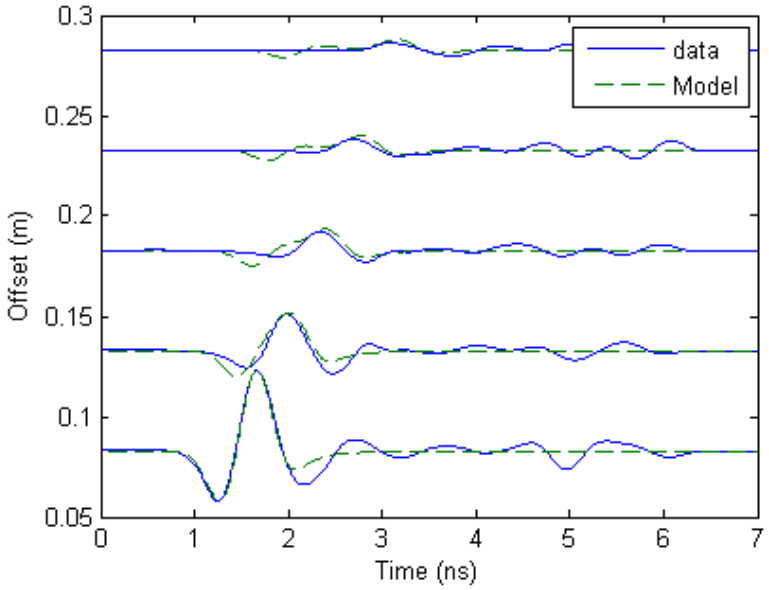

Figure 3.13: Simulated and measured received signals at different offset on dry concrete

3.4.5 Conclusion

Here we have discussed about the GPR and its system we employ in our study. Some settings, such as the central frequency, time window, sampling interval..., have to be carefully chosen before the measurements. The emitting signals of GPR have been analysed in frequency domain. The measurements on concrete in different moisture conditions are

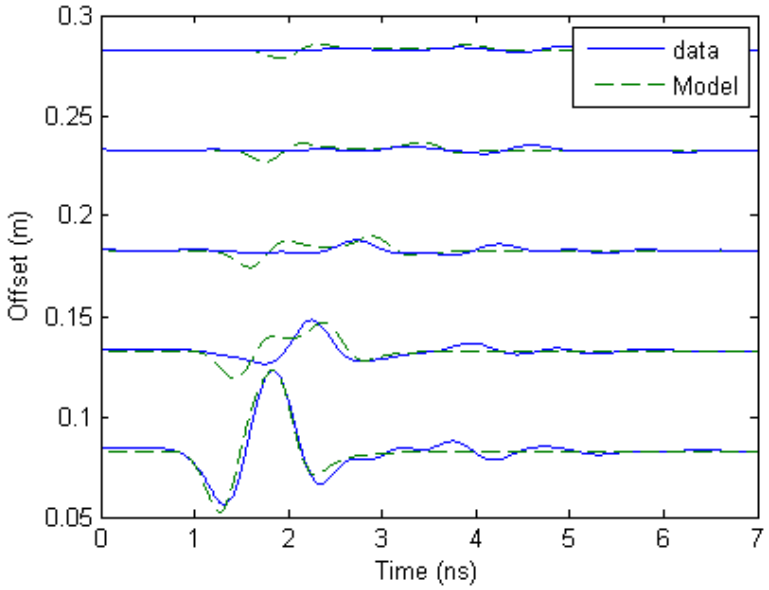

Figure 3.14: Simulated and measured received signals at different offset on saturated concrete

compared to the wave-field modelled by GprMax 2D. Generally, the waves match well with each other. When the concrete is saturated, the error increases as the propagation increases. Concerning this point, Debye's model is not very well adapted to characterize very dispersive materials. However, it is still satisfying to our study. Moreover, GprMax is a very efficient simulation tool with Debye's model integrated in it. When we do simulations with GprMax, we will assume the media as low-dispersive media.

3.5 Conclusion

In this chapter, we have firstly discussed about the basic theories of electromagnetic wave propagation in dispersive media. There is a brief review of Maxwell's equations and solutions of electromagnetic fields in this process. Based on the above discussion, we have studied several dispersion - absorption models for concrete's description of dielectric properties. Two of them, Debye's model and Jonscher's model, are compared through their applicability of describing concrete by fitting concrete's EM cell data in different moisture conditions. Jonscher's model is proved to have good fitting performance on the whole frequency band of the data. Debye's model turns out to have some limits of fitting at lower (for ε') or higher (for ε'') frequencies. But it works well with low-dispersive materials. And it is the model employed by GprMax. Finally, we constructed some response waveforms in time domain on a dry and saturated concrete with GprMax 2D. The signals are in accordance with the real measured ones. This helps us better understand the working performance of GprMax and the dielectric properties of concrete.

Chapter 4

Characterization of Dispersive Media Using Surface Guided Waves

Contents

4.1 Introduction

Among all the NDT methods, the electromagnetic techniques are mostly based on an analysis of the temporal content of electromagnetic (EM) waves propagated in concrete [Rhim, 2001; Laurens et al., 2002; Bungey, 2004; Hugenschmidt and Loser, 2007; Dérobert et al., 2008; Lai et al., 2009; Villain et al., 2012]. Some efforts for exploiting the EM wave's dispersion focused on the dielectric nature of materials [Ihamouten et al., 2012]. Besides, certain applications derived from seismic techniques have revealed the existence of a second dispersion phenomenon due to the geometry and boundary conditions of the propagation medium [Gabriels et al., 1987; Roth and Holliger, 1999; Xia et al., 2004].
In the field of GPR application, the notion of geometric dispersion was introduced as a multi-modal propagation of EM waves through waveguides [Arcone, 1984; Arcone et al., 2003; Liu et al., 1998]. Through the waveguide layer, where EM energy undergoes multiple reflections, leading to a series of constructive interferences between the various propagation modes. In these conditions, the temporal methods used to estimate the propagation velocities of EM waves from WARR or CMP configurations [Smith, 1984; Dai and Young, 1997; van der Kruk and Slob, 2002] becomes totally inappropriate.
In the presence of a strong dielectric contrast between the various layers composing the investigated medium, the EM energy is "trapped" in the upper layer of the structure, a situation that imposes a modal approach on studying EM wave propagation [Annan, 1973; Annan et al., 1975]. Arcone [Arcone, 1984] is recognized as the precursor of this approach for the EM characterization of a thin ice layer bounded by air on its upper surface and water below. Since the air /ice and ice /water dielectric contrasts are extremely high (i.e. strong reflectors), the ice layer behaves like an EM waveguide. In assuming that the dominant frequencies of dispersive waves are sufficient to calculate the waveguide cut-off frequency, it was able to determine the dielectric permittivity of various ice layers.
More recently, van der Kruk et al. [van der Kruk et al., 2006; van der Kruk and Arcone, 2007] demonstrated the possibility of deriving the physical properties of each layer constituting the dielectric medium from the dispersion of GPR waves propagated in waveguides with media of both strong [van der Kruk and Arcone, 2007] and weak [van der Kruk et al.,

2006] permittivities beneath. The results of these studies have shown that the propagation of Transverse Electric (TE) modes, which implies the use of "broadside" antenna orientations, are less sensitive to the EM leakage phenomenon [van der Kruk and Arcone, 2007; Ihamouten, 2011; Villain et al., 2015b].
As a follow-up to this work, an innovative procedure is developed in this chapter, for applying EM waveguide dispersion within the spectral domain to characterize multi layers presenting in concrete structures. As formed due to water penetration into concrete, the situations can be defined as gradients or decomposed into two parts: dry and wet layers. The chapter will therefore begin with an introduction to the extraction of dispersion curve from GPR data. Then followed by the modal propagation theory adapted to the case of multi-layer waveguide media delimited by air (upper surface) and a strong reflector (lower surface). An analytical EM model, called the Waveguide Model (WGM), will be associated with an inversion procedure to allow estimating the permittivities and thicknesses of the studied medium through inverting the phase velocity dispersion curves. This model will be validated using both synthetic data generated from an FDTD (Finite Difference Time Domain) numerical model and experimental data stemming from the EM characterization of standard materials using multi-offset GPR antennas.

4.2 Extraction of Dispersion Curve From GPR Data

The objective of this section is to introduce a technique to extract the dispersion curve of phase velocity from multi-offset GPR data. When the electromagnetic wave is propagating in a dispersive medium like concrete, the phase velocity and permittivity are varying frequency dependently. Here we present a complete procedure of the extraction of phase velocity dispersion curves by experimental and synthetic GPR multi-offset data on concrete slabs. The effect of signal processing and various wave interference on dispersion phenomenon are also discussed.

4.2.1 Temporal drift of GPR system

We have found that during the first hour of our experiments, a temporal drift of the signal occurs due to the heating of the GPR system [Fauchard et al., 2015]. It appears like that the signals have moved up on the travel time axis as the measuring continues. This phenomenon appears mainly when the GPR system has been turned on recently, and is not thermally stable. It is highly recommended to be removed because it has influence on the accuracy of GPR signal processing. Therefore, at the beginning and end of each measurement, we put two antennas at minimum offset and shot in the air to quantify the drift. We suppose that the change is linearly related to measuring time, so the temporal drift of a B-scan can be removed by moving each scan with an increasing shift, as shown in Fig.4.1.

Fig.4.2 is an example of B-scan measured on concrete before and after temporal drift adjustment.

4.2.2 Calculation of dispersion curves

Generally speaking, the multi-offset GPR data can be described as temporal wave fields in the form of $s(t, x)$, where t is the propagation time and x is the distance between

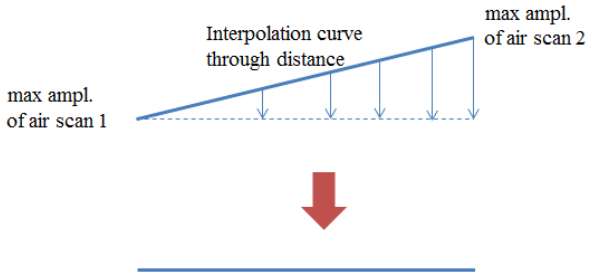

Figure 4.1: Diagram of removing temporal drift on a B-scan

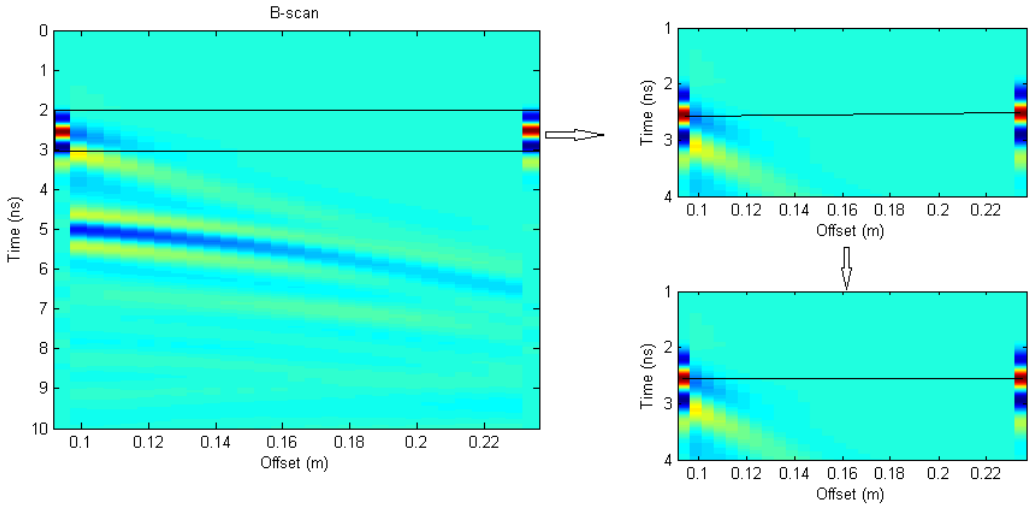

Figure 4.2: Removing temporal drift on a B-scan of GPR CMP measurement

Table 4.1: Concrete's parameter setting for GprMax 2D

Water Condition	ε_∞	ε_s	τ [ns]	σ_{dc} [S/m]
Dry	5.20	5.52	2.65	0.0012
Saturate	9.58	13.89	0.86	0.025

antennas. As we know from former study [Arcone, 1984; Arcone et al., 2003], despite the dispersion related to materials' dielectric nature, there exists another strong dispersion effect due to the multi reflections in the surface waveguide. To quantify this dispersion, we have to study the propagation phenomenon in the frequency domain.
This calculation technique, allowing the wave field transform from the time domain to the frequency domain, was firstly developed by Park [Park et al., 1998] in the study of seismic waves. Then it was employed in the applications of GPR CMP (Common Mid Point) data [van der Kruk et al., 2006; Ihamouten et al., 2012]. The temporal data $s(x,t)$ are firstly transformed to frequency signals $S(f,x)$ using FFT (Fast Fourier Transform). Then the signals are transformed into $f-\beta$ domain by the expression:

$$V(f,\beta) = \sum_x \frac{S(f,x)}{|S(f,x)|} e^{j\beta x} \tag{4.1}$$

where V(f,β) is the dispersion image of the wave field $s(t,x)$. The phase velocity $\widetilde{v}_\phi = \frac{2\pi f}{\widetilde{\beta}}$, related to the propagation constant $\widetilde{\beta}$ and frequency f, is picked up from the maximum at each frequency point, as its best approximation:

$$\widetilde{v}_{data}\,(f_n) = \max\left[V(f_n,\widetilde{\beta})\right] \tag{4.2}$$

where the symbol $\sim$ denotes the frequency dependency, n is the index of frequency points. The phase velocity dispersion curve is used to invert the properties of the waveguide media [Ihamouten, 2011; Villain et al., 2015b].

4.2.3 Time-domain filtering

Time-domain filtering is the process of selecting effective wave field before calculating the dispersion curves. It helps us get higher signal/noise ratio from the data to extract useful waves to be taken into account in the forward waveguide model (see §4.4).
In our study, the guided waves are used to estimate material's dielectric and geometric properties by one inversion procedure, which we will discuss in the following sections. It is necessary to properly filter the wave field if the air wave or the edge effects have important impacts on the dispersion curve calculation. We still employ the GPR simulation from Chapter 3 to validate the pre-processing problems. The Debye's parameters of concrete are therefore defined in the Table 4.1, representative of a dry and saturated standard concrete.

The diagram of GPR modeling configuration is shown in Fig.4.3. A concrete slab with the thickness of 0.13 m is placed on a perfect electric conductor (PEC). The source signal used in GpaMax 2D is a Ricker wave with a central frequency of 1.55 GHz, as we found for the 2.6 GHz antennas on concrete measurements. This decrease of the central frequency is caused by the interactions between the antenna and the materials (concrete and the plastic box outside). This phenomenon, mainly because of the infinite reflections between

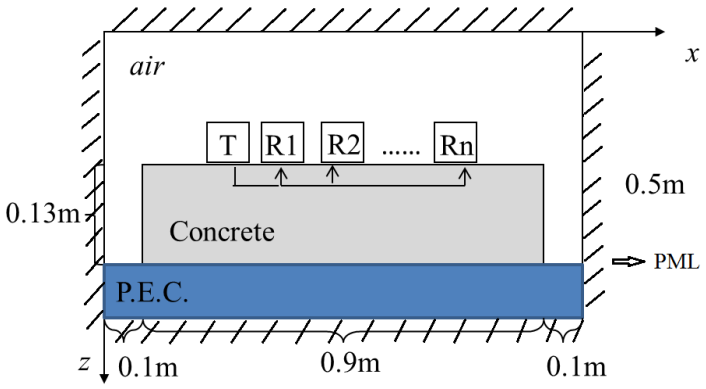

Figure 4.3: GPR modeling diagram of WARR data acquisition (not to scale)

the antenna and the media is important. However, in the simulation of GprMax, it has not been taken into account. That is the reason why we define a lower frequency in GprMax. The position of the transmitter is fixed and the displacement of the receiver starts from $X_{\min} = 0.094$ m to $X_{\max} = 0.294$ m, with the step $\Delta x = 0.01$ m. The whole modeling domain is surrounded by the perfectly matched layers (PML), absorbing the reflections from the edges of the domain. It is noted that all the simulations in this chapter have the same boundary condition.

Fig.4.4 exhibits the temporal filtering window adapted to the selection of guided waves. In our study, the effective guided waves include direct material wave and multiple reflections. The direct material wave (DM) refers to the wave transmitted directly from the transmitter to the receiver inside the material. It is also called direct ground wave in some literature of geophysical applications [Galagedara et al., 2005; Steelman and Endres, 2009]. RW1 and RW2 are respectively the first and second reflected waves from the bottom. In GPR measurements, the air wave (AW) and some reflections from the edges and reinforcements may cause unwanted interference to the measurements. To reduce such interference, we often mute the AW and waves after RW2.

We have calculated the dispersion curves of simulated dry concrete from the raw data and the filtered data. The results can be seen in Fig.4.5. We can see that the presence of the AW and other reflections after RW2 add new model components in the form of a noise in the dispersion image the curve. These added interferences can lead to a bias in inversions using our forward model. Apparently, the curves are much better shaped after time-domain filtering.

However, another phenomenon we can see from the figure is the phase velocities from one mode to another are not well isolated. This phenomenon is not appreciated since it may affect the accuracy of the phase velocity in estimation, and as a result, affect the accuracy of inversion results. This is caused by the limitation of $X_{\max}$ where the propagated guided waves are not fully sampled by the receiver. In this case, a longer moving distance is preferred in the multi-offset measurements of GPR. As we know, several factors can cause change to the travel time and wavelengths of the waves, such as GPR's central frequency, the displacements of antennas, the wave-guide's thickness and the material's permittivity. Besides, in some experiments, the maximum offset is usually limited to a small value, like 0.2m, to avoid edge effects and reflection from reinforcement. A compromise is therefore required to properly define the GPR configurations of measurements. Under this circumstance, we have done a parametric study to find the configurations, which will be discussed in the following (§4.3.2).

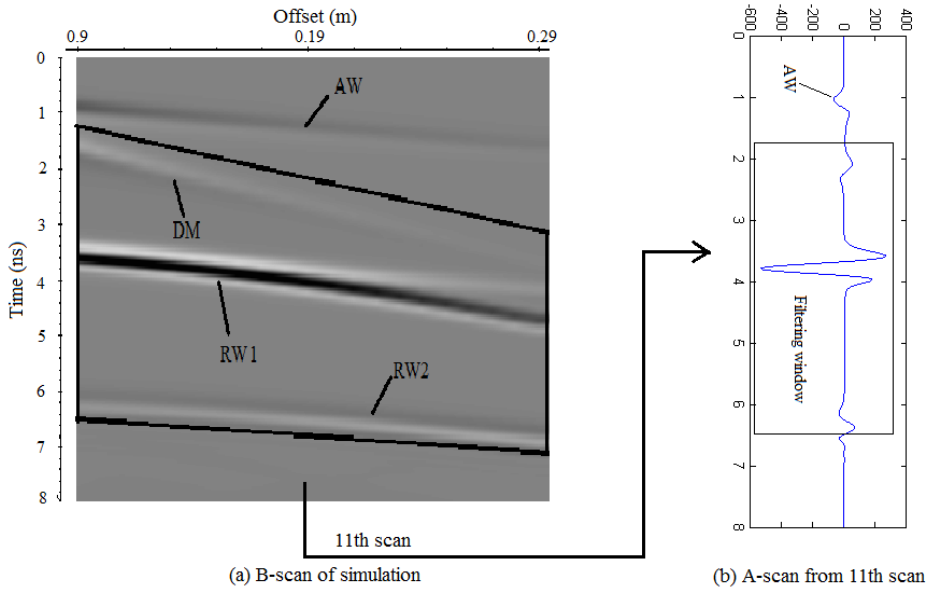

Figure 4.4: Temporal filtering window applied to B-scan (a) and A-scan (b) out of the simulation for saturated concrete

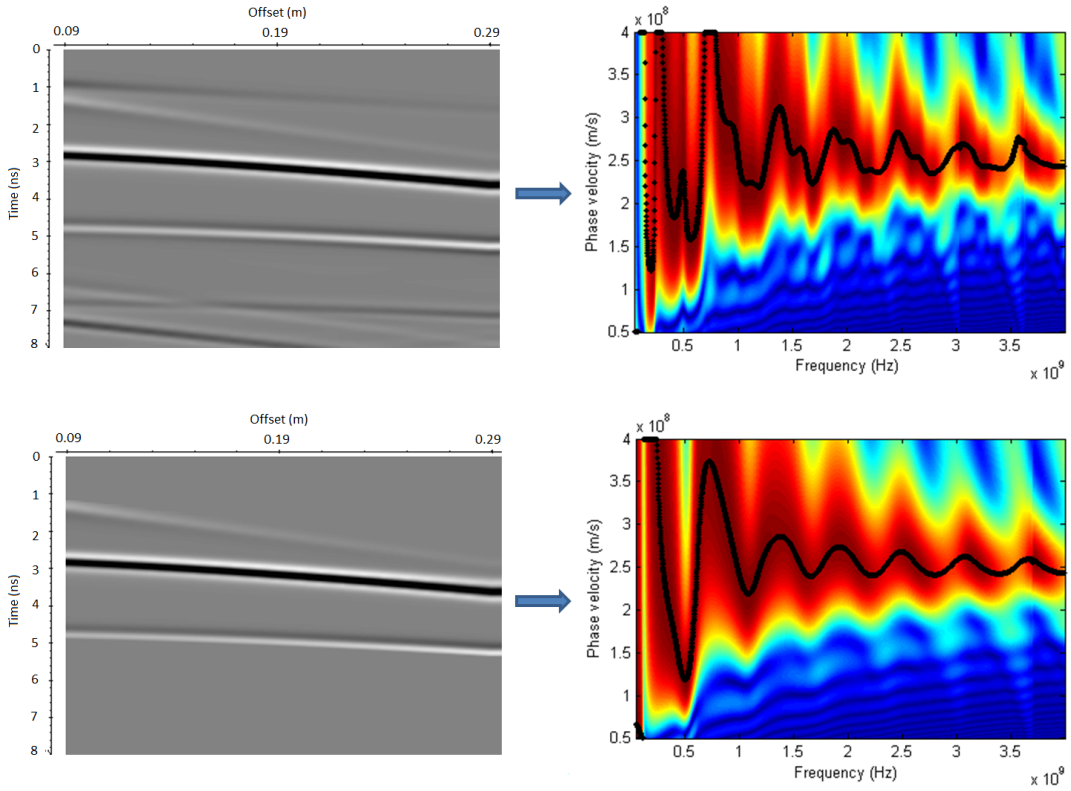

Figure 4.5: B-scans and dispersion curves of raw (a) and filtered (b) data on dry concrete

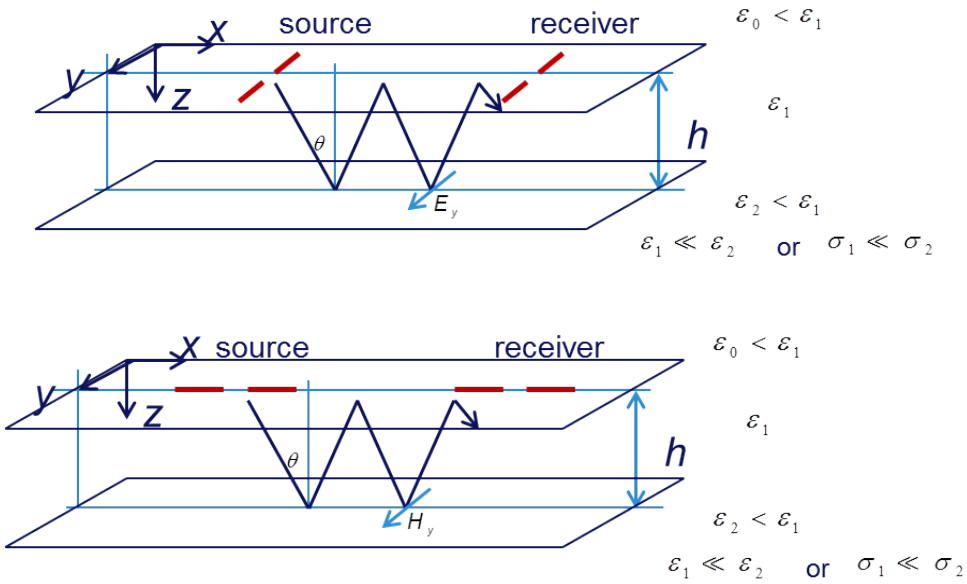

Figure 4.6: GPR measurement on waveguide medium by TE (up) and TM (down) configurations

4.3 Fundamental Equation of Modal Theory

The aim of this section is to introduce some basis related to EM modal theory that will subsequently allow us setting up the multi-layer waveguide model (WGM). Only the geometric dispersion is considered in this equation, so the dielectric constant is not frequency dependent. Furthermore, the waveguide media should be taken as lossless. A parametric study on the multi-offset configuration of GPR will be conducted to find the optimized configuration.

4.3.1 Equation of modal theory

The diagram of the GPR measurement is presented in Fig.4.6 on a waveguide medium by TE (transverse electric) and TM (transverse magnetic) configurations. The waveguide medium (ε_1') is supposed to be a one-layer medium, placed between the air (ε_0') and a material with smaller or much stronger permittivity (ε_2'). The EM waves can propagate in a waveguide when the total thickness of the waveguide is smaller than or close to the wavelength. If the medium below waveguide has much stronger permittivity or conductivity ($\varepsilon_1' \ll \varepsilon_2'$ or $\sigma_1 \ll \sigma_2$), it forms the leaky waveguide [van der Kruk and Arcone, 2007]. It can be applied to the situations such as an ice layer over water, or a concrete slab over water or metal plate. To reduce the leaky effect, TE configuration was chosen to conduct all the measurements in our study.

It is essential to respect these criteria to find a proper waveguide for the studied materials. Some basic theories describing the propagation of guided waves will be introduced in the following and will be developed into multi-layer waveguide integrating the Parallel model.

From Fig.4.6 we find that the dielectric properties of the media only varies in one direction, the z direction. In this case, the vector wave equations need not be solved in their full forms [Chew, 1995]. The fundamental equation of the modal theory [Arcone, 1984;

van der Kruk et al., 2006; Budden, 1961] can be defined as follows:

$$1 - \widetilde{R}_{12}(\widetilde{\theta})\widetilde{R}_{10}(\widetilde{\theta}) \exp\left[-2\widetilde{\gamma}_1 h \cos\left(\widetilde{\theta}\right)\right] = 0 \tag{4.3}$$

where the symbol $\sim$ denotes the frequency dependency of variables, $\widetilde{R}_{10}$ and $\widetilde{R}_{12}$ are respectively the reflection coefficients at the upper and lower boundaries of the waveguide (Fig.4.6), $\widetilde{\theta}$ is the incidence angle, $\widetilde{\gamma}_1$ is the propagation constant, given by:

$$\widetilde{\gamma}_1 = j\omega\sqrt{\varepsilon'_1}/c_0 \tag{4.4}$$

where $j = \sqrt{(-1)}$, ε'_1 is the real part of the equivalent relative permittivity of the waveguide and c_0 is the light speed in vacuum. The reflection coefficients of the TE-mode configuration are given by:

$$\widetilde{R}_{10}^{TE} = \frac{\widetilde{\Gamma}_1 - \widetilde{\Gamma}_0}{\widetilde{\Gamma}_1 + \widetilde{\Gamma}_0}, \tag{4.5}$$

$$\widetilde{R}_{12}^{TE} = \frac{\widetilde{\Gamma}_1 - \widetilde{\Gamma}_2}{\widetilde{\Gamma}_1 + \widetilde{\Gamma}_2} \tag{4.6}$$

where

$$\widetilde{\Gamma}_a = \sqrt{\widetilde{\gamma}_a^2 - \widetilde{\gamma}_1^2 \sin^2\left(\widetilde{\theta}\right)} \quad \text{with} \quad a \in \{0, 2\} \tag{4.7}$$

For optimal constructive interferences, the total phase variation (after successive reflections on the upper and lower interfaces of the waveguide) must be equal to $2m\pi$ radians, where m is an integer, therefore:

$$\Phi\left(\widetilde{\theta}\right) - 4\pi f\sqrt{\varepsilon'_1} h \cos\left(\widetilde{\theta}\right)/c_0 = -2m\pi \tag{4.8}$$

where

$$\Phi\left(\widetilde{\theta}\right) = \tan^{-1}\left[\frac{\Im\left(\widetilde{R}_{10}\right)}{\Re\left(\widetilde{R}_{10}\right)}\right] + \tan^{-1}\left[\frac{\Im\left(\widetilde{R}_{12}\right)}{\Re\left(\widetilde{R}_{12}\right)}\right] \tag{4.9}$$

The various values of m correspond to the multiple propagation modes where the fundamental mode is $m = 0$. To satisfy this equation, the propagation requires total reflections at both interfaces. Thus, the incidence angle must be greater than the critical angle, which can be defined as:

$$\theta_c = \sin^{-1}\left(\sqrt{\frac{\varepsilon'_a}{\varepsilon'_b}}\right) \tag{4.10}$$

where $a, b = 0$, 1 or 2. We assume that $\widetilde{R}_{12} = -1$ in this waveguide condition, where the interface between media 1 and 2 can be considered as a perfect reflector. Equation (4.9) thus becomes:

$$\Phi\left(\widetilde{\theta}\right) = \tan^{-1}\left[\frac{\Im\left(\widetilde{R}_{10}\right)}{\Re\left(\widetilde{R}_{10}\right)}\right] + \pi \tag{4.11}$$

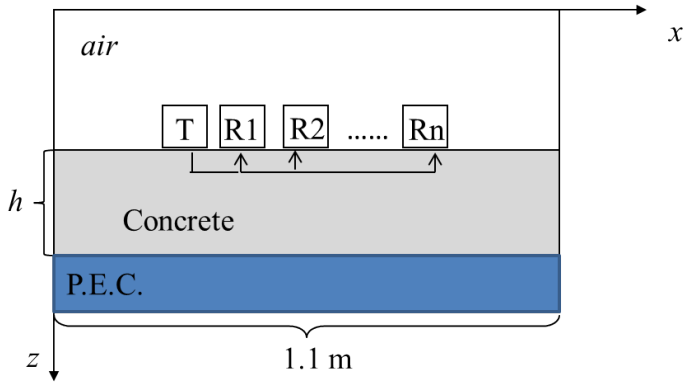

Figure 4.7: Schematic diagram of GPR monitoring with a WARR antenna configuration on one-layer waveguide

The phase velocity $\widetilde{v}$ is frequency dependent and closely related to the variation of the incidence angle $\widetilde{\theta}$:

$$\widetilde{v} = \frac{c_0}{\sqrt{\varepsilon_1'} \sin \widetilde{\theta}} \tag{4.12}$$

where $c_0 = 3 \times 10^8$ m/s. The waveguide layer is assumed to be lossless ($\sigma \to 0$) and non-magnetic ($\mu = 1$). Without special instructions, the permittivity we mention here is always the real part of relative permittivity (also expressed as dielectric constant).

4.3.2 Optimization of multi-offset configuration by parametric study

To focus on physical phenomenon related to the guided wave propagation, it is important to minimize the bias due to the effects of antennas' displacements on the acquisitions of data. In this parametric study, we use the one-layer waveguide model [Ihamouten, 2011] to avoid the edge effects, shown in Fig.4.7. GprMax 2D is used for the simulations. The air wave is filtered in time domain. The thickness h, the maximum offset $X_{\max}$ and step displacement Δx will be widely studied. The main objective is to find a way to determine the optimized values of $X_{\max}$ and Δx for different states of concrete with thickness and permittivity varying. Still, we employ the parameters in Table 4.1 to model the concrete. We have conducted a parametric study for the concrete in both dry and saturate states.

4.3.2.a Maximum offset

The source signal of GPR is Ricker wave at 1.55 GHz. The position of the transmitter is fixed and the displacement of the receiver starts from $X_{\min} = 0.094$ m with the step $\Delta x = 0.01$ m. To quantify the variation of phase velocity due to the change of $X_{\max}$, we apply the definition of mean absolute error (MAE):

$$MAE = \Sigma_i MAE_i = \Sigma_i \Sigma_n \frac{|v_i^{WG} - v_i|}{N} \tag{4.13}$$

where n is the index of frequency points, N is the number of frequency points, v_i^{WG} is the phase velocity at TE_i mode derived from the waveguide model [Ihamouten, 2011; Villain et al., 2015b] and v_i is the phase velocity at TE_i mode calculated from the numerical model

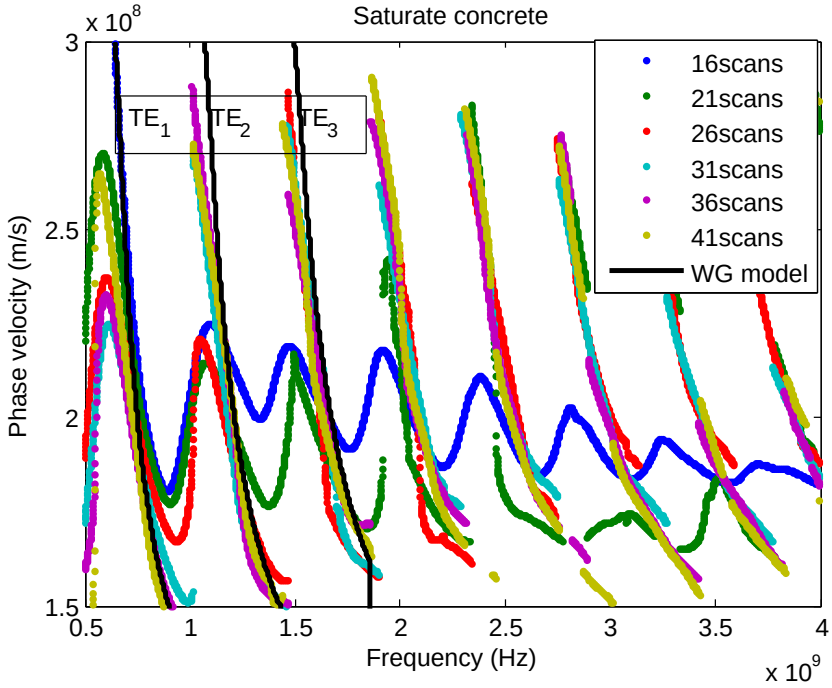

Figure 4.8: Example of dispersion curves of saturate concrete where $h = 0.12$ m

using GprMax 2D. Since $X_{\max}$ is changing, we have got different values of v_i. Fig.4.8 shows the dispersion curves derived from the saturate concrete with different number of scans where $h = 0.12$ m. As we can see, the more scans we take, the closer we get the curve to the synthetic waveguide model. We pick up two modes (TE_1 and TE_2) to calculate the MAE, as what we will do in the following inversion. Each mode is limited within 200 MHz to reduce the dispersion of concrete, and also, to make sure the selected frequencies are above the cut off frequency. The results are shown in Fig.4.9. We can find, generally, that the error increases as the thickness increases. This is because the longer h is, the longer distance of antennas we need to move to get a complete reflected wave. Also, the value of MAE decreases as $X_{\max}$ increases. Certainly, we prefer to measure with longer distance. But the distance can be limited by different reasons, such as the dimensions of materials and the existence of reinforcements for most of civil engineering structures. In our test, the maximum distance usually cannot exceed 0.35 m (corresponding to experimental limitations, to be discussed in the following chapter). Therefore, we hope to keep the MAE under 2×10^7 m/s as a compromise of the configuration. We can see the MAE is below 2×10^7 m/s at $X_{\max}$= 0.344 m for both cases of concrete when h is smaller than 0.15 m. When $h = 0.2$ m, MAE is obviously high, even higher than 4.5×10^7 m/s when $X_{\max} < 0.3$ m for saturate state. Since the wavelength of the antennas is near 0.2 m with a central frequency f_c=1.55 GHz, this confirms the criterion to form a waveguide that $h \leq \lambda$.

4.3.2.b Step displacement

In the study of the impacts of displacement step Δx, we use the configuration in Fig.4.7 where $h = 0.12$ m and $X_0 = 0.094$ m. The same maximum offset is kept at $X_{\max} = X_0$+0.2 m, so we can define the number of scans according to Δx:
$\Delta x = 0.005$ m $\rightarrow$ 41 scans, $\Delta x = 0.01$ m $\rightarrow$ 21 scans,

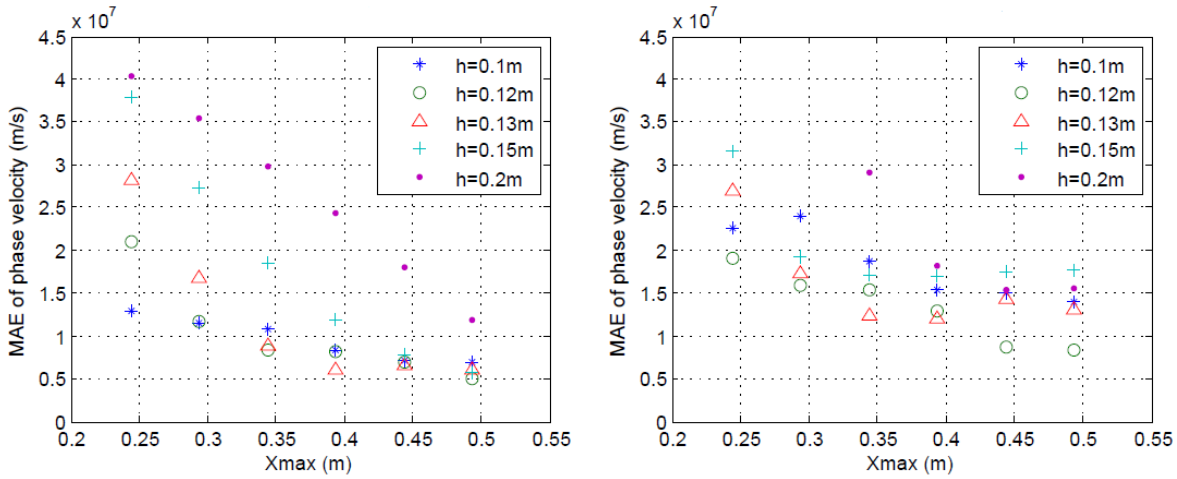

Figure 4.9: MAE for TE_1 and TE_2 of (a) dry and (b) saturate concrete with varying thickness h and maximum offset $X_{\max}$

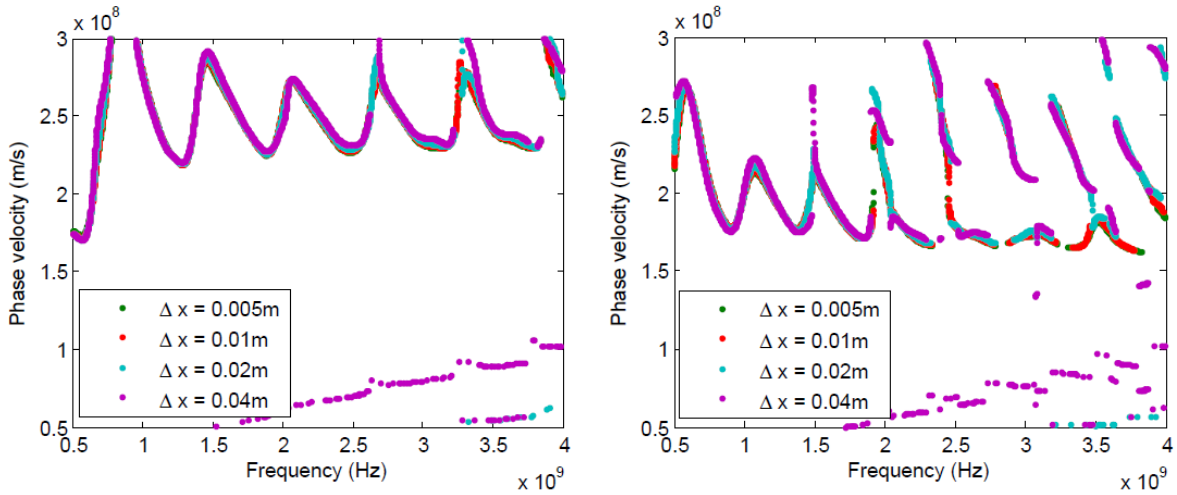

Figure 4.10: Dispersion curves of (a) dry and (b) saturate concrete with different displacements

$\Delta x = 0.02$ m $\rightarrow$ 11 scans, $\Delta x = 0.04$ m $\rightarrow$ 6 scans.
Fig.4.10 shows the phase velocity dispersion curves calculated from modelled data with the same $X_{\max}$ and different Δx. We can see, for $\Delta x = 0.005$, 0.01 or 0.02 m, the difference between the curves are rather small. Therefore, we consider that the velocity dispersion curve is correctly calculated roughly between 0.5 and 2.5 GHz for a central frequency of 1.55 GHz. It also depends on concrete conditions, where for the saturate state, the effective frequency bandwidth is narrowed. Besides, when Δx is over 0.02 m, we observe some outliers of phase velocities in the figures, especially for $\Delta x = 0.04$ m. In fact, inadequate displacement could result in aliasing in the calculation.

4.3.3 Conclusion

We have conducted a parametric study on the experimental configuration of the GPR antennas: the maximum offset X_{max} and step displacement Δx. From the results, we

find the decision of maximum offset is closely related to the dielectric and geometrical characteristics of the material, and also the central frequency of the antenna. To test the concrete with the antennas at around 1.55 GHz, the acceptable thickness of the material is below 0.15 m. For thicker sample, for example $h = 0.2$ m, we should change the antennas with lower frequency. Below 1 GHz is actually acceptable, which in practice, could correspond to 1.5 GHz antennas in the air or on concrete. Also, before the test, a knowledge of the permittivity range for the material is helpful to define the maximum offset. For the displacement at each step, we can see for both configurations, Δx below 0.01 m is always preferred. Indeed, as the step distance increases, some outliers appears at high frequencies, which will cause noise to the inversion. It is believed that the problem would be worse if we test on heterogeneous materials, such as concrete. To be noted, the criterion $h \leq \lambda$ also applies to the total thickness h of multi-layer media.

4.4 Forward study of multi-layer waveguide model

To present the newly developed multi-layer WGM, we will start by the verification of forward model. The multi-layer WGM adapted to 2 layers, 3 layers and even a gradient function will be verified in a numerical approach.
In some inhomogeneous media, we can try to divide the whole material into several layers, such as the ground and concrete [Kalogeropoulos, 2012]. To simplify this problem, the Parallel model (Eq. 3.47) is integrated in the WGM to replace the dielectric constant of the waveguide medium ε'_1 by a multi-layer medium ε'_e:

$$\varepsilon'_e = \frac{\Sigma_l h_l \varepsilon'_l}{\Sigma_l h_l} \tag{4.14}$$

where l is the index of the layer. In this section, we are going to start by a forward study on two-layer waveguide, and furthermore, to model the WARR configuration acquirement on some multi-layer media. The phase velocities obtained from the multi-layer WGM are to be compared to the dispersion curves extracted from the simulated GPR data. This study assumes that the multi-layer medium generates a guided propagation of EM waves as a horizontal planar layer and moreover that EM field components polarize axially to the incident wave plane [Dai and Young, 1997]. The validity and workability of the multi-layer WGM will be discussed with these comparisons.

4.4.1 Two-layer media

Fig.4.11 illustrates a new configuration developed from the EM leaky WGM, based on a model of a two-layer medium (ε'_1 and ε'_2) surrounded by air (ε'_0) on its upper surface and a very high-permittivity medium (ε'_3) on its lower surface. It might, for example, correspond to a concrete structure with increasing water content which can be adopted as two layers, laying on a perfect electric conductor or water. But in order to validate the new approach, homogeneous, lossless and known media have been chosen to study: granite and limestone. According to the Parallel model (Eq. (4.14)), the waveguide medium is characterized by an equation of the equivalent dielectric constant ε'_e of two layers:

$$\varepsilon'_e = \frac{\varepsilon'_1 h_1 + \varepsilon'_2 h_2}{h_1 + h_2} \tag{4.15}$$

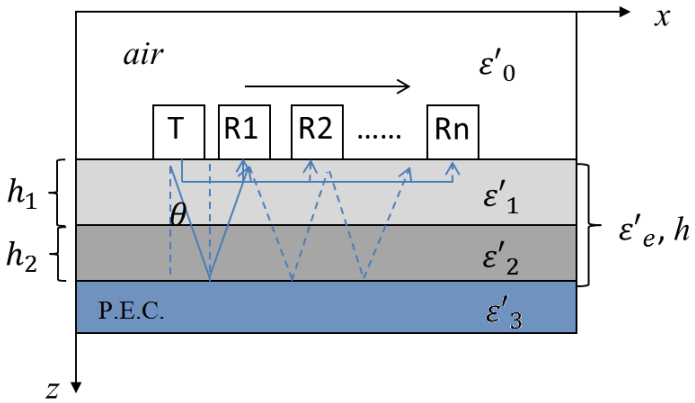

Figure 4.11: Schematic diagram of GPR monitoring with a WARR antenna configuration on two-layer waveguide

Using GprMax 2D to conduct the FDTD numerical modelling, a wave field in WARR configuration has thus been modeled in order to simulate a test configuration similar to that described in Fig.4.11. The input parameters of the waveguide model are $\varepsilon'_1 = 5$ and $\varepsilon'_2 = 8$, presenting slabs of granite and limestone on a steel plate. The values of the thicknesses are $h_1 = 0.04$ m and $h_2 = 0.10$ m. The simulated source corresponds to a Hertzian dipole emitting a Ricker pulse, with a central frequency equals to 1.55 GHz in the air. The offset between transmitter and receiver has been chosen from 0.094 m to 0.394 m with a step of $\Delta x = 0.01$ m. Perfectly Matched Layer (PML) has been implemented over the entire contour of the simulation domain. Fig.4.12 shows the B-scan of the simulated wave field. The direct waves (surface waves), refracted waves and multiple reflections can all be identified in this figure. The refracted waves are the waves refracted from the media to the air. Also noteworthy is that, sometimes, EM energy transported by the direct wave in the air might be an interference of the guided waves. Here, we calculate the dispersion curve with the whole wave field since the edge effects have been avoided, and the interference becomes negligible.

Fig.4.13 displays the dispersion curves calculated from the above EM wave field (Fig. 4.12) using the $f - \beta$ transform and the forward two-layered WGM. On the whole, an excellent correlation can be observed between the phase velocity dispersion curves derived from either the FDTD model of the direct model (black dots) and the curves generated from the multi-layer WG model (blue curves), by taking into account the modes TE_0 to TE_7.

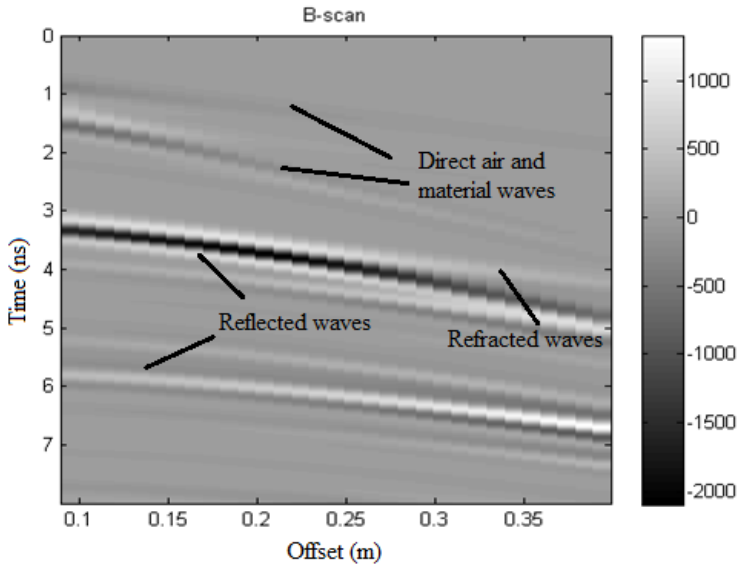

Figure 4.12: B-scan of synthetic EM wave propagating in a two-layer waveguide

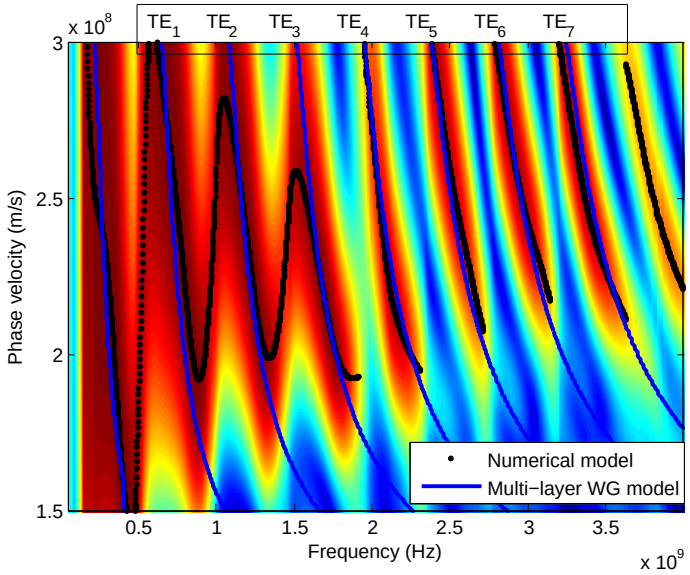

Figure 4.13: Dispersion image and dispersion curves derived from the FDTD model (black) and curves stemming from the 2-layer WGM (blue)

Table 4.2: Composition of 3-layer media for numerical models

Configurations	ε'_1	ε'_2	ε'_3	h_1 **(m)**	h_2 **(m)**	h_3 **(m)**	ε'_e
c1-1	5	6	7	0.03	0.03	0.03	6
c1-2	5	7	6	0.03	0.03	0.03	6
c1-3	6	5	7	0.03	0.03	0.03	6
c2-1	5	6	7	0.06	0.04	0.02	5.67
c2-2	5	7	6	0.06	0.02	0.04	5.67
c2-3	6	5	7	0.04	0.06	0.02	5.67

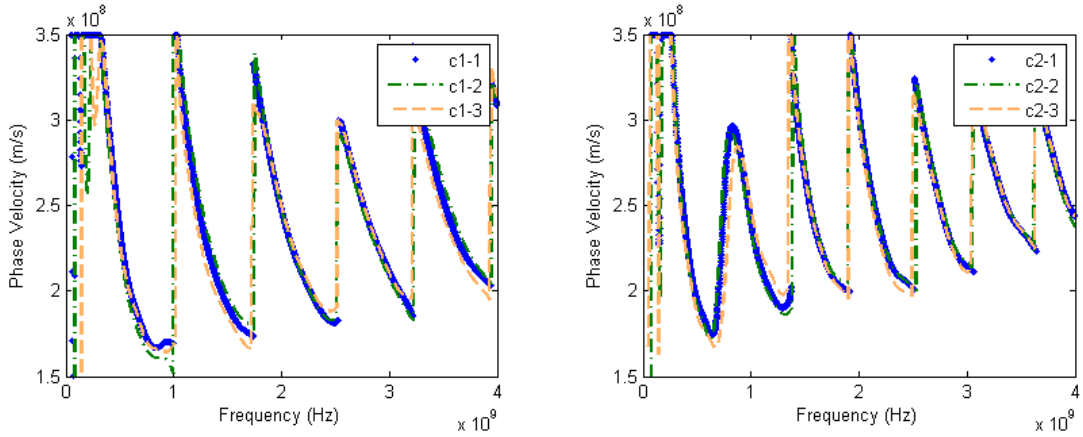

Figure 4.14: Dispersion curves extracted from numerical 3-layer WG models (a) c1 and (b) c2

4.4.2 Three-layer media

As a further study step of multi-layer WGM, we are going to discuss about the validation of three-layer waveguide model. The two-layer waveguide is thus replaced by a three-layer one. Like in the forward study of the two-layer WGM, the three-layer models are built with WARR measurement configuration by GprMax 2D. The waveguide medium ε'_1 is replaced by a three-layer medium:

$$\varepsilon'_e = \frac{\varepsilon'_1 h_1 + \varepsilon'_2 h_2 + \varepsilon'_3 h_3}{h_1 + h_2 + h_3} \tag{4.16}$$

This model is developed to study some civil engineering materials, such as concrete, with changing permittivities along with the depth.
We proposed two strategies to detect the composition of the multi-layer media. First, we know the total thickness of the medium. We divide the medium horizontally into several layers with the average thickness to look for the effective permittivity of each layer. The more layers we divide, the more precise the result will be. Second, we know neither the thickness nor the permittivity of each layer. We look for the permittivity and the thickness of each layer at the same time. The problem becomes more complex because the unknown parameters have been doubled. To study the two cases, we have define two categories (c1 and c2) of configurations, as shown in Table 4.2. The GPR settings are the same as for two-layer model. The curves shown in Fig.4.14 are the phase velocities extracted from the 6 configurations. From Fig.4.14 we can find for each category of configurations, the difference between the curves are so small that can be negligible. The curves of media

with the same ε'_e and h match well with each other. However, the problem is that we cannot distinguish the configurations from each other using this homogenization model. To realize the inversion, we have to estimate the dielectric constant of each layer before the inversion. Moreover, the more parameters in the model, the more difficult it will be for the inverse problem. More study and new development is still needed if we want to work on more layers.
Fortunately, if there is an initial variation law of the permittivities inside the waveguide, we can define the equivalent permittivity with a function describing this variation law. It is actually one of the advantages of our model.

4.4.3 Inhomogeneous media with arctan(x) function

According to the measurements of gammadensimetry for the imbibition of concrete (to be presented in Chapter 5), we can assume that when water penetrates into concrete from the bottom, the change of water content inside is like a reverse arctan function with respect to the depth. We thus define a function of permittivity to describe this change with respect to the position of the sample's height x:

$$\varepsilon'(x) = \frac{b-c}{\pi}\arctan(\frac{2d}{a} - \frac{2x}{a}) + \frac{b+c}{2} \tag{4.17}$$

In equation (4.17), $x \in [0, h]$, b and c are respectively the upper and lower limit of the permittivity, d is the middle of the gradient curve and a is the shape factor of the curve that when $a \to 0$, the medium can be regarded as two layers and d is the thickness of the wet layer. Applying the Parallel model, the effective permittivity of the medium is given by:

$$\varepsilon'_e = \frac{\int_0^h \varepsilon'(x)\mathrm{d}x}{h} \tag{4.18}$$

We have modeled a waveguide medium with gradient using GprMax 2D. The parameters of the function are set as: $h = 0.13$, $a = 0.01$, $b = 15$, $c = 6$ and $d = 0.02$, to form the gradient of permittivity in Fig. 4.15. The red curve in the figure corresponds to the case that $a \to 0$.
From the figure we can see the permittivity from the bottom (ε'_2) and the top (ε'_1) of the medium is a little different from the values of b and c. It is an extreme case that when $a \to 0$, the medium becomes a two-layer medium thus $\varepsilon'_2 = b$ and $\varepsilon'_1 = c$. So we need to be careful about the difference for the inversion.
In GprMax 2D, the medium with gradient has been defined as a 27-layer medium with varying ε_∞ for Debye's model. The conductivity $\sigma = 0.00004$ S/m so the medium is nearly lossless. The other parameters are defined as zero so there is no dispersion. To conduct the study, like the configurations above, we have chosen the WARR configuration with a PEC under the waveguide. The central frequency equals to 1.55 GHz. The offset between transmitter and receiver is from 0.094 m to 0.394 m with a step of $\Delta x = 0.01$ m. Fig. 4.16 shows the dispersion curves of the gradient models, from numerical model and synthetic arctan(x) model. From the figure we observe that the curves match well with each other at TE_2 and TE_3 modes. The error at lower frequencies is due to the low resolution of $f - \beta$ transform and the limited X_{max}. The mismatch at the higher frequencies is believed to be the limit of arctan(x) model. The approximate definition of the medium with gradient in GprMax may also induce some error. However, the results

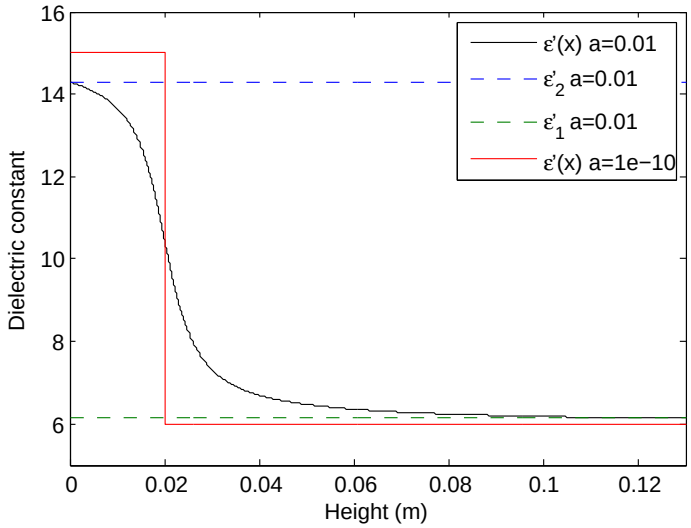

Figure 4.15: Arctan curves of permittivity gradient for simulation

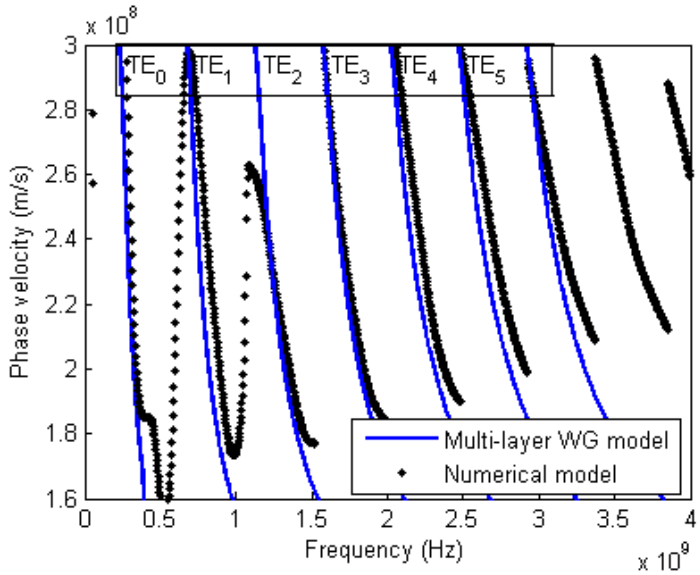

Figure 4.16: Dispersion curves of permittivity gradient from FDTD model (black) and arctan(x) model (blue) with $h = 0.13$, $a = 0.01$, $b = 15$, $c = 6$ and $d = 0.02$

are still satisfying because they enable us to get useful information around the central frequency of the antennas 1.55 GHz.

4.4.4 Conclusion

In this section, we have first introduced some basis about the waveguide modal theory, then conducted some forward study of the multi-layer WG model. We have composed the waveguides with two layers, three layers and even with gradient defined by an arctan function. Generally speaking, the Parallel model has good working performance to simplify the multi-layer waveguides. However, as the number of layers increases, the error at high frequencies increases. In the following section of the inverse study, we should be careful about this error. The propagation modes around the central frequency of used GPR antennas is therefore preferred in the study.

4.5 Validation of Multi-layer Waveguide Inversion on Two-layer Model

The two-layer model has been confirmed to have good performance in forward problem. We thus expect to adapt it to the characterization of concrete samples that can be considered as two layers. The objective of this section is to validate the inversion procedure of two-layer WGM. To achieve this, we will start by some numerical simulations with various configurations, and then with a measurement on homogeneous materials.

4.5.1 Inversion of the dispersion curves

We employ the Parallel model (Eq. (4.14)) to replace the permittivity of the one-layer waveguide medium ε'_1 by a two-layer medium:

$$\varepsilon'_e = \frac{\varepsilon'_1 h_1 + \varepsilon'_2 h_2}{h_1 + h_2} \tag{4.19}$$

The first step in the EM waveguide model (WGM) parameterization is to determine the values of incidence angle by integrating Eq. (4.19) into equation (4.8) and solving Eq. (4.8) using a zero-finding routine with model parameters $[\varepsilon'_1, \varepsilon'_2, h_1, h_2]$. Therefore, the phase velocity V_ϕ is obtained as:

$$\widetilde{V}_\phi\left(\widetilde{\theta}\left(f, \varepsilon'_1, \varepsilon'_2, h_1, h_2\right)\right) = \frac{c_0}{\sqrt{\varepsilon'_e}\sin\widetilde{\theta}\left(f, \varepsilon'_1, \varepsilon'_2, h_1, h_2\right)} \tag{4.20}$$

The unknown parameters $[\varepsilon'_1, \varepsilon'_2, h_1, h_2]$ are inverted by minimizing the cost function for TE_i mode:

$$CF^{TE_i} = \sum_{n=1}^{N} \frac{\left|V_\phi\left(\widetilde{\theta}\left(f, \varepsilon'_1, \varepsilon'_2, h_1, h_2\right)\right) - v_{sol}\right|}{N} \tag{4.21}$$

where v_{sol} is the phase velocity in the working range selected from v_{data} , n is the frequency index and N is the number of frequency points. The choice of frequency band and propagation modes for inversion depends on the shape of the dispersion curve and normally around the central frequency of GPR. More details will be explained later (see

§4.5.2).
However, as Eq. (4.19) shows, parameters $[\varepsilon'_1, \varepsilon'_2, h_1, h_2]$ are correlated with each other. Numerous combinations of the 4 parameters can provide the minimum cost function. The dielectric constants of the two layers ε'_1 and ε'_2 cannot be identified from this model directly. In other words, only when ε'_1 and ε'_2 are known parameters, h_1 and h_2 can be determined. Vice versa. In case we cannot know h_1 or h_2 before the inversion, we choose to pre-approximate ε'_1 and ε'_2 before the inversion. Moreover, as we can obtain the total thickness h in most cases, h_2 can be determined by $h_2 = h - h_1$. The cost function for TE_i mode thus becomes:

$$CF^{TE_i} = \sum_{n=1}^{N} \frac{\left| V_\phi \left(\widetilde{\theta}\left(f, h_1\right) \right) - v_{sol} \right|}{N} \tag{4.22}$$

Since these dispersion curves show a divergent velocity calculation at the propagation mode cut-off frequencies, the overall cost function of TE modes can then be defined as a piecewise continuous function expressed as follows:

$$CF = CF^{TE_{0\ldots m}} = \frac{\sum_{i=1}^{m} CF^{TE_i}}{m} \tag{4.23}$$

where m corresponds to the number of working modes.

4.5.2 General process of waveguide inversion on two-layer media

This section introduces the procedure employed to obtain the dielectric and geometric characteristics of a two-layer medium from multi-offset GPR data.
The flow chart in Fig.4.17 exhibits the whole calculation process of the inversion. The frequency dependent phase velocity $\widetilde{v}_{data}$ is derived from multi-offset GPR data. To limit the material dispersion, we usually select 100 MHz or 200 MHz bandwidth for each mode. The inversion can be conducted with one single mode or several combined modes.
The parameters $[\varepsilon'_1, \varepsilon'_2, h]$ have to be known before the inversion. The dielectric constants ε'_1 and ε'_2 can be calculated by the group velocity of the wave propagates directly through the surface layer. Or by some calibration methods, such as taking cores to be measured by EM cell to get the material's permittivity on the wide frequency band [50 MHz - 1.6 GHz] [Adous et al., 2006]. It is a device using transition line system to assess complex permittivity for material characterization of specimens, with the dimension ⌀ 75 mm × 70 mm and are supposed to be homogeneous.
The inversion process includes two steps. First, the incidence angle $\widetilde{\theta}_i$ for TE_i mode is approximated solving Eq. (4.8) using a zero-finding routine. The theoretical phase velocity $\widetilde{V}_{\phi i}$ is thus obtain from it. Second, the cost function CF^{TE_i} for TE_i mode is calculated by the absolute average difference between the theoretical phase velocity $\widetilde{V}_{\phi i}$ and the experimental phase velocity $\widetilde{v}_{sol}$. The solution is found by nonlinear least-squares algorithm using MATLAB®. If the general cost function CF is above the threshold ($CF > CF_{thres}$), the starting values of the parameters will vary slightly and the procedure will go back to the first step. If $CF < CF_{thres}$, we will assume that we find the minimum CF. The corresponding value of h_1 is the right value we are looking for. This process can also be adapted to the inversions of other WG models.

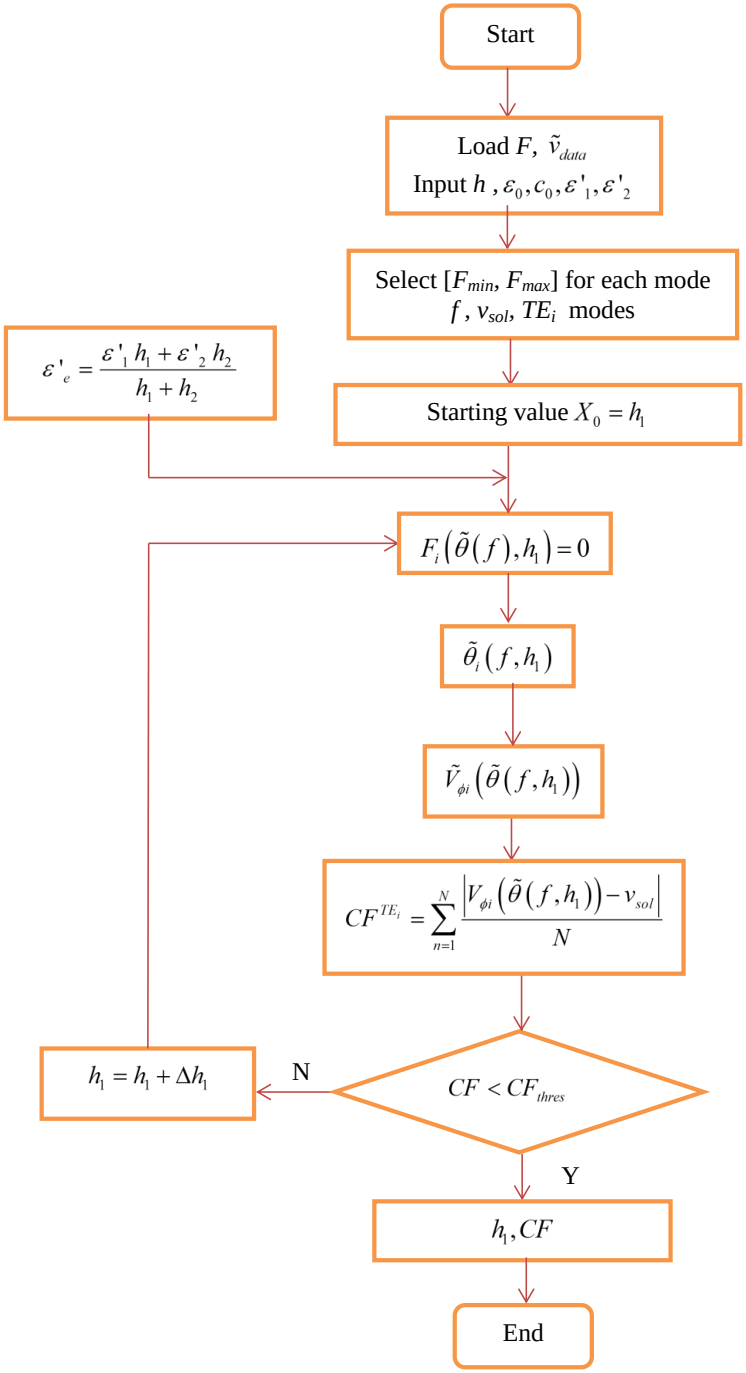

Figure 4.17: Flow chart of waveguide inversion on two-layer WGM

4.5.3 Numerical validation of inversion process

A validation of the two-layer WG inversion has been conducted with synthetic data over several WARR configurations.

4.5.3.a Modelling parameters and configurations

This validation step utilizes wave fields modeled with GprMax 2D [Giannopoulos, 2005] using the FDTD numerical method. Seven WARR configurations (WARR1 to WARR7) have thus been modeled in order to simulate a test configuration similar to that described in Fig.4.11. The input parameters of the waveguide media model are $\varepsilon'_1 = 5$ and $\varepsilon'_2 = 8$, presenting slabs of granite and limestone on a steel plate. The values of the thicknesses h_1 and h_2 are changing from 0.01 to 0.14 m. The simulated source corresponds to a Hertzian dipole emitting a Ricker pulse, with a central frequency equals to 1.55 GHz. The offset between transmitter and receiver has been chosen from 0.094 m to 0.394 m with a step of $\Delta = 0.01$ m. Perfectly Matched Layer (PML) has been implemented over the entire contour of the simulation domain. Fig.4.12 shows one of the simulated wave fields (WARR1) where $h_1 = 0.04$ and $h_2 = 0.10$ m. The direct waves (surface waves) and multiple reflections can all be identified in this figure.

4.5.3.b Details of inversion process

Fig.4.13 (see §4.4.1) displays the dispersion curves calculated from the above EM wave field (Fig.4.12) using $f - \beta$ transform and the forward two-layer WGM. The objective of our inversion is to invert h_1 from the picked dispersion curve (black). Several steps included in the inversion process will be explained below.

1) Working band of inversion We observe in Fig.4.13 that higher modes correlate with the forward model better than the fundamental mode (TE_0). This phenomenon is caused by the low resolution of the dispersion image at low frequencies. This anomaly has been identified as a limitation of the wave field transforms in $f - \beta$ domain [Ihamouten et al., 2012]. It is also due to the limitation of maximum distance between the transmitter and receiver. When the waves propagate at lower frequencies, the wavelengths are longer. The displacement of 0.3 m of the antenna is not sufficient for sampling a wave with a frequency below 1 GHz. However, in most cases of our realistic tests, the maximum offset $X_{\max}$ has to be limited as 0.15 to 0.2 m in order to avoid the edge effects and the reflections from any reinforcement. Also, the strong attenuation of EM waves inside the medium limits the length of $X_{\max}$. Therefore, the higher modes (e.x. TE_2 to TE_5 in Fig.4.13) are preferred in the inversion process.
In combining our initial analysis results with the findings of van der Kruk et al. [van der Kruk and Arcone, 2007], we opted to perform the inversions simultaneously on the TE_2 mode [1.1 - 1.3 GHz] and TE_3 mode [1.6 - 1.8 GHz], though on limited frequency bandwidths.

2) Initial value of iteration As we discussed before, ε'_1 and ε'_2 need to be estimated before the inversion. In this simulation, the input values are set to be the estimated values $\varepsilon'_1 = 5, \varepsilon'_2 = 8$.
To make sure the cost function falls as the minimum location, the initial value of h_1 is

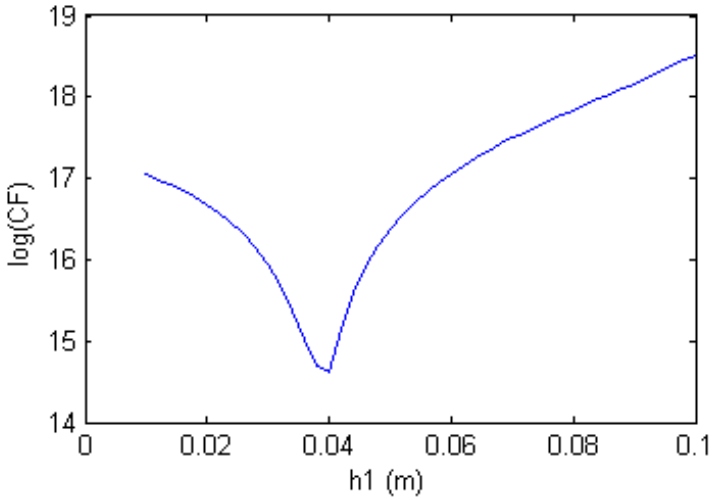

Figure 4.18: Cost function $\log(CF)$ of multi-layer WGM generated curve for configuration $\varepsilon_1' = 5, \varepsilon_2' = 8, h_1 = 0.04$ m and $h_2 = 0.10$ m (blue curve in Fig.4.13) at TE_3 mode

Table 4.3: Inversion results of WARR1 on TE_2, TE_3 and combined TE_2-TE_3 modes, in considering the FDTD model as the direct model and WGM as the inverse model- $\varepsilon_1' = 5, \varepsilon_2' = 8$

Mode	h_1 **(m) Inv.**	h_1 **(m) Forward**	$\min(CF)$ **($\times 10^6$ m/s)**
TE_2	0.044	0.04	6.12
TE_3	0.040	0.04	2.19
$TE_2 - TE_3$	0.032	0.04	3.79

defined as $h_1 \in [0.01,\ h]$, with the interval 0.01 m. Then we have 14 initial values of h_1 for the inversion of configuration WARR1 where $h = 0.14$ m.

3) Minimum CF searching For each starting model of h_1, one CF is obtained in the end. We also call it the residue of the non-linear regression. The minimum of the cost functions CF from all the initial values is identified as the global minimum or very close to it.
To invert h_1, the searching of global minimum of the cost function CF becomes very efficient with one varying parameter. Figure 4.18 is the cost function curve calculated from the multi-layer WGM with varying h_1. We can see that $h_1 = 0.04$ m when CF reaches the minimum point.

4.5.3.c Results and discussions

Table 4.3 shows the results obtained from the simulation of Config. WARR1 in Fig.4.12, using TE_2, TE_3 and combined $TE_2 - TE_3$ modes. Each mode is selected with a bandwidth of 200 MHz. TE_3 mode works better than TE_2 mode since the frequency band is closer to the central frequency of the emitted signal in the material. The combined $TE_2 - TE_3$ mode also has smaller residue than TE_2 mode, but the calculation time is doubled. Considering the efficiency and accuracy of the inversion, we choose TE_3 mode to conduct the inversion for the other WARR configurations. Except for those where TE_3 mode is at very high

Table 4.4: Inversion results, in considering the FDTD model as the direct model and WGM as the inverse model - $\varepsilon'_1 = 5, \varepsilon'_2 = 8$ - Variation in media heights

Configurations	**Mode**	h_1 **(m) Inv.**	h_1 **(m) Forward**	h **(m) Forward**	$\min(CF)$ **($\times 10^6$ m/s)**
WARR1	TE_3	0.040	0.04	0.14	2.19
WARR2	TE_3	0.063	0.06	0.14	2.97
WARR3	TE_3	0.100	0.10	0.14	2.63
WARR4	TE_2	0.064	0.06	0.10	8.96
WARR5	TE_2	0.039	0.04	0.08	2.64
WARR6	TE_3	0.040	0.04	0.10	1.13
WARR7	TE_3	0.040	0.04	0.16	2.85

frequencies (over 2.5 GHz). This is because it exceeds the effective bandwidth of GPR in our simulation. When the frequencies are over 2.5 GHz, the error of the dispersion curve will increase. Finally, all the estimation results on TE_3 (or lower) mode are shown in Table 4.4. For all the configurations, we find very good agreement between the input values and inversion results. However, for experiments, inversion with only one single TE mode is not reliable to reconstruct the parameters [Strobbia and Cassiani, 2007], the point which will be discussed in the following section.

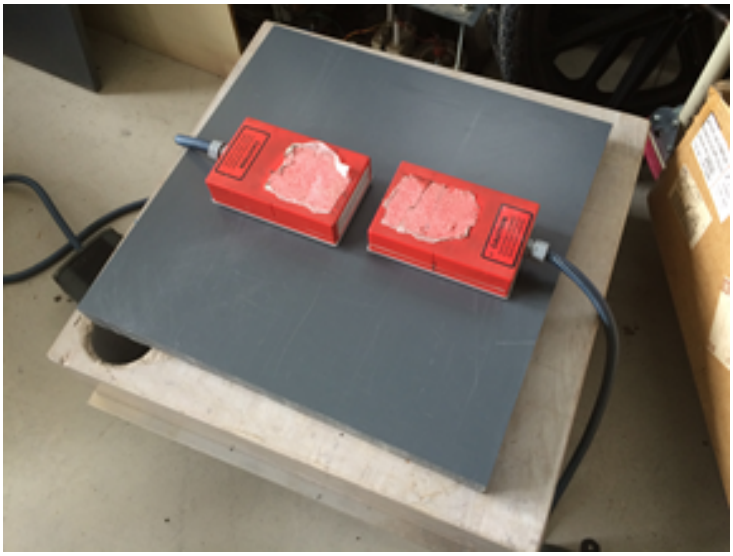

Figure 4.19: GPR experimental set-up conducted with the CMP-TE configuration of antennas on PVC+limestone slabs

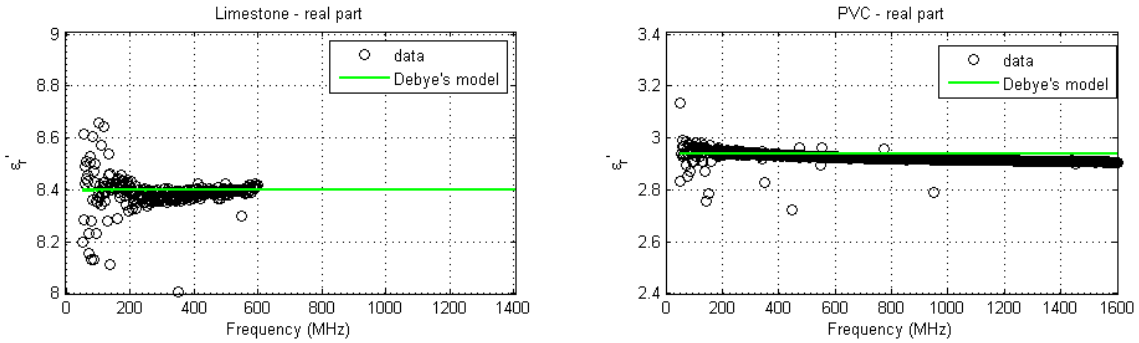

Figure 4.20: Extrapolation of dielectric constant data within [50- 600 MHz] to [50 - 1600 MHz] for (a) limestone and (b) PVC using Debye's model

4.5.4 Experimental validation on homogeneous materials

The second step in the multi-layer WGM validation process requires introducing GPR wave fields measured on standard materials. We have chosen two homogeneous materials PVC and limestone to form a two-layer waveguide and measured by GPR with 2.6 GHz antennas. The waveguide has an equivalent permittivity similar to the concrete samples in dry state despite of the effects of concrete's heterogeneities. We perform this validation to make sure it works well for measurements.

4.5.4.a Materials in test

We have used a PVC slab (dimension: $0.5 \times 0.5 \times 0.043$ m^3) and a limestone slab (dimension: $0.6 \times 0.6 \times 0.142$ m^3) placed on a metal plate (Fig.4.19) to form a waveguide media with the height $h = 0.185$ m. For these two materials, we have corresponding core samples for an EM characterization technique via the EM cell. Therefore, the dielectric constants of the two layers can be extracted from the results of EM cell.

In the measurements of EM cell, the available data cannot reach 1.6 GHz due to the resonance of the cell, sometimes even limited to lower than 1 GHz for material with high

Table 4.5: Inversion results corresponding to GPR wave propagation in a low-permittivity waveguide (PVC and limestone slabs between air and a steel plate)

Mode	h_1 **(m) Forward**	h_1 **(m) Inv.**	$\min(CF)(\times 10^7$ **m/s)**
TE_4	0.043	0.050	1.11
TE_5	0.043	0.040	1.85
TE_6	0.043	0.051	0.60
$TE_4 - TE_5$	0.043	0.041	1.74
$TE_4 - TE_5 - TE_6$	0.043	0.049	1.19

permittivity. So we extrapolate the data to higher frequency band using Debye's model. Fig.4.20 shows the values of dielectric constants of limestone and PVC from the EM cell and the extrapolated curves from the data in the frequency range of [50 - 600 MHz]. The data used for extrapolation was picked under 600 MHz because the measured permittivity of limestone starts to increase after 600 MHz where it was suppose to decrease. Nevertheless, we have got satisfying data of PVC over the whole frequency band and it matches with the results from Debye's model.
At this stage of the study, the frequency variations of complex permittivities have not yet been taken into account in the inversion procedure. Therefore, the values of the permittivities from EM cell are picked at the frequency 1 GHz obtained from the extrapolation: $\varepsilon'_1 = 2.94$ (PVC as medium 1) and $\varepsilon'_2 = 8.40$ (limestone as medium 2), these materials being considered as lossless.

4.5.4.b CMP measurements

An SIR-3000 GPR system, coupled with two 2.6 GHz antennas, was used for CMP radar acquisitions with a "broadside" antenna polarization (Fig.4.19). The temporal sampling of signals is performed in a time window of 10 ns with 2048 points. At the beginning and end of each measurement series, air "shots" were performed in order to quantify the temporal drift of the radar system employed. The CMP configuration here is set as Δx = 0.01 m over 23 steps to avoid the edge effects of the slabs.

4.5.4.c Inversion results

According to the pre-estimation of the permittivities from EM cell, the dielectric constants of the two layers are known as $\varepsilon'_1 = 2.94$, $\varepsilon'_2 = 8.40$. The total thickness is measured as $h = 0.185$ m.
The initial value of the thickness of the first layer is given by $h_1 \in [0.01, 0.18]$, with the interval 0.01 m. According to the shapes of the curves and frequency ranges where the modes locate (modes around 2 GHz are preferred for 2.6 GHz antennas), TE_4, TE_5 and TE_6 modes are chosen to do the inversion. The inversion results of the experimental data are gathered in Table 4.5.
Fig.4.21 shows the picked dispersion curves from the measured wave field via the $f - \beta$ transform and from the inversion of WGM. As regards the WGM validation results on synthetic data, a good correlation has been observed between the phase velocity dispersion curves stemming from GPR measurements (black dots) and the curves derived from TE_4 (blue line) inversion, while combined $TE_4 - TE_5$ modes correlate worse. However, as we see in Table 4.5, the thickness h_1 inverted from $TE_4 - TE_5$ is closer to the reference values

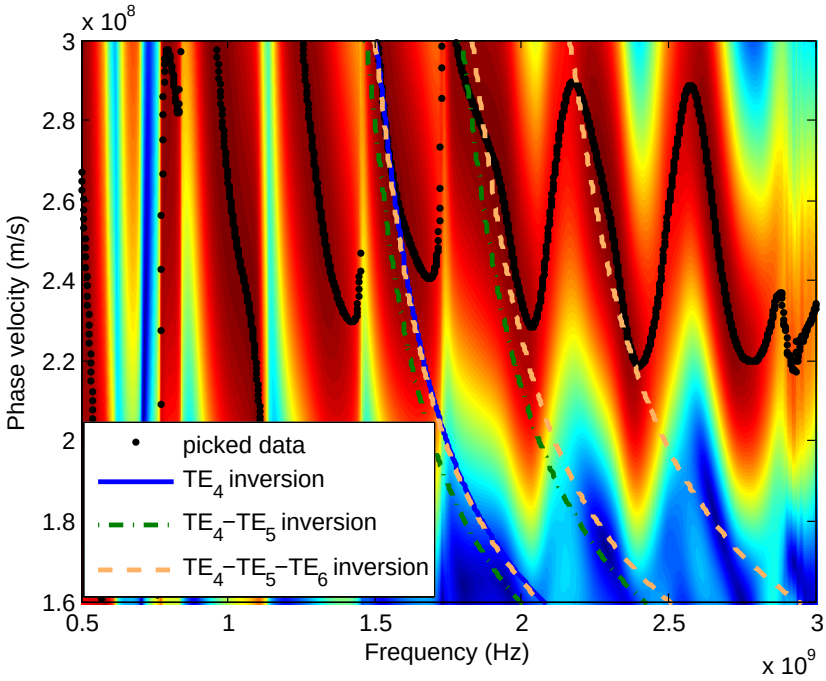

Figure 4.21: Dispersion image and dispersion curves of experimental (black dots) and inversion (colored lines) data of PVC and limestone over steel

than those from TE_4 mode. This can be the slight difference between the measurements from the two equipments: EM cell and GPR. One more important thing we find from the results is that in the inversion process, using a single mode can bring good results (TE_5) or bad results (TE_4 or TE_6) as well. Compared to the single mode inversion, a combined mode inversion with two or three modes is more reliable. This also proves the point of view we have mentioned in 5.2.3.

4.5.5 Conclusion

Finally, we can conclude from this validation study that the Parallel model simplifies the composition of layered materials with their thicknesses and dielectric properties. It is also accessible to WGM used to invert the phase velocity dispersion curves accurately describing the modal propagation in two-layer EM waveguides (either simulated numerically or measured experimentally) and furthermore allowing estimating the dielectric and geometric properties of these media. It can be applied to the concrete after imbibition, which can be divided into two layers: the dry layer and the wet layer. The inversion procedure will be used in the following chapters to characterize concrete specimens during a water absorption process in concrete slabs. Nevertheless, some drawbacks remain for the two-layer model. The main problem is the 4 parameters $[\varepsilon'_1,\varepsilon'_2,h_1,h_2]$ are correlated, so it is impossible to invert the 4 parameters at the same time. We have to approximate the values of ε'_1 and ε'_2 in other ways before the inversion.

Table 4.6: Input parameters of arctan(x) model for numerical models

Configurations	a	b	c	d	h **(m)**
gradient1	0.01	15	6	0.02	0.13
gradient2	0.02	15	6	0.05	0.13

4.6 Validation of Multi-layer Waveguide Inversion on Arctan(x) Model

In this section, we are going to discuss about the inversion with arctan(x) function. The objective is to find out its possibility to be applied to the detection of inhomogeneous materials.
By integrating the arctan function equations (4.17) and (4.18) into the WG model, our inversion is targeted at the estimation of the parameters $[a, b, c, d]$. To realize it, we have conducted two steps of validation. The first step is to study the cost function with the analytical model. The second step is to validate the inversion with numerical models. Then the arctan(x) model can be applied to the experiments on concrete of imbibition, where we find the water content gradients inside the concrete slabs shape like the reverse arctan function, which will be developed in the following chapters.

4.6.1 Modelling parameters and configurations

We have set two models of gradients in GprMax2D in order to study the inversion of arctan(x) model. The values of the parameters are defined in table 4.6. Fig.4.22 shows the change of the permittivity along with the height of the material. Comparing the two curves, we can see that even the values of b and c are the same, the resulted ε'_2 and ε'_1 are different. They are determined by not only the upper and lower limits, but also the shape and position of the gradient. Furthermore, the total thickness can also have impact on it. This model can therefore be more precise than the two-layer model, especially when we do not have very sharp water front inside the material.

The multi-offset data is collected on the waveguide surface by WARR methods, with 1.6 GHz antennas. The position of the receiver displaced from 0.8 m to 0.38 m from the transmitter, by step $\Delta x = 0.01$ m.

4.6.2 Parametric study of inversion on analytical model

First of all, let us recall the arctan(x) function equation:

$$\varepsilon'(x) = \frac{b-c}{\pi} \arctan(\frac{2d}{a} - \frac{2x}{a}) + \frac{b+c}{2} \tag{4.24}$$

where $x \in [0, h]$, h is the total thickness, b and c are respectively the upper and lower limit of the permittivity, d is the middle of the gradient curve and a is the shape factor of the curve. Applying the Parallel model, the effective permittivity of the medium is given by:

$$\varepsilon'_e = \frac{\int_0^h \varepsilon'(x)\mathrm{d}x}{h} \tag{4.25}$$

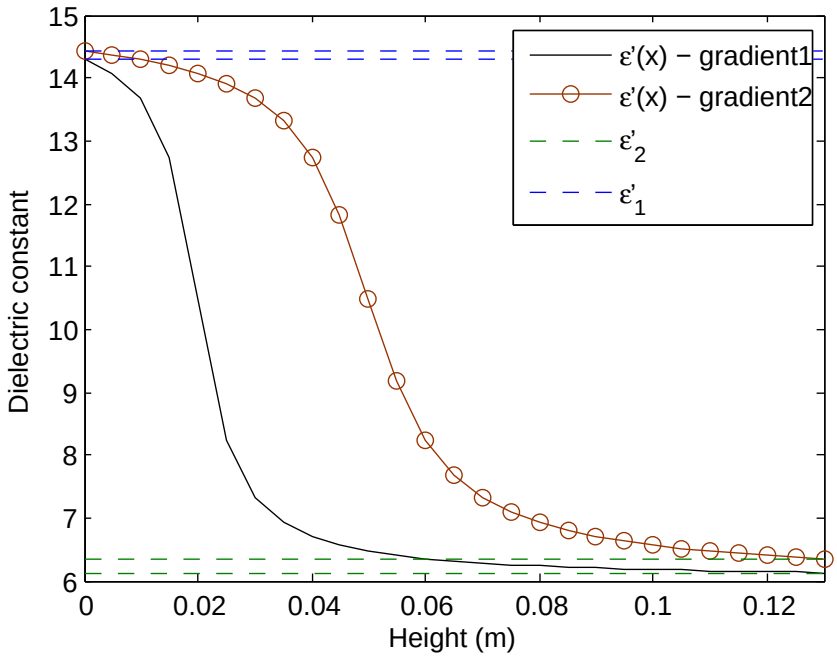

Figure 4.22: Gradient curves of permittivity for two simulations

As h is supposed to be a known value, our objective is to invert the parameters $[a, b, c, d]$ by minimizing the cost function in the following:

$$CF = \sum_{i=1}^{m} \sum_{n=1}^{N} \frac{\left| V_{\phi i} \left(\widetilde{\theta}\left(f, a, b, c, d\right) \right) - v_{sol} \right|}{N} \tag{4.26}$$

To study the formation of the cost function, we have calculated the values of CF by varying 2 out of the 4 parameters to study its global minimum $\min(CF)$. The phase velocities derived from the analytical WGM at TE_2 (1 - 1.2 GHz) are picked for the calculation. To show the variation of the CF more clearly, the maps and curves of $\log(CF)$ are drawn in figure 4.23. From the figure we find that when 2 parameters are known, we have one global minimum of the cost function for the other two parameters. If we change the value of one known parameter, the value of $\min(CF)$ will be apparently increased. For example, in figure 4.23(a), if we change the value of c to calculate the map of cost function, the global minimum will be higher than the one for $c = 6$ (see figure 4.24). However, we cannot guarantee that only one global minimum exists with 3 parameters varying in wide ranges. Determining proper starting values are very important if we want to invert 3 parameters at the same time. It will be proved in the following inversions. We can imagine that for 4 unknown parameters, it would be much more difficult. Therefore, our inversion process becomes to pre-estimate one of the 4 parameters, then to invert the other 3 parameters by $\arctan(x)$ WGM. The steps of inversion are described in the follows.

1) Working band of inversion The best choice of working frequency band for inversion is around the central frequency in the air. The pick of frequencies also depends on the shape of the curve because the error of velocities can cause error in inversion results. Like in Fig.4.26, all modes have good shapes except for the fundamental mode below 0.5

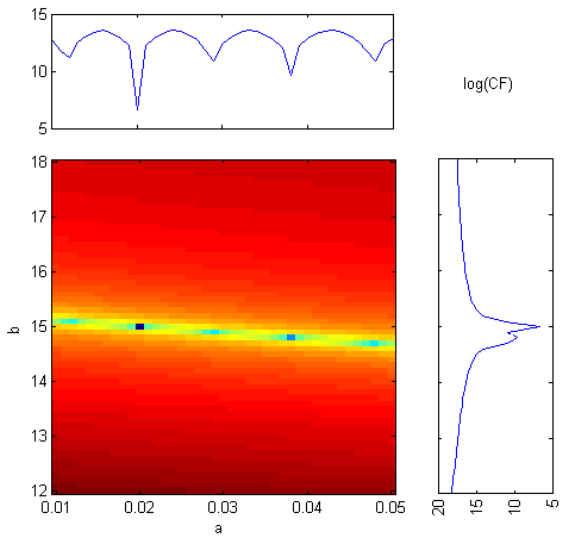

(a) c = 6, d = 0.05

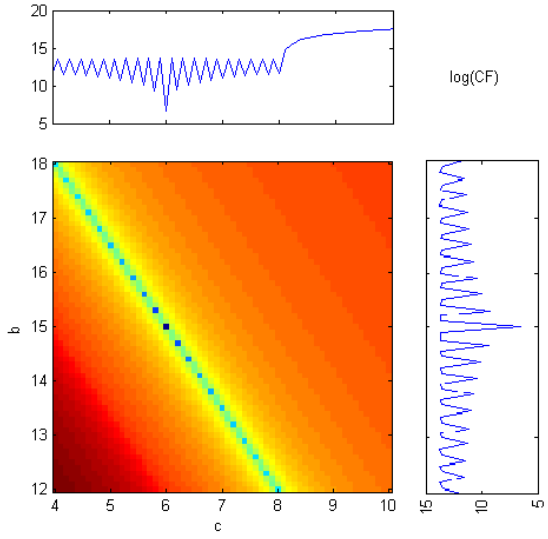

(b) a = 0.02, d = 0.05

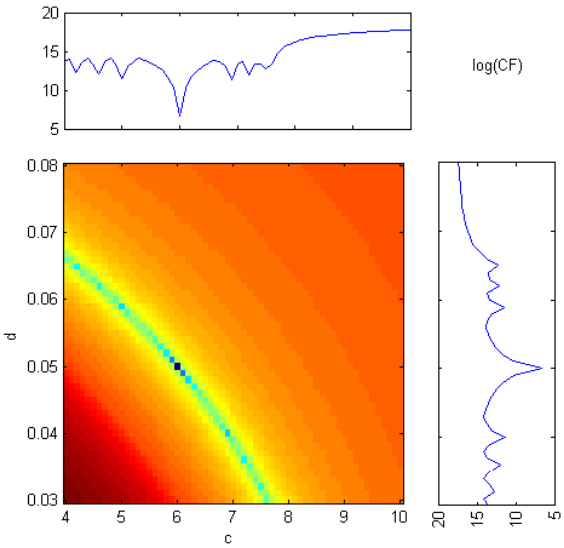

(c) a = 0.02, b = 15

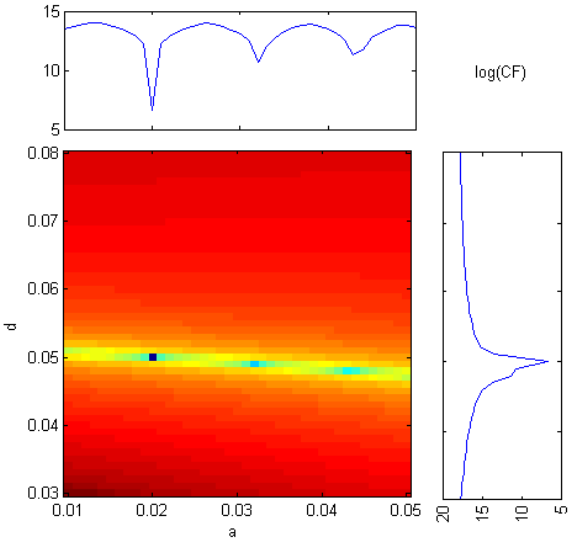

(d) b = 15, c = 6

Figure 4.23: Cost functions $\log(CF)$ of $\arctan(x)$ WGM generated curve at TE_2 mode of Config. gradient2: $a = 0.02$, $b = 15$, $c = 6$ and $d = 0.05$

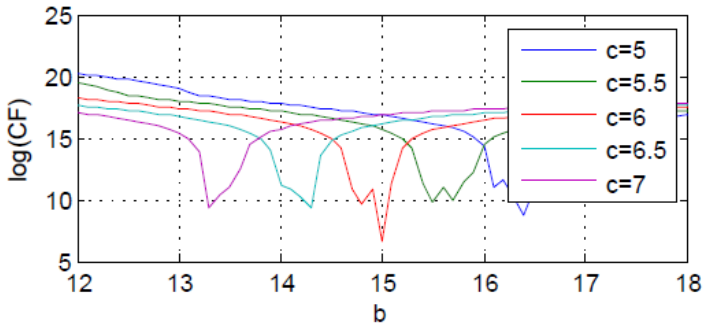

(a) Variation of b-c

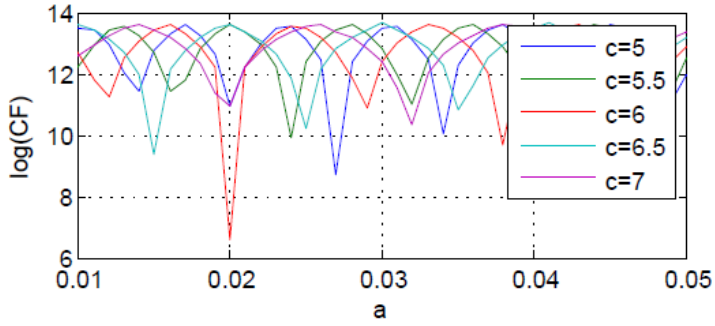

(b) Variation of a-c

Figure 4.24: Cost functions $\log(CF)$ of Config. gradient2 generated curve at TE_2 mode with (a) varying b, c, (b) varying a, c

GHz. As the central frequency is 1.6 GHz, we prefer to choose the TE modes between 1 and 2 GHz. Finally, we pick one single mode TE_2 (1 - 1.2 GHz) since combining two modes takes double time to do the calculation.

2) Starting values of iteration From Fig.4.23, we find it easy to fall into other local minima, especially for the varying b and c. Our solution to this problem is for each parameter, to define several initial values in a wide range for the iterations of the inversion. For the $\arctan(x)$ model, the difficulty is that we cannot invert the 4 parameters at the same time. So we need to find out a parameter to be the "known parameter". It should not be very sensitive to the inversion results and should be easy to be estimated. With model Config. gradient2, we have defined the starting values in two tasks, which are summarized in table 4.7.
The parameters b and c are close to the dielectric constants of the upper and lower surfaces of the waveguide. For concrete and some inhomogeneous materials, we are able to limit the values in a certain range by experience. The shape factor a is normally located between 0.01 and 0.04. The value of d corresponds to the position of the water front, which we can determine it between 0 and the total thickness h. But here we use the range [0.01 - 0.06] to save the time. We change the value of the one known parameter to study its impact on the inversion results.

3) Minimum CF searching For each starting model of the 3 parameters, one $\min(CF)$ is obtained in the end. We also call it the residue of the non-linear regression. The minimum of the cost functions $\min(CF)$ from all the starting models is identified as the

Table 4.7: Definition of starting values of inversion for Config. gradient2

Task	Input	Range	Interval
1	b	12 - 18	1
	c	5 - 8	1
	d	0.01 - 0.06	0.01
2	a	0.01 - 0.04	0.005
	b	12 - 18	1
	d	0.01 - 0.06	0.01

global minimum or very close to it, where we get the values of $[b, c, d]$ or $[a, b, d]$ that we are looking for.

Our objective of the two tasks of inversion for Config. gradient2 is to study the sensitivity of the known parameter to the results, in order to define a suitable known parameter for the global inversion methodology. To avoid other interference of the data and get more precise inversion results, we use the dispersion curve from the analytical model. The inverted gradient curves of dielectric constants are shown in Fig.4.25. The first figure is about the inversion results of task 1 by changing the value of a. When $a = 0.02$, the inverted curve is exactly the same as the forward model. However, we can see that a is very sensitive to the inversion results. Furthermore, as it is a shape factor, it is difficult to be approximated directly from the measurements. Even though it is limited in a small range, it is not suitable for the known parameter.

The second figure is about the inversion results of task 2 by changing the parameter c. Still, the direct model and the inverted curve are the same when c has the right value. This parameter is much less sensitive than a. Moreover, it is a parameter closely related to the dielectric constant of one surface. In the experiments of imbibition, it is close to the dielectric constant of the dry surface. Even though we cannot approximate its value directly, we can easily get the value of the dielectric constant on the dry surface from a CMP measurement before imbibition. It therefore can be used as a known parameter.

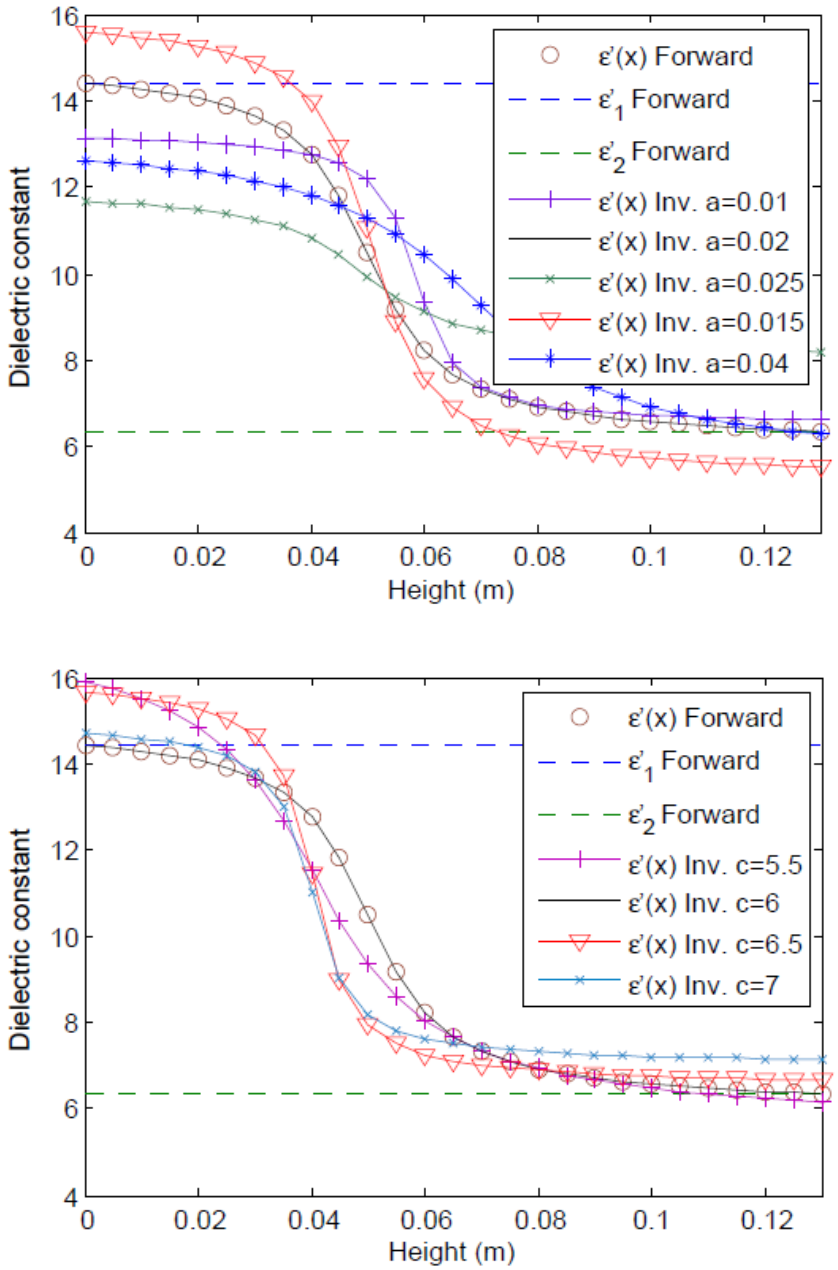

Figure 4.25: Direct and Inverted gradient curves of dielectric constants of analytical model Config. gradient2 with known varying parameter (a) a and (b) c

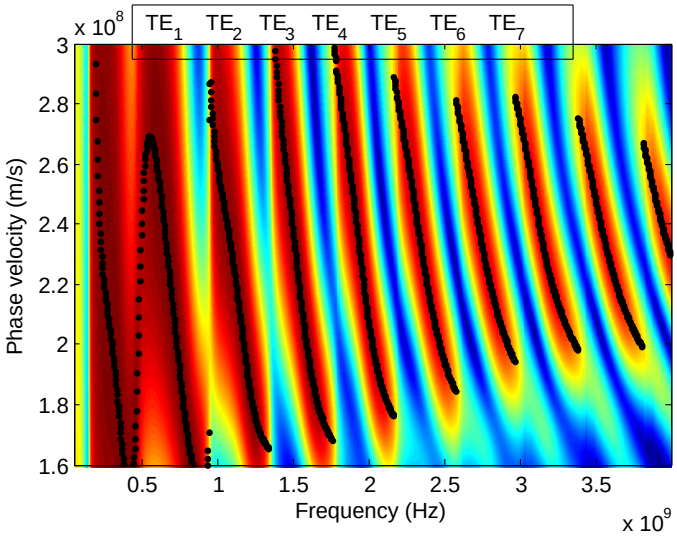

Figure 4.26: Dispersion image and dispersion curves derived from the numerical model, Config. gradient2 from Table4.6

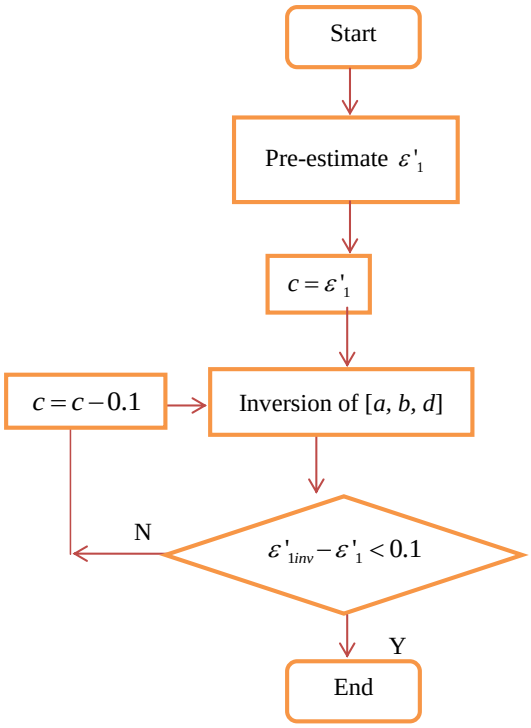

Figure 4.27: Flow chart of arctan waveguide inversion for determining known parameter c

4.6.3 Inversion on numerical model

Then we are able to do the inversion for the dispersion curves extracted from the two numerical models Configs. gradient1 and gradient2 (Table4.6).

Fig. 4.26 is the dispersion image and the phase velocity curves of the GPR data simulated by the numerical model 'gradient2'. To get more reliable inversion results, we choose two TE modes for the calculation: first, use one single mode for the inversion; second,

Table 4.8: Inversion results of gradient1 of the dispersion curves derived from the FDTD model

gradient1	a	b	c	d	ε'_2	ε'_1	ε'_e	$\min(CF)(\times 10^6$ **m/s)**
Direct	0.01	15.0	6.0	0.02	14.30	6.13	7.67	-
TE_2 **Inversion**	0.01	14.0	6.0	0.02	13.38	6.12	7.48	4.27
TE_3 **Inversion**	0.01	12.0	6.0	0.03	11.68	6.10	7.53	2.42
$TE_2 - TE_3$ **Inversion**	0.02	17.0	5.9	0.01	14.23	6.19	7.50	3.31

Table 4.9: Inversion results of gradient2 of the dispersion curves derived from the FDTD model

gradient2	a	b	c	d	ε'_2	ε'_1	ε'_e	$\min(CF)(\times 10^7$ **m/s)**
Direct	0.02	15.0	6.0	0.05	14.43	6.36	9.60	-
TE_2 **Inversion**	0.02	16.1	6.0	0.04	15.49	6.27	9.36	1.48
TE_3 **Inversion**	0.02	16.3	5.9	0.04	15.25	6.33	9.35	0.68
$TE_2 - TE_3$ **Inversion**	0.01	16.8	6.0	0.04	16.33	6.18	9.42	1.08

use combined $TE_2 - TE_3$ mode. Thus, for gradient1, TE_2 = [1.2 - 1.4 GHz], TE_3 = [1.6 - 1.8 GHz]; for gradient2, TE_2 = [1 - 1.2 GHz], TE_3 = [1.4 - 1.6 GHz]. For both configurations, we assume ε'_1 as the known parameter, as what we can get in practice before the imbibition monitoring. To find the right value of c, we conduct an iterative approach during the inversion, which is explained in Fig.4.27.
For the starting values of $[a, b, d]$, we employ the starting values of task 2, as determined in table.4.7.

4.6.4 Results and discussions

The inversion results are shown in Tables 4.8 and 4.9. Fig.4.28 shows the dispersion curves of the configurations gradient1 and gradient2 directly from the numerical models and from the inversions.
Compared to the perfect match from the inversion of the curves from analytical model, the inversion results from the numerical data have very important error in ε'_2. Generally speaking, the inversion results are very sensitive to the difference between the numerical and the analytical model. That is to say, if the dispersion curves we obtain are not accurate enough, the approximation of ε'_2 might be unacceptable. Meanwhile, the inverted values of other parameters are mostly acceptable. One more thing to notice is that, different from the two-layer waveguide inversion, we cannot get best approximations from the combined modes inversion. For gradient1, the TE_2 inversion obtains the best results; while for gradient2, TE_2 and TE_3 inversion results are better than those of $TE_2 - TE_3$ inversion.

4.6.5 Conclusion

In this section, we have applied the multi-layer waveguide inversion to the media with gradient described by $\arctan(x)$ function. It has been validated by synthetic data using the analytical model with the modal theory and the numerical model with GprMax 2D. If we compare this model to the two-layer WGM, it has both advantages and disadvantages. The advantage is that the parameters to be pre-estimated have been reduced from [ε'_1,ε'_2]

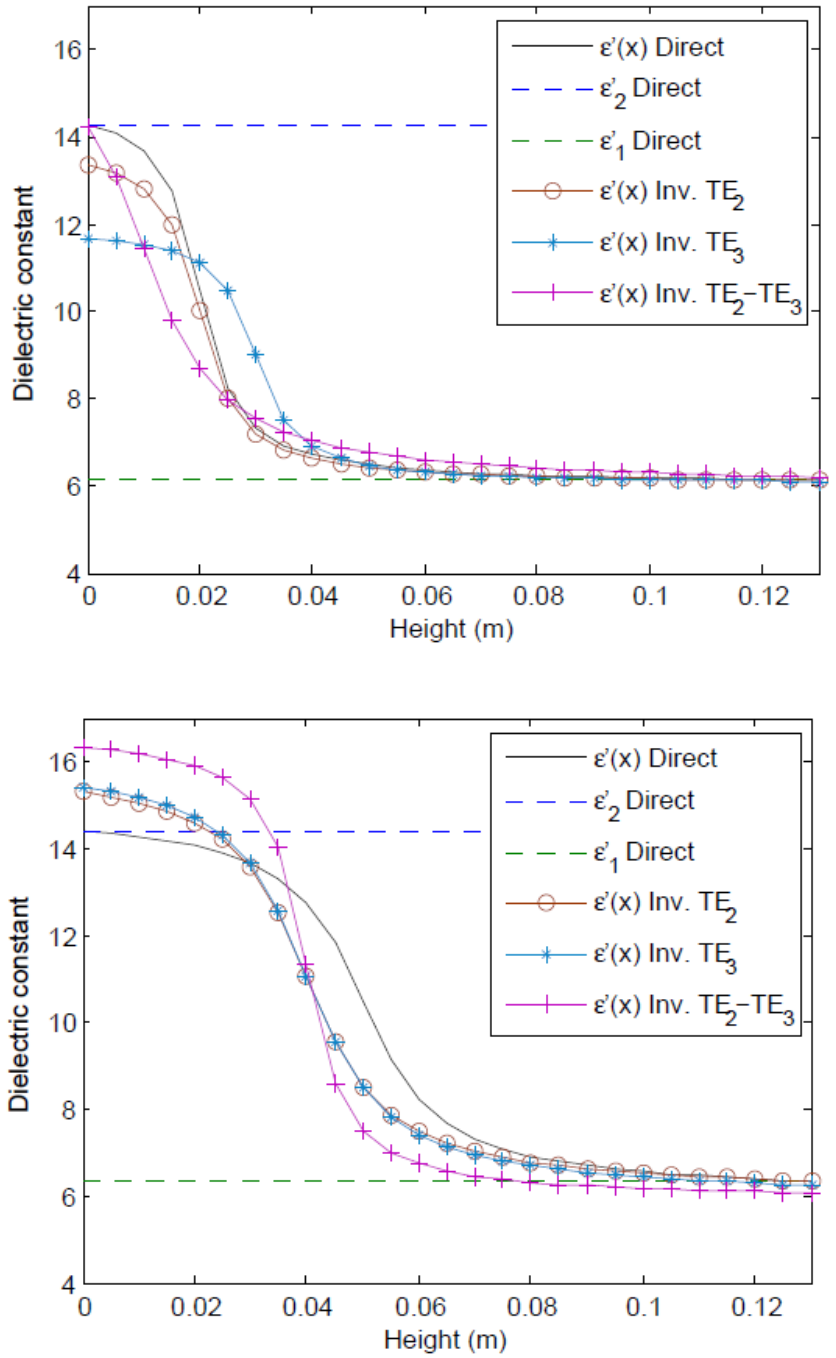

Figure 4.28: Direct and Inverted gradient curves of dielectric constants of numerical models Configs. gradient1 and gradient2

to ε'_1. It greatly facilitates the process of inversion under certain circumstances. Also, it helps us understand better the change tendency of water inside the concrete. The disadvantage is that the approximation of ε'_2 is not accurate enough. It will not be a problem if we do not care about the value of ε'_2. Otherwise, we will need to pre-estimate the parameter to get better inversion results.

4.7 Conclusion

In this chapter, we have first introduced the processing of GPR data: from multi-offset data to phase velocity dispersion curves. The geometric dispersion of guided waves is considered in the dispersion curves. In some cases, the pre-processing of the data, like filtering, is necessary. Then a new multi-layer WGM is developed from the modal theory by integrating the Parallel model based on Lichtennecker-Rother equation. It has been studied in both forward and inverse problems.

We have done forward study on two-layer model, three-layer model and arctan(x) model by numerical modeling using GprMax 2D. For arctan(x) model, the permittivity gradient was built by a 27-layer medium. Generally, the multi-layer WGM works well to homogenize the waveguide. The problem is, as the number of layers increases, the error of phase velocity increases at lower and higher frequencies.

Then we have validated the inversion of the two-layer model with simulation and measurements on homogeneous materials. The main difficulty of this model is due to the numerous minima of the cost function CF. To realize the inversion, we pre-estimated the values of ε'_1 and ε'_2 by extrapolating EM cell data. Knowing the values of h, ε'_1 and ε'_2, the parameter $h1$ can be inverted by the two-layer model.

The arctan(x) model inversion is validated with simulation by GprMax2D. The gradient curve is very sensitive to the shape factor a. But we are able to invert 3 parameters together using the arctan(x). It can be applied to the monitoring of concrete imbibition to describe a more precise water gradient inside.

For the next chapter, we will present the plans of experiments and design of concrete in use.

Chapter 5

Plans of Experiments on Concrete

Contents

5.1 Introduction

The experiments on concrete in this thesis are supported by a French national project ANR - EvaDéOS and an internal research project (Ifsttar - Cerema) called APOS.
The aim of project EvaDéOS (Evaluation non destructive pour la prédiction de la Dégradation des structures et l'Optimisation de leur Suivi) is to combine different non destructive tests to evaluate the structures for damage prediction and optimization of the follow-up [Balayssac et al., 2015; Villain et al., 2015c]. To conduct this project, an assessment methodology based on a combination of different non-destructive tests (NDT) was proposed during a previous national project ANR - SENSO [SENSO, 2009; Balayssac et al., 2009]. With the applications of EM NDT, we have participated in two series of experiments: the carbonation and imbibition by water.
The second project APOS (Auscultation Pour des Ouvrages Sûrs) is established to propose a comprehensive approach to non-destructive evaluation of materials, extended to the structures, to improve their maintenance and durability. The general objective is to advance research methods for concrete, reinforcement and cables, to develop non-destructive auscultation methods for monitoring structures in reinforced and pre-stressed concrete. The water penetration and chloride ingress into concrete is assessed in controlled conditions in laboratory over time to understand the condition of the structures in terms of durability and predict the long-term behavior [Thauvin et al., 2015; Villain et al., 2015a].
Following the two projects, we have done some EM ND evaluations on concrete samples in homogeneous state (EM cell and GPR) and with gradients (GPR and gammadensimetry). The main objective of our work is to develop an efficient way to determine the water content gradient in concrete by EM methods. The results of EM cell and gammadensimetry, offering frequency dependent permittivities and the water content variation of concrete, respectively, are used as reference for the GPR results. Thanks to project APOS, we have also some study on gradients of chloride.
This chapter will introduce the plans of experiments corresponding to the two projects

Table 5.1: Formulation parameters and mix designs of concrete G8 and B1

Codification	SENSO G8	EvaDéOS B1
Type of aggregates	Round siliceous D_{max} = 14 mm	
Cement CEM I 52.5 N (kg/m^3)	240	240
Sand 0/2 or 0/4 (kg/m^3)	938	941
Gravel 4-14 or 10-14 (kg/m^3)	1016	1019
Total water (kg/m^3)	217	193
W/C	0.9	0.8
ρ **accessible to water (%)**	18.1	18.3

and integrated in our study. The introduction will be presented as two parts: plans of concrete and programs of EM NDT techniques.

5.2 Planning of Experiments for Project EvaDéOS

5.2.1 Objectives

In this section, we will present the formulations of concrete specimens to be used in the experiments of EvaDéOS project. Then the two campaigns of experiments will be introduced in the following. The first one is to study the carbonated concrete with different carbonation depths. The second one is to study the water penetration by monitoring the water front depth during imbibition. The results to be analysed in the next chapter will also be decided here.

5.2.2 Concrete formulation

In the experiments of carbonation, all the slabs of concrete B1 are made with nearly the same mix design as concrete G8 used in SENSO project [SENSO, 2009; Villain et al., 2015c; Gomez et al., 2015]. In fact, we have also tested concrete B2 according to G2 in SENSO. However, since the porosity of B2 is too low (ρ = 12.7%), the slabs could not get carbonated on time for our study. Table 5.1 shows the formulation parameters of G8 in SENSO and B1 in EvaDéOS. From the table, we can find that concretes G8 and B1 have the same aggregates and cement, but a little difference in water content. So water to cement (W/C) ratios are different, causing different porosities.

5.2.3 Planning of carbonation program

5.2.3.a Presentation of specimens

We have about 20 concrete slabs (dimension: 500 × 250 × 120 mm^3) with different carbonation depths on the surface 250 × 500 mm^2 for NDT. Table 5.2 includes more details about the slabs.
Codification:

- 1, 2, 3 and 4: referred to carbonation depth (1: 0; 2: 10; 3: 20; 4: 40 mm)

Table 5.2: Distribution of concrete slabs

Concrete type	B1 (G8 SENSO)			
Aimed carbonation depth (mm)	0	10	20	40
Codification	B1-1-x-y	B1-2-y	B1-3-y	B1-4-y
Nb. of slabs/partner	2	1	1	1
Nb. of total slabs	8	4	4	4

- x: number only for slabs B1-1 (from 1 to 8, where 7 and 8 have been sent to Nantes)
- y: team partner (T: Toulouse; N: Nantes; A: Aix-en-Provence; B: Bordeaux)

Besides, we have 4 non-carbonated cylindrical samples of B1 with the dimension Ø75×120 mm for the measurements by EM cell. The samples were controlled under 3 different saturation degrees: S = 20% ± 2%, S = 83% ± 3%, S = 100%. The results of EM cell will be used as a calibration of frequency dependent permittivity with respect to the water content.
After the measurements on slabs, we have taken 2 cores (Ø75 × 120 mm) from each slab of the slabs for Nantes to do destructive test. The objective is to observe their real carbonation depths.

5.2.3.b Preconditioning of concrete

It was decided to aim for the following depths of carbonation: 0 mm (reference), 10 mm, 20 mm and 40 mm, except for the depth 0 mm that is non-carbonated and regarded as reference slab.
After casting compositions and one day after the release, the slabs were stored moist curing for 28 days to stabilize the hydration. Then the slabs were waterproofed on all sides except one, so that the carbonation happens only on one face. The slabs were then conserved in the atmosphere of 20°C et 60% of *RH* (Relative Humidity) until having a constant weight. Slabs B1-1 (non carbonated) were placed in an enclosure to let in outside air, but with a solution of lime milk to capture as much carbon dioxide as possible to avoid carbonation. The other slabs were placed in an accelerated carbonation chamber with a CO_2 rate of 50%. The evolution of the carbonation depth was controlled by 6 cylindrical cores (Ø60×120 mm) from a reference slab, and having undergone the same conditions as the slabs (curing, storage and chamber) and experienced in different time frameworks. Once the desired depth reached on the controlling core, 4 slabs were taken out of the carbonation chamber [Gomez et al., 2015].
The test has been programmed in two steps:

- Once the carbonation is completed for all the slabs, the slabs were measured together in Toulouse under saturated condition, in order to quantify the variability of the measurements in a controlled state of moisture.

- After a certain drying period to reach the mass corresponding to $S \approx 50\%$ and a certain sealing period to homogenize the water content, slabs for each group were sent to each location to be measured in a non-saturated state.

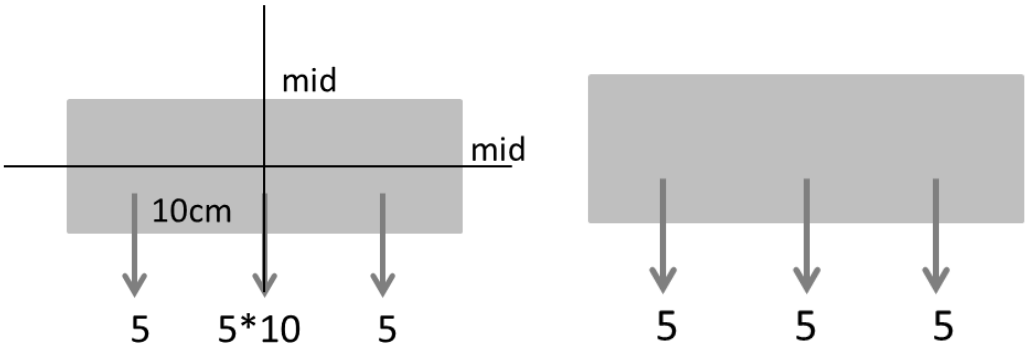

(a) Series - T (b) Series - A/B/N

Figure 5.1: Locations and the number of measurements on the upper face of carbonated slabs (a) Series - T and (b) Series - A/B/N

For our work, 5 slabs were sent to Nantes and measured when the saturation degree S is kept near 45%. As we found with destructive test of carbonation depth (see Table 5.3 in the following), the aimed carbonation depths were not reached during the tests. Therefore, after measuring the 5 slabs in Nantes, C1-4-N was put back into an accelerated carbonation chamber until the carbonation depth reached 40 mm. For this measurement, we call the slab C1-4-Nbis.

5.2.3.c Non-destructive tests planning

In the whole campaign of tests, the moisture distribution of the slabs was expected to be homogeneous. The indicator, referred to in these tests, is carbonation depth. Several NDT methods were applied to the tests, such as: capacitive probes, resistivity test, ultrasonic method and GPR.
In the first stage, the measurements of saturated slabs were conducted in LMDC Toulouse (Laboratoire Matériaux et Durabilité des Constructions de Toulouse) in February, 2013. Twenty slabs with different carbonation depths were measured by GPR with 4-offsets. Then some slabs were measured by CMP method (as described in §2.4.3.c).

Figure 5.1 shows the plan of measurements, applied to all the techniques, the arrows and the numbers indicating the location and the number of the measurements. For GPR, we mainly used the 4-offset method. The central frequency of GPR is 1.5 GHz. For each concrete slab, 3 measuring points have been considered, one in the center of the slab and the other two at 10 cm from each side thereof along the mid-line. We measure 3 points on the surface (non-carbonated surface of B1-1 and carbonated surfaces of B1-2, B1-3, B1-4) and 5 times at each point. Except for the slabs of Toulouse, where we measured for the middle point 5×10 times. The dielectric constant of one slab is obtained from an average of the 3 points on the slab. Slabs B1-1-1-T, B1-2-T, B1-3-T and B1-4-T were also measured by CMP method with 2.6 GHz antennas. The displacement of the transmitter and the receiver is $\Delta x = 0.5$ cm at each moving step, with the maximum offset $X_{max} =$ 14 cm.
Then 5 of the slabs were sent to Nantes to be measured with the saturation degree of 45%. They were measured in the same process at $S = 45\%$ in July, 2013. Slabs B1-1-7-N, B1-1-8-N, B1-2-N, B1-3-N, B1-4-N and B1-4-Nbis were first measured with 4-offset

Table 5.3: Real carbonation depths measured with method "AFPC-AFREM 1997"

Codification	Aimed depth (mm)	Real depth (mm)	S (%)
B1-1-7-N	0	0	46.5
B1-1-8-N	0	0	48.6
B1-2-N	10	6.5±0.6	45.2
B1-3-N	20	16.3±0.9	48.6
B1-4-N	40	not measured	47.5
B1-1-1-T	0	0	44.5
B1-1-2-T	0	0	46.9
B1-2-T	10	10.5	50.3
B1-3-T	20	17	45.3
B1-4-T	40	31	43.9

method, then with CMP method of the same configuration as in Toulouse.

5.2.3.d Reference results

Measuring the carbonation depth was made following the recommendations of AFPC-AFREM [AFPC-AFREM, 1997]. Table 5.3 gives the results of real carbonation depths tested on the cores (Ø75 × 120 mm) out of slabs of Nantes.

5.2.3.e Preview of experimental results

We have used two methods applying GPR on 20 concrete slabs with different carbonation depths and moisture conditions. One is the 4-offset method, using the 1.5 GHz antennas. The other one is CMP measurement, using the 2.6 GHz antennas.
In saturate state, we measured all the 20 slabs with the 4-offset method. The 4 slabs of Toulouse were measured with CMP method (Slab B1-1-2-T was missing). In non-saturate state ($S \approx 45\%$), the 5 slabs of Nantes were measured with both 4-offset and CMP methods.
Figures 5.2 and 5.3 are the normalized GPR signals, picked from the measurements of the slabs at X_0, by 1.5 GHz and 2.6 GHz antennas. Figure 5.2 shows the signals for slabs T at $S = 100\%$. We observe an evolution of the direct wave (DW) and reflected wave (RW) along with the increasing of carbonation depth, where the amplitudes of DW and RW increases and the travel time of RW decreases. The other saturate slabs are suppose to have the similar signals since they are from the same concrete and conditioned at the same time. Figure 5.3 shows the signals for slabs N at $S = 45\%$. Tough the variation is not so strong as in saturate state, we can see the same evolution. The RW of C1-4-Nbis at 1.5 GHz is unexpectedly decreased since the slab was put on the ground while measuring. We can also see from the two figures, the 2.6 GHz antennas are more sensitive to the variation of carbonation depth.

Figure 5.4 shows the dispersion curves of the slabs T when $S = 100\%$ and slabs N when $S \approx 45\%$. Unfortunately, the curves do not show very good propagations of EM waves in modes. The main reason is the strong leakage over the bottom of the slab as we did not put it on a strong reflector. In this condition, it is very difficult to apply the waveguide

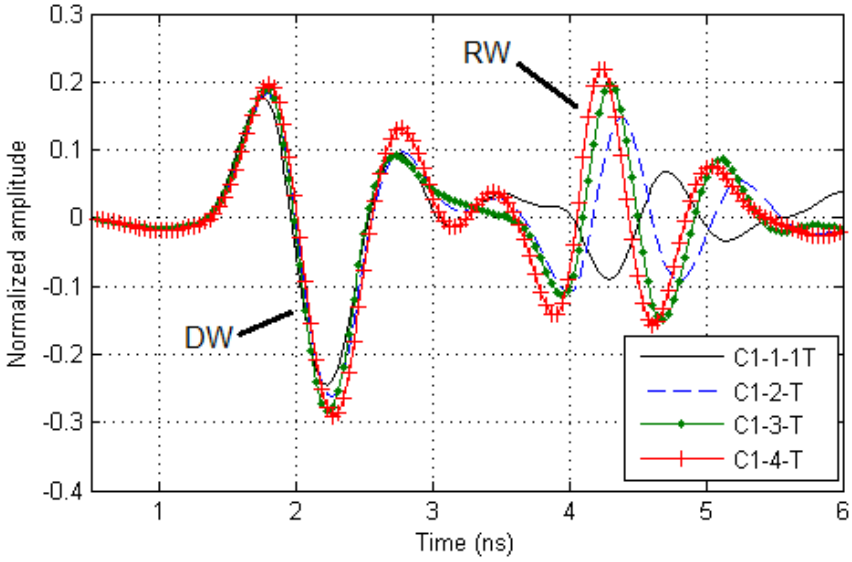

(a) 1.5 GHz antennas - S=100%

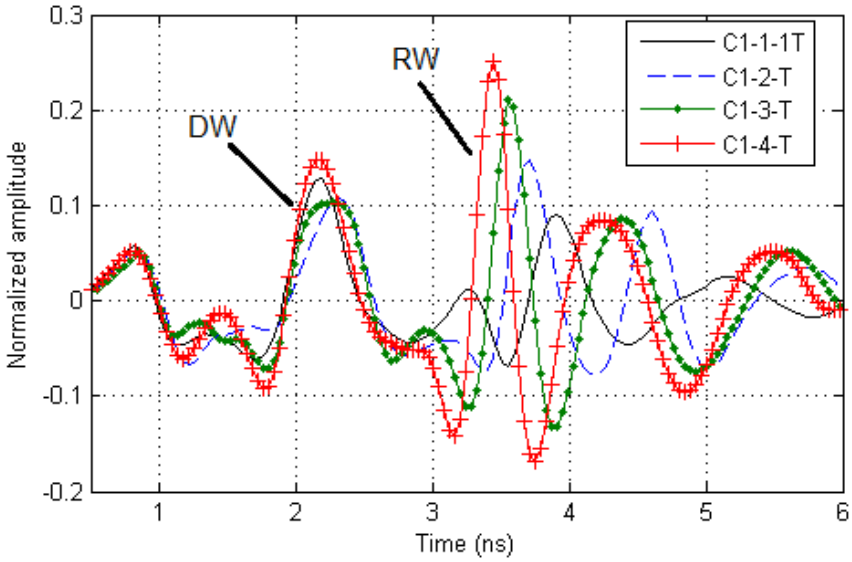

(b) 2.6 GHz antennas - S=100%

Figure 5.2: Normalized GPR signals received from saturate slabs T at minimum offset X_0 by (a) 1.5 GHz antennas (b) 2.6 GHz antennas

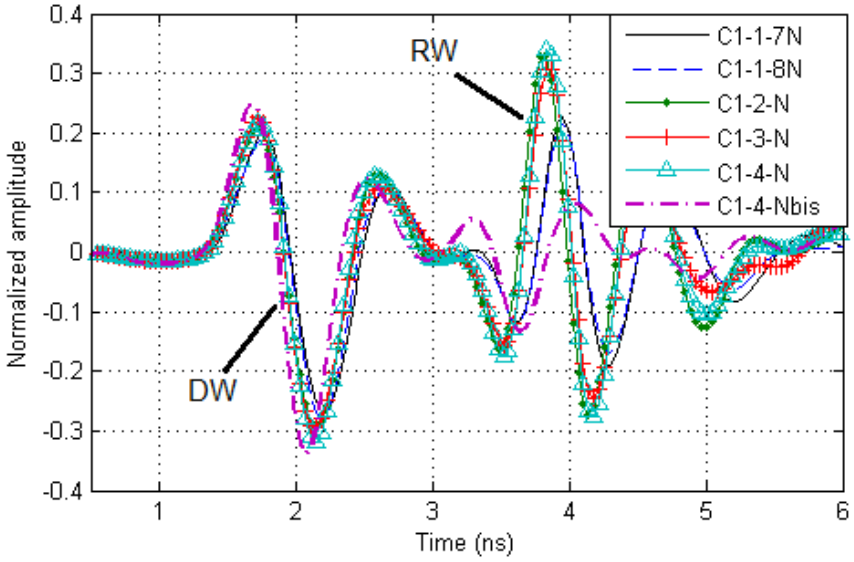

(a) 1.5 GHz antennas - S=45%

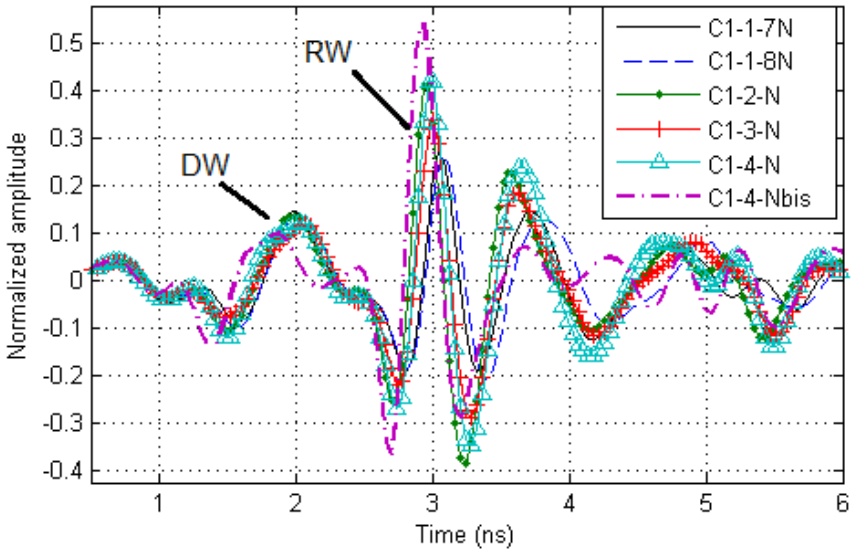

(b) 2.6 GHz antennas - S=45%

Figure 5.3: Normalized GPR signals received from non-saturate slabs N at minimum offset X_0 by (a) 1.5 GHz antennas (b) 2.6 GHz antennas

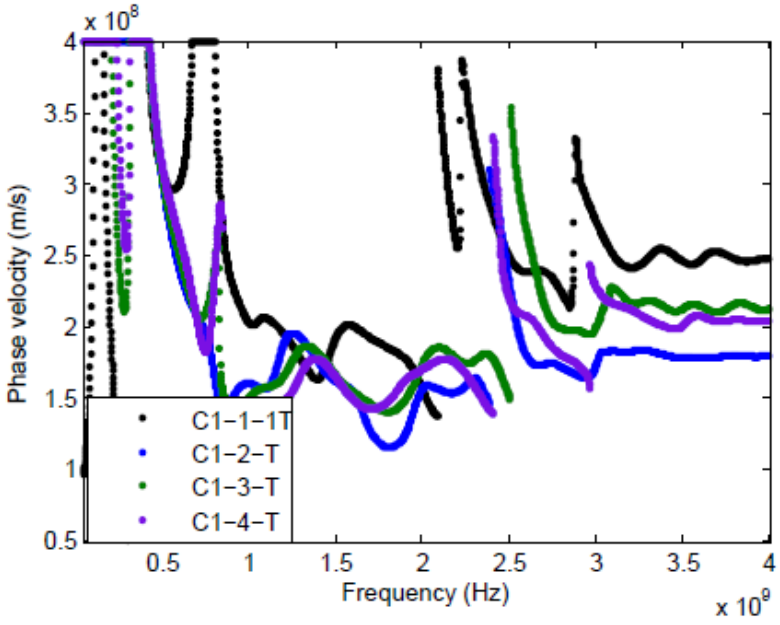

(a) Series T - S=100%

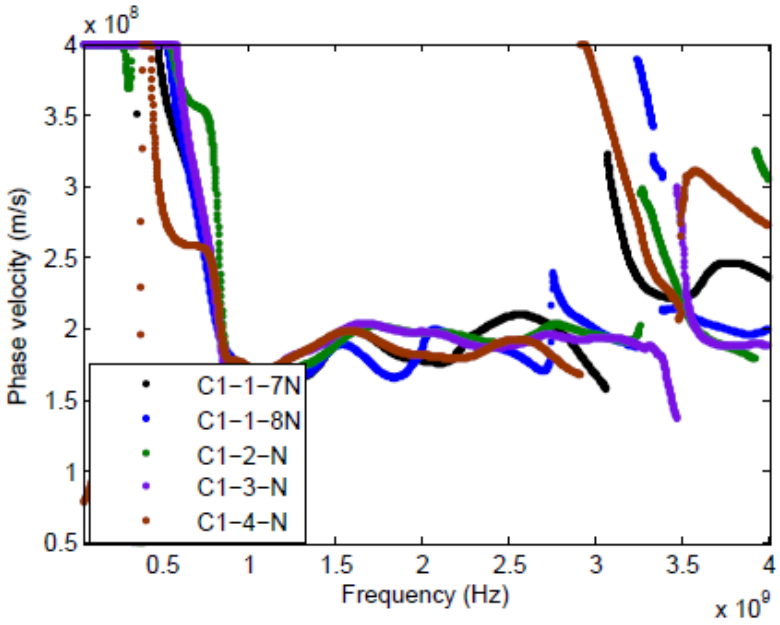

(b) Series N - S=45%

Figure 5.4: Dispersion curves of phase velocity from CMP measurements on (a) saturate slabs of series T (b) non-saturate slabs of series N

inversion to it.
According to the preview of the measurements, we will focus on our analysis on the GPR signals and the dielectric constants obtained from the 4-offset method. More experimental results of the 20 saturate slabs and the 5 non-saturate slabs of Nantes will be presented in Chapter 6.

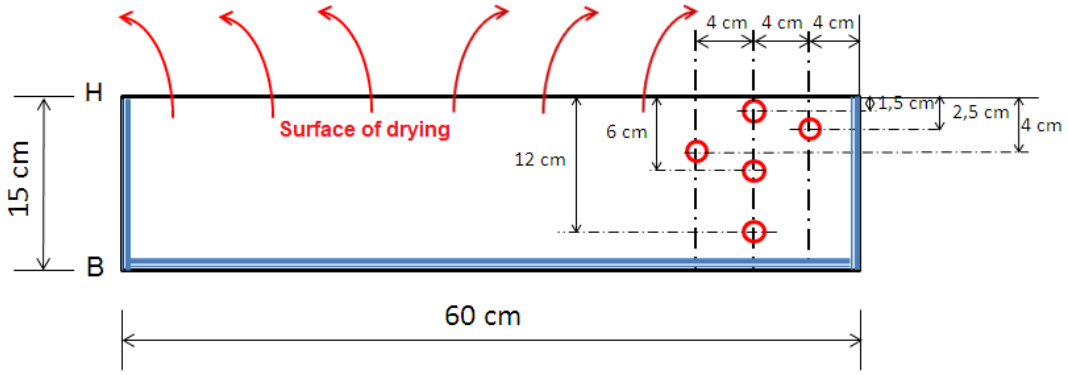

Figure 5.5: Location of THR sensors in concrete slab

5.2.4 Planning of water imbibition program

Here we introduces the program of imbibition experiments with tap water. Three slabs of the same concrete and two campaigns of imbibition experiments were included in the program.

5.2.4.a Presentation of specimens

To study the water content penetrating into the concrete, we prepared 3 slabs, named B1-26, B1-27 and B1-28 for the experiments of water imbibition. The dimension of the slabs is defined as $600 \times 260 \times 150$ mm^3. We have embedded some humidity sensors at different depths (1.5 cm, 2.5 cm, 4 cm, 6 cm, 12 cm) to monitor the relative humidity of concrete during the imbibition process. Figure 5.5 shows the location of sensors in the concrete slabs.

Besides, several cylindrical specimens with the dimension $\varnothing 100 \times 120$ mm from the same concrete were processed with the same imbibition protocol to be measured by gammadensimetry, as reference.

5.2.4.b Preconditioning of concrete

The production of concrete slabs was similar to the moulds and slabs of the carbonation program. After casting and curing, the slabs were sealed by aluminium foils and put in an oven at $T = 40$°C for one month to obtain a homogeneous moisture distribution. After taken out of the oven, aluminium at 4 sides of each slab were kept to make the imbibition in obe straight direct.

The measurements of GPR, gammadensimetry and initial weighing were all carried out at T_0 corresponding to the time before the slabs were put in the water. Figure 5.6 is the protocol diagram of the water ingress experiment. The cores (intended for weighing and gammadensimetry measurements) and slabs (intended for weighing and GPR measurements) were then placed simultaneously on plastic supports immersed in container with water at the height 10 ± 2 mm from the slab's bottom.

We have done 2 campaigns of imbibition with the same slabs.

The first campaign of experiments was conducted from September to October, 2013. The B face (figure 5.5) of the slabs was contacted with the water. After 30 hours' imbibition, the 3 slabs were put in an oven at 40°C for drying until reaching a constant weight. The second campaign was conducted from January to February, 2014. We have conducted

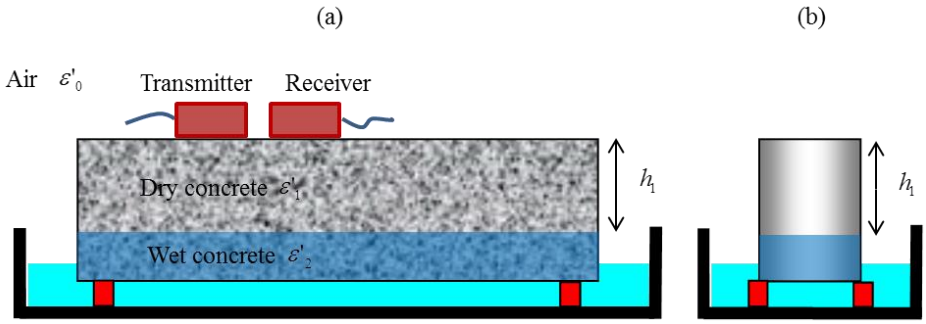

Figure 5.6: Protocol diagram of water ingress into: (a) concrete slabs intended for weighing and GPR measurements; (b) concrete cores intended for weighing and gammadensimetry measurements

Table 5.4: Imbibition and drying measuring process of concrete B1

Imbib. time	**Camp.1**	**Camp.2**	**Drying time**	**Camp.1**	**Camp.2**
T_0	0	0 h	T_8	4 h	4 h
T_1	2 h	2 h	T_9	25 h	22 h
T_2	4 h	4 h	T_{10}	4 days	3 days
T_3	6 h	6 h	T_{11}	13 days	7 days
T_4	8 h	8 h	T_{12}	-	15 days
T_5	12 h	14 h			
T_6	16 h	32 h			
T_7	32 h	128 h			

the similar imbibition and drying process for the slabs. The difference here from the first campaign is the H face was contacted with the water.

5.2.4.c Non-destructive tests planning

The time framework of the 2 campaigns for ND tests are summarized in Table 5.4. Several NDT methods were applied to the tests, such as: capacitive probes, resistivity test [Fares et al., 2015], ultrasonic method [Abraham et al., 2015] and GPR [Balayssac et al., 2015]. At each time, they were conducted on the two faces of the slabs one by one.

For GPR, we used 2.6 antennas to do CMP measurements. The displacement of the transmitter and the receiver is $\Delta x = 0.5$ cm at each moving step, with the maximum offset $X_{max} = 14$ cm. The slabs were in the water while measuring from the dry face and put on a metal plate while measuring on the wet face.

5.2.4.d Reference results

The humidity sensors were measured the same time when we did the NDT during the imbibition. The results of the sensors give us the variation of relative humidity along with the height as a function of time. Then the saturation degree or water content can be calculated by adsorption isotherm curves [Thiery et al., 2007a; Villain, 2012]. Besides, we have a cylindrical sample to be measured by gammadensimetry. These two methods were used as the reference methods.

The results of gammadensimetry can be seen in figure 5.7. The height of the sample at 0

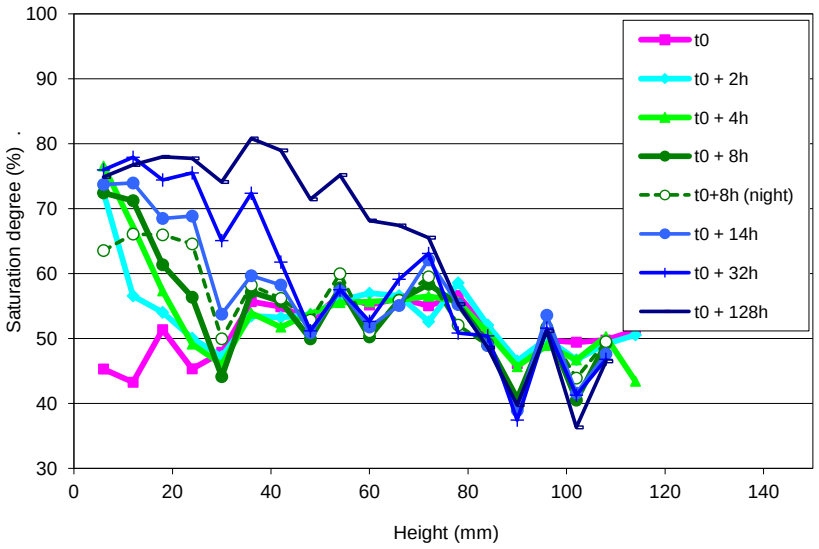

Figure 5.7: Evolution of saturation degree of concrete B1 on function of imbibition time obtained by gammadensimetry

mm is the face put in the water for imbibition. From the curve at T0, we can find that the water content at the two ends of the sample is a bit lower than in the middle. After the imbibition starts, the water front keeps increasing during the first 128 h. However, the saturation degree of the bottom is just between 70% and 80%, instead of getting saturated.

Figure 5.8 gives the results obtained by the humidity sensors from the 2 campaigns of imbibition. In the first campaign, the B face was contacted with the water. We can see from the results that the first sensor was placed 30 mm from the bottom. Its saturation degree keeps increasing during the 32 hours of imbibition. From the second sensor, we can find after 32 hours, the water still has not reached the height of 60 mm, 90 mm from the bottom. The results of the second campaign give the similar evolution, where the H face was contacted with the water. Since we have processed longer imbibition time, we can find the bottom of the slab is saturated after 128 hours. However, the water front is still below 60 mm.

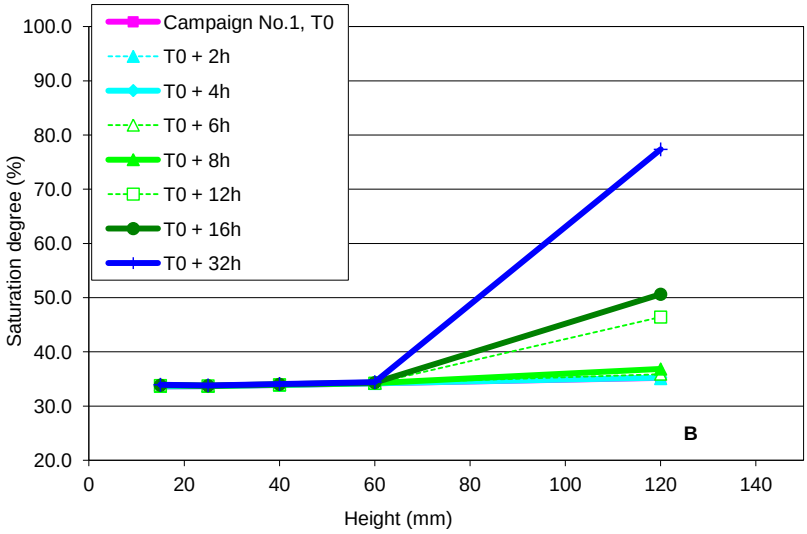

(a) Campaign No.1

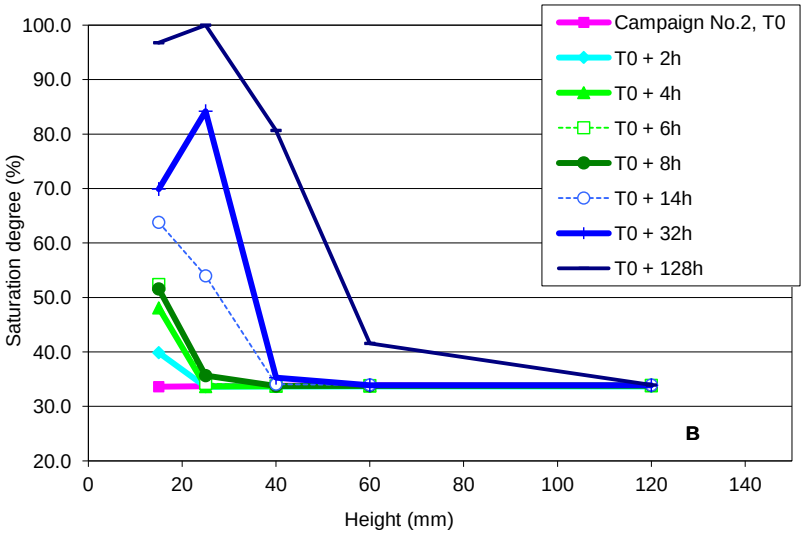

(b) Campaign No.2

Figure 5.8: Evolution of saturation degree of concrete B1 on function of imbibition time obtained by humidity sensors: (a) campaign No.1; (b) campaign No.2

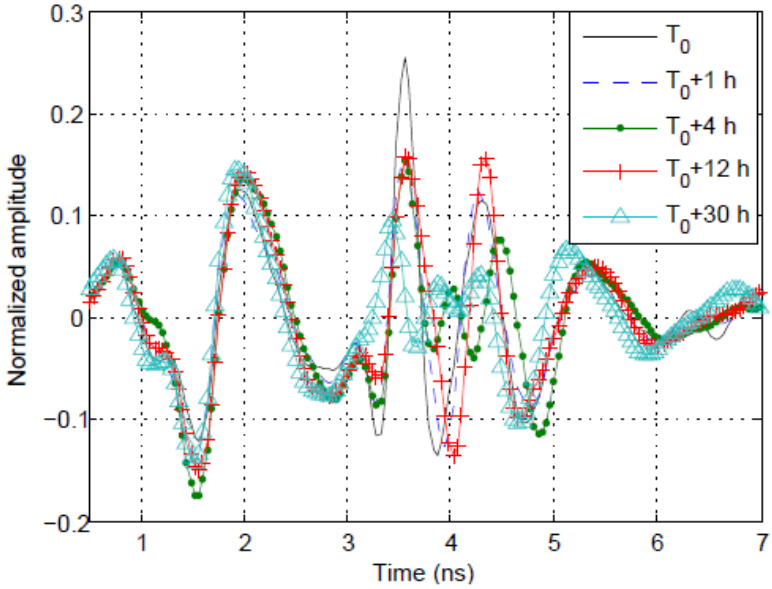

Figure 5.9: Normalized GPR signals at minimum offset X_0 of slab B1-26 from H face (dry face) in 1st campaign of imbibition

5.2.4.e Preview of experimental results

Figures 5.9 and 5.10 are the first results of CMP measurements on the slab B1-26 from the dry face (face H for 1st campaign, face B for 2nd campaign). In figure 5.9, waves are picked from the minimum offset X_0 of each measurement in imbibition No.1. At T_0, the amplitude of RW is obviously higher than other times as the slab is not yet put in water. The amplitude of RW at T_0+30 h decreased a lot, as the slab is supposed to have the most water inside. However, during the first 12 hours of imbibition time, we cannot see any logical evolution of the signals.
The dispersion curves in figure 5.10 (a) do not show satisfying evolution either. From the dispersion curves in figure 5.10 (b), we can see that, the results in imbibition No.2 also failed to show the evolution of the water content.
As the reference methods can see the progress of water penetration during the imbibitions, we believe it is the problem of the GPR measurements. The antennas were not able to detect the variation of water content is probably because of two reason: first, the thickness of the concrete slabs is too much for the 2.6 GHz antennas; second, the dielectric contrast between the concrete and the water is not high enough. Due to the two reasons, the GPR signals were strongly attenuated during the propagation. In this case, we will not conduct any further analysis for the experiments in next chapter.

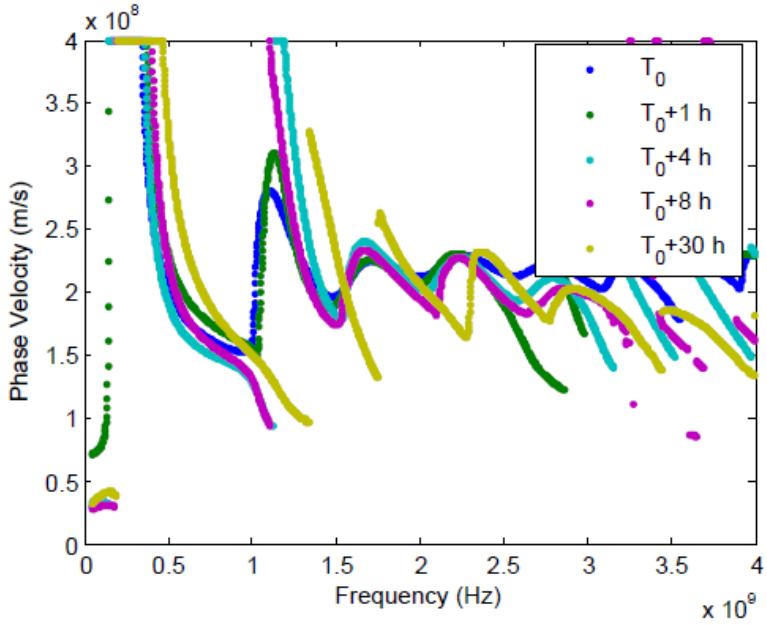

(a) Imbib.1, B1-26-H

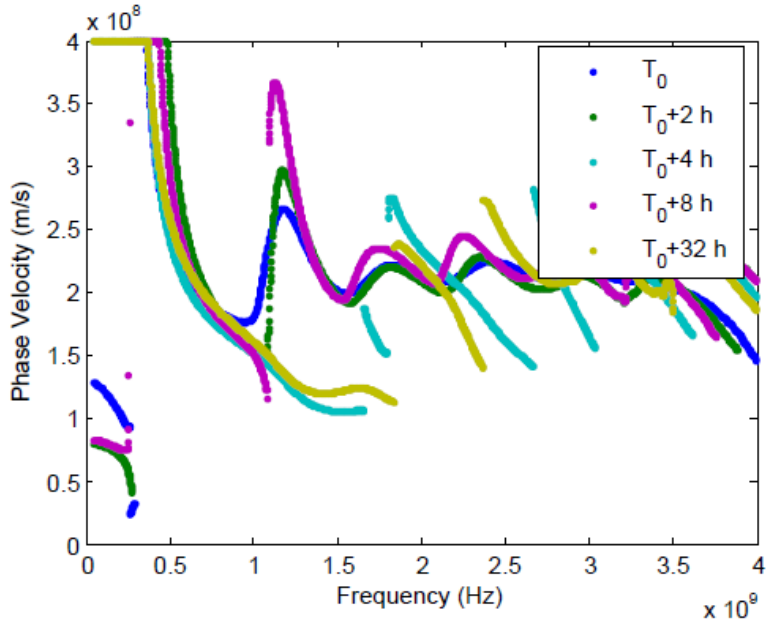

(b) Imbib.2, B1-26-B

Figure 5.10: Dispersion curves of phase velocity of slab B1-26 from the dry side in (a) 1st campaign and (b) 2nd campaign of imbibition

5.3 Planning of Experiments for Project APOS

5.3.1 Objectives

This section will introduce the two campaigns of imbibition experiments for project APOS: first, water imbibition; second, sea water imbibition with chloride content 35 g/L. Two concrete mix designs were used in the experiments. The objective is to monitor the normal water and sea water penetrating into the concrete with combined NDT and to determine the water content gradients by GPR measurements.
We will first introduce the formulation and specimens of the concretes. Then we will introduce the planning of the two campaigns of imbibition. In the end, we will discuss about the reference results from gammadensimetry and decide the data to be analysed in the next chapter.

5.3.2 Concrete formulation

For project APOS, we have two mix designs of concrete (C1 and C3), different from those for EvaDéOS. The two mix designs of concrete are expected to have the same aggregates, porosity (ρ), compression strength (R_c) and the same water to cement ratio (W/C), but with different cements.
We put cement CEM I for C1 and cement CEM III for C3 (types of cement are described in European standard [EN197-1, 2000]), as type CEM III has more ground granulated blastfurnace slag (GGBS), which helps prevent the penetration of chlorides. Table 5.5 shows the formulation parameters and characteristics of concretes C1 and C3 in APOS project.

Table 5.5: Mix designs and characteristics of concretes C1 and C3

Codification	C1	C3
Type of aggregates	Siliceous D_{max} = 22 mm	
Type of cement	CEM I 52.5N CP2 NF	CEM III/A 52.5L CP1 NF
Cement (kg/m^3)	305	260
Sand 0/2 or 0/4 (kg/m^3)	860	860
Gravel 6/10 (kg/m^3)	320	330
Gravel 11/22 (kg/m^3)	760	760
Total water (kg/m^3)	190	177
W/C	0.62	0.68
ρ **accessible to water (%)**	15.9±0.5	15.3±0.2
R_c **after 28 days (MPa)**	36.3±0.9	34.9±0.4
Density (kg/m^3)	2346.3±6.0	2332.4±18.7

5.3.3 Planning of water imbibition program

5.3.3.a Presentation of specimens

The experiments of water imbibition were conducted in the lab of Ifsttar, Nantes. In this campaign, we have tested two slabs (dimension: $450 \times 360 \times 130$ mm^3) without any

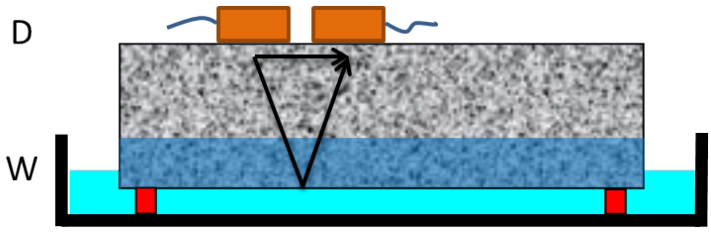

Figure 5.11: CMP measurement on the dry side of a concrete slab in the water imbibition campaign

reinforcement for each concrete. They are coded as C3-1 and C3-3 for concrete C3 and C1-1 and C1-3 for concrete C1. The objective is to monitor the water penetrating into the concrete with combined NDTs and to determine the water content gradient by GPR measurements.
Meanwhile, for each concrete of C1 and C3, we make a core with the dimension of Ø100 × 120 mm for the measuring of Gammadensimetry, as reference.

5.3.3.b Preconditioning of concrete

After making the slabs and curing, we painted the resin on the 4 sides of each slabs to keep straight the direction of imbibition. One night after, the slabs were put in a climate chamber conditioning at $T = 20°C$ and $RH = 70\%$ for 2 months to obtain the homogeneous moisture distribution.
The slabs were first taken out to be weighed and measured by GPR at the initial time T_0, corresponding to the time before the imbibition. Then the slabs were placed simultaneously on plastic supports immersed in container with water at the height 10 ± 2 mm from the slab's bottom.

5.3.3.c Non-destructive tests planning

We started measuring the two slabs C3-1 and C3-3 in April, 2015. After one month's imbibition of the C3 slabs, we start imbibition of C1 slabs. Therefore, we spent 2 months to complete the experiments for the 4 slabs. The time frameworks of the two campaigns are summarized in Table 5.6.
We had three NDTs integrated in the experiments: capacitive probes, resistivity test and GPR. The tests were conducted one by one at each time. Gammadensimetry was conducted with similar time frameworks.

For GPR, the slabs were measured by CMP method with 1.5 GHz antennas. The displacement of the transmitter and the receiver is $\Delta x = 1$ cm at each moving step, with the maximum offset $X_{max} = 28$ cm.

Figure 5.11 is the diagram of one CMP measurement on the dry side, where 'D' means 'dry side' and 'W' means 'wet side'. For measuring the other side, the slab was taken out of the water and put on a metal plate. For the slabs of C3, we measured the dry side twice at each time, marked as D3-1 and D3-3. For the slabs of C1, we measured the dry side and the wet side once at each time, marked as D1-1, D1-3, W1-1 and W1-3.

Table 5.6: Imbibition measuring process of concrete C1 and C3

Time in water	C1	C3
T_0	0	0
T_1	0.5 h	0.5 h
T_2	1 h	1.5 h
T_3	2 h	3.5 h
T_4	4 h	5.5 h
T_5	6 h	7.5 h
T_6	10 h	12.5 h
T_7	14 h	16 h
T_8	30 h	31.5 h
T_9	36 h	38.5 h
T_{10}	7 days	5 days
T_{11}	11 days	8 days
T_{12}	13 days	12 days
T_{13}	17 days	15 days
T_{14}	30 days	40 days

5.3.3.d Reference results

The density variation curves, as a function of imbibition time for concretes C1 and C3, are shown in figures 5.12 and 5.13, measured by gammadensimetry. This variation corresponds to the variation of saturation degree S. We have just got the measurements in the first 5 days at the moment. But we can see a good evolution of the density. The increment near the top surface ($h > 90$ mm) may be because of the error in the gammadensimetry equipment.

Since $\varepsilon' \propto W$ [Klysz and Balayssac, 2007; Villain et al., 2010], and $W = \phi S$ (§2.2.3), the results of gammadensimetry predict the variation tendency of dielectric constant ε'. It therefore can be used as a reference for GPR inversion results.

In the two figures, the height 0 mm corresponds to the surface contacted with the water. The water penetrates very fast into C1. The water content keeps growing during the first 124 hours. However, for C3, we cannot see very obvious variation of water content during 122 hours of imbibition. Besides, we observe an error near the top surface of the sample. Some curves go up after 90 mm where they are expected to be zero, which questions the validity of the last sensors.

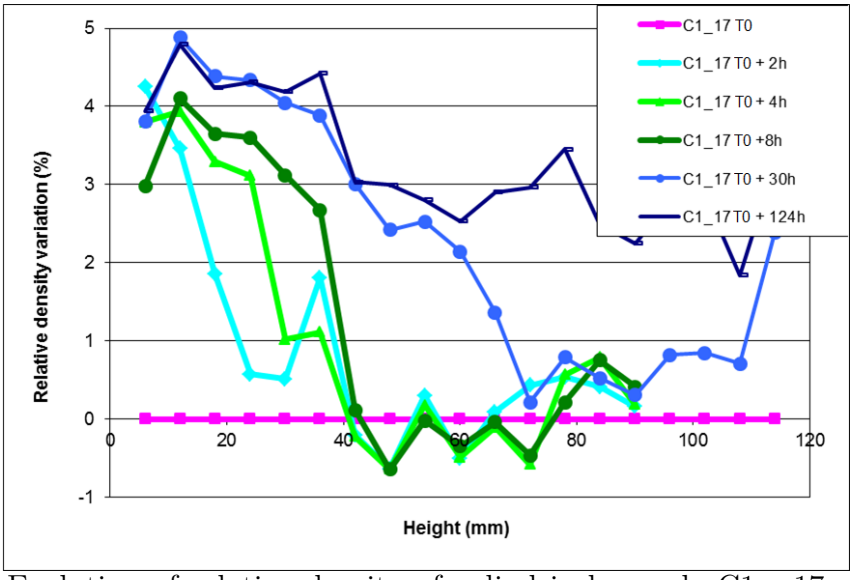

Figure 5.12: Evolution of relative density of cylindrical sample C1 - 17 as function of imbibition time obtained by gammadensimetry

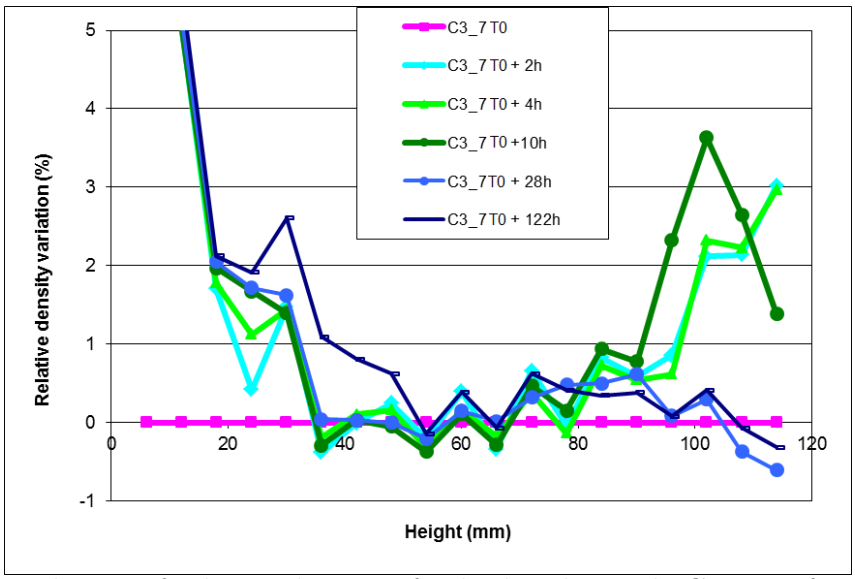

Figure 5.13: Evolution of relative density of cylindrical sample C3 -7 as function of imbibition time obtained by gammadensimetry

5.3.3.e Preview of experimental results

To verify the impacts of the water penetration on the propagation velocity of EM waves, we have calculated the dispersion curves of phase velocity from the GPR data.
Figure 5.14 shows the dispersion curves of the slabs D3-1 and D3-3. We observe a leftward movement from T_0 to T_0+30 days. However, there is no obvious variation during the imbibition time. This can be because of two reasons. First, from the results of gammadensimetry (Figure 5.13), we find that the water penetration is rather slow. In this case, it is difficult for GPR to detect such small variation of water content. Second, the measurements were conducted while the slabs were in the water. The air-concrete-water combination forms a leaky waveguide [van der Kruk and Arcone, 2007] as the water is not a perfect electric reflector. The leakage causes the inaccuracy of the calculations of the phase velocity.

Figure 5.15 shows the dispersion curves of the slab C1-1 (D1-1 and W1-1). The velocity at each mode moves leftward on the frequency band along with the imbibition time. The dispersion curves of the other slab C1-3 in figure 5.16 have the same tendency of movement. This is because as the water content increases in the concrete, the equivalent permittivity of the slab increases. The increment of the permittivity ε'_e leads to the decrease of the cut-off frequency f_{cut} of each propagation mode.
In summary, GPR measurements on the slabs of C3 cannot be used to analyse the imbibition of water since the evolution of dispersion curves is not clear. On the contrary, the measurements on the slabs of C1 give a good evolution of phase velocity. We will conduct more analysis on C1 with the GPR signals and the water front depth, which can be inverted from the phase velocity of the guided waves.

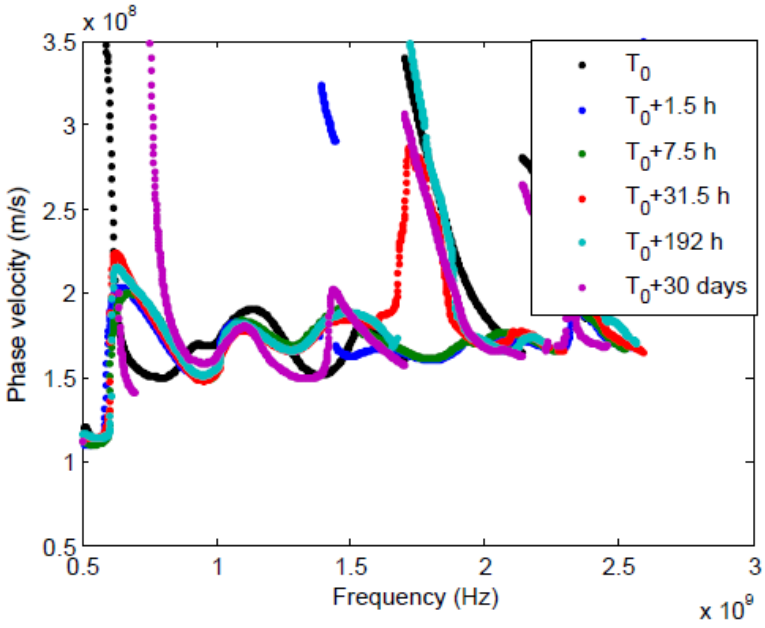

(a) D3-1

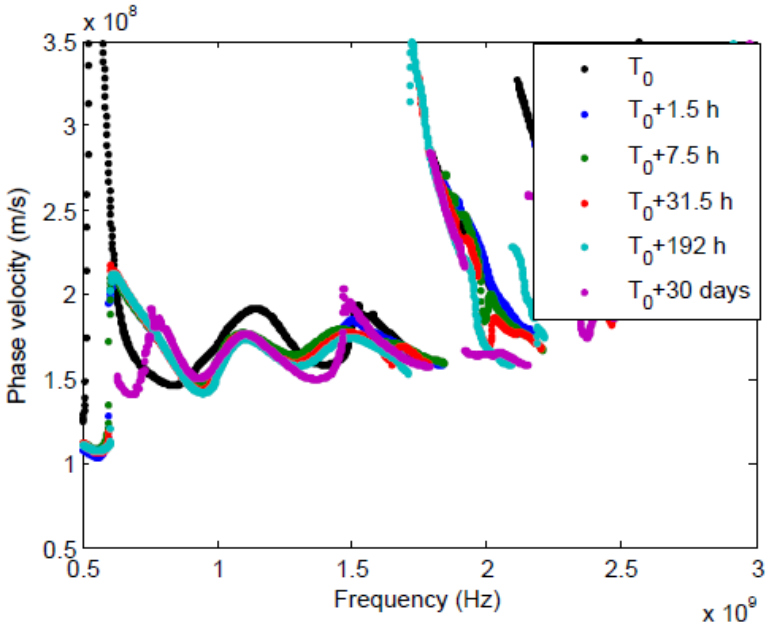

(b) D3-3

Figure 5.14: Dispersion curves derived from CMP measurements of slabs (a) D3-1 and (b) D3-3

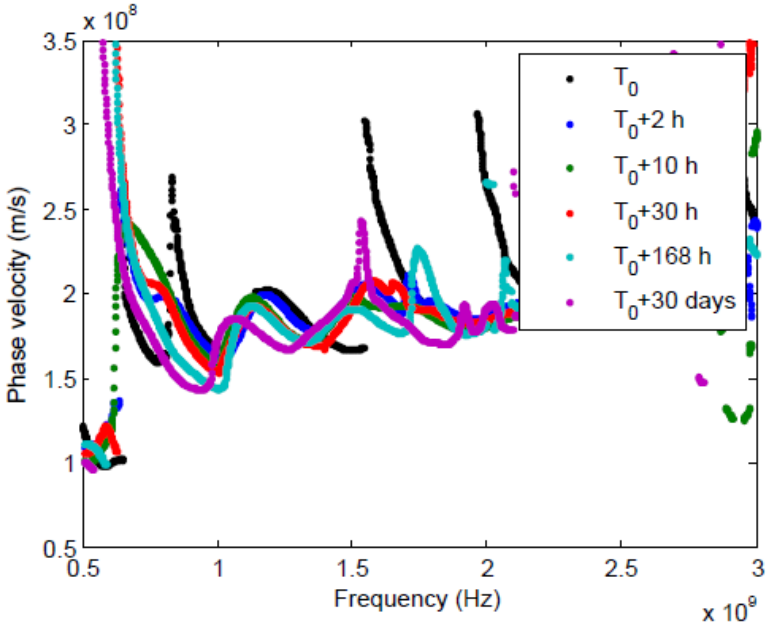

(a) D1-1

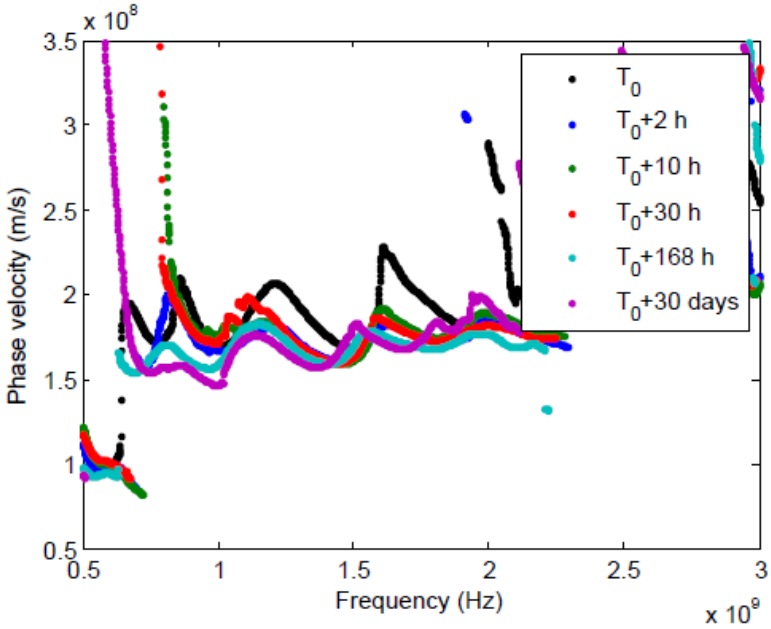

(b) W1-1

Figure 5.15: Dispersion curves derived from CMP measurements of slab C1-1 from (a) dry side and (b) wet side

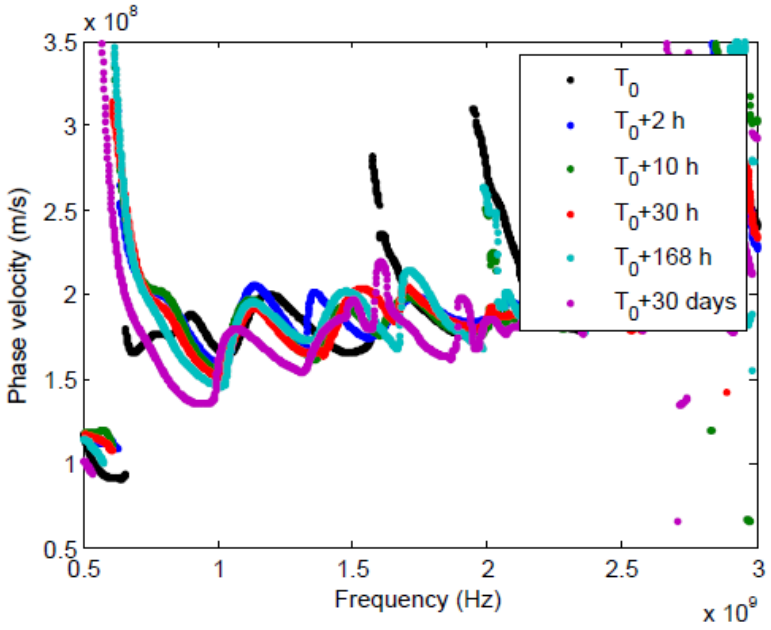

(a) D1-3

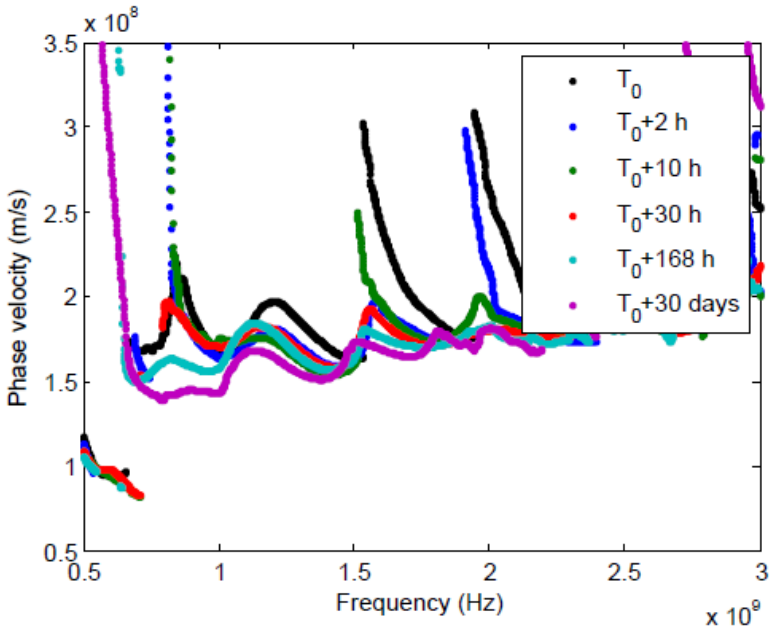

(b) W1-3

Figure 5.16: Dispersion curves derived from CMP measurements of slab C1-3 from (a) dry side and (b) wet side

Table 5.7: Concrete slabs in imbibition campaign No.1

Slab	Name of concrete	Reinforcement	Solution of imbibition
03-NS	C3	Non	Chloride solution
04-CS	C3	Carbon steel	Chloride solution
05-CS	C3	Carbon steel	Chloride solution
07-CW	C3	Carbon steel	Water
13-NS	C1	Non	Chloride solution
14-CS	C1	Carbon steel	Chloride solution
15-CS	C1	Carbon steel	Chloride solution
17-CW	C1	Carbon steel	Water

5.3.4 Planning of sea water imbibition program

5.3.4.a Presentation of specimens

In the sea water imbibition experiments, we have selected 8 slabs (dimension: $900 \times 700 \times 130$ mm^3) out of 16 slabs to do the GPR tests. Table 5.7 shows the difference among the 8 slabs. So slabs 03 and 13 have no reinforcements inside. Slabs 07 and 17 have no chlorides in the water. Slabs 04, 05, 14 and 15 are in the same condition of different concretes.
The codification is recalled below:

- N: non-reinforced
- C: reinforced with carbon steel
- S: sea water (chloride solution)
- W: water

For the 6 slabs with reinforcements, the distribution of iron rebars are shown in figure 5.17.

5.3.4.b Preconditioning of concrete

After casting in December 2013, the moulds were kept for 5 days when the cure took place in the laboratory in uncontrolled moisture condition. The slabs were left for curing until February 2014. Then, enough resin has been applied on the 4 sides of each slabs to keep straight the direction of imbibition. The slabs were put in a big hall with numerous fans to accelerate drying.
The measurements of GPR, gammadensimetry and initial weighing were all carried out in accordance with T_0 corresponding to the time before the slabs were put in the water. The slabs were then placed simultaneously on plastic supports immersed in container with water (or sea water) at the height 10 ± 2 mm from the slab's bottom.

5.3.4.c Non-destructive tests planning

The campaign of sea water imbibition tests was conducted in Cerema (Direction Territoriale Ouest - St. Brieuc) from September 2014 to December 2014. There were totally

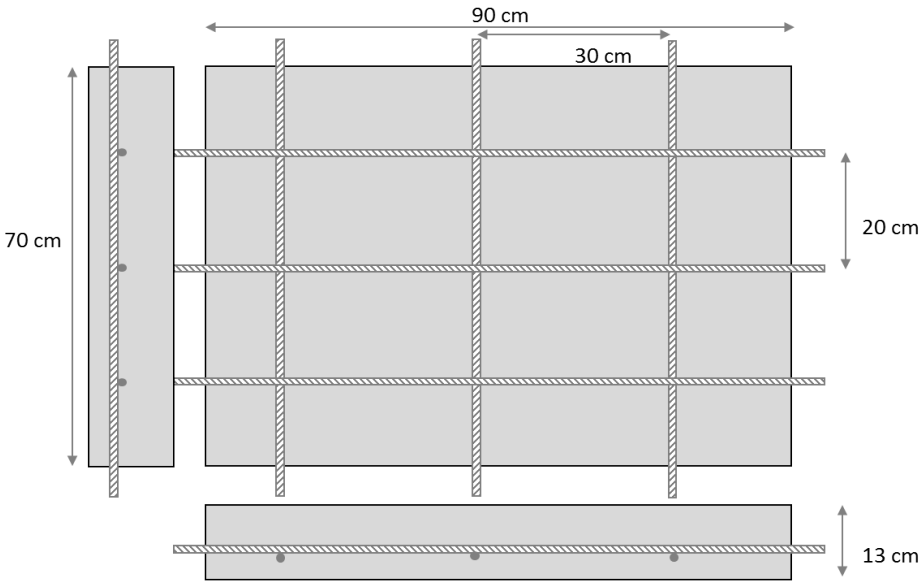

Figure 5.17: Distribution of reinforcements for slabs 04, 05, 07, 14, 15 and 17

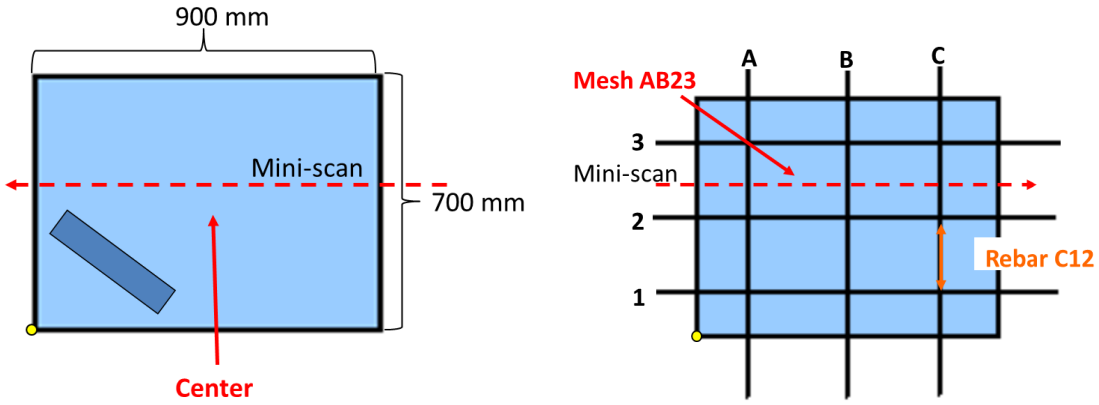

(a) slabs without reinforcement (b) slabs with reinforcement

Figure 5.18: CMP measurement locations and horizontal scan on slabs of imbibition in St. Brieuc: (a) slabs without reinforcement; (b) slabs with reinforcement

16 slabs of two concretes to be tested by different labs. So several ND techniques were employed in the tests, including resistivity test [Marie-Victoire et al., 2015], capacitive probes [Fares et al., 2015], ultrasonic test, GPR, etc. In this campaign, we measured at only 8 time points: T_0, $T_1 = T_0 + 1$ h, $T_2 = T_0 + 4$ h, $T_3 = T_0 + 20$ h, $T_4 = T_0 + 44$ h, $T_5 = T_0 + 168$ h, $T_6 = T_0 + 1$ month, $T_7 = T_0 + 4$ months, since it took time to complete measurements for all the partners. Still, T_0 refers to the time before the slabs were put in the water.

Eight slabs were selected to do the tests with GPR, as we have mentioned before. Before each measuring time, the slabs were taken out of the water to be put on steel plates (first put on the wet side, then on the dry side). Figure 5.18 shows the measurements of GPR on the slabs. The solid arrows point the locations of CMP measurement and the dashed arrows point out the direction to do the horizontal B-scan on the dry surface. Though we have no reinforcements in slabs 3 and 13, there are embedded probes for resistivity test on the left-down corner (Figure 5.18(a)).

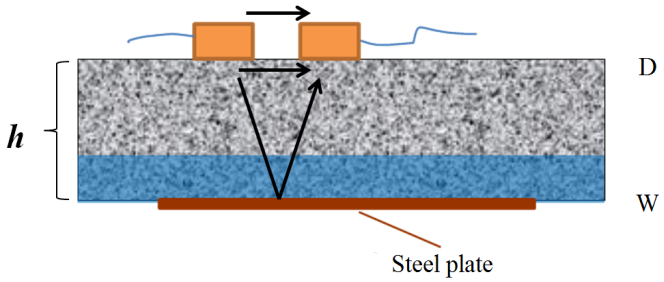

Figure 5.19: CMP measurement on the dry side of a concrete slab in the sea water imbibition campaign

To realize the measurements, two equipments of GPR are used during this campaign. First, the SIR - 3000 system from GSSI equipped with 2.6 GHz antennas is used to do the CMP measurements. The time window is 10 ns. The transmitter and receiver are moving from the middle to the two ends of the location with the step $\Delta x = 5$ mm. The maximum offset is $X_{max} = 14$ cm to reduce the impact of the reinforcement and the embedded probes in the concrete. Second, a mini structure-scan GPR with 2.6 GHz antennas united in one box was used to do a profile scan. The direction is shown in figure 5.18 as the dashed arrows.
Figure 5.19 is the diagram of one CMP measurement on the dry side, where 'D' means 'dry side' and 'W' means 'wet side'. We have also measured the wet side for slabs 3, 7, 13 and 17 with the same configuration. The compared results will be discussed in next chapter.

5.3.4.d Reference results

The gammadensimetry results of water imbibition in concrete C1 and C3 are shown in figures 5.12 and 5.13. The method gammadensimetry is only able to monitor the variation of water content gradient inside concrete. It cannot be used to detect the concentration of chlorides. In this case, we actually have reference results for the water front growing, but not for the chlorides penetrating.
A calibration of chloride content will be conducted in the following by EM cell.

5.3.4.e Preview of experimental results

Figures 5.20 and 5.21 give the reflected wave (RW) of GPR pulse response picked from the b-scans of the mini structure scanner at different imbibition times. For all the slabs, we find the same tendency of variation: the amplitude decreases and the travel time increases along with the imbibition time. This tendency verifies the impacts of the water and chloride on EM waves with the central frequency 2.6 GHz. Compare the signals of the two concretes at T_0, the amplitudes of RW from C3 are generally higher than those from C1. That is to say, concrete C3 at T_0 causes smaller attenuation to EM waves. Further analysis of the amplitudes will be presented in Chapter 6.

The measurements on slabs 03-NS and 13-NS are relatively more representative to the dielectric properties of the concretes, because they have no effects of reinforcement. Figures 5.22 and 5.23 are the dispersion curves derived from CMP measurements on slabs 03-NS and 13-NS from the two sides. The propagation modes are not well isolated in the figures since the response signals were not completely sampled due to the limitation

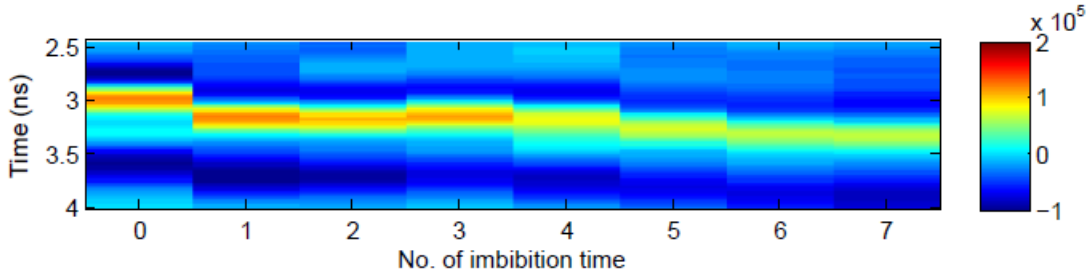

(a) D03

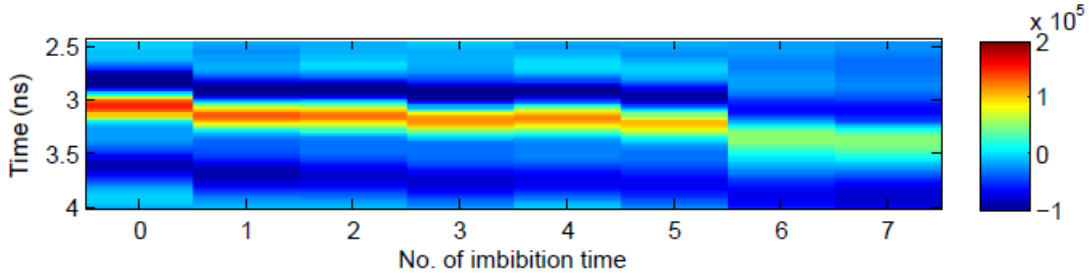

(b) D04

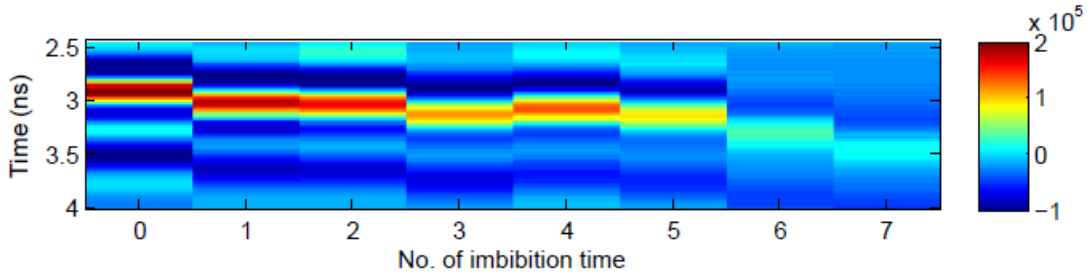

(c) D05

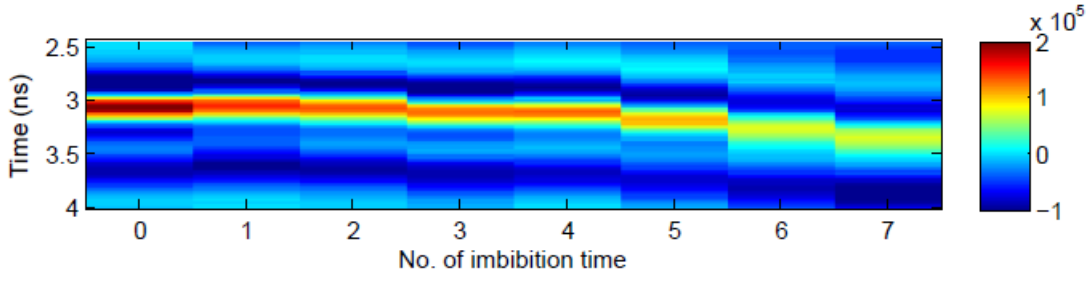

(d) D07

Figure 5.20: RW of GPR pulse response from the mini scanner on the concrete slabs of C3 before and during imbibition at 8 different test times: T_0 to T_7 for slabs (a) D03, (b) D04, (c) D05 and (d) D07

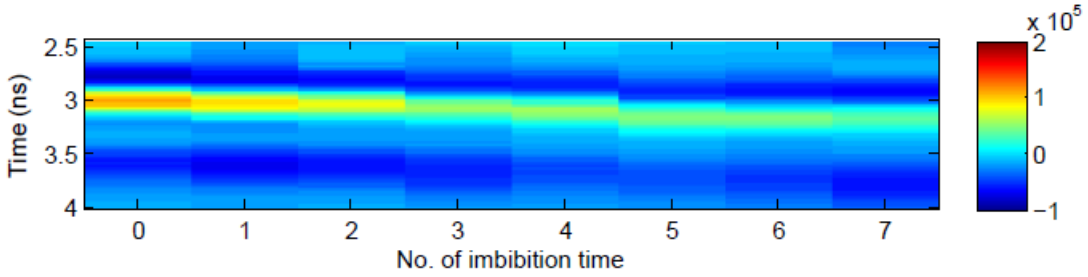

(a) D13

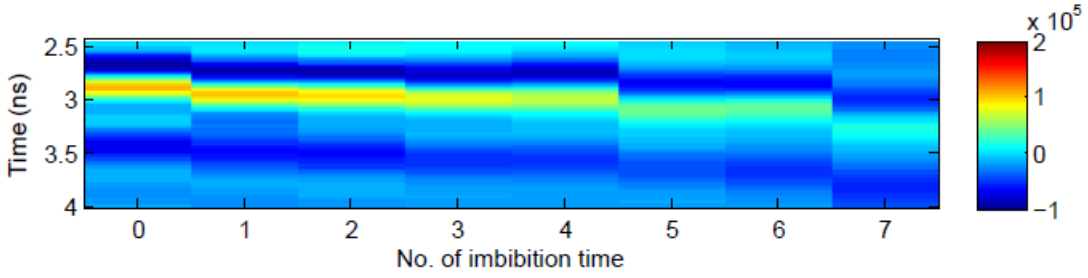

(b) D14

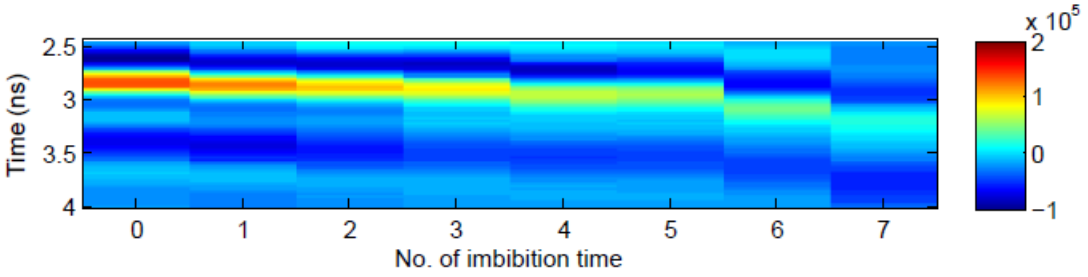

(c) D15

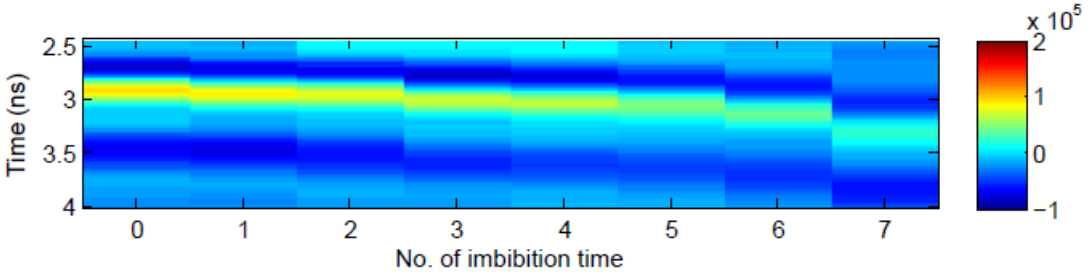

(d) D17

Figure 5.21: RW of GPR pulse response from the mini scanner on the concrete slabs of C1 before and during imbibition at 8 different test times: T_0 to T_7 for slabs (a) D13, (b) D14, (c) D15 and (d) D17

of X_{max}. However, we still observe some logical evolution of the curves according to the imbibition time; for example, modes between [1.5 - 2.3 GHz] for D03, mode between [2 - 2.5 GHz] for D13 and mode around 1.5 GHz for W13. When we test from the wet side, as the first layer has higher permittivity than the second layer, some waves will probably be trapped in the first layer. This leads to a bias of the phase velocity approximation of the waves propagating in the whole slab. That is the reason why the dispersion curves obtained from the dry side seem to be better than those from the wet side. In next chapter, to get more accurate inversion results, we will apply the WG inversion only to the measurements from the dry side.

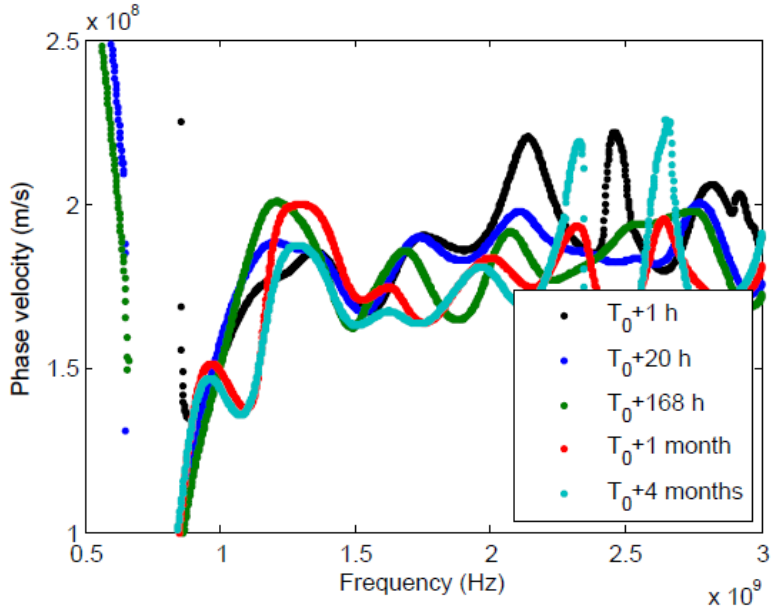

(a) D03

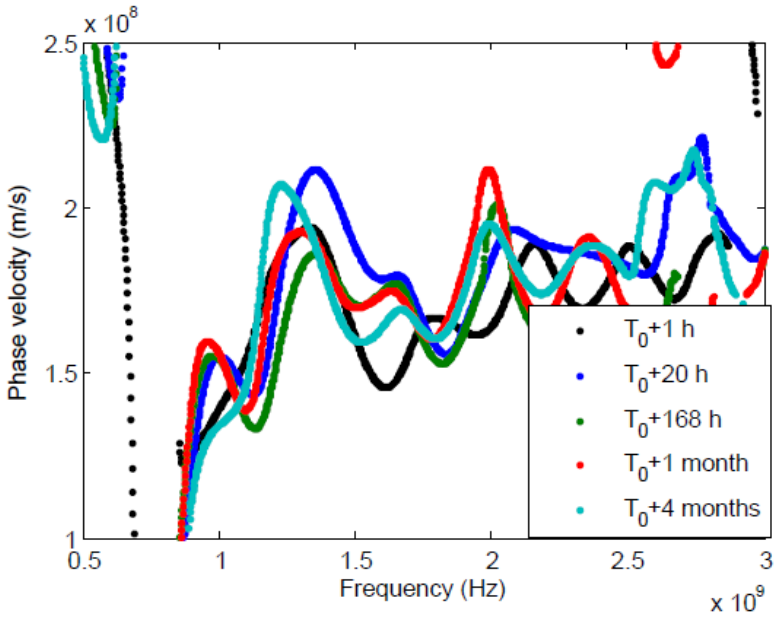

(b) W03

Figure 5.22: Dispersion curves derived from CMP measurements of slab 03-NS from (a) dry side and (b) wet side

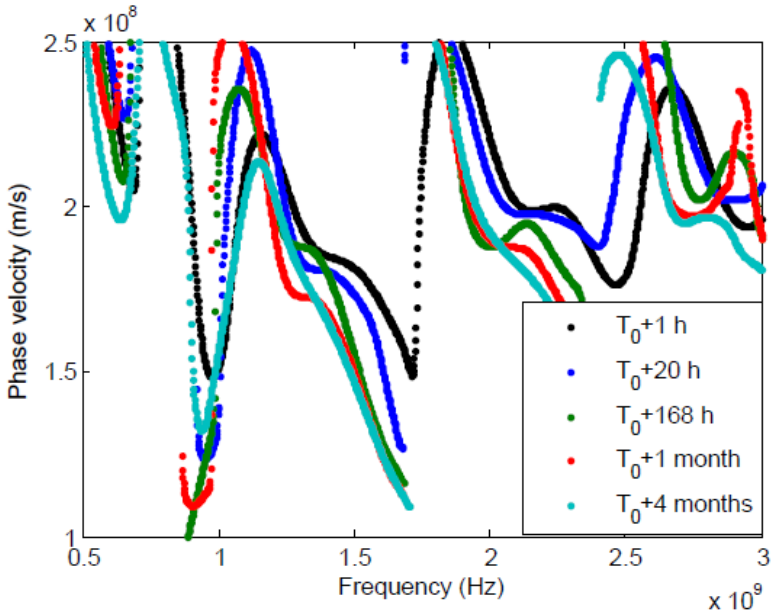

(a) D13

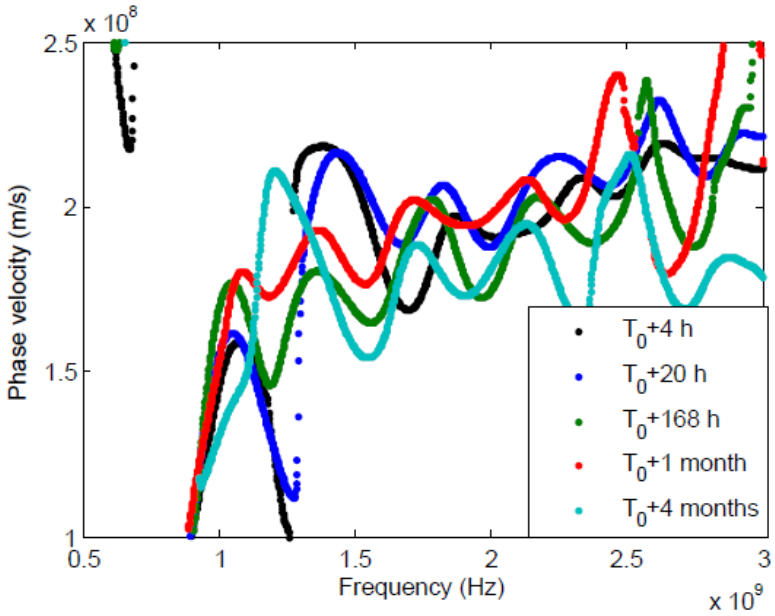

(b) W13

Figure 5.23: Dispersion curves derived from CMP measurements of slab 13-NS from (a) dry side and (b) wet side

5.4 Calibration Using EM Cell

After each campaign of experiments, some cylindrical samples are taken out of the concretes to be measured by EM cell (presented in §2.4.4) as a calibration. The aim is to get relationships between the NDT observables (e.g. permittivity for GPR) and the durability indicators (e.g. water content or chloride content) [Villain et al., 2014]. The results of EM cell are extrapolated from [50 - 600 MHz] to [33 - 4000 MHz] using Jonscher's model.

5.4.1 Project EvaDéOS

5.4.1.a Specimens, preconditioning and measurements

For the slabs of EvaDéOS project, we have 4 cores taken from the non-carbonated slabs, named B1-1, B1-2, B1-3 and B1-4. The dimension of the cores is Ø75 × 70 mm.
All the cores were controlled under 3 different saturation degrees S. To obtain homogeneous moisture distribution, the following protocol was conducted:

- First, all the samples were saturated with water in a vacuum chamber [AFPC-AFREM, 1997] to reach $S = 100\%$.

- Second, all the samples were put in a climatic chamber at $RH = 75\%$ and $T = 20°C$ until a constant mass was reached.

- Third, to obtain S at round 85%, all the samples scaled in aluminium foils were put in an oven at $T = 40°C$ for 1 month to homogenize the moisture distribution according to the protocol of Parrott [Parrott, 1994; Villain et al., 2014].

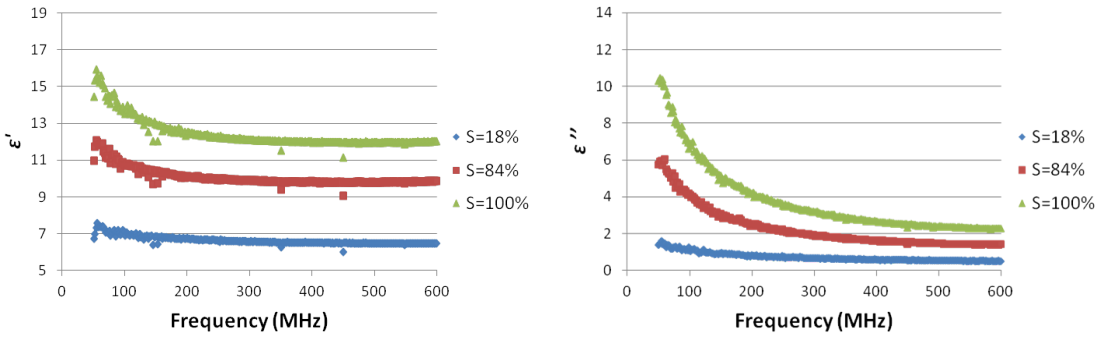

(a) Real part (b) Imaginary part

Figure 5.24: Frequency dependent permittivity of sample B1-1 measured by EM cell: (a) real part (b) imaginary part

Figure 5.24 is an example of the results obtained by EM cell. We have similar tendency of curves for other cores.
The measuring frequency band of EM cell is [50 - 1600 MHz]. However, the permittivity values are usually not available at high frequencies near 1 GHz due to the resonance effect. To calibrate the results of the other NDTs, we need to extrapolate the data to a wider bandwidth.

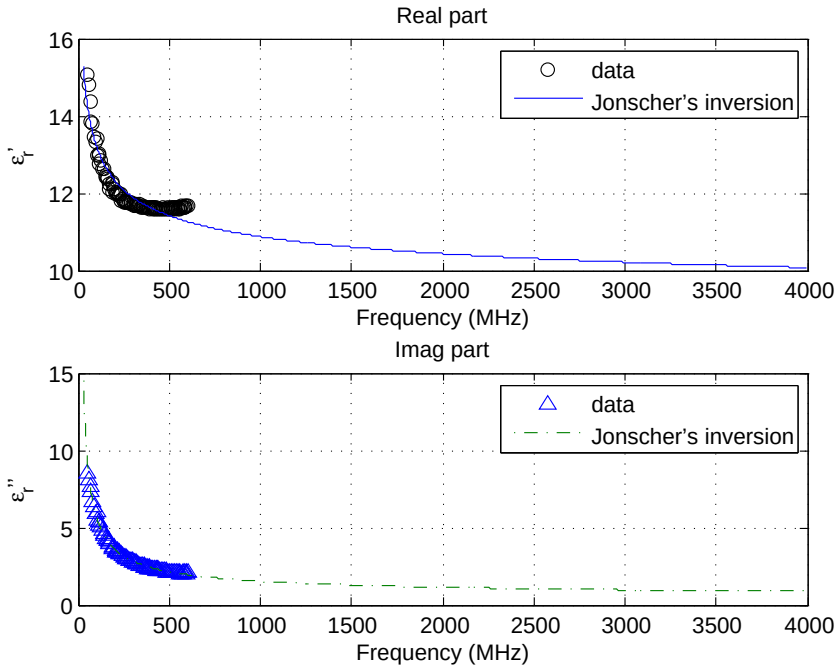

Figure 5.25: Fitting of the real and imaginary parts of relative permittivity for concrete B1-4 at S=100%

5.4.1.b Extrapolated results with Jonscher's model

We have extrapolated the data of EM cell to a wider frequency band: 33 MHz for capacitive probes; 1 GHz and 2 GHz for GPR. Using Jonscher's model, the fitting process is describe in §3.3.3. Figure 5.25 is a comparison of the complex relative permittivity between the selected data and the extrapolated curves.
Table 5.8 summarizes the fitting results with Jonscher's model of 4 cores of concrete B1 in 3 different saturation degrees S. In this table, χ_r is the value of χ' under a reference frequency, n is the dispersion index and $0 < n < 1$, ε_∞ is the instantaneous dielectric response, σ_{dc} is DC conductivity and η is the average relative error as determined in §3.3.3. From the results, we can see the conductivity σ_{dc} increases as the saturation degree increases. It is the same for the permittivity at high frequency ε_∞. However, we find that σ_{dc} decreases for B1-1 as the saturation degree increases. This may be because this specimen was not well conditioned.

Figure 5.26 shows the extrapolated dielectric constants ε' at 1 GHz and 2 GHz of each concrete sample varying along with the saturation degree. The permittivity varies very slowly at high frequencies above 1 GHz, so the values of ε' at 2 GHz are very close to those at 1 GHz. For concrete B1, the dielectric constants at 1 GHz and 2 GHz show very good linear relationship with saturation degree, except for B1-1. The loss factor ε'' have the same linear relationship with saturation degree. Since it is not yet employed in our methods, it is not presented here.
The permittivity at 33 MHz is more sensitive to the change of saturation degree that the permittivity over 1 GHz. This frequency dependency is due to the dispersion of saturated concrete as explained in §3.3.1. The discussion of results at 33 MHz corresponds to the work of Fares [Fares, 2015].

Table 5.8: Jonscher's parameters and fitting results of 4 cores of concrete B1

Concrete	S (%)	χ_r	n	ε_∞	σ_{dc} (S/m)	η (%)
B1-1	18	0.86	0.71	5.38	0.0016	0.58
B1-2	17	0.94	0.70	5.48	0.0017	0.60
B1-3	22	1.00	0.73	5.39	0.0019	0.63
B1-4	21	0.97	0.70	5.53	0.0018	0.63
B1-1	84	1.54	0.66	7.67	0.009	1.05
B1-2	83	4.63	0.88	5.49	0.013	1.25
B1-3	80	1.89	0.69	7.68	0.012	1.24
B1-4	86	6.48	0.91	3.91	0.013	1.22
B1-1	100	1.39	0.56	7.53	0.006	1.38
B1-2	100	3.23	0.69	9.16	0.021	1.71
B1-3	100	3.31	0.73	8.55	0.019	1.76
B1-4	100	3.09	0.70	8.53	0.018	1.69

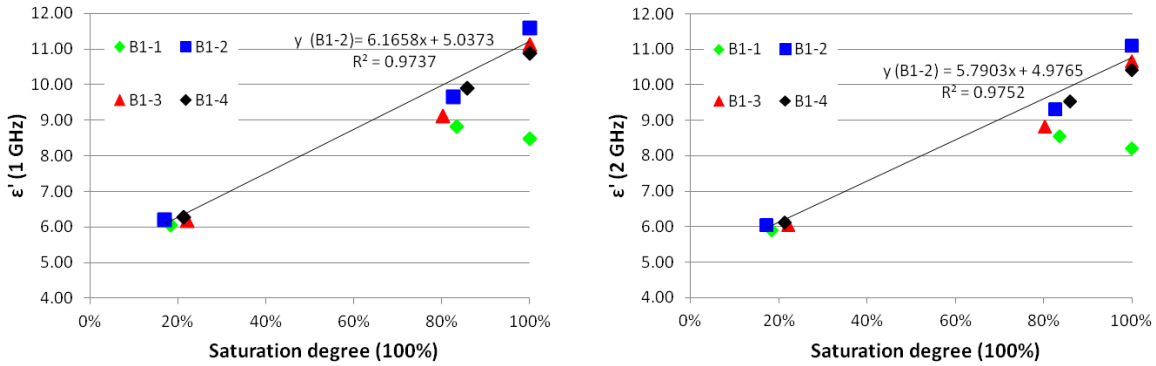

(a) 1 GHz (b) 2 GHz

Figure 5.26: Frequency dependent dielectric constant ε' of concrete B1 as a function of saturation degree: (a) at 1 GHz (b) at 2 GHz

5.4.2 Project APOS

5.4.2.a Specimens, preconditioning and measurements

For the calibration of water content, we have taken 3 samples out of each concrete with the dimension Ø75 × 70 mm. However, one of the sample for C3 was not properly cut. So we have only 5 cores: C1-1, C1-2, C1-3, C3-1 and C3-3.
For the calibration of chloride content, we have taken 6 samples out of each concrete with the same dimension as before. The samples are coded as: C71, C72, C73, C74, C75 and C76 for C3; C171, C172, C173, C174, C175 and C176 for C3.

Preconditioning of water content All the cores were controlled under 3 different saturation degrees S with homogeneous moisture distribution. Two of them were obtained by putting the samples into a chamber with the relative humidity $RH = 75\%$ or 100% at

$T = 20°C$ for one month. The saturation degree was calculated by equation (2.2). The third one was obtained by putting certain amount of water in the sample and cover it with aluminium foil for one month, in order to obtain the saturation degree S at round 85%. It is actually the same process as the conditioning of the cores for EvaDéOS project.

Preconditioning of chloride content The dried cores were put into solutions, submerged up to 20 mm from the bottom, with different chloride contents (C71, C72, C171, C172: 15 g/L; C73, C74, C173, C174: 35 g/L; C75, C76, C175, C176: 90 g/L NaCl). The cores were put in solutions until a constant mass was reached.

5.4.2.b Extrapolated results with Jonscher's model

Figure 5.27 shows the extrapolated dielectric constants ε' at 1 GHz and 2 GHz of each concrete sample of C1 and C3 varying along with the saturation degree. The permittivity varies very slowly at high frequencies above 1 GHz, so the values of ε' at 2 GHz are very close to those at 1 GHz. However, we observe that at $S = 100\%$, the ε' decreases faster from 1 GHz to 2 GHz. That is because as the water content increases, the dispersion of concrete increases. Generally speaking, the dielectric constants at 1 GHz and 2 GHz show very good linear relationship with saturation degree for both C1 and C3.
Figure 5.28 shows the extrapolated complex relative permittivity ε' and ε'' at 1 GHz along with the chloride content. The results of the loss factor ε'' are presented here because it is very sensitive to the chlorides. Though it is not concerned as observables in our study, it can be a prospective for our future research on the evaluation of chloride content. Each point of value is an average of the values from two concrete samples. For concrete C1, both the ε' and ε'' have the same linear relationship with chloride content. For concrete C3, the samples were probably not well conditioned since the cement CEM III helps prevent the penetration of chlorides. So the results are not so satisfying as the results of C1.

5.4.3 Conclusion

The EM cell is used as a calibration method for the tests in the projects EvaDéOS and APOS. It can provide us the frequency dependent complex permittivity of cylindrical concrete samples in different controlled conditions, including various water contents and chloride contents. Jonscher's model is used to extrapolate the data from [50 - 600 MHz] to [33 - 4000 MHz]. The results shown in this section verified the linear relationship between the permittivity and the water content (or chloride content) of the concrete samples.

5.5 Conclusion

In summary, we mainly talked about 3 parts in this chapter: project EvaDéOS, project EvaDéOS and EM cell. In the first 2 parts, we respectively introduced the objectives of each project, the concrete samples used in the experiments (formulation, dimensions, distribution of samples) and the planning of tests.
The durability monitoring parameters, carbonation depth, water content and chloride content, were concerned in two kinds of experiments. First, EM measurements on unreinforced concrete slabs with different carbonation depths, where the real depths were

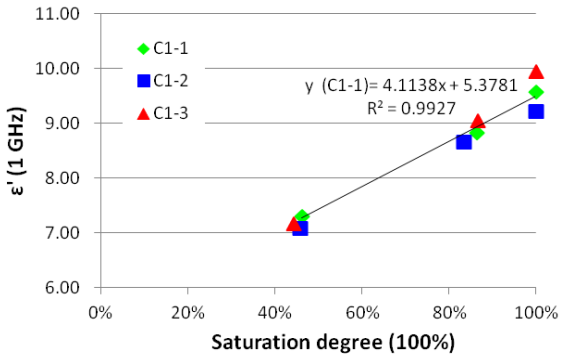

(a) C1 at 1 GHz

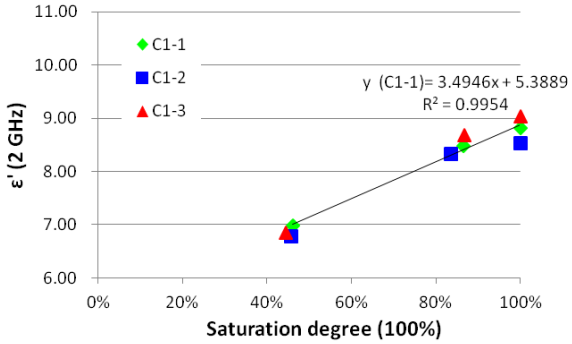

(b) C1 at 2 GHz

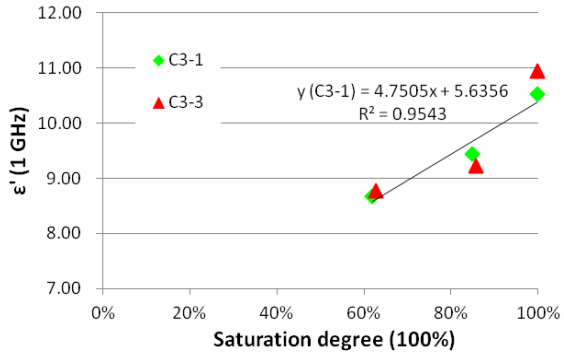

(c) C3 at 1 GHz

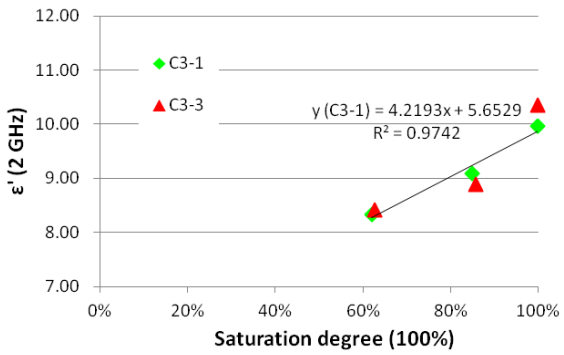

(d) C3 at 2 GHz

Figure 5.27: Frequency dependent dielectric constant ε' of concretes C1 and C3 as a function of saturation degree: (a) C1 at 1 GHz (b) C1 at 2 GHz (c) C3 at 1 GHz (d) C3 at 2 GHz

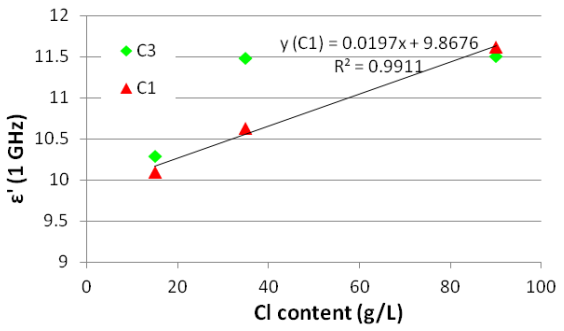

(a) Real part

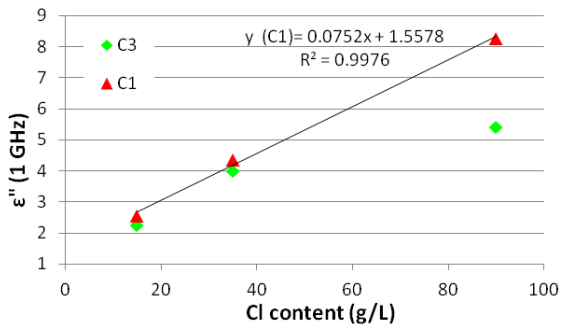

(b) Imaginary part

Figure 5.28: Frequency dependent complex permittivity as a function of chloride content: (a) ε' at 1 GHz (b) ε'' at 1 GHz

measured by destructive method. Second, measurements on reinforce concrete slabs during imbibition process. The penetration of tap water or salty water with chloride concentration 35g/L due to capillary effects was monitored by guided EM waves. Then we introduced the EM ND methods that used in the experiments and their experimental programs. The results of gammadensimetry are used as reference. A preview of the experimental results is also presented in the end of each program.
In the last part, EM cell, obtaining the frequency dependent permittivities of cylindrical samples, was applied for calibration. The results of EM cell showed good correlation between dielectric permittivity and water content (or chloride content).
In Chapter 6, we will analyse the results of B1 with carbonation depths and concretes C1 and C3 within water imbibition by capillarity effect. We will correlate EM observables from the characterization by ND measurements with the 3 durability monitoring parameters.
With the definition of the experimental protocol to monitor and characterize the water status of the two concretes in the study, we are now able to carry out the ND characterization materials whose water conditions are carefully controlled. The characterization of concrete with water content gradient will provided by the inversion of dispersion curves in phase velocity from the EM multi-layer waveguide model.

Chapter 6

Results and analysis of experiments

Contents

6.1 Introduction

This chapter is about the experimental results, data analysis and interpretation that are related to the experiments programmed in Chapter 5. The main objective of the experimental work is to find the relationships between the electromagnetic properties (dielectric permittivity) and durability monitoring parameters (carbonation depth, water content and chloride content) of concrete. Furthermore, to determine the gradients of dielectric constants inside concrete with EM ND methods.

We will process two steps of data analysis in the following of this chapter. First, the variation of amplitudes of GPR pulses will be analysed along with the carbonation depths and the imbibition time. Second, the dielectric and geometrical properties of the concrete slabs will be inverted from the phase velocities of guide EM waves. This step requires the main development of this thesis: the multi-layer waveguide (WG) inversion. With the multi-layer WG model, we are able to estimate the carbonation depth and water (or chloride) content gradient using the phase velocities, quantifying the geometrical dispersion of concrete slabs, derived from GPR CMP data.

6.2 Normalization of Transmitted Signals

As we can find from some former study on the evaluation of water or chloride content, the amplitudes of GPR pulse responses are used as means to quantify the variation of these durability parameters [Laurens et al., 2002; Sbartaï et al., 2006b; Lai et al., 2012]. For carbonation, we can still find very few study on carbonated concrete with the application of GPR. The carbonation of concrete leaves $CaCO_3$ in the pores reducing the porosity of concrete [Villain, 2012]. The water content of saturated concrete will be changed due to the change of porosity, which also has impacts on the dispersion and attenuation of EM waves. Therefore, from the experiments, we want to highlight the effect of carbonation, water and chloride on the GPR signal amplitude.
Since the gain for GPR antennas we defined for the measurements is not always the same, we cannot compare the amplitude of all the signal together directly. The first step of analysing the amplitude is to normalize the received signals, with respect to the air wave. Before and after each measurement, we put the transmitter and receiver at minimum offset in the air and measured 5 times to quantify the temporal drift, as we mentioned in §2.1. Therefore, we are able to pick up the amplitude of the air wave. The way of normalization is defined in the following. Figure 6.1 is an example of the a-scans in the air and on the concrete slab C3-3 for the water imbibition at time T6.

The scan on concrete can be normalized by the following equation:

$$x_n(t) = \frac{x(t)}{A^+ - A^-} \tag{6.1}$$

where $x_n(t)$ is the normalized wavelet in time domain, $A^+ - A^-$ is the peak-to-peak amplitude of the air wave. Then the normalized amplitude of the direct wave (DW) transmitted directly from the transmitter to the receiver through concrete is given by:

$$A_d = \frac{A_d^+ - A_d^-}{A^+ - A^-} \tag{6.2}$$

The normalized amplitude of the reflected wave (RW) from the bottom of the slab can be calculated by:

$$A_r = \frac{A_r^+ - A_r^-}{A^+ - A^-} \tag{6.3}$$

Then, in each section of the analysed results, we will present the normalized peak-to-peak amplitude of DW and RW of each slab.

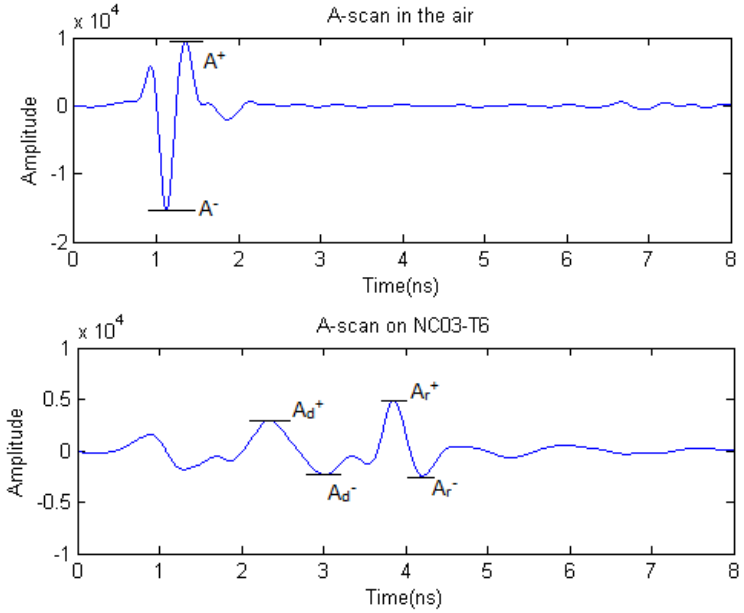

Figure 6.1: Example of a-scans in the air and on concrete slab C3-3

6.3 Characterization of Carbonated Concrete

As we have mentioned in Chapter 5, we have measured 20 slabs with vary carbonation depths: 0 mm, 10 mm, 20 mm and 40 mm, from the project EvaDéOS. The configuration used for GPR is mainly the 4-offset method, which can determine the dielectric constant of the material. In this section, we will first analyse the effects of carbonation on GPR signals by picking the normalized amplitude of signals. Then, we will discuss about the effects of carbonation on dielectric constant of the concrete slabs. The main objective is to highlight the effects of carbonation on EM waves and the dielectric properties of concrete, in order to build some relationships between the carbonation depths and EM observables.

6.3.1 Effects of carbonation on GPR signals

The propagation of EM waves in the carbonated concrete slabs is analysed by the variation of normalized amplitude. The amplitude value was picked to be compare among different concrete slabs and different moisture conditions, as a function of carbonation depth.

Figure 6.2 shows the normalized peak-to-peak amplitude of direct wave for all saturated slabs, and also for the series of slabs B1-N (for Nantes) at two saturation degrees: S=45% and S=100%, as a function of carbonation depth. The real carbonation depths were tested by destructive method in Toulouse and Nantes. Since we have not got the measurements for series B1-A and B1-B, we employ the values from Toulouse for the slabs of series B1-A and B1-B. An extra value exists for series B1-N at S=45% because after the tests on the 5 slabs, we put the slab B1-4-N back into the carbonation chamber until the carbonation depth reached 40 mm. The wavelets are picked from the measurements by 1.5 GHz antennas at the minimum offset.

At both saturation degrees, we can observe the increment of amplitude as the carbonation depth increases. As the carbonation depth increases, the porosity of the slabs decreases.

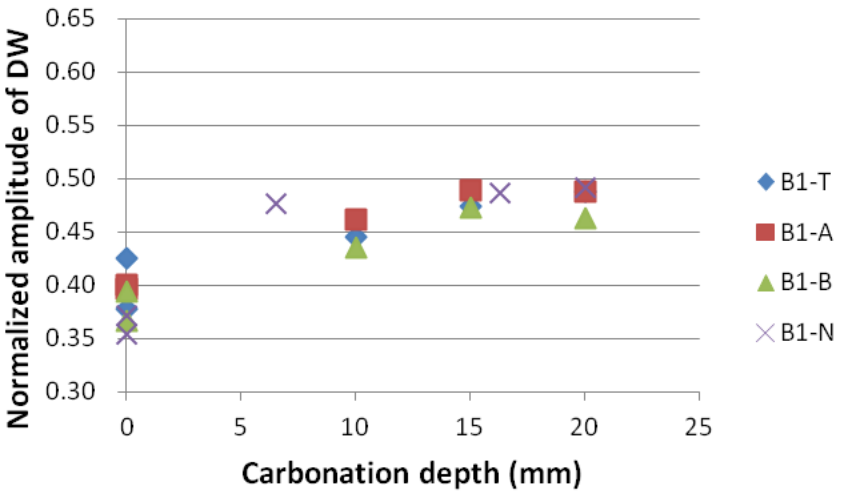

(a) S=100%

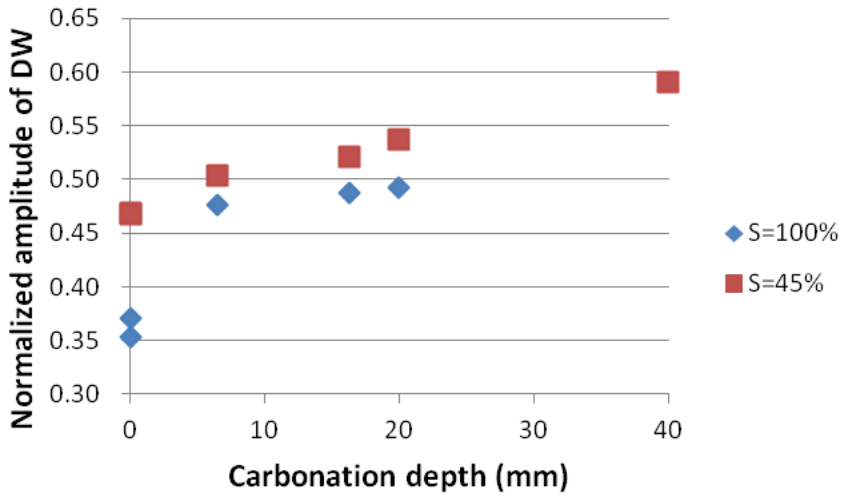

(b) B1-N

Figure 6.2: Normalized amplitude of direct wave as a function of carbonation depth for (a) all saturated slabs and (b) series B1-N at S=45% and S=100%

This leads to the decreasing of water content inside concrete. Moreover, as part of the concrete became carbonated, some $CaCO_3$ was produced by the chemical reactions between carbon dioxide and the ions inside concrete. The interstitial solution in concrete contains less mobile ions. The EM waves are therefore less attenuated when propagating through the concrete.
By comparing the amplitudes between the two saturation degrees ($S = 100\%$ and $S = 45\%$), we find that at the same carbonation depth, the amplitude for $S = 45\%$ is higher than that for $S = 100\%$. Obviously, the concrete slabs with the same carbonation depth has less water content at $S = 45\%$. The concrete slab has less mobile ions because of less amount of solution. The EM waves are therefore less attenuated in the concrete at $S = 45\%$ than in that at $S = 100\%$.

6.3.2 Determination of dielectric constant

The dielectric constant of concrete is linearly related to the variation of water content [Dérobert et al., 2008]. Moreover, the carbonation of concrete at the same degree of saturation reduces the water content inside the concrete. Under this circumstance, we measured the dielectric constant of the concrete slabs with different carbonation depths. The aim is to find some correlations between the carbonation depth and the dielectric constant.
For the slabs of carbonation, the values of dielectric constants are determined by the 4-offset method, as described in §2.4.3. The results are given in figure 6.3. For the saturated slabs, we can find a slight tendency of decreasing of ε' as carbonation depth increases. For series B1-N at 45%, ε' keeps decreasing after the carbonation depth reaches 7 mm. Similar to the effects on amplitude, the decreasing of dielectric constant is caused by the decreasing of water content and the mobile ions inside the concrete.
However, we find the evolution of ε' is not so well correlated with the carbonation depth as the variation of amplitude. This is because the variation of concrete's permittivity in radar frequency range is not very obvious. Furthermore, some interference like heterogeneity of concrete and the edge effects of the slabs or waveguide effects may reduce the accuracy of the test. That is why sometimes we find the value of ε' increases as carbonation depth increases, which is not logical for the effects of carbonation.

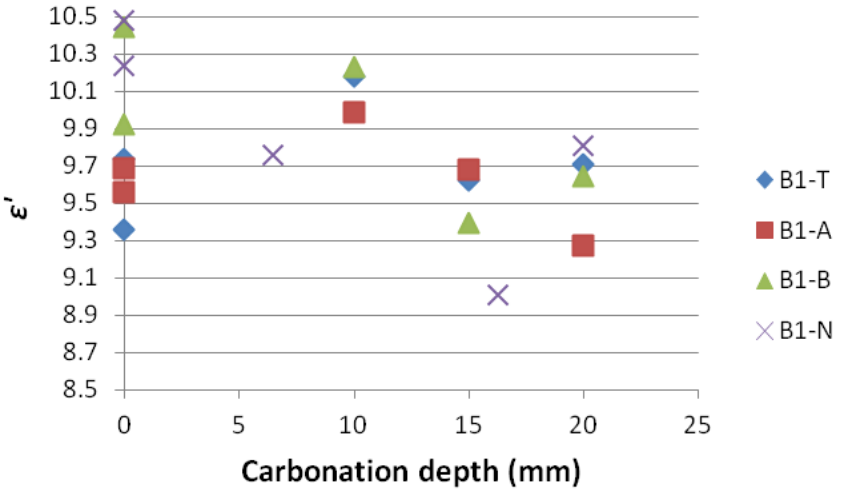

(a) S=100%

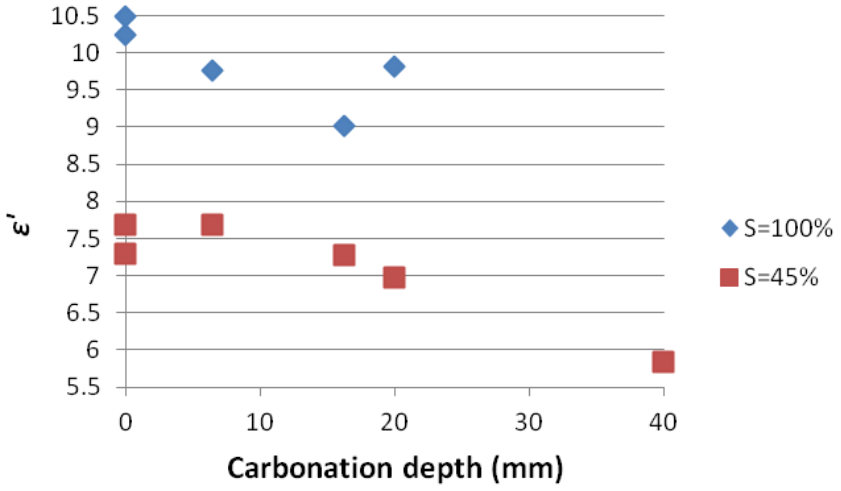

(b) B1-N

Figure 6.3: Dielectric constant ε' as a function of carbonation depth for (a) all saturated slabs and (b) series B1-N at S=45% and S=100%

6.4 Characterization of Concrete with Water Imbibition

The experiments of the water imbibition is aimed at proposing a comprehensive approach of non-destructive evaluation for monitoring the water penetration into concrete. GPR, as one of the main techniques, is used to monitor the penetration depth of water during the imbibition. The effects of imbibition on EM observables, the amplitude and the dielectric constant, will be analysed in this section. The experimental results for analysis are from the water imbibition campaign conducted in Ifsttar, Nantes. We had respectively two slabs for each of the two concretes of APOS project, C1-1, C1-3, C3-1 and C3-3, to be studied in this experimental campaign. For the analysis, we will start by the effects of water content gradients on the amplitude of GPR signals. Then, the water penetration depth during the imbibition will be assessed by the inversion of two-layer WG and $\arctan(x)$ WG models.

6.4.1 Effects of water content gradients on GPR signals

From some former study on the water content with GPR tests, we find the attenuation of EM waves is linearly related to the water content [Laurens et al., 2005; Sbartaï et al., 2006b]. Furthermore, the penetration of water increases the dispersion of concrete. Therefore, monitoring the attenuation and dispersion of GPR signals helps us understand the imbibition process. We therefore start the analysis by picking the EM waves' amplitudes. In the experiments, the 1.5 GHz antennas were used to do the measurements. The advantage of them is the 1.5 GHz antennas couple better to the material and the longer wavelength is less sensitive to the heterogeneity of the concrete. The disadvantage is they can receive more edge effects from the borders of the slabs.
For concrete C3, we have received two slabs C3-1 and C3-3 (dimension: $450 \times 360 \times 130$ mm^3). For each slab, we measured the dry side twice at each time and no measurement on the wet side. Considering the weight of the slabs, we left the slabs in the water while measuring the dry side. The results therefore correspond the average of the two measurements.
Figure 6.4 shows the normalized peak-to-peak amplitudes of the GPR signals collected from the minimum offset of the CMP measurement as a function of time's natural logarithm $\ln(t)$. However, the results seemed to have no correlation with time. This may be because the water penetrates very slowly into the concrete. The instability of the GPR system has greater impacts on the results than the water.
If we compare the amplitude between the dry side of the two slabs, marked as D3-1 and D3-3, the direct waves (DW) of the two slabs are mostly close to each other, since they are the same concrete and same conditioned. However, the first reflected waves (RW1) of D3-3 are obviously higher than D3-1, meaning that the slab C3-1 has higher water content than C3-3, if the two slabs are exactly the same concrete.
Considering the received signals of the two slabs did not show satisfying results, we are not going to do further analysis.
For concrete C1, we have received two slabs C1-1 and C1-3 (dimension: $450 \times 360 \times 130$ mm^3). At each test time, one measurement was done from the dry side while the slab was left in water and one measurement was done from the wet side while the slab was put on a metal plate. Figure 6.5 shows the amplitudes of slabs C1-1 and C1-3, from concrete C1

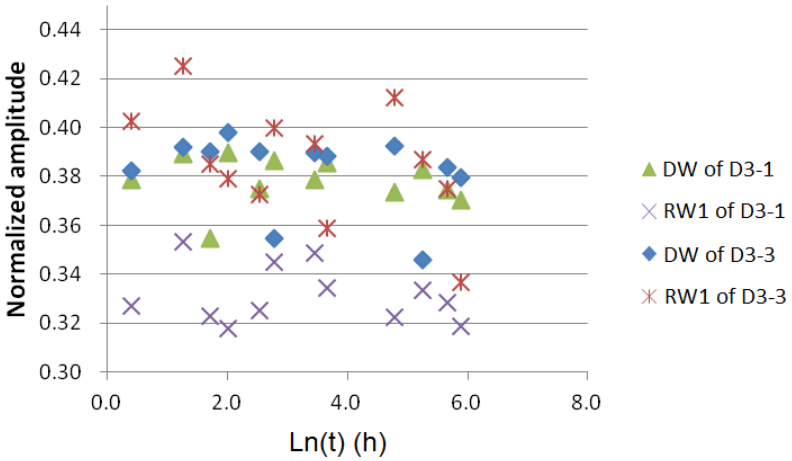

Figure 6.4: Normalized amplitude of direct wave (DW) and first reflected wave (RW1) from dry side of slabs D3-1 and D3-3 as a function of the natural logarithm of imbibition time $\ln(t)$

during 1 month of imbibition, from T_2 to T_{14}. The DW from the dry side (D1-1 and D1-3) looks stable before T_{11} (where $\ln(t) \leq 5.1$, during 1 week's imbibition), where the direct waves are not affected by the penetration of water. The same situation can be found for the RW1s. But after one week, we observe obvious decrease on the amplitudes of DW and RW1. However, the results from the wet side are exactly different. As we can see in figure 6.5 (b), the DW from the wet side keeps decreasing during the first week, but becomes stable after that. We can know the water front is close to the dry surface and do not affect the direct waves in the wet part. However, the RW1 continues decreasing after that, showing that the concrete keeps saturating during the 30 days.
The variation of DW and RW1's amplitudes helps us observe the penetrating of water. We saw a good tendency of variation for the amplitudes of DW and RW1 from C1. However, we failed to see any evolution of the amplitudes from C3. As the two concretes were made with different types of cement, we believe it was the added GGBS in C3 that helped prevent the penetration of water. With the study on the phase velocities of EM waves guided in the concrete slabs, we will be able to monitor the water front depth using waveguide inversion. The results of the inversion will be discussed in the following.

6.4.2 Results of waveguide inversion

During the experiments of water imbibition of the experimental campaign for APOS project in Nantes, we have not got very satisfying GPR data for concrete C3, according to the analysis on GPR signals (figure 6.4). Therefore, we are going to conduct some further analysis with the waveguide inversion only for concrete C1. The process includes the extraction of phase velocity dispersion curve, the selection of frequency range, the definition of initial values for parameters to be inverted and the search of minimum cost function. Two models, two-layer model and $\arctan(x)$ model, will be applied to the inversion.
The measurements were obtained by GPR with 1.5 GHz antennas. One thing to notice is that, we have the CMP measurements on the concrete slabs C1-1 and C1-3 from both dry side and wet side. When we measure on the wet surface, the permittivity of the second

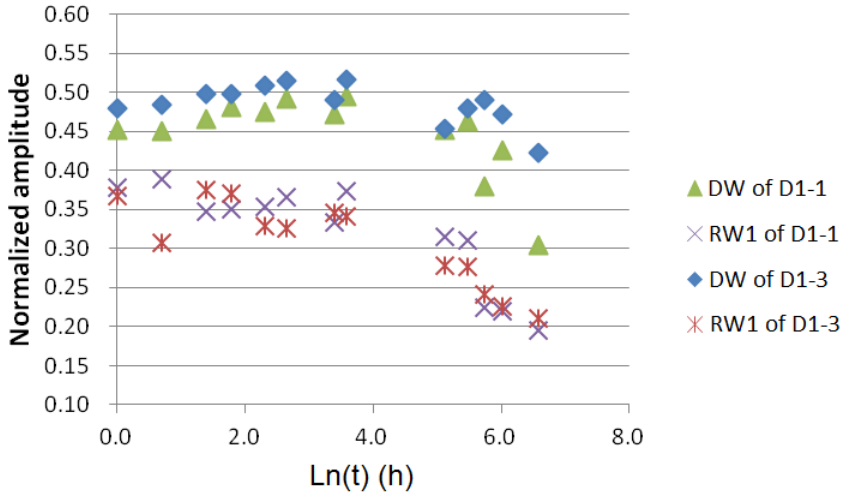

(a) Dry side

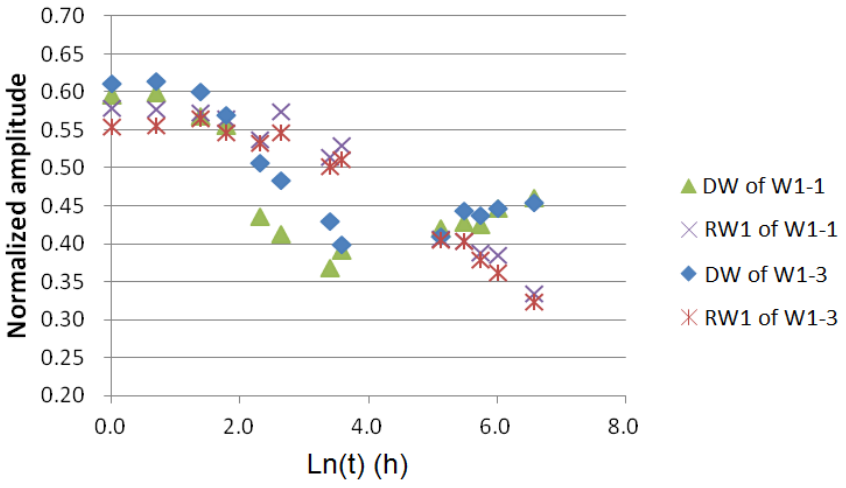

(b) Wet side

Figure 6.5: Normalized amplitude of direct wave (DW) and first reflected wave (RW1) of slabs C1-1 and C1-3 as a function of the natural logarithm of imbibition time $\ln(t)$ from (a) dry side (b) wet side

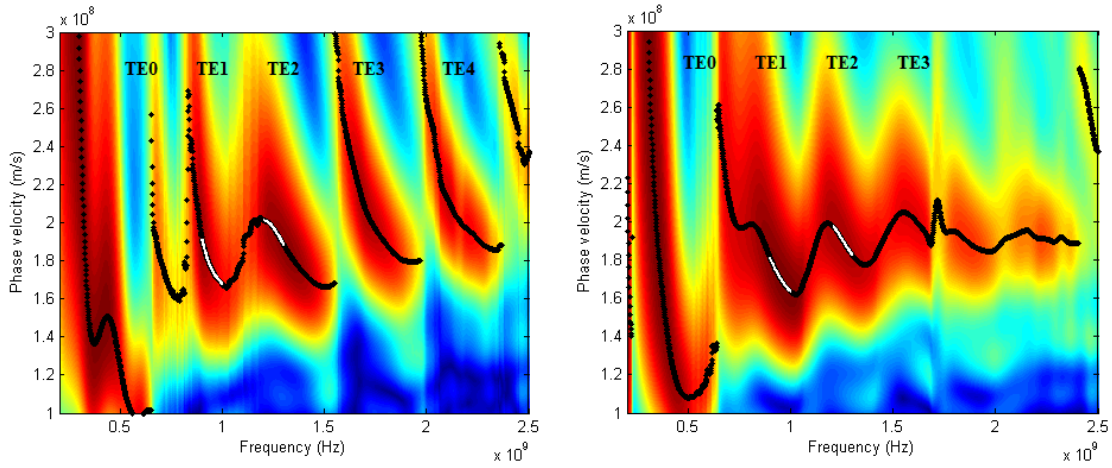

(a) T_0 (b) T_0+2 h

Figure 6.6: Phase velocity of EM waves propagating in modes (black) and selected range (white) for the waveguide inversion for C1-1 from the dry side at (a) T_0 (b) T_0+2 h

layer is lower than the first layer. Theoretically, the wet layer will form a waveguide for EM waves. However, as the water front is not sharp enough to be an interface between the two layers, waves propagate easily into the second layer of the concrete. In this case, we can use the multi-layer homogenization model regarding the whole slab as an equivalent medium.

6.4.2.a Two - layer waveguide model

Similar to the process we did for the numerical data in §4.4, several steps have been employed in the inversion for concrete slabs C1-1 and C1-3. As it takes a long time to do one inversion (around 1 hour), we have selected 7 test times out from all the measurements: T_0, T_0+2 h, T_0+4 h, T_0+10 h, T_0+30 h, T_0+168 h, T_0+30 days. The measurements of gammadensimetry respected the similar time framework.

Details of inversion process

1) Working band

First of all, we have to properly choose the propagation mode and its working frequency band for the inversion. There are generally 2 rules to respect: first, it should be a decreasing curve along the frequency as defined in the modal theory; second, it is preferred to be around the central frequency. According to the curves we get from the measurements on the 2 slabs, we finally decided to do the inversion with the combined TE_1 mode [0.9 - 1.0 GHz] and TE_2 mode [1.2 - 1.3 GHz]. Figure 6.6 shows the phase velocity dispersion curves derived from the tests on slab C1-1 from the dry side (D1-1) at two different times T_0 and T_0+2 h. The white parts refer to the working range for the inversions.

2) Starting values of iteration

We suppose the dry layer and the saturated layer keep the same dielectric properties during the imbibition, even if the slab is not homogeneous at T_0. The value of ε'_1 is obtained from the waveguide inversion of concrete at T_0, before putting in water. The wet part ε'_2 = 9.6 is the extrapolated value from the measurement of EM cell at 1 GHz. The starting

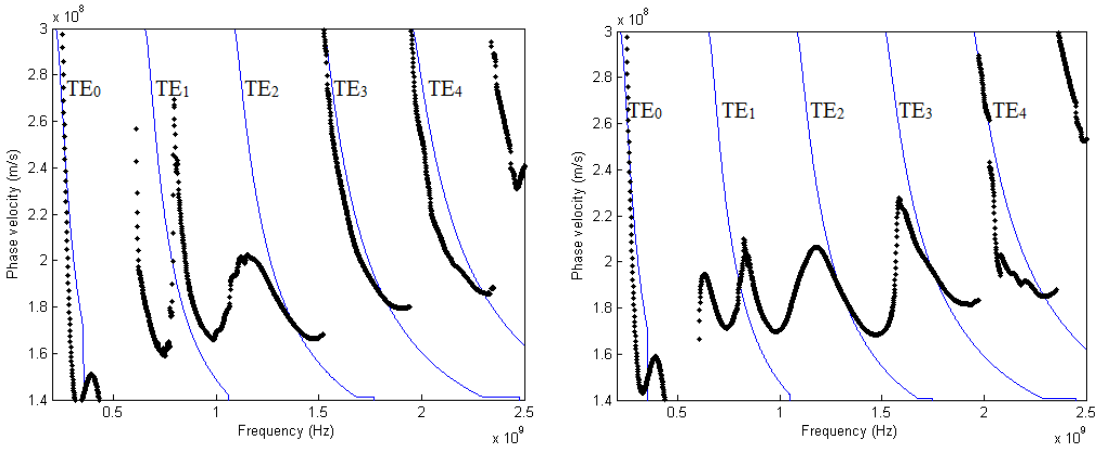

(a) Dry side (b) Wet side

Figure 6.7: Phase velocity derived from CMP measurement and two-layer waveguide inversion of slab C1-1 at T_0 from (a) dry side and (b) wet side

values in the inversion iteration are defined as $h_1 \in [0.01, 0.13]$, with the interval 0.01 m.

3) Minimum cost function

For each starting model of parameters h_1, one CF is obtained in the end. The minimum of all the CF is identified as the global minimum cost function min(CF) or very close to it.

Results and Discussions

Figures 6.7 and 6.8 are the comparisons of phase velocity dispersion curves resulting from the measurement analysis and from the inversions at time T_0 and T_0 + 2 h for slab C1-1. In figure 6.7, we chose to combine the modes TE_2 and TE_3 to do the waveguide inversion at T_0 of the two sides. In figure 6.8, we find it more difficult to pick up the modes for the inversions at T_0+2 h than at T_0. That is because the water penetrating into the concrete causes strong attenuation and dispersion. We have actually the same problem during all the process of imbibition. That is why we can see in figure 6.7, the two dispersion curves match very well with each other. But in figure 6.8, the curves do not so well as the results at T_0.

Tables 6.1 and 6.2 are the inversion results of the water front depth h_2 for slabs C1-1 and C1-3, measured from the dry side (D1-1 and D1-3). The inverted values of h_2, obtained by $h_2 = h - h_1$, at different imbibition times are compared to those from gammadensimetry. The water front depth of D1-1 (Table 6.1) shows a good evolution according to the imbibition time. Compared to the results of gammadensimetry, the value of h_2 from the inversion increases more slowly. The water front depth of D1-3 (Table 6.2) at T_1 appears to be higher than h_2 at T_2, which is too high comparing to the results of gammadensimetry. Furthermore, the value of h_2 at T_5 seems to be lower than we expected. These errors exist since the GPR signals are easily affected by some interferences, resulting in errors in dispersion curves. Generally speaking, the water front increases faster in slab C1-3 than in C1-1 according to the inversion results from the dry side. The slab was almost saturated after 30 days of imbibition. This may be because of the difference in CMP measurements, or the difference in initial condition at T_0 between the two slabs.

Tables 6.3 and 6.4 are the inversion results of the water front depth h_1 for slabs C1-1

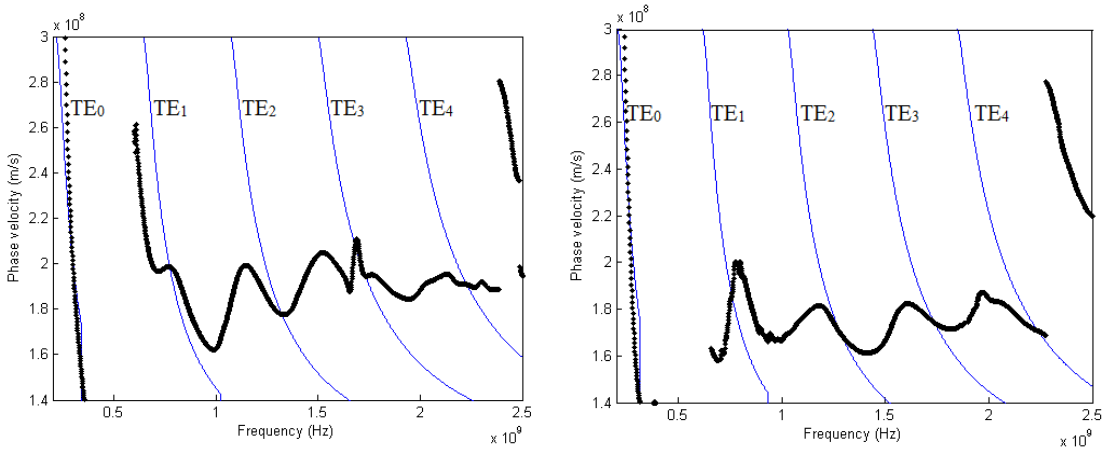

(a) Dry side (b) Wet side

Figure 6.8: Phase velocity derived from CMP measurement and two-layer waveguide inversion of slab C1-1 at T_0 + 2 h from (a) dry side and (b) wet side

Table 6.1: Inversion results of water front depth h_2 from CMP measurements on D1-1 on combined $TE_1 - TE_2$ ($TE_2 - TE_3$ for T_0) mode using two-layer waveguide model as the inverse model + gammadensimetry results

Time in water **GPR/Gamma.**	$\min(CF^{TE_{0\ldots m}})$ ($\times 10^6$)	ε'_e **Inv.**	ε'_1 **Inv.**	ε'_2 **Inv.**	h_2 **(m) Inv.**	$h_{2\,\min}$ **(m) Gamma.**	$h_{2\,\max}$ **(m) Gamma.**
T_0	2.32	8.1	8.1	-	0	0	0
T_1 (2 h/2 h)	2.77	8.2	8.1	9.6	0.011	0	0.024
T_2 (4 h/ 4 h)	2.71	8.4	8.1	9.6	0.023	0.024	0.030
T_3 (10 h/ 8 h)	4.69	8.5	8.1	9.6	0.035	0.036	0.048
T_4 (30 h/ 30 h)	5.25	8.6	8.1	9.6	0.044	0.054	0.072
T_5 (168 h/ 124 h)	6.07	8.8	8.1	9.6	0.060	-	-
T_6 (30 days/ -)	6.01	9.2	8.1	9.6	0.098	-	-

Table 6.2: Inversion results of water front depth h_2 from CMP measurements on D1-3 on combined $TE_1 - TE_2$ ($TE_2 - TE_3$ for T_0) mode using two-layer waveguide model as the inverse model + gammadensimetry results

Time in water **GPR/Gamma.**	$\min(CF^{TE_{0\ldots m}})$ ($\times 10^6$)	ε'_e **Inv.**	ε'_1 **Inv.**	ε'_2 **Inv.**	h_2 **(m) Inv.**	$h_{2\,\min}$ **(m) Gamma.**	$h_{2\,\max}$ **(m) Gamma.**
T_0	2.19	8.0	8.0	-	0	0	0
T_1 (2 h/2 h)	2.21	8.5	8.0	9.6	0.038	0	0.024
T_2 (4 h/ 4 h)	2.54	8.4	8.0	9.6	0.034	0.024	0.030
T_3 (10 h/ 8 h)	5.02	8.7	8.0	9.6	0.055	0.036	0.048
T_4 (30 h/ 30 h)	5.76	8.8	8.0	9.6	0.061	0.054	0.072
T_5 (168 h/ 124 h)	5.90	8.7	8.0	9.6	0.058	-	-
T_6 (30 days/ -)	8.09	9.5	8.0	9.6	0.125	-	-

Table 6.3: Inversion results of water front depth h_1 from CMP measurements on W1-1 on combined $TE_2 - TE_3$ mode using two-layer waveguide model as the inverse model + gammadensimetry results

Time in water	$\min(CF^{TE_{0\ldots m}})$	ε'_e	ε'_1	ε'_2	h_1 **(m)**	$h_{1\,\min}$ **(m)**	$h_{1\,\max}$ **(m)**
GPR/Gamma.	**($\times 10^6$)**	**Inv.**	**Inv.**	**Inv.**	**Inv.**	**Gamma.**	**Gamma.**
T_0	2.53	8.1	-	8.1	0	0	0
T_1 (2 h/2 h)	2.73	9.0	9.6	8.1	0.081	0	0.024
T_2 (4 h/4 h)	2.79	9.0	9.6	8.1	0.080	0.024	0.030
T_3 (10 h/8 h)	2.75	9.0	9.6	8.1	0.082	0.036	0.048
T_4 (30 h/ 30 h)	2.80	9.1	9.6	8.1	0.089	0.054	0.072
T_5 (168 h/124 h)	2.87	9.3	9.6	8.1	0.109	-	-
T_6 (30 days/-)	3.49	9.6	9.6	8.1	0.130	-	-

and C1-3, measured from the wet side (W1-1 and W1-3). The inversion results are compared to the results from gammadensimetry. The results from W1-1 (Table 6.3) show the dielectric constant at T_0 is higher than the results from the dry side. We can expect that there is a gradient inside the slab. The water front depth h_1 is over 0.080 m in the first 30 hours of imbibition, which is obvious wrong as h_1 is too high after 2 hours' imbibition and the variation of h_1 is too small during the 30 hours. The results for W1-3 (Table 6.4) show the similar problem during the 30 hours. For both slabs, the inverted water front depths after 30 hours are also much higher than those inverted from the measurements on the dry side. It is probably because when we measured from the wet side, some waves were trapped in the wet layer. There were in fact two waveguides for EM waves: one formed by the wet layer, considered as one WG, and one formed by the two layers. The existence of the one-layer waveguide disturbs the waves propagating in the two-layer waveguide, resulting in some errors in approximating the phase velocity dispersion curves.
From the inversion results of the water front depth from the two sides, we find that the measurements on the dry side give more available data for the inversion using the two-layer waveguide model. Many factors can affect the accuracy of the inversion results, such as the initial condition of the material, the experimental configuration, the data processing, etc.

Table 6.4: Inversion results of water front depth h_1 from CMP measurements on W1-3 on combined $TE_2 - TE_3$ mode using two-layer waveguide model as the inverse model + gammadensimetry results

Time in water	$\min(CF^{TE_{0\ldots m}})$	ε'_e	ε'_1	ε'_2	h_1 **(m)**	$h_{1\,\min}$ **(m)**	$h_{1\,\max}$ **(m)**
GPR/Gamma.	**(**$\times 10^6$**)**	**Inv.**	**Inv.**	**Inv.**	**Inv.**	**Gamma.**	**Gamma.**
T_0	2.17	8.3	-	8.3	0	0	0
T_1 (2 h/2 h)	2.47	8.8	9.6	8.3	0.047	0	0.024
T_2 (4 h/4 h)	2.86	8.9	9.6	8.3	0.061	0.024	0.030
T_3 (10 h/8 h)	3.03	8.9	9.6	8.3	0.061	0.036	0.048
T_4 (30 h/30 h)	3.11	8.9	9.6	8.3	0.061	0.054	0.072
T_5 (168 h/124 h)	2.89	9.5	9.6	8.3	0.119	-	-
T_6 (30 days/-)	3.08	9.6	9.6	8.3	0.130	-	-

6.4.2.b Arctan(x) waveguide model

The two-layer WG model requires the pre-estimation of the dielectric constants ε'_1 and ε'_2. Furthermore, from the results of gammadensimetry, we find the water distribution in concrete slabs of imbibition is like a gradient curve of reversed arctan function, instead of two layers. Therefore, we developed the arctan(x) WG model for the data analysis of the experiments of imbibition.
Since the arctan(x) model is developed for the test on the dry side, we have inverted the data of the 2 slabs from the dry side: D1-1 and D1-3.

Details of inversion process

In the process of inversion with arctan(x) model, we use the same working frequency band and propagation modes as with the two-layer model.
The starting values of the 4 parameters $[a, b, c, d]$ in the inversion iteration are defined as $a = \{0.01, 0.02\}$, $b = \{8, 9, 10, 11\}$, $c = 8.1$ and $d = [0.01, 0.13]$, with the interval 0.01. The shape factor a is defined according to the parametric study in §4.5. The values of b corresponds to the upper limit of the function, which is close to ε'_2. It is therefore defined between 8 and 11 by experience. The values of c corresponds to the lower limit of the function, which is close to ε'_1. From the inversion at T_0, the average ε'_1 of the two slabs is 8.1, so we give $c = 8.1$ at the beginning of the inversions. Then we employ the iteration in figure 4.30 (see in Chapter 4) until $\varepsilon'_{1inv} - \varepsilon'_1 < 0.1$. The value of d corresponds to the middle point of the gradient curve, so it must be among the range [0.01, 0.13].

Results and Discussions

The results are summarized in Tables 6.5 and 6.6. The values of h_2 at different imbibition times are compared to those from gammadensimetry. In the inversion process of this model, the value of ε'_1 is kept around the pre-estimated value 8.1. However, the inverted value of ε'_2 is not so stable. The equivalent permittivity ε'_e keeps increasing during the whole imbibition period. But at T_0 + 30 days, we cannot get a gradient curve because the concrete is nearly saturated.

Figure 6.9 shows the gradient curves of the relative density as a function of imbibition time, obtained by gammadensimetry. This result can be a reference of the variation of the permittivity because the concrete sample's density is varied by the massive water content.

Table 6.5: Inversion results of parameters $[\varepsilon_1, \varepsilon_2, h_2]$ from CMP measurements on D1-1 on combined $TE_1 - TE_2$ mode using $\arctan(x)$ waveguide model as the inverse model + gammadensimetry results

Time in water	$\min(CF^{TE_{0\ldots m}})$	ε'_e	ε'_1	ε'_2	$h_{2\,\min}$ **(m)**	$h_{2\,\max}$ **(m)**
GPR/Gamma.	**($\times 10^6$ m/s)**	**Inv.**	**Inv.**	**Inv.**	**Inv./Gamma.**	**Inv./Gamma.**
2 h/2 h	2.70	8.2	8.1	9.2	0/0	0.020/0.024
4 h/4 h	2.56	8.4	8.1	8.9	0.030/0.024	0.050/0.030
10 h/8 h	4.68	8.5	8.2	9.7	0.015/0.036	0.035/0.048
30 h/30 h	5.25	8.6	8.0	9.5	0.045/0.054	0.060/0.072
168 h/124 h	6.07	8.8	8.1	9.1	0.085/-	0.100/-
30 days/-	4.04	9.6	8.3	10.5	-	-

Table 6.6: Inversion results of parameters $[\varepsilon_1, \varepsilon_2, h_2]$ from CMP measurements on D1-3 on combined $TE_1 - TE_2$ mode using $\arctan(x)$ waveguide model as the inverse model + gammadensimetry results

Time in water	$\min(CF^{TE_{0\ldots m}})$	ε'_e	ε'_1	ε'_2	$h_{2\,\min}$ **(m)**	$h_{2\,\max}$ **(m)**
GPR/Gamma.	**($\times 10^6$ m/s)**	**Inv.**	**Inv.**	**Inv.**	**Inv./Gamma.**	**Inv./Gamma.**
2 h/2 h	2.21	8.5	8.1	9.8	0.015/0	0.030/0.024
4 h/4 h	2.50	8.4	8.1	8.9	0.030/0.024	0.050/0.030
10 h/8 h	5.04	8.7	8.2	9.0	0.080/0.036	0.100/0.048
30 h/30 h	5.75	8.8	8.1	9.0	0.085/0.054	0.115/0.072
168 h/124 h	5.88	8.7	8.1	9.0	0.080/-	0.110/-
30 days/-	8.12	9.3	8.2	9.9	-	-

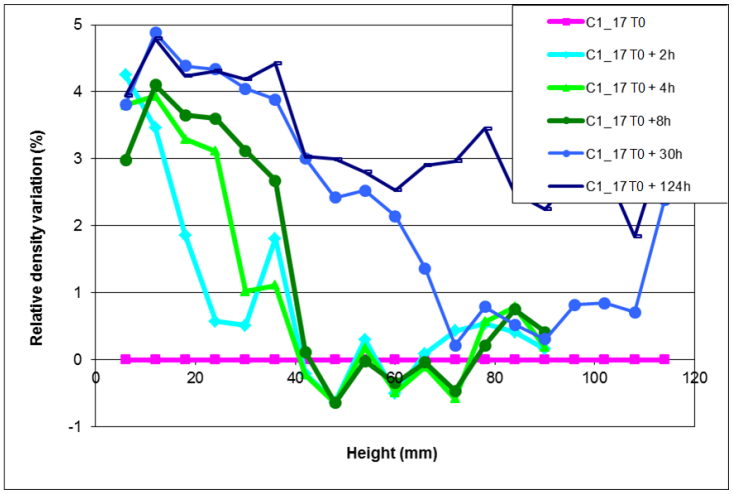

Figure 6.9: Evolution of relative density variation of cylindrical sample C1 - 17 as function of imbibition time obtained by gammadensimetry

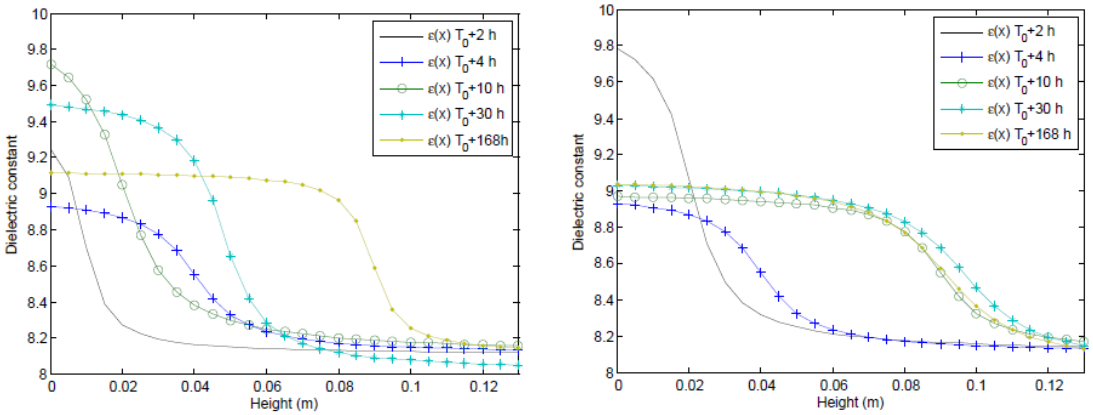

(a) D1-1 (b) D1-3

Figure 6.10: Evolution of inverted dielectric constant gradient on function of imbibition time of (a) D1-1 and (b) D1-3

And the permittivity is linearly related to the volumetric water content.
Figure 6.10 shows the gradient curves of dielectric constant inside the concrete slabs D1-1 and D1-3 inverted by arctan(x) WG model. We can see for D1-1, the value of ε'_2 is not very stable so that the evolution of h_2 is not very good. As some errors exist in the dispersion curves of phase velocity, there will also remain some errors in the inversion results. In our inversion process, the value of ε'_1 was kept around 8.1. This introduced higher error into the inversion of ε'_2. From the equivalent value ε'_e, we can see the water content is increasing. For D1-3, h_2 keeps increasing during the first 30 hours of imbibition. However, at $T_0 + 168h$, the curve is very close to $T_0 + 10h$, which is lower than we expect.

6.4.3 Conclusion

The experiments of water imbibition were conducted in Nantes. Four slabs of two concretes C1 and C3 were made without any reinforcement. All of them were tested by GPR with CMP configuration. The central frequency of GPR is 1.5 GHz.
For concrete C3, we have slabs C3-1 and C3-3 tested from the dry side. At each measuring time during the imbibition, the slabs were kept in the water and tested twice from the surface. For concrete C1, we have slabs C1-1 and C1-3 tested from two sides at each time. From the dry side, the slabs were put in the water. From the wet side, the slabs were put on a metal plate.
The first step of the analysis is to analyse the effects of water content on GPR signals. We picked the signals at the minimum offset from each measurement, to monitor the amplitude of the direct wave (DW) and amplitude of the first reflected wave (RW1). We find good correlation between the amplitudes and the imbibition time. From the analysis, we find concrete C1 is near saturated after 1 month's imbibition. At the same time, we did not get any evolution of amplitudes from the measurements on concrete C3.
Then we did the WG inversion with CMP measurements from the slabs of C1. Two models have been employed in the inversion: the two-layer model and arctan(x) model. The results are compared to the results of gammadensimetry. From the results of the two-layer WG inversion, we find that the measurements from the dry side obtain better results than from the wet side. The inversion results from arctan(x) model determine the

gradients of dielectric constant with respect to the depth. With $\arctan(x)$ model, we are able to approximate the water front depth from the dispersion curves without knowing the value of ε_2'. However, the inverted ε_2' is not very stable. The inversion process should be optimized in the future.

6.5 Characterization of Concrete with Sea Water Imbibition

Like the experiments of water imbibition, our main objective for the sea water imbibition is to monitor the penetration depth of sea water during the imbibition with the application of GPR. The effects of imbibition on EM observables, the amplitude and the dielectric constant, will be analysed in this section.
The experimental results for analysis are from the imbibition campaign conducted in Cerema, St. Brieuc. We had generally 8 slabs (dimension: $900 \times 700 \times 130$ mm^3) for the two concretes of APOS project to be studied in this experimental campaign: 03, 04, 05, 07 for C3 and 13, 14, 15, 17 for C1. Slabs 03 and 13 have no rebars inside while the other slabs have the rebars with 20×30 cm^2 meshes inside. Slabs 07 and 17 were put in the water for imbibition while the rest are put in the chloride solution with a concentration of 35 g/L.
For the analysis, we will start by the effects of chloride content gradients on the amplitude of GPR signals. Like the effects of water content, the attenuation of EM waves is linearly related to the chloride concentration in saturated state [Sbartaï et al., 2006a]. Then, the chloride penetration depth during the imbibition will be assessed by the inversion of two-layer WG and arctan(x) WG models.

6.5.1 Effects of chloride content gradients on GPR signals

Let us recall some experimental configurations at the beginning. The central frequency of the antennas we choose in this campaign is 2.6 GHz. We measured 8 slabs (03, 04, 05, 07, 13, 14, 15, 17) on the dry side and 4 slabs (03, 07, 13, 17) on the wet side with CMP method. The 8 slabs were also scanned by a mini structure scanning GPR at 2.6 GHz. All the slabs were put on steel plates while measuring.
Figures 6.11, 6.12 and 6.13 are the normalized peak-to-peak amplitudes of the GPR signals collected from the minimum offset of the CMP measurement. To better present the variation as a function of time, the imbibition time t (h) has been replaced by its natural logarithm $\ln(t)$.
The two slabs 03 and 13 in figure 6.11 were put in the water with a chloride concentration of 35 g/L, measured from the two sides. They are the only slabs that have no reinforcement inside to influence the waves' propagation. The difference between the RW1 of the dry side (D03) and the wet side (W03) of the slab 03 is probably caused by the thermal drift of the GPR system at the beginning of 30 minutes [Fauchard et al., 2015] since we always start from D03 for measuring each time. Furthermore, the radiation pattern was changed by the different surface layers, resulting in the variation of amplitude. So we also observe a difference between the RW1 of D13 and W13. From the second time point, we observe the DW of D03 is stronger that the DW of W03. This is because the direct wave from the wet side is attenuated by water and chloride. The difference of DW between D13 and W13 is even higher, meaning that slab 13 is more accessible to water. This is also the reason why slab 03 has higher amplitude of RW1 than 13.
For both slabs, the water penetrates very little during the first 30 minutes (1st time point T1). The DW of D03 becomes much lower from T_6 (1 month), where we believe the water front affects the direct wave on the dry surface. But it is not verified that the concrete becomes saturated. And for D13, this change appears at T_7 (4 months).

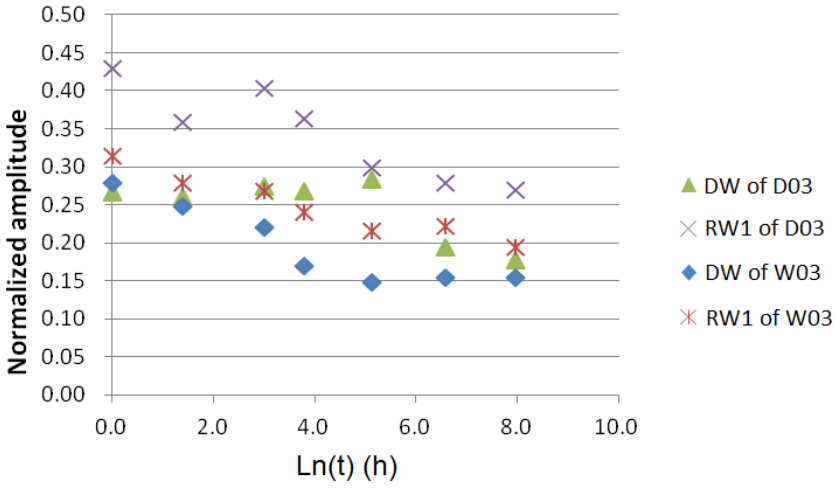

(a) Slab 03

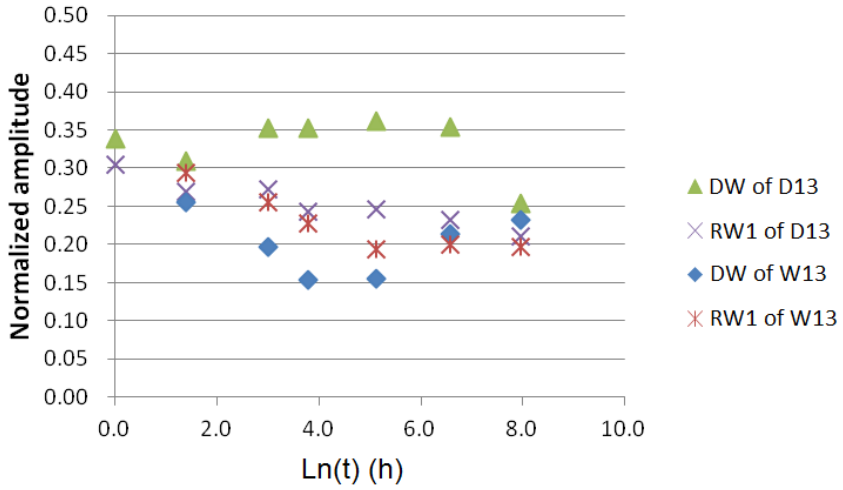

(b) Slab 13

Figure 6.11: Normalized amplitude of direct wave (DW) and first reflected wave (RW1) as a function of the natural logarithm of imbibition time $\ln(t)$ from 2 sides of (a) slab 03 and (b) slab 13

Figure 6.12 shows the amplitudes for the two slabs 07 and 17 put in the water without chloride and measured from the two sides. Unlike the amplitudes for slabs 03 and 13, the DW from the wet side is higher than that from the dry side for the two slabs 07 and 17 at the beginning of the imbibition. We can conclude that some gradients of water exist in the slabs. Moreover, the amplitudes of RW1 are higher than those for slabs 03 and 13. This means that the chloride has stronger attenuation impacts on EM waves than water. The amplitudes of RW1 for slab 17 are much smaller than those of slab 07, since slab 17 has better permeability to water.

Figure 6.13 shows the amplitudes for the 4 slabs: 04, 05, 14 and 15. All were tested from the dry side. The 4 slabs were put in the water with a chloride concentration of 35 g/L. As slabs 04 and 05 used the same concrete C3, the measurements are supposed to be the same. The same situation should be seen for slabs 14 and 15 since they both use concrete C1. We can see in figure 6.13 (a) that for slabs 04 and 05, the results are satisfying except

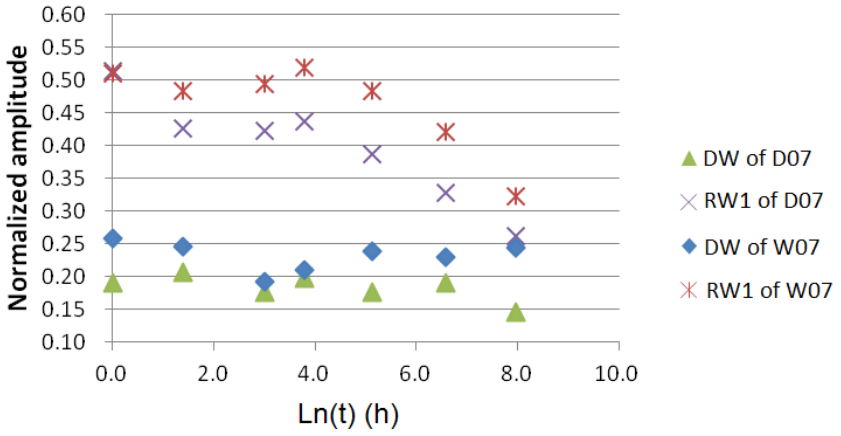

(a) Slab 07

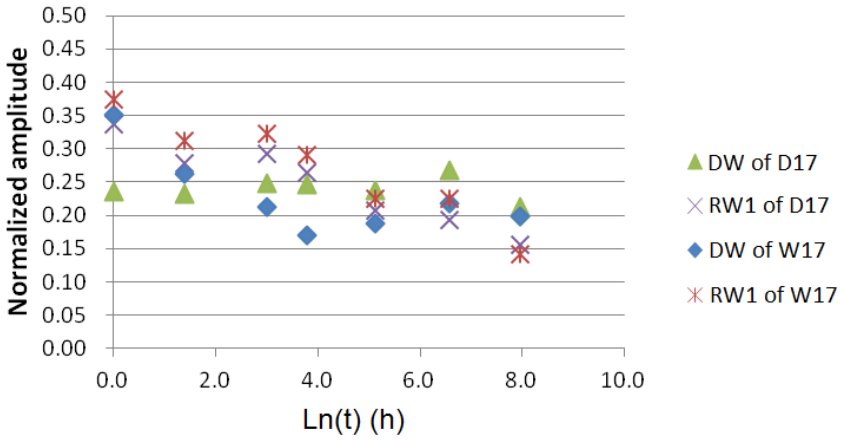

(b) Slab 17

Figure 6.12: Normalized amplitude of direct wave (DW) and first reflected wave (RW1) as a function of the natural logarithm of imbibition time $\ln(t)$ from 2 sides of (a) slab 07 and (b) slab 17

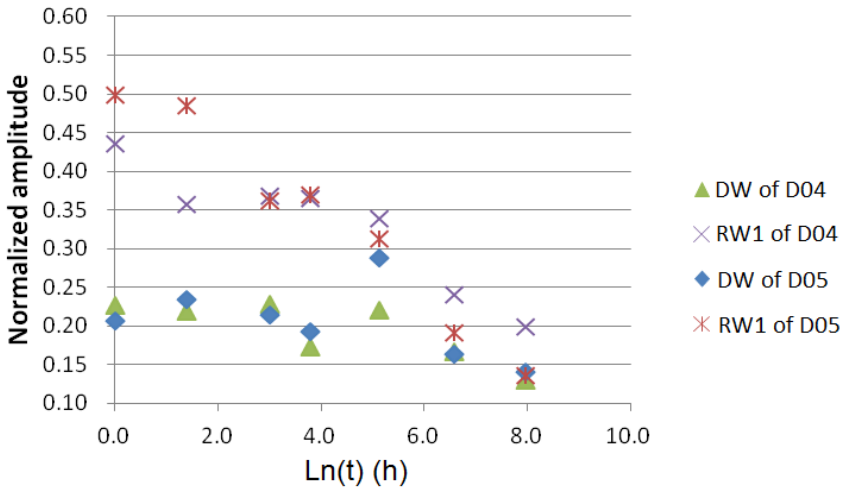

(a) 04, 05 - dry side

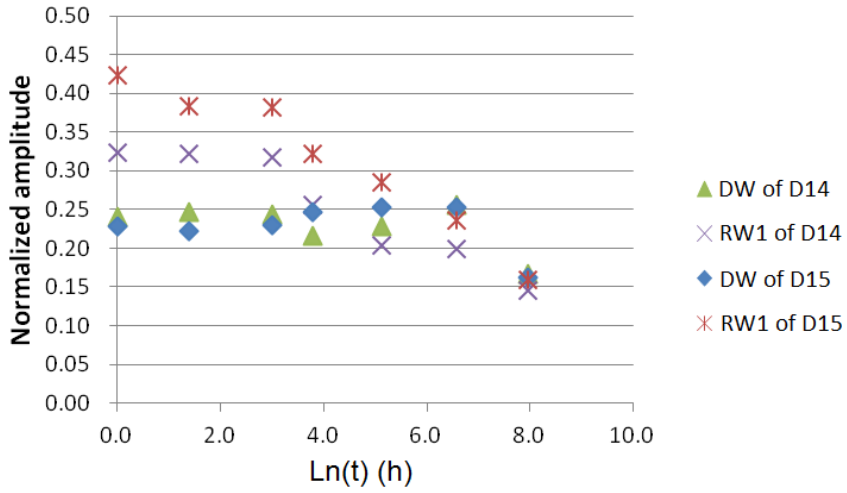

(b) 14, 15 - dry side

Figure 6.13: Normalized amplitude of direct wave (DW) and first reflected wave (RW1) as a function of the natural logarithm of imbibition time $\ln(t)$ from dry side of (a) slabs 04, 05 and (b) slabs 14, 15

for DW at T_5 and RW1 at T_1, T_2, T_6, T_7 as the amplitudes are quite different between the two slabs. For slabs 14 and 15 in figure 6.13 (b), the amplitudes of RW1 for slab 15 are generally higher than those for slab 14.

The reflected waves of all the slabs have the tendency of decreasing on amplitude as a function of time. That means the water and chloride continued penetrating into the concrete during the 4 months. In general, we can see that the water and chloride penetrate faster in concrete C1 than in C3.

Table 6.7: Inversion modes for different concrete slabs

Slab	Mode
03	$TE_2 - TE_4$
13	$TE_2 - TE_4$
04	$TE_1 - TE_3$
14	$TE_2 - TE_4$
07	$TE_2 - TE_3$
17	$TE_4 - TE_5$

6.5.2 Results of waveguide inversion

We are going to conduct some further analysis with the waveguide inversion for the dry side of concrete slabs 03, 04, 05, 07, 13, 14, 15 and 17. Because from the inversion results of the water imbibition in Nantes, we find that the measurement from the dry side can obtain better results than from the other side. The measurements were obtained by GPR with 2.6 GHz antennas. Two models, two-layer model and arctan(x) model, are applied to the inversion.

6.5.2.a Two - layer waveguide model

Some details of the two-layer WG inversion process are introduced in the follows.

Details of inversion process

1) Working band

According to the curves we get from the measurements on the 8 slabs, we find for each slab, the modes of available phase velocity for the inversion are not always the same. So we finally decided on different modes to do the inversion, summarized in Table 6.7. For each mode, a frequency band of 100 MHz is selected.

2) Starting values of iteration

In the imbibition experiments of St. Brieuc, we put slabs 07 and 17 in the water while the other slabs were put in the salty water with the chloride content 35 g/L. We obtained different values of the permittivities from the extrapolation of EM cell data in saturated state. According to the results of EM cell, the permittivity of saturated concrete with chloride is higher than that without chloride.

The dielectric constant of the dry layer ε'_1 is calculated by WG inversion from the measurement on concrete slabs at initial time T_0. The value of ε'_2 is extrapolated from the EM cell data at 1 GHz. Therefore, we obtain the dielectric constants of the dry layer and the wet layer as follows: for slabs 03, 04 and 05, $[\varepsilon'_1, \varepsilon'_2] = \{6.9, 11.5\}$; for slab 07, $[\varepsilon'_1, \varepsilon'_2] = \{6.9, 10.7\}$; for slabs 13, 14 and 15, $[\varepsilon'_1, \varepsilon'_2] = \{8.2, 10.6\}$; for slab 07, $[\varepsilon'_1, \varepsilon'_2] = \{8.2, 9.6\}$.

Unfortunately, we have not got the measurements of all the slabs at T_0 due to some technical problems on the first day (only D05, D13 and D15). To find more reliable dielectric constants for each slab, we processed the inversion in two steps.

First, the 3 unknown parameters $[\varepsilon'_1, \varepsilon'_2, h_1]$ were inverted at T_1. The starting values of the 3 unknown parameters $[\varepsilon'_1, \varepsilon'_2, h_1]$ in the inversion iteration of concrete C1 (13, 14, 15)

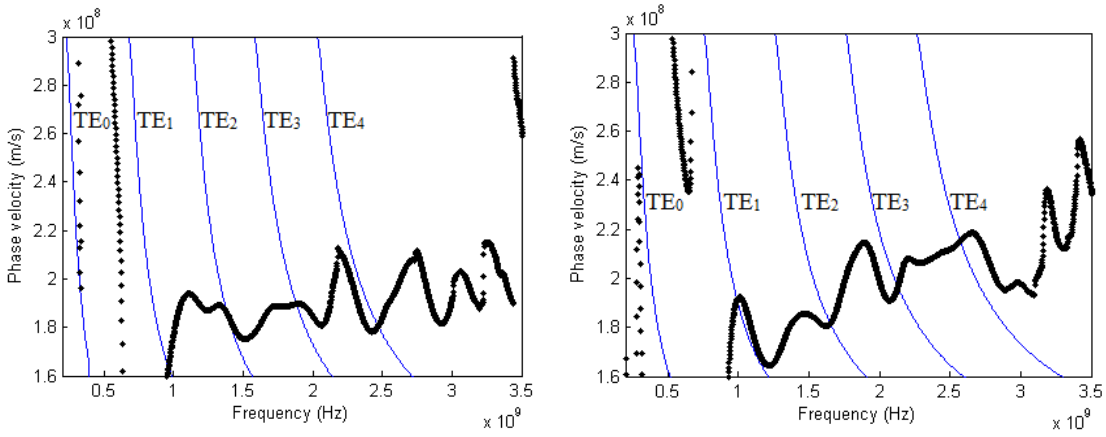

(a) D03 (b) D04

Figure 6.14: Phase velocity derived from CMP measurement and two-layer waveguide inversion at T_0 + 4 h of slabs (a) D03 (b) D04

were defined as $\varepsilon'_1 = 8.2$, $\varepsilon'_2 = \{10.4, 10.6, 10.8\}$ and $h_1 \in [0.01, 0.13]$, with the interval 0.01 m. For slab 17, we first gave $\varepsilon'_2 = \{9.4, 9.6, 9.8\}$. Similarly, for C3 (03, 04), the starting values were $\varepsilon'_1 = 6.9$, $\varepsilon'_2 = \{11.3, 11.5, 11.7\}$ and $h_1 \in [0.01, 0.13]$, with the interval 0.01 m. For slab 07, $\varepsilon'_2 = \{10.5, 10.7, 10.9\}$. The value of ε'_1 was obtained from the waveguide inversion of concrete at T_0, before putting in water. The dielectric constant of the wet part ε'_2 was the extrapolated value from the measurement of EM cell at 1 GHz since the value of dielectric constant changes very slightly above 1 GHz. We added 2 values close to it as the staring values.
Then, the values of ε'_1 and ε'_2 from the inversion were considered as known parameters from T_2 to T_7. The thickness of the first layer was inverted with the initial value $h_1 \in [0.01, 0.13]$, with the interval 0.01 m.

3) Minimum cost function

For each starting model of parameters $[\varepsilon'_1, \varepsilon'_2, h_1]$, one $CF^{TE_{0...m}}$ is obtained in the end. The minimum of all the $CF^{TE_{0...m}}$ is identified as the global minimum cost function $\min(CF^{TE_{0...m}})$.

Results and Discussions

1) Slabs of C3 - 03, 04, 05, 07

Figure 6.14 gives 2 examples of the comparisons of the phase velocity dispersion curves between the measurements from slabs 03 and 04 on the dry side (marked as D03 and D04) and the inversions at time T_0+4 h. In figure 6.14 (a), we chose to combine modes TE_2 and TE_4 to do the inversion for slab 03 from the dry side. For D04, we used TE_1 and TE_3 modes, as shown in figure 6.14 (b). From the figure, we find it even more difficult to pick up the working band than the tests in Nantes as we change the antennas to 2.6 GHz. So the curves do not match very well as we find in figure 6.7. However, they are supposed to be the best solutions in this campaign.

Tables 6.8 and 6.9 are the inversion results of the water front depth h_2 for D03 and D04, showing the pre-estimated dielectric constants ε'_1 and ε'_2, the inverted water front depth h_2 and the equivalent permittivity ε'_e. The 2 slabs are put in the salty water with the chloride content 35 g/L, close to the chloride concentration of the sea water. The

Table 6.8: Inversion results of water front depth h_2 from CMP measurements on D03 on combined $TE_2 - TE_4$ mode using two-layer waveguide model as the inverse model + gammadensimetry results

Time in water	$\min(CF^{TE_{0\ldots m}})$	ε'_e	ε'_1	ε'_2	h_2 **(m)**	$h_{2\,\min}$ **(m)**	$h_{2\,\max}$ **(m)**
GPR/Gamma.	**($\times 10^6$)**	**Inv.**	**Inv.**	**Inv.**	**Inv.**	**Gamma.**	**Gamma.**
T_1 (1 h/2 h)	0.79	7.9	6.9	11.3	0.029	0	0.018
T_2 (4 h/4 h)	0.95	7.7	6.9	11.3	0.023	0	0.018
T_3 (20 h/10 h)	2.16	8.2	6.9	11.3	0.038	0.030	0.036
T_4 (44 h/30 h)	1.20	7.8	6.9	11.3	0.027	0.030	0.036
T_5 (168 h/122 h)	1.32	8.5	6.9	11.3	0.046	0.030	0.048
T_6 (1 month/ -)	1.60	8.7	6.9	11.3	0.053	-	-
T_7 (4 months/ -)	2.08	9.2	6.9	11.3	0.067	-	-

difference between the 2 slabs is that slab 03 has no reinforcement inside while slabs 04 has rebars composing 20×30 cm^2 meshes.
From Table 6.8, we can see that the water front h_2 has a good tendency of increasing according to the imbibition time. However, the penetrating is very slow so that the slab is not saturated after 4 months. Compared to the results of gammadensimetry, the value of h_2 during the beginning 4 hours seems to be too high, which could be the error caused by the WG leakage.
From Table 6.9, we find that ε'_e is generally smaller than the results of D03. This is caused by the effects of the reinforcement. And due to the effects, the inverted ε'_1 is lower than that of D03. Generally, the variation of h_2 matches with that from gammadensimetry.
The slab 05 is supposed to be in the same condition as slab 04. The inversion results of D05 are summarized in Table 6.10. However, as we observe from the results, the increasing of h_2 and ε'_e is much slower than that of D04 during the first week. On the contrary, the h_2 and ε'_e for D05 becomes higher than those of D04. We believe that there is a small difference in the initial condition between the two slabs. The porosities may also be different as the values of ε'_2 are different. Considering the amplitudes of the signal responses, the DW from D04 and D05 are generally the same while the RW has some difference at the beginning test times. The slabs may have some gradients inside at initial time T_0.

Table 6.11 gives the inversion results of slab 07 from the dry side. As the slab 07 was put in the water without chloride, the dielectric constant of the wet part ε'_2 is a bit lower than other slabs of C3. Indeed, the variation tendency is very similar to 03.
From the results for the 4 slabs, we find the h_2 at T_1 is always higher than that at T_2. Since the water content kept increasing during the imbibition, it is an error from the CMP measurement. As it always exists at the beginning of the imbibition, it should be quantified in the future study.

2) Slabs of C1 - 13, 14, 15, 17

Tables 6.12 and 6.13 are the inversion results of slabs 13 and 14 from the dry side (marked as D13 and D14). Observing the variation of h_2 from the inversion and gammadensimetry, we can find that the water penetrates faster than in slabs 03 and 04. For the results of D13 in Table 6.12, the water front h_2 keeps increasing except for T_4, where h_2 is higher

Table 6.9: Inversion results of water front depth h_2 from CMP measurements on D04 on combined $TE_1 - TE_3$ mode using two-layer waveguide model as the inverse model + gammadensimetry results

Time in water	$\min(CF^{TE_{0\ldots m}})$	ε'_e	ε'_1	ε'_2	h_2 **(m)**	$h_{2\min}$ **(m)**	$h_{2\max}$ **(m)**
GPR/Gamma.	**($\times 10^6$)**	**Inv.**	**Inv.**	**Inv.**	**Inv.**	**Gamma.**	**Gamma.**
T_1 (1 h/2 h)	2.06	6.8	6.4	10.6	0.018	0	0.018
T_2 (4 h/4 h)	5.09	6.5	6.4	10.6	0.004	0	0.018
T_3 (20 h/10 h)	2.31	7.3	6.4	10.6	0.028	0.030	0.036
T_4 (44 h/30 h)	2.55	7.4	6.4	10.6	0.030	0.030	0.036
T_5 (168 h/122 h)	2.17	7.7	6.4	10.6	0.039	0.030	0.048
T_6 (1 month/ -)	1.35	8.0	6.4	10.6	0.049	-	-
T_7 (4 months/ -)	3.88	8.6	6.4	10.6	0.069	-	-

Table 6.10: Inversion results of water front depth h_2 from CMP measurements on D05 on combined $TE_1 - TE_4$ mode using two-layer waveguide model as the inverse model + gammadensimetry results

Time in water	$\min(CF^{TE_{0\ldots m}})$	ε'_e	ε'_1	ε'_2	h_2 **(m)**	$h_{2\min}$ **(m)**	$h_{2\max}$ **(m)**
GPR/Gamma.	**($\times 10^6$)**	**Inv.**	**Inv.**	**Inv.**	**Inv.**	**Gamma.**	**Gamma.**
T_1 (1 h/2 h)	6.58	6.9	6.5	11.1	0.013	0	0.018
T_2 (4 h/4 h)	3.81	6.7	6.5	11.1	0.007	0	0.018
T_3 (20 h/10 h)	2.86	6.8	6.5	11.1	0.008	0.030	0.036
T_4 (44 h/30 h)	3.44	7.1	6.5	11.1	0.017	0.030	0.036
T_5 (168 h/122 h)	2.32	7.5	6.5	11.1	0.027	0.030	0.048
T_6 (1 month/ -)	2.25	9.6	6.5	11.1	0.087	-	-
T_7 (4 months/ -)	-	-	-	-	-	-	-

Table 6.11: Inversion results of water front depth h_2 from CMP measurements on D07 on combined $TE_2 - TE_3$ mode using two-layer waveguide model as the inverse model + gammadensimetry results

Time in water	$\min(CF^{TE_{0\ldots m}})$	ε'_e	ε'_1	ε'_2	h_2 **(m)**	$h_{2\min}$ **(m)**	$h_{2\max}$ **(m)**
GPR/Gamma.	**($\times 10^6$)**	**Inv.**	**Inv.**	**Inv.**	**Inv.**	**Gamma.**	**Gamma.**
T_1 (1 h/2 h)	0.53	7.6	6.2	9.5	0.034	0	0.018
T_2 (4 h/4 h)	0.22	6.8	6.2	9.5	0.022	0	0.018
T_3 (20 h/10 h)	1.71	7.1	6.2	9.5	0.035	0.030	0.036
T_4 (44 h/30 h)	1.58	7.2	6.2	9.5	0.039	0.030	0.036
T_5 (168 h/122 h)	0.49	7.7	6.2	9.5	0.058	0.030	0.048
T_6 (1 month/ -)	1.13	8.1	6.2	9.5	0.076	-	-
T_7 (4 months/ -)	1.05	8.3	6.2	9.5	0.081	-	-

Table 6.12: Inversion results of water front depth h_2 from CMP measurements on D13 on combined $TE_2 - TE_4$ mode using two-layer waveguide model as the inverse model + gammadensimetry results

Time in water	$\min(CF^{TE_{0\ldots m}})$	ε'_e	ε'_1	ε'_2	h_2 **(m)**	$h_{2\,\min}$ **(m)**	$h_{2\,\max}$ **(m)**
GPR/Gamma.	**($\times 10^6$)**	**Inv.**	**Inv.**	**Inv.**	**Inv.**	**Gamma.**	**Gamma.**
T_1 (1 h/2 h)	2.60	8.7	8.2	10.6	0.030	0	0.024
T_2 (4 h/4 h)	2.75	8.8	8.2	10.6	0.031	0.024	0.030
T_3 (20 h/8 h)	2.35	9.0	8.2	10.6	0.043	0.036	0.048
T_4 (44 h/30 h)	0.69	9.9	8.2	10.6	0.092	0.054	0.072
T_5 (168 h/124 h)	4.16	9.6	8.2	10.6	0.075	-	-
T_6 (1 month/ -)	0.63	9.6	8.2	10.6	0.077	-	-
T_7 (4 months/ -)	2.63	9.6	8.2	10.6	0.078	-	-

than the following test times. When we conducted a structure scan through the surface of slab 13, we observed an unexpected reflection from the middle of the slabs. It could be a large gravel or bubble inside the slab. The CMP measurements are affected by this reflection. Therefore, the variation of h_2 for D13 is not logical.
Comparing the inversion results of D14 to those of gammadensimetry in Table 6.13, we find that the values of h_2 at T_1, T_2 and T_4 are much higher than we expected. A bias in moving the antennas during the measurement or an inappropriate processing of the data can both cause the error in the inversion results. The results for D15 in Table 6.14 show better evolution of h_2 with respect to the imbibition time.
The results of D17 are shown in Table 6.15. It is surprised to see the value of ε'_2 of D17 is very close to that of D13 and D14, even though slab 17 was put in water without chloride. According to the table, the water front depth increases much faster than than we expected. The slab was nearly saturated after one month, which is similar to the results of D14 and D15. However, the penetration depth seems to be too high during the first 20 hours considering the results of gammadensimetry, which turns out to be the same problem as for D14.
Generally speaking, the water in the slabs of C1 penetrates faster than in the slabs of C3. As we can see from the results of D14, D15 and D17, the water front is very close to the dry surface after 4 months.

6.5.2.b Arctan(x) waveguide model

In the process of inversion with arctan(x) model, we choose to present the results of the slabs 03, 04, 13 and 14 from the dry side.

Details of inversion process

We use the same working frequency band and propagation modes as the two-layer model. For slabs 03 and 04, the starting values of the 4 parameters $[a, b, c, d]$ in the inversion iteration are defined as $a = 0.01, 0.02$, $b = 8, 9, 10, 11$, $c = 6.9$ and $d = [0.01, 0.13]$, with the interval 0.01.
For slabs 13 and 14, the starting values of the 4 parameters $[a, b, c, d]$ in the inversion iteration are defined as $a = 0.01, 0.02$, $b = 8, 9, 10, 11$, $c = 8.2$ and $d = [0.01, 0.13]$, with

Table 6.13: Inversion results of water front depth h_2 from CMP measurements on D14 on combined $TE_2 - TE_4$ mode using two-layer waveguide model as the inverse model + gammadensimetry results

Time in water	$\min(CF^{TE_{0\ldots m}})$	ε'_e	ε'_1	ε'_2	h_2 **(m)**	$h_{2\min}$ **(m)**	$h_{2\max}$ **(m)**
GPR/Gamma.	$(\times 10^6)$	**Inv.**	**Inv.**	**Inv.**	**Inv.**	**Gamma.**	**Gamma.**
T_1 (1 h/2 h)	3.67	9.3	8.0	10.6	0.065	0	0.024
T_2 (4 h/4 h)	3.83	9.3	8.0	10.6	0.064	0.024	0.030
T_3 (20 h/8 h)	4.50	8.9	8.0	10.6	0.044	0.036	0.048
T_4 (44 h/30 h)	5.18	9.8	8.0	10.6	0.089	0.054	0.072
T_5 (168 h/124 h)	4.05	9.6	8.0	10.6	0.082	-	-
T_6 (1 month/ -)	1.63	10.1	8.0	10.6	0.105	-	-
T_7 (4 months/ -)	7.56	10.5	8.0	10.6	0.125	-	-

Table 6.14: Inversion results of water front depth h_2 from CMP measurements on D15 on combined $TE_4 - TE_5$ mode using two-layer waveguide model as the inverse model + gammadensimetry results

Time in water	$\min(CF^{TE_{0\ldots m}})$	ε'_e	ε'_1	ε'_2	h_2 **(m)**	$h_{2\min}$ **(m)**	$h_{2\max}$ **(m)**
GPR/Gamma.	$(\times 10^6)$	**Inv.**	**Inv.**	**Inv.**	**Inv.**	**Gamma.**	**Gamma.**
T_1 (1 h/2 h)	4.63	8.5	8.2	10.4	0.015	0	0.024
T_2 (4 h/4 h)	3.61	8.9	8.2	10.4	0.039	0.024	0.030
T_3 (20 h/8 h)	4.12	9.1	8.2	10.4	0.053	0.036	0.048
T_4 (44 h/30 h)	5.72	9.1	8.2	10.4	0.056	0.054	0.072
T_5 (168 h/124 h)	4.34	9.7	8.2	10.4	0.089	-	-
T_6 (1 month/ -)	4.71	10.2	8.2	10.4	0.120	-	-
T_7 (4 months/ -)	5.09	10.3	8.2	10.4	0.125	-	-

Table 6.15: Inversion results of water front depth h_2 from CMP measurements on D17 on combined $TE_4 - TE_5$ mode using two-layer waveguide model as the inverse model + gammadensimetry results

Time in water	$\min(CF^{TE_{0\ldots m}})$	ε'_e	ε'_1	ε'_2	h_2 **(m)**	$h_{2\min}$ **(m)**	$h_{2\max}$ **(m)**
GPR/Gamma.	$(\times 10^6)$	**Inv.**	**Inv.**	**Inv.**	**Inv.**	**Gamma.**	**Gamma.**
T_1 (1 h/2 h)	2.45	9.4	8.2	10.5	0.065	0	0.024
T_2 (4 h/4 h)	3.47	9.2	8.2	10.5	0.058	0.024	0.030
T_3 (20 h/8 h)	3.57	9.6	8.2	10.5	0.081	0.036	0.048
T_4 (44 h/30 h)	3.75	9.5	8.2	10.5	0.071	0.054	0.072
T_5 (168 h/124 h)	1.27	10.1	8.2	10.5	0.109	-	-
T_6 (1 month/ -)	3.31	10.3	8.2	10.5	0.120	-	-
T_7 (4 months/ -)	3.70	10.4	8.2	10.5	0.125	-	-

Table 6.16: Inversion results of parameters $[\varepsilon_1, \varepsilon_2, h_2]$ from CMP measurements on D03 on combined $TE_2 - TE_4$ mode using $\arctan(x)$ waveguide model as the inverse model + gammadensimetry results

Time in water	$\min(CF^{TE_{0\ldots m}})$	ε'_e	ε'_1	ε'_2	$h_{2\,\min}$ **(m)**	$h_{2\,\max}$ **(m)**
GPR/Gamma.	**($\times 10^6$ m/s)**	**Inv.**	**Inv.**	**Inv.**	**Inv./Gamma.**	**Inv./Gamma.**
T_1 (1 h/2 h)	0.76	7.9	7.0	8.8	0.05/0	0.07/0.018
T_2 (4 h/4 h)	-	-	-	-	-	-
T_3 (20 h/10 h)	2.13	8.2	7.0	9.6	0.05/0.030	0.07/0.036
T_4 (44 h/30 h)	0.92	7.9	6.9	8.9	0.055/0.030	0.065/0.036
T_5 (168 h/122 h)	0.51	8.6	6.9	9.9	0.07/0.030	0.085/0.048
T_6 (1 month/ -)	1.60	8.7	6.9	9.9	0.075/-	0.09/-
T_7 (4 months/ -)	1.68	9.1	7.0	10.6	0.07/-	0.09/-

the interval 0.01.
The shape factor a is defined according to the parametric study in §4.5. The values of b corresponds to the upper limit of the function, which is close to ε'_2. It is therefore defined between 8 and 11 by experience. The values of c corresponds to the lower limit of the function, which is close to ε'_1. From the inversion at T_0, we get ε'_1. Then we employ the iteration in figure 4-30 until $\varepsilon'_{1inv} - \varepsilon'_1 < 0.1$. The value of d corresponds to the middle point of the gradient curve, so it must be among the range [0.01, 0.13].

Results and Discussions

The inversion results of D03 and D04 are summarized in Tables 6.16 and 6.17. Some results, such as the results at $T_0 + 4h$ for D03 and $T_0 + 4h$, $T_0 + 20h$ for D04, are not presented here because sometimes we cannot get good inversion results with this model. For the results of D03, the value of ε'_1 is very stable, while the value of ε'_2 varies from 8.8 to 10.6. The minimum values and maximum values of the water front depth h_2 are picked from the inverted gradient curves, which will be shown in the following. Compared to the results of two-layer model, the value of ε'_2 is much lower. On the contrary, the increment of h_2 looks much faster than the results of two-layer model. Comparing to the results of gammadensimetry, we find the inverted h_2 is much higher than the reference value. The ε'_2 is probably underestimated in this inversion. For the results of D04, the value of ε'_2 varies from 7.8 to 9.0, which is even lower than D03. The water front has a good tendency of increasing. The gradient curves of dielectric constant can be seen in figure 6.15. From the figure, we find a good evolution of water front depth for D04. For D03, we need to get more stable ε'_2 to keep h_2 increasing.

The inversion results of D13 and D14 are summarized in Tables 6.18 and 6.19. For the results of D03, the value of ε'_2 varies from 9.8 to 10.7, which is more stable than D03. However, the water front depth of slab 13 at T_4 and T_5 seems too high compared to the results of gammadensimetry. Besides, we observe no change from 1 month to 4 months. The results of D14 obtain the similar values of ε'_1 and ε'_2 as D13. At T_2, the value of h_2 is too high to be accepted. Like we observed from other slabs of concrete C1, the water front is close to the dry surface after one month. The gradient curves of dielectric constant for D13 and D14 can be seen in figure 6.16. As the time increases, most of the curves move to higher value of h_2 or increase the upper limit value, corresponding to ε'_2. This change

Table 6.17: Inversion results of parameters $[\varepsilon_1, \varepsilon_2, h_2]$ from CMP measurements on D04 on combined $TE_1 - TE_3$ mode using $\arctan(x)$ waveguide model as the inverse model + gammadensimetry results

Time in water	$\min(CF^{TE_{0\ldots m}})$	ε'_e	ε'_1	ε'_2	$h_{2\,\min}$ **(m)**	$h_{2\,\max}$ **(m)**
GPR/Gamma.	**($\times 10^6$ m/s)**	**Inv.**	**Inv.**	**Inv.**	**Inv./Gamma.**	**Inv./Gamma.**
T_1 (1 h/2 h)	0.30	6.9	6.8	7.8	0/0	0.015/0.018
T_2 (4 h/4 h)	-	-	-	-	-	-
T_3 (20 h/10 h)	-	-	-	-	-	-
T_4 (44 h/30 h)	2.51	7.3	6.9	7.9	0.045/0.030	0.060/0.036
T_5 (168 h/122 h)	2.12	7.6	6.9	8.7	0.045/0.030	0.060/0.048
T_6 (1 month/-)	1.31	8.0	7.0	8.9	0.060/-	0.085/-
T_7 (4 months/-)	3.92	8.6	7.0	9.0	0.100/-	0.115/-

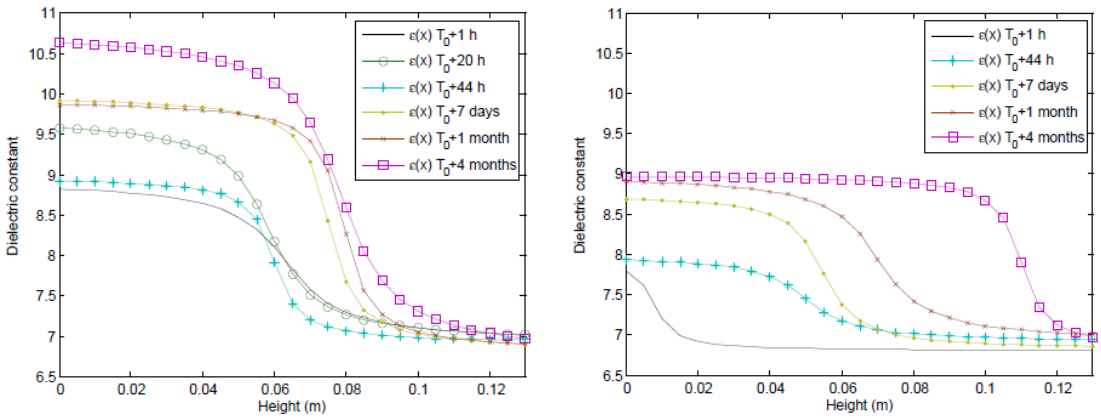

(a) D03 (b) D04

Figure 6.15: Evolution of inverted dielectric constant gradient on function of imbibition time of (a) D03 and (b) D04

Table 6.18: Inversion results of parameters $[\varepsilon_1, \varepsilon_2, h_2]$ from CMP measurements on D13 on combined $TE_2 - TE_4$ mode using $\arctan(x)$ waveguide model as the inverse model + gammadensimetry results

Time in water	$\min(CF^{TE_{0\ldots m}})$	ε'_e	ε'_1	ε'_2	$h_{2\,\min}$ **(m)**	$h_{2\,\max}$ **(m)**
GPR/Gamma.	**($\times 10^6$ m/s)**	**Inv.**	**Inv.**	**Inv.**	**Inv./Gamma.**	**Inv./Gamma.**
T_1 (1 h/2 h)	-	-	-	-	-	-
T_2 (4 h/4 h)	2.37	8.8	8.3	9.8	0.035/0.024	0.055/0.030
T_3 (20 h/8 h)	2.39	9.0	8.3	9.8	0.045/0.036	0.065/0.048
T_4 (44 h/30 h)	0.69	9.9	8.3	10.8	0.080/0.054	0.100/0.072
T_5 (168 h/124 h)	4.12	9.5	8.3	10.0	0.095/-	0.110/-
T_6 (1 month/ -)	0.54	9.6	8.2	10.7	0.065/-	0.085/-
T_7 (4 months/ -)	2.63	9.6	8.2	10.7	0.065/-	0.085/-

Table 6.19: Inversion results of parameters $[\varepsilon_1, \varepsilon_2, h_2]$ from CMP measurements on D14 on combined $TE_2 - TE_4$ mode using arctan(x) waveguide model as the inverse model + gammadensimetry results

Time in water	$\min(CF^{TE_{0\ldots m}})$	ε'_e	ε'_1	ε'_2	$h_{2\,\min}$ **(m)**	$h_{2\,\max}$ **(m)**
GPR/Gamma.	**($\times 10^6$ m/s)**	**Inv.**	**Inv.**	**Inv.**	**Inv./Gamma.**	**Inv./Gamma.**
T_1 (1 h/2 h)	-	-	-	-	-	-
T_2 (4 h/4 h)	3.73	9.3	8.3	9.8	0.080/0.024	0.095/0.030
T_3 (20 h/8 h)	4.52	8.9	8.2	9.9	0.045/0.036	0.060/0.048
T_4 (44 h/30 h)	5.31	9.8	8.2	10.7	0.085/0.054	0.095/0.072
T_5 (168 h/124 h)	4.04	9.6	8.2	10.7	0.070/-	0.090/-
T_6 (1 month/ -)	1.71	10.1	8.2	10.8	0.095/-	0.110/-
T_7 (4 months/ -)	-	-	-	-	-	-

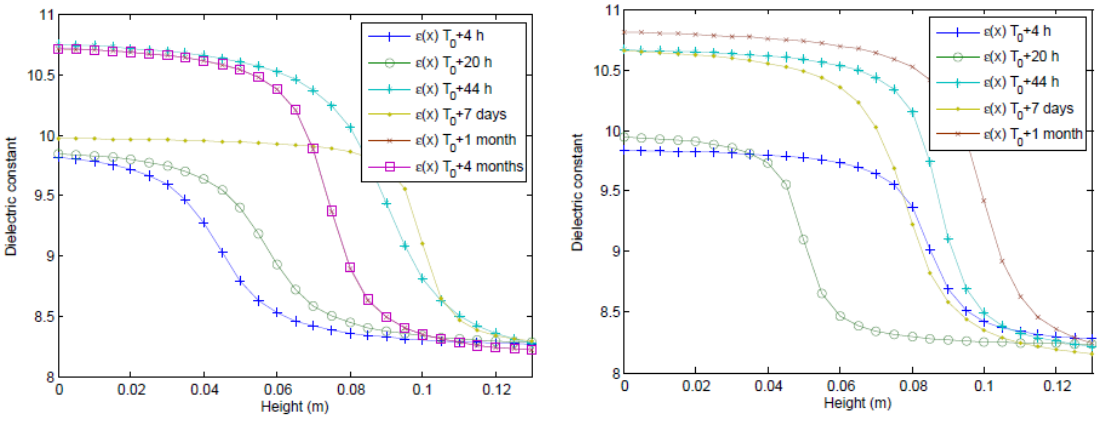

(a) D13 (b) D14

Figure 6.16: Evolution of inverted dielectric constant gradient on function of imbibition time of (a) D13 and (b) D14

of the curves is related to the increment of water content inside the concrete.

6.5.3 Conclusion

The experiments of sea water imbibition were conducted in St. Brieuc. We have chosen 8 slabs of two concretes for the CMP measurements. The central frequency of GPR is 2.6 GHz. Slabs 03, 04, 05 and 07 are from the same concrete C3. Slabs 13, 14, 15 and 17 are from the same concrete C1. We have two slabs, 07 and 17, to conduct the water imbibition. At the same time, the other slabs were put in the salty water with the chloride content 35 g/L.
The GPR data were analysed in the same process as the water imbibition in Nantes. From the results, we observe a stronger attenuation on GPR signals during the penetrating of sea water. For both concretes, the water front goes up with the same speed for the water and sea water. The accuracy of the inversion results are strongly dependent on the accuracy of GPR data. In saturated state, the permittivity of concrete with sea water is higher than that with normal water.

6.6 Conclusion

We have analysed the GPR measurements from several experimental campaigns, which are classified as 3 parts here: carbonated concrete, concrete with water imbibition and concrete with sea water imbibition.
For carbonated concrete, the GPR data have been analysed by picking the amplitude of response signals and determining the dielectric constant of each slab. With the analysis, we are able to build some relationships between the EM observables and the carbonation depths.
In the two parts of imbibition, the GPR data have been analysed by picking the amplitude of response signals and determining the dielectric and geometric characteristics of concrete slabs using two-layer and $\arctan(x)$ WG inversions.
We have shown that the combination of the multi-layer WG model and GPR measurements allowed to estimate the dielectric and geometric characteristics of the concrete slab with gradient inside. The inversion results from the GPR data are sensitive to the noise in the measurements. But it is interesting to be applied to monitoring the water penetration into concrete as it provides the water content gradient. To improve the accuracy of the inversion results, it is recommended to prepare for the experiments carefully with the choosing of antennas and the measuring configuration.

Chapter 7

Conclusions and future works

Contents

7.1 Conclusions

Nowadays, concrete, especially reinforced concrete, is certainly the most popular material in civil engineering structures. Its working performance and durability has gained important attention over the service life. Traditional destructive tests to monitor its properties are commonly expensive, time consuming, and the most importantly, cause damage to the tested structures. In this case, non-destructive testing (NDT) techniques have been rapidly developed in recent years to supplement or even replace the destructive techniques. Electromagnetic (EM) NDT techniques are particularly suitable for monitoring concrete conditions as EM waves are sensitive to the indicators and parameters related to the durability of concrete. Among these techniques, Ground Penetrating Radar (GPR) is one of the most widely used methods, which can see through the material structure. In the beginning, most GPR applications were focused on locating the internal characteristics of concrete, such as reinforcement, voids and layer thickness. Then, in the past ten years, some studies were conducted on the evaluation of durability indicators, such as porosity, carbonation depth, water content and chloride content, since the EM observables are sensitive to these parameters. However, there is still comparatively little effort that has been done in this field.

In most published works, the water or chlorides inside concrete is conditioned as homogeneous for the evaluation. However, in real concrete structures, the distribution of these factors is much more complex. And to monitor the penetration of water and chloride is essentially important to the durability of concrete as they are the main factors causing corrosion of the reinforcement inside concrete.

Under this circumstance, this thesis focused on developing the EM evaluation technique with the application of GPR, in order to determine gradients of water content (or chloride

content) inside concrete. The carbonation depth of concrete was also studied as it can cause the depassivation of reinforcement and accelerate the corrosion.
Knowing the intrinsic relationship between the EM observables (e.g. amplitude, permittivity) and the durability monitoring parameters (e.g. water content and chloride content), we applied two measuring configurations for the acquirement of multi-offset GPR data. One semi-destructive EM test, EM cylindrical/coaxial cell, is used as a calibration method for the water content and chloride content.
The first configuration is a simple approach to obtain 4 measurements with 4 offsets. Using the surface wave transmitted directly from the transmitter to the receiver through the material, the dielectric constant ε' of the material is calculated from the group velocity v_g of the surface wave. Due to the limit of the direct wave's penetration depth, this method is just used to measure the ε' of the material's surface. Moreover, the accuracy of it may be disturbed by some reflections from the subsurface or reinforcement inside.
The second configuration is to use wide-angle reflection and refraction (WARR) or common midpoint (CMP) method to get multi-offset data, determining the propagation velocity of guided waves, and then to characterize the dielectric and geometric properties of the waveguide with the velocity. A robot prototype moving GPR antennas with CMP mode has been developed in the lab of GERS, IFSTTAR. This prototype facilitates us to conduct CMP measurements with smaller displacements and more moving steps in an automatic way.
Generally speaking, the first configuration is able to characterize the surface of the material while the second configuration can see through the structure. As our main objective is to determine the gradients inside concrete, the second configuration was mainly integrated in our process of study. Moreover, since the heterogeneity of concrete was not taken into account in our study, we chose CMP method to acquire multi-offset data in all the experiments.
The formation of the waveguide (ε'_1) requires the waveguide medium to be placed between the air (ε'_0) and a material with smaller or much stronger permittivity ($\varepsilon'_1 > \varepsilon'_2$ or $\varepsilon'_1 \ll \varepsilon'_2$). The EM waves can propagate in a waveguide when the total thickness of the waveguide is smaller than or close to the wavelength: $h \leq \lambda$. This criterion was satisfied for the concrete slabs with the thicknesses from 12 cm to 15 cm, as the GPR antennas in tests were near 1 GHz and 2 GHz.
Then a multi-layer waveguide model was developed by integrating the Parallel model into the fundamental modal theory equation to determine the gradients. The phase velocity dispersion curves taking into account the geometric dispersion were used to determined the dielectric and geometric properties of the multi-layer medium using this model.
However, as we can find in the Parallel model, the dielectric constant and thickness of each layer is correlated with each other. We are not able to determine each parameter without any additional constraints. Finally, we have validated the inversion of the multi-layer waveguide with the two-layer model and $\arctan(x)$ model. The limitation of the inversion is that the results are very sensitive to the choice of initial values since the convergence of the cost function is not unique. This can be solved by reducing the parameters for the inversion. In the two-layer model, the values of ε'_1 and ε'_2 need to be estimated before the inversion. In the $\arctan(x)$ model, the value of ε'_1 need to be known. To estimate the two parameters, we can calculate the permittivity of the first layer from the velocity of the surface wave. The values of them can also be extrapolated from the measurement of EM cell. These two models, derived from the multi-layer model, can be applied to monitoring

the water or chloride penetration.
In our experiments for monitoring the water or chloride penetration, concrete slabs were placed in the water or sea water submerged to 1 cm from the bottom. The water and chlorides went up inside the concrete by capillary effects. With the two-layer waveguide model, the slab was divided into two layers: the dry layer and the wet layer. By assuming that the dielectric property of each layer is unchangeable, we are able to monitor the variation of water front depth according to the imbibition time. However, the permittivity of each layer cannot be determined directly from the inversion due to the correlation of the parameters. This makes the model less effective for the monitoring. The correlation of the dielectric constants of multi layers can be avoided if there is an intrinsic relationship among them. As we found from the reference results by gammadensimetry, the shape of the water content curve is like a reversed arctan function. We therefore developed the arctan(x) model to assess the gradient curves inside concrete, benefiting from the characteristics of Parallel model.
The experiments in this thesis were conducted in several collaborative experimental campaigns from two projects: EvaDéOS and APOS. Several NDT techniques, such as resistivity test, ultrasonic test and capacitive probes, were applied in the campaigns. To combine the results of GPR with other methods, we will be able to have better assessment of the concrete's performance and durability.
In summary, the main tasks completed in the research presented in this thesis are listed as follows:

I Two dispersion models, Debye's model and Jonscher's model, were adopted to their applicability of describing concrete by fitting the frequency dependent complex permittivity of various concrete samples in different moisture conditions.

II The GPR signals propagating in the air and different non-dispersive and dispersive media were modeled by Debye's model using GprMax2D.

III A two-layer waveguide model was validated to determine the thickness of each layer from the phase velocity of guided EM waves. It can be applied to detecting the two-layer media or concrete that can be regarded as two layers.

IV An arctan(x) waveguide model was validated to determine the gradient curve of dielectric constant from the phase velocity of guided waves. It can be applied to the monitoring of concrete imbibition by capillary effects to describe a more precise water gradient curve inside.

V The links between the durability indicators (e.g. carbonation depths, water content, chloride content) and the permittivity of each concrete were built by combining GPR results with several reference results and the calibration from EM cell.

VI The penetration of water and chlorides into concrete slabs from several concrete was monitored by the two-layer and arctan(x) waveguide models.

The findings reported in this thesis demonstrate the potential of EM NDT techniques, especially GPR, to evaluate the durability indicators of concrete non-destructively and to monitor the evolution of parameters related to corrosion over time. The working principles of GPR allows it to investigate the variation of material properties through depth. It is therefore practical to apply GPR to the non-destructive evaluation of concrete structures under inhomogeneous conditions.

7.2 Future Works

The evaluation process of dielectric and geometric properties of two-layer media or media with gradients is based on the experiments in laboratory for controlled conditions. For in situ tests, the conditions of concrete can be much more complex. The developed multi-layer waveguide model works only when the dielectric constant of each layer is known or the internal variation law of the dielectric property is known. For detecting a material where its dielectric properties are multi-layered or distributed as gradients, some work are expected in the future following the achievements of current research:

I The simple approach of GPR with 4 offsets can be used to estimate the dielectric constant of the surface layer. It can be applied to the assessment of cover concrete. However, the propagation velocity of the surface wave can be affected by the sub-surface or reinforcement inside concrete. It is necessary to quantify the penetration depth of the surface wave, in order to predict the accuracy of the estimations.

II The CMP measurements on carbonated slabs were not well planned since they were not aimed for the study in the beginning. In fact, from the GPR response from the slabs, we can see that carbonation has obvious impacts on the dielectric properties of concrete. It can be a direction to study the carbonation depth of concrete by EM NDT techniques.

III The current way of filtering with rectangular time window is sometimes difficult to separate different waves. The approximation of phase velocity will be affected by losing some effective waves and keeping some interferences. In this case, a new procedure of filtering the GPR data is required for the extraction of dispersion curves.

IV The EM observable involved in this thesis is mainly the dielectric constant. In fact, the presence of chlorides contributes more to the attenuation variation, corresponding to the parameters: the imaginary part of permittivity ε'' and conductivity σ. The waveguide model can be completed by taking into account the parameters ε'' or σ.

V The waveguide model integrated with the Parallel model cannot be applied to the inversion of the parameters $[\varepsilon'_1, h_1, \varepsilon'_2, h_2, \varepsilon'_3, h_3, ...]$ because the solution will not be unique due to the correlation of the parameters. As the number of layers increases, the approximation of the properties for each layer becomes impossible. A more practical multi-layer model can be built by changing the equation of modal theory from one layer to multi layers, based on the reflection and transmission in a layered medium [Kong, 1986].

7.3 List of Publications

7.3.1 International journal publications

. X. Xiao, A. Ihamouten, G. Villain and X. Dérobert, "Use of Electromagnetic Two-layer Wave-Guided Propagation in the GPR Frequency Range to Characterize Water Transfer in Concrete", NDT & E international (under review), 2015.

. X. Xiao, A. Ihamouten, B. Guan, G. Villain and X. DÃŀrobert, "The use of GPR for characterizing water transfers in Tuffeau walls ", to be submitted, 2016.

7.3.2 Publications in the proceedings of conferences

. X. Xiao, A. Ihamouten, G. Villain, and X. Dérobert, "Parametric study on processing GPR signals to get a dispersion curve", Proceedings of the 15th Internarional Conference on Ground Penetrating Radar, Brussels, Belgium, July 2014.

. X. Xiao, A. Ihamouten, X. Dérobert, and G. Villain, "Use of electromagnetic waves propagating in multilayer waveguide to characterize water transfer in concrete", 8th International Workshop on Advanced Ground Penetrating Radar, Florence, Italy, July 2015.

. X. Xiao, A. Ihamouten, G. Villain, and X. Dérobert, "Application of electromagnetic waves propagating in multi-layered waveguide to monitor chloride ingress into concrete", International Symposium Non-Destructive Testing in Civil Engineering (NDT-CE 2015), Berlin, Germany, September 2015.

Bibliography

Abraham, O., Métais, V., Villain, G., Plantier, G., Le Duff, A., and Durand, O. (2015). Influence of water gradient on surface wave measurements in concrete. In *International Symposium on Non Destructive Testing in Civil Engineering (NDT-CE 2015)*, Berlin, Germany. 104

ACI (2008). *Guide to Durable Concrete (ACI 201.2R)*. American Concrete Institute. 9

Adous, M., Quéffélec, P., and Laguerre, L. (2006). Coaxial/cylindrical transition line for broadband permittivity measurement of civil engineering materials. *Measurement Science and Technology*, 17(8):2241. xv, 26, 27, 74

AFGC (2007). *Concrete Design for a Given Structure Service Life: Durability management with regard to reinforcement corrosion and alkali-silica reaction*. Association Française de Génie Civil(AFGC), Paris. 1, 2, 8, 9, 11, 12, 15

AFPC-AFREM (1997). *Compte-Rendu des Journées Techniques Durabilité des bétons, Méthodes recommandées pour la mesure des grandeurs associées á la durabilité*. Laboratoire Matériaux et Durabilité des Constructions, INSA. 14, 98, 125

Andrade, C. and Alonso, C. (2004). Test methods for on-site corrosion rate measurement of steel reinforcement in concrete by means of the polarization resistance method. *Materials and Structures*, 37(9):623–643. 13

Andrade, C., Sarria, J., and Alonso, C. (1999). Relative humidity in the interior of concrete exposed to natural and artificial weathering. *Cement and Concrete Research*, 29:1249–1259. 10

Annan, A. (1996). Transmission dispersion and GPR. *Journal of Environmental and Engineering Geophysics*. 37

Annan, A., Waller, W., Strangway, D., Rossiter, J., Redman, J., and Watts, R. (1975). The electromagnetic response of a low-loss two-layer dielectric earth for horizontal electric dipole excitation. *Geophysics*, 40(2):285–298. 56

Annan, A. P. (1973). Radio interferometry depth sounding Part I : Theoretical discussion. *Geophysics*, 38(3):557–580. 56

Arcone, S. A. (1981). Distortion of model subsurface radar pulses in complex dielectrics. *Radio Science*, 16(5):855–864. 37

Arcone, S. A. (1984). Field observations of electromagnetic pulse propagation in dielectric slabs. *Geophysics*, 49(10):1763. 37, 56, 59, 62

Arcone, S. A., Peapples, P. R., and Liu, L. (2003). Propagation of a ground-penetrating radar (GPR) pulse in a thin surface waveguide. *Geophysics*, 68(6):1922–1933. 56, 59

Ardekani, M. and Lambot, S. (2014). Full-wave calibration of time- and frequency-domain ground-penetrating radar in far-field conditions. *Geoscience and Remote Sensing, IEEE Transactions on*, 52(1):664–678. 2

ASTM (2009). *Test Method for Corrosion Potentials of Uncoated Reinforcing Steel in Concrete*. American Society for Testing and Materials (ASTM) International, the US. 18

ASTM:C1583/C1583M-13 (2010). Standard Test Method for Tensile Strength of Concrete Surfaces and the Bond Strength or Tensile Strength of Concrete Repair and Overlay Materials by Direct Tension (Pull-off Method). *Annual Book of ASTM Standards*, 93(Reapproved 1998):1–5. 13

ASTM:C39/C39M-12a (2012). Standard Test Method for Compressive Strength of Cylindrical Concrete Specimens. *ASTM International*, pages 1–7. 13

Babaei, K. (1986). Evaluation of half-cell corrosion detection test for concrete bridge decks. 2, 18

Balayssac, J., Garnier, V., Villain, G., Sbartaï, Z., Dérobert, X., Piwakowski, B., Breysse, D., and Salin, J. (2015). An overview of 15 years of french collaborative projects for the characterization of concrete properties by combining ndt methods. In *International Symposium on Non Destructive Testing in Civil Engineering (NDT-CE 2015)*, Berlin, Germany. 94, 104

Balayssac, J., Laurens, S., Arliguie, G., Ploix, M., Breysse, D., Derobert, X., and Piwakowski, B. (2009). Evaluation of concrete structures by combining non-destructive testing methods (senso project). In *7th International Symposium on Non Destructive Testing in Civil Engineering, NDTCE'09*, pages 391–398, Nantes, France. 94

Balayssac, J.-P., Laurens, S., Arliguie, G., Breysse, D., Garnier, V., Dérobert, X., and Piwakowski, B. (2012). Description of the general outlines of the French project SENSO - Quality assessment and limits of different NDT methods. *Construction and Building Materials*, 35:131–138. 2, 20, 26, 32

Baroghel-Bouny, V. (1994). *Caractérisation des pâtes de ciment et des bétons, méthodes, analyse , interprétations*. LCPC. 10

Baroghel-Bouny, V., Andrade, C., and Kropp, J. (2002). Which toolkit for durability evaluation as regards chloride ingress into concrete? part ii: Development of a performance approach based on durability indicators and monitoring parameters. In *Third International RILEM Workshop on Testing and Modeling Chloride Ingress into Concrete*, pages 137–163. 14

Baroghel-Bouny, V., Thiéry, M., and Wang, X. (2011). Modelling of isothermal coupled moisture-ion transport in cementitious materials. *Cement and Concrete Research*, 41(8):828–841. 9

Baroghel-Bouny, V., Wang, X., Thiery, M., Saillio, M., and Barberon, F. (2012). Prediction of chloride binding isotherms of cementitious materials by "analytical" model or "numerical" inverse analysis. *Cement and Concrete Research*, 42(9):1207–1224. 9

Baron, J. and Sauterey, R. (1982). *Le béton hydraulique: connaissance et pratique*. Presses de l'Ecole Nationale des Ponts et Chaussées. 7

Breysse, D. and Abraham, O. (2005). *Méthodologie d'évaluation non destructive de l'état d'altération des ouvrages en: béton*. Presses de l'école nationale des ponts et chaussées. 15

Buck, A. L. (1981). New Equations for Computing Vapor Pressure and Enhancement Factor. 10

Budden, K. (1961). *The Wave-Guide Mode Theory of Wave Propagation*. Logos Press, London. 63

Bungey, J. (2004). Sub-surface radar testing of concrete: a review. *Construction and Building Materials*, 18(1):1–8. 32, 56

Bungey, J. H., Grantham, M. G., and Millard, S. (2006). *Testing of concrete in structures*. Crc Press. 12, 19

Butler, D. K. (2005). *Near-surface geophysics*. Society of Exploration Geophysicists Tulsa, pp. 415–416. 24

Büyüköztürk, O. (1998). Imaging of concrete structures. *NDT & E International*, 31(4):233–243. 2

Castellote, M., Andrade, C., and Alonso, C. (2001). Measurement of the steady and non-steady-state chloride diffusion coefficients in a migration test by means of monitoring the conductivity in the anolyte chamber. Comparison with natural diffusion tests. *Cement and Concrete Research*, 31(10):1411–1420. 14

Chew, W. C. (1995). *Waves and fields in inhomogeneous media*. IEEE Press, New York. 62

Cole, K. S. and Cole, R. H. (1941). Dispersion and Absorption in Dielectrics I. Alternating Current Characteristics. *The Journal of Chemical Physics*, 9:341–351. 38

Cole, K. S. and Cole, R. H. (1942). Dispersion and Absorption in Dielectrics II. Direct Current Characteristics. *The Journal of Chemical Physics*, 10:98–105. 38

Collepardi, M. (1995). Quick method to determine free and bound chlorides in concrete. In *Proceedings of the 1st International RILEM Workshop "Chloride penetration into concrete"*, pages 10–16, Saint-Rémy-lès-Chevreuse, France. 14

Dai, R. and Young, C. T. (1997). Transient Fields of a Horizontal Electric Dipole on a Multilayered Dielectric Medium. *IEEE Transactions on Antennas and Propagation*, 45(6):1023–1031. 56, 67

Daily, W., Ramirez, A., Binley, A., and Henry-Poulter, S. (1993). Electrical resistance tomography of concrete structures. Technical report, Lawrence Livermore National Lab., CA (United States). 20

Daily, W., Ramirez, A., Binley, A., and LeBrecque, D. (2004). Electrical resistance tomography. *The Leading Edge*, 23(5):438–442. 20

David K. Cheng (1989). *Field and Wave Electromagnetics.pdf*. Pearson Education, 2nd edition. 34

Davidson, D. W. and Cole, R. H. (1951). Dielectric relaxation in glycerol, propylene glycol, and n-propanol. *The Journal of Chemical Physics*, 19(12):1484–1490. 38

De Larrard, F. and Sedran, T. (2002). Mixture-proportioning of high-performance concrete. *Cement and Concrete Research*, 32(11):1699–1704. 8

Debye, P. (1929). Polar molecules. *Journal of the Society of Chemical Industry*, 48(43):1036–1037. 32, 37

Dérobert, X., Iaquinta, J., Klysz, G., and Balayssac, J.-P. (2008). Use of capacitive and GPR techniques for the non-destructive evaluation of cover concrete. *NDT & E International*, 41(1):44–52. 2, 21, 22, 24, 26, 43, 56, 135

Dérobert, X., Villain, G., Cortas, R., and Chazelas, J. L. (2009). EM characterization of hydraulic concretes in the GPR frequency-band using a quadratic experimental design. In *NDTCE 2009*, pages pp 177–182, France. xv, 26, 27, 29, 37

du Plooy, R. (2013). *The development and combination of electromagnetic non-destructive evaluation techniques for the assesment of cover concrete condition prior to corrosion.* Theses, Université Nantes Angers Le Mans. 2, 18

du Plooy, R., Villain, G., Palma Lopes, S., Ihamouten, A., Dérobert, X., and Thauvin, B. (2015a). Electromagnetic non-destructive evaluation techniques for the monitoring of water and chloride ingress into concrete: a comparative study. *Materials and Structures*, 48:369–386. xv, 2, 20, 21

du Plooy, R., Villain, G., Palma Lopes, S., Ihamouten, a., Dérobert, X., and Thauvin, B. (2015b). Electromagnetic non-destructive evaluation techniques for the monitoring of water and chloride ingress into concrete: a comparative study. *Materials and Structures*, 48(1-2):369–386. 32

EN197-1 (2000). *Cement - part 1: composition, specifications and conformity criteria for common cements*. European Committee for Standardisation. 7, 109

Fares, M. (2015). *Utilisation des méthodes de mesures non destructives dans la modélisation probabiliste de la durée de vie des ouvrages en béton.* PhD thesis, Ecole centrale de Nantes, France. 29, 126

Fares, M., Villain, G., Fargier, Y., Thiery, M., and Dérobert, X. (2015). Estimation of water gradient and concrete durability indicators using capacitive and electrical probes. In *International Symposium on Non Destructive Testing in Civil Engineering (NDT-CE 2015)*, Berlin, Germany. 21, 104, 118

Fauchard, C., Beaucamp, B., and Laguerre, L. (2015). Non-destructive assessment of hot mix asphalt compaction/ density with a step-frequency radar: case study on a newly paved road. *Near Surface Geophysics*, 13(2068). 57, 148

Gabriels, P., Snieder, R., and Nolet, G. (1987). In situ measurements of shear-wave velocity in sediments with higher-mode rayleigh waves. *Geophysical Prospecting*, 35:187–196. 56

Galagedara, L. W., Parkin, G. W., and Redman, J. D. (2005). Measuring and modeling of direct ground wave depth penetration under transient soil moisture conditions. *Subsurface Sensing Technologies and Applications*, 6:193–205. 60

Garnier, V., Piwakowski, B., Abraham, O., Villain, G., Payan, C., and Chaix, J. F. (2013). Acoustic techniques for concrete evaluation: Improvements, comparisons and consistency. *Construction and Building Materials*, 43:598–613. 2, 16

Giannopoulos, A. (1997). *The Investigation of Transmission-Line Matrix and Finite-Difference Time-Domain Methods for the Forward Problem of Ground Probing Radar*. PhD thesis, The University of York. 37

Giannopoulos, A. (2005). Modelling ground penetrating radar by gprmax. *Construction and Building Materials*, 19(10):755 – 762. Non Destructive Testing: Selected papers from Structural Faults and Repair 2003. 43, 50, 76

Gomez, C., Sbartaï, Z., Villain, G., Bonnet, S., Lataste, J., Balayssac, J., and Dérobert, X. (2015). Influence of concrete carbonation on ndt methods used for moisture assessment. *to be submitted to Construction and Building Materials Journal*. 95, 96

Gu, P. and Beaudoin, J. J. (1998). *Obtaining effective half-cell potential measurements in reinforced concrete structures*. Institute for Research in Construction, National Research Council of Canada. 18

Havriliak, S. and Negami, S. (1967). A complex plane representation of dielectric and mechanical relaxation processes in some polymers. *Polymer*, 8(0):161 – 210. 38

Hudec, P., MacInnis, C., and Moukwa, M. (1986). The capacitance effect method of measuring moisture and salt content of concrete. *Cement and Concrete Research*, 16(4):481 – 490. 21

Hugenschmidt, J. and Loser, R. (2007). Detection of chlorides and moisture in concrete structures with Ground Penetrating Radar. *EMPA Activities*, page 37. 2, 13, 56

Huisman, J. A., Hubbard, S. S., and Annan, A. P. (2003). Measuring soil water content with Ground Penetrating Radar: A review. *Vadose Zone Journal*, 2(4):476–491. 24

Ihamouten, A. (2011). *Caractérisation physique et hydrique de bétons d'ouvrage par propagation d'ondes électromagnétiques*. PhD thesis, Université de Nantes. 26, 29, 57, 59, 64

Ihamouten, A., Chahine, K., Baltazart, V., Villain, G., and Dérobert, X. (2011). On Variants of the Frequency Power Law for the Electromagnetic Characterization of Hydraulic Concrete. *IEEE Transactions on Instrumentation and Measurement*, 60:3658–3668. 39, 51

Ihamouten, A., Villain, G., and Dérobert, X. (2012). Complex permittivity frequency variations from multioffset gpr data: Hydraulic concrete characterization. *Instrumentation and Measurement, IEEE Transactions on*, 61(6):1636–1648. 37, 56, 59, 76

Irving, J. D. and Knight, R. J. (2003). Removal of Wavelet Dispersion from Ground-Penetrating Radar Data. *Geophysics*, 68:960–970. 37

Jiang, Q. J. (2015). 2014-2015 precast concrete industry report. Technical report, China Concrete& Cement-based Products Association. 1

Jones, R. and Făcăoaru, I. (1969). Recommendations for testing concrete by the ultrasonic pulse method. *Matériaux et Constructions*, 2(4):275–284. 16

Jonscher, A. (1983). *Dielectric Relaxation in Solids*. Chelsea Dielectrics Press. 32, 38, 42

Kalogeropoulos, A. (2012). *Non-Destructive Determination of Chloride and Water Content in Concrete Using Ground Penetrating Radar*. PhD thesis, Ecole polytechnique fédérale de Lausanne, Suisse. 67

Kalogeropoulos, A., van der Kruk, J., and Hugenschmidt, J. (2011). Monitoring the evolution of water and chloride in concrete using GPR full-waveform inversion. *2011 6th International Workshop on Advanced Ground Penetrating Radar (IWAGPR)*, pages 1–6. 26

Kalogeropoulos, A., Van Der Kruk, J., Hugenschmidt, J., Bikowski, J., and Brühwiler, E. (2013). Full-waveform GPR inversion to assess chloride gradients in concrete. *NDT and E International*, 57:74–84. 2, 26

Khoury, G. A. (2000). Effect of fire on concrete and concrete structures. *Progress in Structural Engineering and Materials*, 2(4):429–447. 1

Klysz, G., Balayssac, J., and Ferrières, X. (2008). Evaluation of dielectric properties of concrete by a numerical FDTD model of a GPR coupled antennaâĂŤParametric study. *NDT & E International*, 41(8):621–631. 26

Klysz, G. and Balayssac, J.-P. (2007). Determination of volumetric water content of concrete using ground-penetrating radar. *Cement and Concrete Research*, 37(8):1164–1171. 2, 24, 32, 111

Kong, J. (1986). *Electromagnetic Wave Theory*. A Wiley-Interscience publication. John Wiley&Sons. 34, 36, 166

Kosmatka, S. H. and Wilson, M. L. (2011). Design and control of concrete mixtures: The guide to applications, methods, and materials. *Portland Cement Association*. 1

Kraus, J. D. and R.Carver, K. (1973). *Electromagnetics*. McGraw-Hill New York, 2nd edition. 32

Lai, W., Kind, T., and Wiggenhauser, H. (2011). Frequency-dependent dispersion of high-frequency ground penetrating radar wave in concrete. *NDT & E International*, 44(3):267–273. 37

Lai, W., Kou, S., and Poon, C. (2012). Unsaturated zone characterization in soil through transient wetting and drying using GPR joint time-frequency analysis and grayscale images. *Journal of Hydrology*, 452-453:1–13. 132

Lai, W., Kou, S., Tsang, W., and Poon, C. (2009). Characterization of concrete properties from dielectric properties using ground penetrating radar. *Cement and Concrete Research*, 39(8):687–695. 56

Lai, W., Tsang, W., Fang, H., and Xiao, D. (2006). Experimental determination of bulk dielectric properties and porosity of porous asphalt and soils using GPR and a cyclic moisture variation technique. *Geophysics*, 71(4). 9

Lambot, S., Slob, E., van den Bosch, I., Stockbroeckx, B., and Vanclooster, M. (2004). Modeling of ground-penetrating Radar for accurate characterization of subsurface electric properties. *IEEE Transactions on Geoscience and Remote Sensing*, 42(11):2555–2568. 2

Lambot, S., Slob, E., and Vereecken, H. (2007). Fast evaluation of zero-offset Green's function for layered media with application to ground-penetrating radar. *Geophysical Research Letters*, 34(21):L21405. 2

Laurens, S., Balayssac, J., and Rhazi, J. (2005). Non-destructive evaluation of concrete moisture by GPR: experimental study and direct modeling. *Materials and Structures*, 38(November):827–832. 137

Laurens, S., Balayssac, J. P., Rhazi, J., and Arliguie, G. (2002). Influence of concrete relative humidity on the amplitude of Ground-Penetrating radar (GPR) signal. *Materials and Structures*, 35(4):198–203. 26, 56, 132

Lichtenecker, K. and Rother, K. (1931). Die herleitung des logarithmischen mischungsgesetzes aus allgemeinen prinzipien der stationären strömung. *Physikalishce Zeitschrift*, 31:255–260. 32, 39

Liu, L., Arcone, S. A., and Branchm, I. (1998). Numerical Simulation of the Wave-Guide Effect of the Near-Surface Thin Layer on Radar Wave Propagation. *Journal of Environmental & Engineering Geophysics*, 8:53–61. 56

Liu, Y.-W., Yen, T., and Hsu, T.-H. (2006). Abrasion erosion of concrete by water-borne sand. *Cement and concrete research*, 36(10):1814–1820. 1

LMDC (2009). Projet ANR SENSO Stratégie d'Evaluation Non destructive pour la Surveillance des Ouvrages en béton. Technical report, Université De Toulouse. 24

Louis, A., Van Der Wielen, A., Courard, L., and Nguyen, F. (2012). GPR detection of saturated areas into concrete in the presence of a water gradient. *2012 14th International Conference on Ground Penetrating Radar (GPR)*, pages 473–478. 2

MacGregor, J., Wight, J., Teng, S., and Irawan, P. (1997). *Reinforced concrete: Mechanics and design*. Prentice-Hall, Inc., 3rd edition. 7

Malhotra, V. and Carino, N. (2004). *Handbook on Nondestructive Testing of Concrete*. Taylor & Francis, 2nd edition. xv, 13, 16, 18, 20

Marie-Victoire, E., Bouichou, M., Jourdan, H., Thauvin, B., Queguiner, R., Olmi, R., and Riminesi, C. (2015). Moisture and salt ingress monitoring in concrete by resistivity and evanescent field dielectrometry techniques. In *International Symposium on Non Destructive Testing in Civil Engineering (NDT-CE 2015)*, Berlin, Germany. 118

Martinez, A. and Byrnes, A. P. (2001). *Modeling dielectric-constant values of geologic materials: An aid to ground-penetrating radar data collection and interpretation.* Kansas Geological Survey, University of Kansas. 39

McCann, D. and Forde, M. (2001). Review of NDT methods in the assessment of concrete and masonry structures. *NDT & E International*, 34:71–84. 17

Mehta, P. Kumar (2006). *CONCRETE: Microstructure, Properties, and Materials.* McGraw-Hill, 3rd edition. 1, 7, 8, 11

Morcous, G. and Erdogmus, E. (2010). Accuracy of Ground-Penetrating Radar for Concrete Pavement Thickness Measurement. 13

Neville, A. (1995). *Properties Of Concrete, 4th Edition.* Longman Scientific & Technical. 7

Nilson, A. H., Darwin, D., and Dolan, C. W. (2010). *Design of concrete structures.* McGraw-Hill, New York, 14th edition. 7, 8

Oppenheim, A. V., Schafer, R. W., Buck, J. R., et al. (1989). *Discrete-time signal processing*, volume 2. Prentice-hall Englewood Cliffs. 45

Park, C., Miller, R., and Xia, J. (1998). Imaging dispersion curves of surface waves on multi-channel resord. *SEG Technical Program Expanded Abstracts*, pages 1377–1380. 59

Parrott, L. (1994). Moisture conditioning and transport properties of concrete test specimens. *Materials and Structures*, 27(8):460–468. 125

PCA (2002). Types and Causes of Concrete Deterioration. Technical report, Portland Cement Association, the US. 9

Rhim, H. C. (2001). Condition monitoring of deteriorating concrete dams using radar. *Cement and Concrete Research*, 31(3):363–373. 56

Rhim, H. C. and Büyüköztürk, O. (1998). Electromagnetic properties of concrete at microwave frequency range. *ACI Materials Journal*, 95(3). 2

Robert, A. (1998). Dielectric permittivity of concrete between 50 mhz and 1 ghz and gpr measurements for building materials evaluation. *Journal of Applied Geophysics*, 40(1-3):89–94. 26, 32

Roth, M. and Holliger, K. (1999). Inversion of source-generated noise in high resolution seismic data. *The Leading Edge*, 18(12):1402–1406. 56

Sansalone, M. J. and Streett, W. B. (1997). Impact-echo: Nondestructive evaluation of concrete and masonry. *Bullbrier Press.* 17

Sansalone, M. J. and Streett, W. B. (2005). *Brochure: Field Instruments for Nondestructive Evaluation of Concrete & Masonry*. Impact-Echo Instruments, LLC. xv, 17

Sbartaï, Z., Laurens, S., Balayssac, J.-P., Arliguie, G., and Ballivy, G. (2006a). Ability of the direct wave of radar ground-coupled antenna for NDT of concrete structures. *NDT & E International*, 39(5):400–407. 26, 32, 148

Sbartaï, Z. M., Laurens, S., Balayssac, J. P., Ballivy, G., and Arliguie, G. (2006b). Effect of concrete moisture on radar signal amplitude. *ACI Materials Journal*, 103(6):419–426. 132, 137

SENSO (2009). Stratégie d'évaluation non destructive pour la surveillance des ouvrages en béton. Technical report, projet SENSO. 94, 95

Sheriff, R. (2002). *Encyclopedic Dictionary of Exploration Geophysics*. Geophysical references series. Society of Exploration Geophysicists, 4th edition. 37

Smith, G. (1984). Directive properties of antennas for transmission into a material halfspace. *IEEE Transactions on Antennas and Propagation*, 32(3):232–246. 56

Sonebi, M. (2006). Laboratory evaluation of effects of water proof admixtures and supplementary cementitious materials on durability of concrete used in hot climate. *International RILEM Workshop on Performance Based Evaluation and Indicators for Concrete Durability*, pages 359–368. 8

Song, H.-W. and Saraswathy, V. (2007). Corrosion Monitoring of Reinforced Concrete Structures - A Review. *International Journal of Electrochemical Science*, 2:1– 28. 1

Steelman, C. M. and Endres, A. L. (2009). Evolution of high-frequency ground-penetrating radar direct ground wave propagation during thin frozen soil layer development. *Cold Regions Science and Technology*, 57(2-3):116–122. 60

Strobbia, C. and Cassiani, G. (2007). Multilayer ground-penetrating radar guided waves in shallow soil layers for estimating soil water content. *Geophysics*, 72(4):J17–J29. 78

Taylor, M. A. and Arulanandan, K. (1974). Relationships between electrical and physical properties of cement pastes. *Cement and Concrete Research*, 4(6):881–897. 18

Thauvin, B., Bouteiller, V., Villain, G., Queguiner, R., and Gaillet, L. (2015). Opération de recherche apos (auscultation pour des ouvrages sûrs) évaluation du processus de corrosion des structures en béton armé, présentation, premiers résultats et perspectives. In *Journées Ouvrages d'Art 2015*, Nantes, France. 94

Thiery, M., Baroghel-Bouny, V., Bourneton, N., Villain, G., and Stéfani, C. (2007a). Modélisation du séchage des bétons: analyse des différents modes de transfert hydrique. *Revue européenne de génie civil*, 11(5):541–577. 104

Thiery, M., Belin, P., Baroghel Bouny, V., and Nguyen, M. D. (2008). Modelling of isothermal drying process in cementitious materials : Analysis of the moisture transfer and proposal of simplified approaches. In *3rd International conference on coupled T-H-M-C, Processes in geo-systems*, pages pp 571–581, France. 11

Thiery, M., Villain, G., Dangla, P., and Platret, G. (2007b). Investigation of the carbonation front shape on cementitious materials: Effects of the chemical kinetics. *Cement and Concrete Research*, 37(7):1047–1058. 9, 11

Torres-Luque, M., Bastidas-Arteaga, E., Schoefs, F., Sánchez-Silva, M., and Osma, J. F. (2014). Non-destructive methods for measuring chloride ingress into concrete: State-of-the-art and future challenges. *Construction and Building Materials*, 68:68–81. 1

Turner, G. (1994). Subsurface radar propagation deconvolution. *GEOPHYSICS*, 59(2):215–223. 37

U.S.B.R. (2005). Materials properties model of aging concrete. Technical report, U.S. Department of the Interior, Bureau of Reclamation. 9

van der Kruk, J. and Arcone, S. (2007). Fundamental and Higher Mode Inversion of Dispersed GPR Waves Propagating in an Ice Layer. *IEEE Transactions on Geoscience and Remote Sensing*, 45(8):2483–2491. 56, 57, 62, 76, 113

van der Kruk, J. and Slob, E. C. (2002). Effective source wavelet determination. *Proceedings of the 9th International Conference on Ground Penetrating Radar*, pages 144–149. 56

van der Kruk, J., Streich, R., and Green, A. G. (2006). Properties of surface waveguides derived from separate and joint inversion of dispersive TE and TM GPR data. *Geophysics*, 71(1):K19–K29. 24, 56, 59, 63

Villain, G. (2012). *Vers une évaluation des indicateurs de durabilité du béton pour le suivi de ses dégradations en laboratoire et sur ouvrage*. Ifsttar. 9, 10, 11, 104, 132

Villain, G., Balayssac, J. P., Garnier, V., Piwakowski, P., Salin, J., Fardeau, V., Dérobert, X., Coffec, O., and Joubert, A. (2014). Comparison of durability indicators obtained by non destructive testing methods to monitor the durability of concrete structures. In *7th European Workshop on Structural Health Monitoring EWSHM 2014*, pages 1497–1504, Nantes, France. 125

Villain, G., Bouteiller, V., Fares, M., Thauvin, B., Queguiner, R., E., M.-V., and Bouichou, M. (2015a). Suivi de la pénétration d'eau et de chlorure dans le béton : mesures non-destructives de résistivité en surface ou par des capteurs noyés. In *Journées Ouvrages d'Art 2015*, Nantes, France. 94

Villain, G., Dérobert, X., and Abraham, O. (2009). Use of ultrasonic and electromagnetic NDT to evaluate durability monitoring parameters of concrete. *Proceedings of the 7th Conf. Non-Destructive Testing in Civil Engineering*. 9, 18, 32

Villain, G., Dérobert, X., Sbartai, Z. M., and Balayssac, J.-P. (2010). Evaluation of concrete water content and other durability indicators by electromagnetic measurements. *Proceedings of the XIII Internarional Conference on Ground Penetrating Radar*, pages 1–6. 9, 13, 24, 111

Villain, G., Ihamouten, A., and Derobert, X. (2011a). Use of frequency power law to link the results of two em testing methods for the characterization of humid concretes. In

2011 6th International Workshop on Advanced Ground Penetrating Radar, IWAGPR 2011. 29

Villain, G., Ihamouten, A., Du Plooy, R., Palma-Lopes, S., and Derobert, X. (2015b). Use of electromagnetic non-destructive techniques for monitoring the chloride ingress into concrete. *Near Surface Geophysics*, 13:299–309. 20, 21, 26, 29, 32, 57, 59, 64

Villain, G., Le Marrec, L., and Rakotomanana, L. (2011b). Determination of the bulk elastic moduli of various concretes by resonance frequency analysis of slabs submitted to impact echo. *European Journal of Environmental and Civil Engineering*, 15(4):601–617. 18

Villain, G., Sbartaï, Z., and Dérobert, X. (2012). Durability diagnosis of a concrete structure in a tidal zone by combining NDT methods: Laboratory tests and case study. *Construction and Building Materials*, 37:893–903. xv, 1, 18, 22, 26, 32, 56

Villain, G., Sbartaï, Z., Lataste, J., Garnier, V., Dérobert, X., Abraham, O., Bonnet, S., Balayssac, J., Nguyen, N., and M., F. (2015c). Characterization of water gradients in concrete by complementary ndt methods. In *International Symposium on Non Destructive Testing in Civil Engineering (NDT-CE 2015)*, Berlin, Germany. 94, 95

Villain, G. and Thiery, M. (2006). Gammadensimetry: a method to determine drying and carbonation profiles in concrete. *NDT&E International Journal*, 39(4):328–337. 2, 27, 29

Villain, G., Thiery, M., and Platret, G. (2007). Measurement methods of carbonation profiles in concrete: Thermogravimetry, chemical analysis and gammadensimetry. *Cement and Concrete Research*, 37(8):1182–1192. 1, 11

Wang, K., Jansen, D. C., Shah, S. P., and Karr, A. F. (1997). Permeability study of cracked concrete. *Cement and Concrete Research*, 27(3):381 – 393. 1

Wierig, H. (1984). Longtime studies on the carbonation of concrete under normal outdoor exposure. In *Proceedings of RILEM Seminar*, pages pp 239–249, Hannover, Germany. 9

Wu, Y., Zhao, X., Li, F., and Fan, Z. (2003). Evaluation of mixing rules for dielectric constants of composite dielectrics by mc-fem calculation on 3d cubic lattice. *Journal of Electroceramics*, 11(3):227–239. 39

Xia, J., Miller, R. D., Park, C. B., Ivanov, J., Tian, G., and Chen, C. (2004). Utilization of high-frequency Rayleigh waves in near-surface geophysics. *The Leading Edge*, 23(8):753. 56

Xiao, X., Ihamouten, A., Villain, G., and Derobert, X. (2014). Parametric study on processing gpr signals to get a dispersion curve. In *Ground Penetrating Radar (GPR), 2014 15th International Conference on*, pages 575–580. 51

Yakuphanoglu, F., Aydogdu, Y., Schatzschneider, U., and Rentschler, E. (2003). DC and AC conductivity and dielectric properties of the metal-radical compound: Aqua[bis(2-dimethylaminomethyl-4-NIT-phenolato)]copper(II). *Solid State Communications*, 128(2-3):63–67. 42

Zhang, Y., Abraham, O., Grondin, F., Loukili, A., Tournat, V., Duff, A. L., Lascoup, B., and Durand, O. (2012). Study of stress-induced velocity variation in concrete under direct tensile force and monitoring of the damage level by using thermally-compensated Coda Wave Interferometry. *Ultrasonics*, 52(8):1038–1045. 2, 16

l'université nantes angers le mans

PÔLE DE RECHERCHE ET D'ENSEIGNEMENT SUPÉRIEUR

UNIVERSITÉ DE NANTES

Thèse de Doctorat

Xiaoting XIAO

Détermination de gradients de teneur en eau dans les bétons par méthodes électromagnétiques

Résumé

Les problèmes de vieillissement des structures de génie civil nécessitent l'évaluation des indicateurs de durabilité (comme la porosité) et des paramètres d'état (comme la teneur en eau et la teneur en chlorure). Parmi les techniques de contrôle non destructif électromagnétique (EM), le radar géophysique (GPR) est utilisé pour estimer la permittivité du béton. L'étude générale est composée de trois objectifs. Tout d'abord, établir une interaction physique et mathématique entre les ondes et les matériaux. Pour mieux comprendre la propagation des ondes EM à l'intérieur du matériau, nous avons étudié plusieurs modèles de dispersion caractérisant les propriétés diélectriques de béton : le modèle de Debye et le modèle de Jonscher proposant de bonnes performances. Deuxièmement, développer une nouvelle méthode d'auscultation pour détecter les gradients de permittivité dans un matériau dispersif en considérant le matériau comme un guide d'ondes. La vitesse de phase des ondes électromagnétiques guidées est utilisée pour extraire les informations diélectrique et géométrique de celui-ci. Une nouvelle méthode d'inversion est mise en oeuvre pour répondre au problème. Le guide d'onde à une couche est ensuite décliné en guide d'ondes à plusieurs couches à l'aide d'un modèle de mélange diélectrique: le modèle parallèle. Ainsi, le nouveau modèle de guide d'onde multi-couches est validé à la fois sur des données synthétiques et expérimentales. Enfin, un suivi expérimental d'imbibition d'eau dans du béton est réalisé avec cette nouvelle méthode d'auscultation, les résultats étant comparés à ceux de gammadensimétrie, considérée comme référence.

Mots clés

Radar géophysique, constante dielectrique, ondes guidées dispersives, inversion, béton, teneur en eau

Abstract

Considering the aging problems of civil engineering structures induces the evaluation of durability indicators (such as porosity) and durability monitoring parameters (such as water content and chloride content). From the electromagnetic (EM) non-destructive testing, Ground penetrating radar (GPR) is used by surveying permittivity inside concrete.
The general study is composed of three objectives. Firstly, establish a physical and mathematical interaction between the waves and the materials. To better understand the propagation of EM waves inside the material, we have studied on several dispersion models characterizing the dielectric properties of concrete, and used Debye's model and Jonscher's model getting good working performance. Secondly, develop a new method for GPR to detect the gradients of relative permittivity in a dispersive material. With knowledge of the speed of radar waves travelling through the medium, we are able to know the relative permittivity of the material. As the material can form a waveguide for EM waves. The phase velocity of the guided EM waves is used to extract the dielectric and geometric information of it. Then, a new inversion method is implemented to estimate the dielectric permittivity and geometry of the waveguides. The one-layer waveguide is developed into multi-layer waveguide by a dielectric mixing model: parallel model. Thus, the new multi-layer waveguide model is validated both on synthetic and experimental data. Finally, monitor water transferring inside the concrete slabs with the new developed method, the results being compared with those from gammadensimetry, considered as reference.

Key Words

Ground penetrating radar, dielectric constant, waveguide dispersion, inversion, concrete, water content